Mesoscale Organization of Nanoparticle Assemblies: Looking Into Superstructures and Aggregates

Jan Bart ten Hove

Mesoscale Organization of Nanoparticle Assemblies: Looking Into Superstructures and Aggregates

Jan Bart ten Hove

Thesis committee

Promotor
Prof. Dr A.H. Velders
Professor of BioNanoTechnology
Wageningen University & Research

Co-promotor
Dr F.W.B. van Leeuwen
Associate professor, Department of Radiology
Leiden University and Medical Center

Other members
Dr J.W.M. van Lent, Wageningen University & Research
Prof. Dr F.A.M. Leermakers, Wageningen University & Research
Dr I.K. Voets, Eindhoven University of Technology
Dr C.A. Nijhuis, National University of Singapore, SG

This research was conducted under the auspices of the Graduate School VLAG (Advanced studies in Food Technology, Agrobiotechnology, Nutrition and Health Sciences).

Mesoscale Organization of Nanoparticle Assemblies: Looking Into Superstructures and Aggregates

Jan Bart ten Hove

Thesis
submitted in fulfilment of the requirements for the degree of doctor
at Wageningen University
by the authority of the Rector Magnificus,
Prof. Dr A.P.J. Mol,
in the presence of the
Thesis Committee appointed by the Academic Board
to be defended in public
on Friday 20 April 2018
at 11 a.m. in the Aula.

Jan Bart ten Hove

Mesoscale Organization of Nanoparticle Assemblies:

Looking Into Superstructures and Aggregates

182 pages.

PhD thesis, Wageningen University, Wageningen, the Netherlands (2018)
With references, with summaries in English and Dutch

ISBN: 978-94-6343-839-1
DOI: https://doi.org/10.18174/443807

This thesis is dedicated to my parents,
For their endless love, support, and encouragement

Pa en Ma, ik draag deze thesis aan jullie op,
vanwege jullie eindeloze liefde, ondersteuning en aansporing.

Mesoscale Organization of Nanoparticle Assemblies:

Looking Into Superstructures and Aggregates

CONTENT:

Chapter 1

Introduction

In this chapter, background information on the concepts, materials and technologies used in this thesis is provided. The prevalence of self-assembly, its use to construct well-defined nanomaterials from molecular building blocks, and the analysis of these materials by electron microscopy are discussed. The initial motivation for this research was to investigate the self-assembly behavior of small, well-defined, building blocks into complex coacervate-core micelles and in particular exploiting the high contrast of gold nanoparticles in Transmission Electron Microscopy, and to investigate the influence of a templating matrix on the subsequent organization of these micelles. At the end of the chapter, the outline of this thesis is given.

1.1 Order and Self-Assembly

Order, defined by the Oxford dictionary as "*the arrangement or disposition of people or things in relation to each other according to a particular sequence, pattern, or method*", is a concept appearing universally and at all length scales, with a few typical examples shown in Figure **1-1**. Order appears at extremely large — almost unfathomable — length scales in galaxies spanning light-years across (Figure **1-1a**), at a macroscopic scale in living organisms such as plants (Figure **1-1b**), and at the extremely small atomic length scale, in, for example, atoms that order and arrange, forming new structures (Figure **1-1c)**. With order also comes symmetry and patterns, which have fascinated and inspired mankind through the ages, not only in science but also in art. Curiosity has led us to investigate and study the order present in nature in great detail through the ages. For example, the enigmatic ordering and symmetry observed in nature was first extensively studied by D'Arcy Thompson in his seminal book, "*On growth and form"* (1917).[1] In nature, order is created by the self-assembly of smaller subunits into a new, larger structure. Understanding the emergence of order is key to design and develop novel materials, for which self-assembly is a versatile method.

*Figure **1-1** Order and organization are present at all length scales: **a**) at extreme length scales in spiral galaxies, **b**) at the macroscopic scale in sunflowers and **c**) at extremely small, atomic length scales in, for example, diamonds, where the carbon atoms are ordered in a diamond-cubic crystal structure.*

Self-assembly is the process in which discrete, disordered, building blocks assemble spontaneously into bigger, more organized structures. Following Whitesides and Grzybowski, self-assembly is defined as the *reversible* process through which order emerges from the recombination of disordered subcomponents that interact autonomously *via* well-defined interactions, for example by chemical or physical interactions, or indirectly *via* their environment, such as by a template or by an applied external field or force.[2] Self-assembly can be subdivided into three main categories, namely static, dynamic, and templated self-assembly. In a static self-assembled system, the free energy of the self-assembled system is in either a local or global minimum, (*i.e.* a kinetically trapped system *versus* a system in thermodynamic equilibrium). Kinetically-trapped are trapped systems that require the input energy in order to overcome an activation barrier. The amount of energy required is larger than provided by thermal fluctuations, hence requiring the input of external energy to overcome this barrier. Systems in a thermodynamic equilibrium constantly break and form again, and hence achieve a global minimum of their free energy. Dynamic self-assembled systems require a continuous energy input in order for them to grow or be sustained.[3,4] Templated self-assembly is the process in which systems organize into higher-order structures under the influence of a template such as a surface, interface or an external field (*e.g.,* under flow, electrical or magnetic fields).[5,6] Building blocks for self-assembly are numerous. Molecular crystals or viruses are widely recognized as self-assembled structures; weather systems, schools of fish, and even galaxies can be considered self-assembled systems.[2] On the mesoscopic or macroscopic scale, self-assembly can take place *via, e.g.,* capillary,[7] gravitational[8] or magnetic interactions.[9] On the molecular scale, a wide variety of building blocks, including macromolecules such as DNA and RNA, polymers and polyelectrolytes, and even nanoparticles, are known to self-assemble into higher order structures. Here, typical examples of interactions that can lead to self-assembly are charge interactions, hydrophobic interactions, **π-π** interactions, hydrogen bonding and coordination bonds. Construction of new (nano)materials can be generalized into both the top-down and bottom-up approaches, similar to carving respectively constructing in the macroscopic world. In the top-down approach, a bigger material is gradually broken down into smaller pieces. The bottom-up approach, on the other hand, uses small building blocks that are combined into a bigger (nano-) material. The latter strategy is often encountered in nature,[10] where hierarchically assembled systems, spanning across many length scales, are found.[11] Examples of such a system are the capsids of viruses, where many capsid proteins self-assembled into the larger, roughly spherical viral coat.[12] The polymerization of actin monomers into large filaments that are involved with cell shape and muscle contraction is another example of a self-assembly process in nature.[13] Colloidal crystals and micelles are, on the other hand, examples of a fabricated self-assembled nanomaterials.

1.2 Self-Assembled Micelles

Among the abundance of self-assembled nanomaterials, micelles are a class of well-defined nanomaterials that are thought to mimic their biological counterparts (for example, viruses, lipoproteins) in the sense that they can encapsulate and transport a payload in their core, operating as a molecular box.[14,15] Micelles self-assemble from the respective molecular building blocks at concentrations above the critical micelle concentration (CMC). Many different types of interactions can lead to the formation of micelles; typical examples of the interactions playing a role in micelle formation include hydrophobic interactions,[16] **π-π**-stacking,[17] metal complexation,[18,19] hydrogen bonding,[20] charge interactions[21,22] or a combination of these,[23,24] as shown in Figure **1-2**.

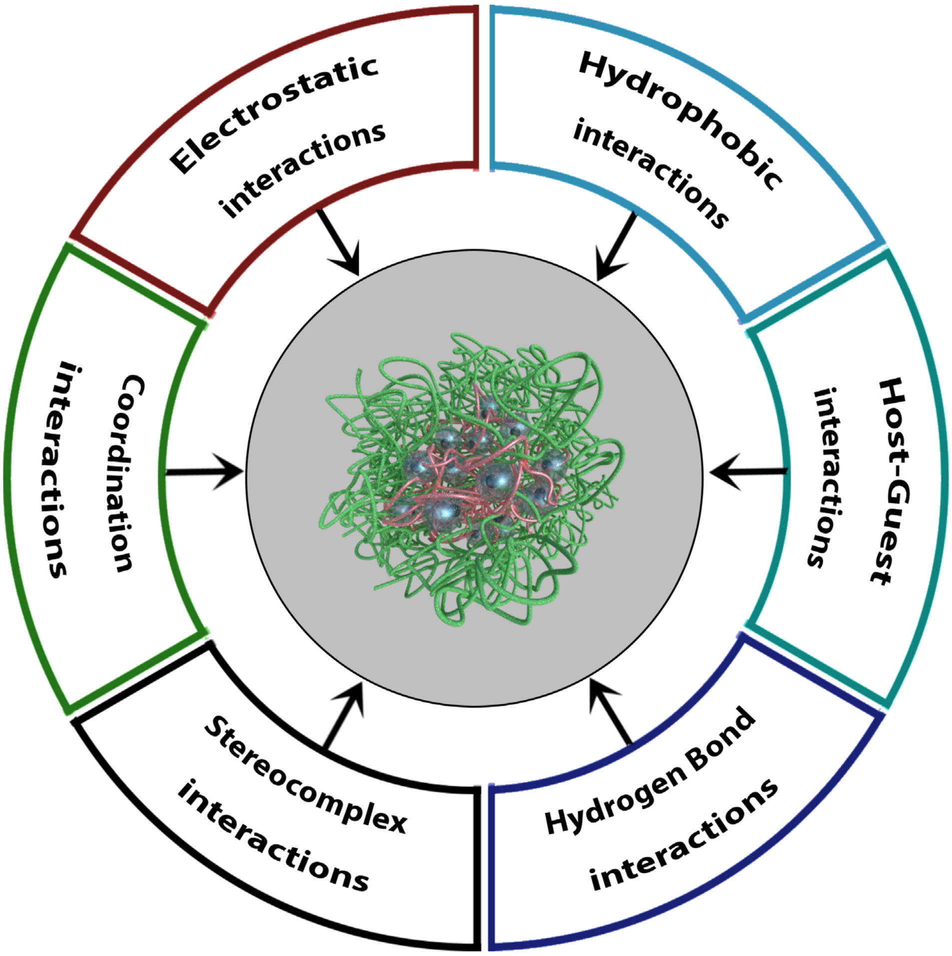

Figure ***1-2*** Overview of the interactions that can lead to the self-assembly of molecular building blocks into micelles. Figure made by the author, adapted from the framework and interactions as described by *J. Ding et al.*[23]

A general drawback of micelles is their limited stability against dilution. If the concentration of the micelles drops below the CMC, the micelles disassemble into the molecular building blocks. Compared to surfactant-based micelles, polymeric micelles have a significantly lowered CMC and dissociation rate, corresponding to an increased stability.[14] Micelles formed by the self-assembly of oppositely-charged block copolymers were first reported by Harada and Kataoka in 1995,[25] and are known under various names (*i.e.* polyion complex micelles, block ionomer complexes, complex coacervate core micelles).[26] They consist of a self-assembled core that is stabilized from macroscopic phase separation by the micelle corona, which often consists of a neutrally charged, water-soluble, poly(ethyleneoxide) (PEO) block.

In this thesis, the term “complex coacervate core micelles” (or C3Ms in short) is used to describe the micelles that self-assembled based on electrostatic interactions. As their name suggests, complex coacervate core micelles have a core that consists of the electrostatically-assembled complex of oppositely-charged (diblock) polymers, which is stabilized against macroscopic phase separation by a neutrally-charged polymeric block. This neutral block can be attached to either – or both – of the charged blocks of the core.[25,27] C3Ms can be made with a narrow size distribution, and are in general more stable than surfactant-based micelles.[28] Because of their stability and potential as drug carriers, microreactors, or imaging agents, C3Ms have been extensively investigated using a wide variety of building blocks, including metal coordination polymers,[18,19,29,30] proteins[31-33] and dendrimers.[22,34] The encapsulation properties of dendrimers and their amphiphilic character, having hydrophilic end groups and a hydrophobic core, has led to their description as molecular boxes or unimolecular micelles.[35,36] Dendrimers resemble supramolecularly assembled micelles in their physical appearance, however, compared to conventional supramolecular micelles, unimolecular dendrimer micelles consist of a well-defined single molecule with a controllable surface composition.[35] Being a single molecule, dendrimers lack some of the drawbacks associated with supramolecular micelles, they neither disassemble upon dilution, nor at increased ionic strength and are stable over a wider pH range.[37]

1.3 PAMAM dendrimers

Dendrimers are well-defined and hyperbranched macromolecules that belong to the class of dendritic polymers.[38,39] Their name is derived from the Greek word *dendron* (meaning tree), reflecting on the tree-like branching of their molecular structure. The tree-like branching of dendrimers gives them a roughly spherical shape and especially the higher generations (>5) can be seen as archetypical soft nanoparticles in the 1-10 nm range. Since the early 1980's, many different types of dendrimers have been synthesized and reported in literature,[39,40] with Poly(AMidoAMine) (PAMAM) dendrimers being the most well-known and studied dendrimers, and the first to be commercialized.[41] PAMAM dendrimers, first reported in literature in 1985 by Tomalia,[42] are synthesized divergently, starting typically from a diamine core (mostly ethylenediamine or 1,4-diaminobutane), which is reacted in the first step with methyl acrylate, followed by reaction with ethylene diamine in the next step, yielding the generation 0 PAMAM dendrimer as depicted in purple in Figure **1-3**.

The first, methyl acrylate, reaction step results in branching of the PAMAM molecule, and the second, ethylene diamine, reaction step provides the amine functionality required to obtain the next generation. To obtain the next dendrimer generation, these reaction steps are repeated, yielding PAMAM generation 1, as shown in green in Figure **1-3**. The branching of the PAMAM dendrimer results in an exponential increase in the number of end groups with increasing generation.[39] Whereas PAMAM generation 1 only has 8 end groups, this is increased to a theoretical 4096 in the case of PAMAM generation 10. As the size of the PAMAM dendrimer increases roughly by $2^{1/3}$ and the number of end groups doubles per generation, this yields a higher density of surface groups for higher generations. For ethylenediamine-core PAMAM, generation 11 is said to be the theoretical limit where the packing density of surface groups reaches the *de Gennes*-limit, restricting further uniform growth.[40,43] PAMAM dendrimers can be synthesized with many different surface groups, with the most common surface functionalities being hydroxyl groups, carboxylic acids or amines.[40] Carboxylic acid terminated dendrimers are usually obtained as half-generations by omitting the last ethylenediamine reaction step, whereas hydroxyl-terminated dendrimers are obtained by substituting ethylenediamine in the last reaction step by an hydroxylamine. The surface groups of PAMAM have an influence on the characteristics of the dendrimer, for example the cytotoxicity of PAMAN is higher for cationic dendrimers than it is for anionic or neutrally-charged PAMAM dendrimers.[44] Moreover, the dendrimer end groups can also affect the type of cargo that can be placed inside the dendrimer.

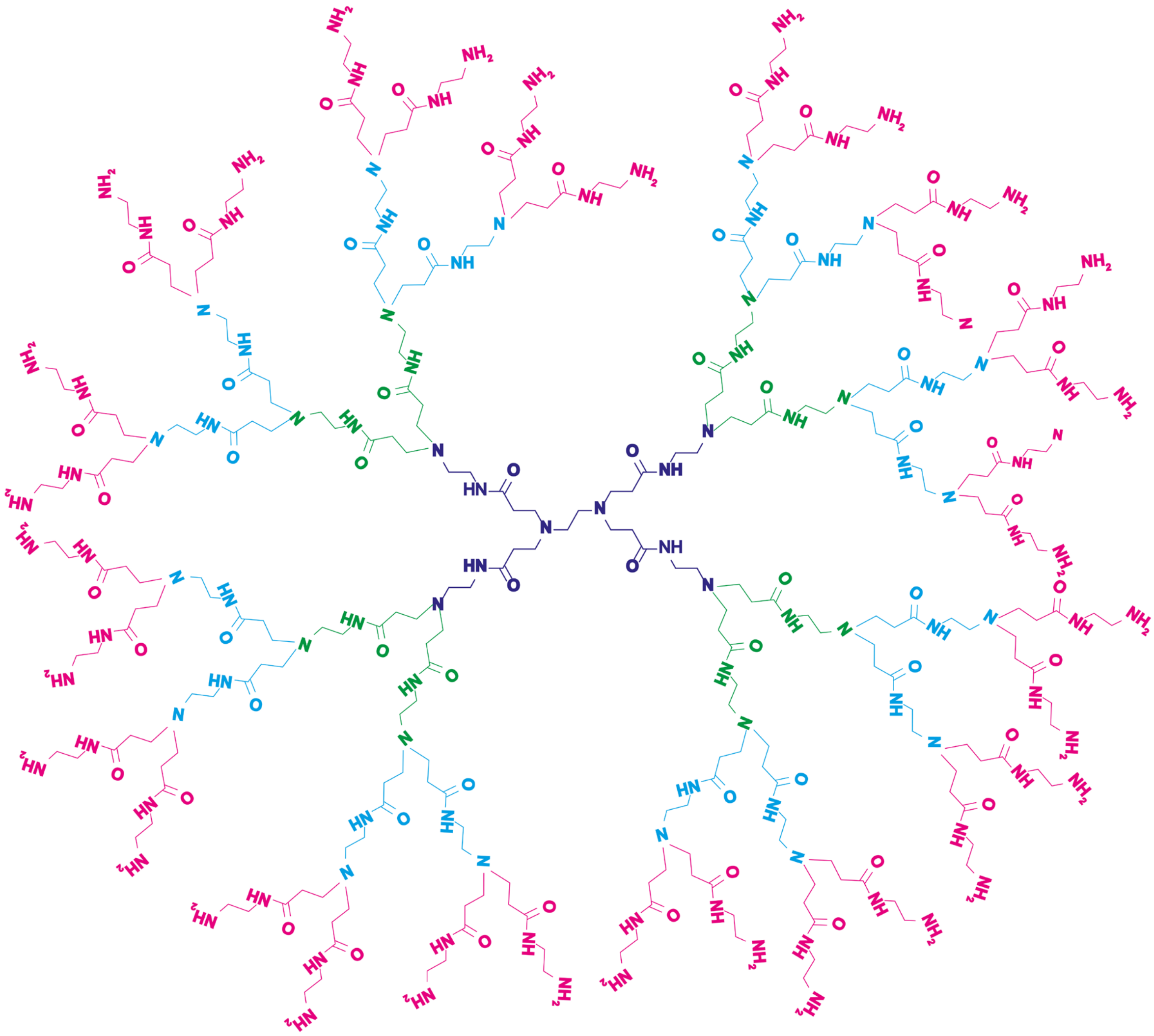

*Figure **1-3** Molecular structure of a PAMAM generation 3 dendrimer. This dendrimer is based on an ethylenediamine-based core (PAMAM generation 0 shown in purple). Generation 1 is shown in green and every increasing generation is depicted with a different color.*

1.4 Dendrimer encapsulated nanoparticles

The void space present in the interior of the dendrimers has the potential to encapsulate molecules or nanoparticles.[45-48] As a result, dendrimers are sometimes being referred to as molecular boxes. The synthesis and encapsulation of nanoparticles inside PAMAM dendrimers has extensively been studied since the late 1990's by Crooks and collaborators.[47,49-54] Many different types of nanoparticles can be synthesized inside PAMAM dendrimers, including monometallic nanoparticles (e.g., Au, Ag, Pd, Cu, Pt),[49] bimetallic or alloyed nanoparticles (*e.g.*, PdAu, AuAg)[52,55] and even non-metallic fluorescent nanoparticles, such as CdS quantum dots.[56] Figure **1-4** schematically depicts the synthesis of a metal nanoparticle inside a PAMAM dendrimer. First, metal ions added to the dendrimer solution form a complex primarily with the dendrimer tertiary amines (*i.e.,* the amines located at the dendrimer branching points). Depending on the type of metal ion, this complexation takes between ~5 minutes (in the case of Cu^{2+}) and 3 days (for Pt^{2+}).[57] Subsequently, reduction of the metal ions using sodium borohydride yields a metal nanoparticle that resides in the dendrimer interior cavity. The maximum number of metal ions that can be complexed in one step inside a PAMAM dendrimer is equal to the number of tertiary amines, which is about the same as the number of end groups.[47,49-54] The size of the formed nanoparticle is determined by the number of metal ions complexed inside the dendrimer, addition of 64 equivalents of metal ions to dendrimer yields dendrimer-encapsulated nanoparticles that consist of an average 64 gold atoms per nanoparticle. The number of tertiary amines inside the dendrimer is directly proportional to the dendrimer generation; this infers that inside higher generation dendrimers, larger nanoparticles can be formed. For example, as a generation 4 PAMAM dendrimer has 64 end groups, the number of metal ions that can be complexed inside this dendrimer is ~64 metal ions, giving ~Au_{64}DENs.

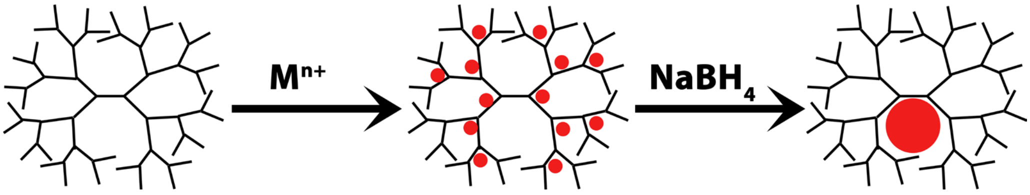

*Figure **1-4** Scheme depicting the formation of dendrimer-encapsulated nanoparticles. First, metal ions (Cu^{2+}, Au^{3+}, Pd^{2+}, etc) added to a PAMAM solution. These ions complex with the tertiary amines located at the dendrimer branching points, and subsequent addition of a reducing agent reduces the ions to zerovalent metal, forming the nanoparticle.*

The work of Crooks and Amis showed that only the higher PAMAM dendrimer generations (*i.e.*, generations 6 through 9) can effectively encapsulate a single nanoparticle inside their interior cavities, yielding the so-called dendrimer-encapsulated nanoparticles (DENs)[49,54]. PAMAM generations 0-3 tend to form dendrimer-stabilized nanoparticles (DSNPs), where a single nanoparticle is stabilized by multiple dendrimers rather than being encapsulated in a single, individual dendrimer. Consequentially, DSNPs are considerably larger than DENS.[54] Fourth- and fifth-generation PAMAM dendrimers can be considered ‘hybrids’ in the sense that both DENs as well as DSNPs can form.[54,58] For example, using nuclear magnetic resonance (NMR) spectroscopy, it was unambiguously proven by Gomez *et al.* that palladium nanoparticles, formed in hydroxyl-terminated generation 4 and 6 PAMAM dendrimers, indeed reside *inside* the PAMAM dendrimers, and hence are DENs.[58,59] The work of Grohn *et al.*, however, showed that amine-terminated PAMAM generation 4 dendrimers yielded dendrimer-stabilized nanoparticles, whereas generation 5 dendrimers resulted in a mix of DSNPs and DENs.[54]

1.5 Dendrimers in Micelles

Charged end groups on dendrimers allow for self-assembly with oppositely-charged building blocks into large assemblies. Most of those reported in literature, however, are ill-defined aggregates instead of well-defined micelles.[60-63] Wang *et al.* were the first to show the well-defined and controlled self-assembly of negatively-charged, carboxylic acid-terminated PAMAM dendrimers into highly stable (dendri)micelles. The dendrimers self-assembled upon addition of an oppositely-charged block copolymer, consisting of a 128 subunit quaternized poly(vinylpyridine) connected to a 477-subunit poly(ethylene oxide) block. Using light scattering techniques, they found that –depending on the dendrimer generation used– stable, 50 nanometer-sized dendrimicelles formed from PAMAM dendrimers generation 2-10. Charge titration experiments showed charge stoichiometry of these dendrimicelles to be around ~1:1 charge mixing of the components, according to expectations for C3Ms. Furthermore, it was derived that the number of dendrimers per dendrimicelles could be controlled between 1 and 100 by changing the dendrimer generation used for micelle formation.[22] Moreover, dendrimicelles made from dendrimers of generations <6 only formed well-defined dendrimicelles at charge-stoichiometry. At off-stoichiometric mixing of block copolymer to dendrimer, larger structures were formed, which was attributed to asymmetrical, worm-like micelles and polydisperse aggregates. Both micelles and dendrimers can be regarded as molecular boxes, and therefore, dendrimicelles can be seen as box-in-a-box system, with the dendrimicelle-'molecular box' containing multiple dendrimer 'molecular boxes'. To investigate the self-assembly of dendrimers into dendrimicelles, we hypothesize a powerful strategy could be to self-assemble DENs into dendrimicelles, forming a particle-in-a-box-in-a-box-system. The dendrimicelle aggregation numbers can then be determined by simply counting the number of nanoparticles per dendrimicelle. Using amine-terminated dendrimers would be the most suitable for this, as carboxylic acid-terminated dendrimers are not compatible with the synthesis of a nanoparticle in their interior voids, and hydroxyl-terminated dendrimers lack the required surface charge for self-assembly into C3Ms. Also, in order to visualize the formed dendrimicelles, visible light microscopy is unsuitable, and instead electron microscopy should be used to visualize the micelles.

1.6 Electron Microscopy

While on the macroscopic scale objects can simply be seen with the naked eye, on the microscopic scale a microscope is required to see the object of interest. For visible-light microscopy, the resolution limit is about equal to half the wavelength of the light used (the so-called *Abbe*-limit).[64] As a result, objects smaller than a few hundred nanometers are too small to be well-resolved by a visible light microscope, requiring a "light" source with a smaller wavelength.[65] Electron microscopy has been developed for this; compared to visible light, the wavelength of electrons is roughly five orders of magnitude smaller, corresponding to an equivalent improvement in the theoretically obtainable resolution. By using electrons as the light source, the resolution of microscopy is increased to the atomic scale, enabling and facilitating the visualization of nanomaterials like nanoparticles and micelles.[66] Transmission Electron Microscopy, TEM, uses electrons as light source, and with this imaging technique, contrast in the obtained image is derived from differences in absorption/scattering of the electron beam between the sample and the support grid on which the sample is deposited; the thickness and density as well as the type of material influence the obtained contrast. For TEM, the presence of a high vacuum inside the microscope is required, both for the electron source to work, as well as to increase the electron mean free path (*i.e.* reducing the number of collisions electrons have before they interact with the specimen).[67] Therefore, removal of solvent from the sample is necessary before imaging with TEM. This drying process can affect the sample by, for example, inducing the aggregation or collapsing of structures in the sample.[68-70] To overcome the effects of drying in normal TEM, cryoTEM has been developed in the 80's by Dubochet and collaborators.[67,71]

For cryoTEM sample preparation, instead of drying the sample on a TEM sample grid, it is placed on a hydrophilic grid containing numerous micrometer-sized holes, as shown in Figure **1-5**. The grid is kept in an environment with a controlled humidity, and after blotting away excess solution, the grid holes are filled with a thin, freestanding water film. The thickness of this film is less than 100 nm, and because of the dual air-water interface is biconcave-shaped.[72,73] Water films this thin are inherently instable,[74] and to prevent collapse of the water film, the humidity is kept at 100%. To vitrify the thin water films, the TEM grid is plunged into a container filled with liquid ethane at its melting point (-183 °C). The heat capacity of ethane results in an extremely fast cooling of the thin water films (cooling rate ~ 10^6 ^{o}C.s^{-1}), freezing the water layer.[73] Because of this extreme cooling rate, water does not have enough time to crystallize, and therefore vitreous ice is formed. Having vitreous ice instead of crystalline ice serves a dual purpose: Not only does this provide a homogeneous background without degradation of the image quality derived from diffraction, it also prevents damage to the sample caused by ice crystals.[75] After vitrification, the sample grid needs to be kept at liquid nitrogen temperatures, to prevent melting or devitrification of the ice.[71] Therefore, subsequent microscopy is done at ~-180 ^{o}C, and both the cryoTEM sample holder as well as the electron microscope are cooled down to ~liquid nitrogen temperatures to prevent degradation of the sample. Besides keeping the sample at low temperatures, another point of consideration during microscopy is the electron dose that the sample receives. The electron dose, expressed as the number of electrons per Angstrom-squared, is a measure for the irradiation that the sample received during the image acquisition. To prevent electron-induced damage to the sample, this dose (expressed as the number of electrons per Angstrom-squared) is kept low, for cryoTEM usually below 20 $e^-/Å^2$ per micrograph.[73]

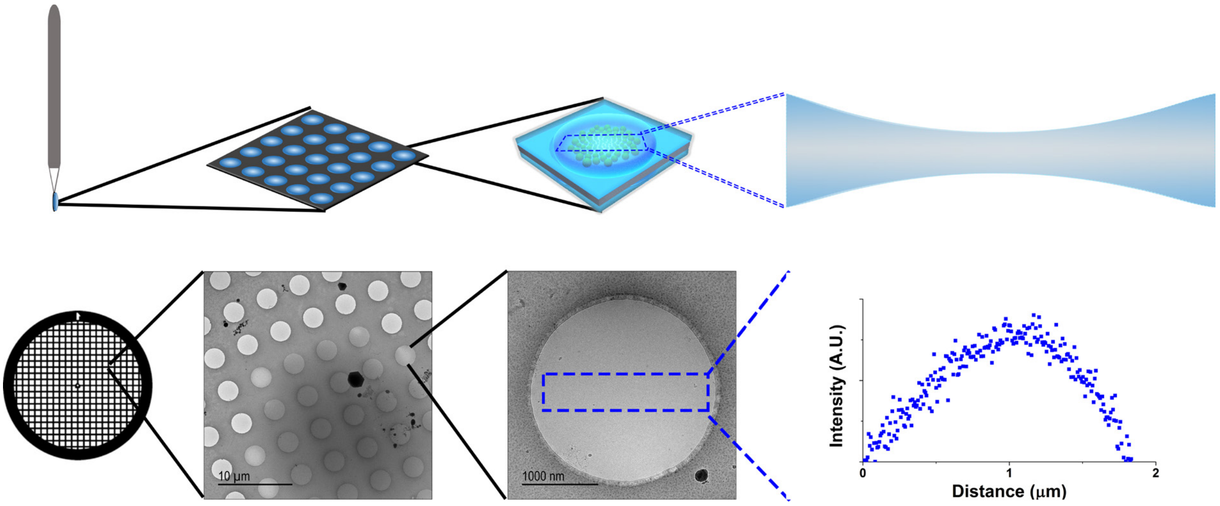

Figure ***1-5*** Top: Schematic overview of cryoTEM sample preparation. From left to right: The sample is placed on a 3 mm copper mesh grid that serves as structural support for a thin carbon film that is placed on top of the grid. The carbon film contains numerous micrometer-sized holes that are filled with a thin layer of water. The water layer is biconcave in shape, and could serve as template to induce the size sorting on nanomaterials embedded inside. Bottom: from left to right: the 3 mm TEM grid, a cryoTEM micrograph of the carbon support film containing the grid holes, some of which are water-filled. Right: an image gray scale intensity profile over the thin water-film inside a grid hole shows that the film is thinnest in the center of the hole.

1.7 Motivation and Outline of this Thesis

At the nanoscale, new materials and structures can be constructed relatively easily from smaller, molecular building blocks using self-assembly or by chemical synthesis. However, the controlled hierarchical assembly of nanomaterials into larger superstructures still remains challenging at the mesoscopic scale —sizes ranging from a few hundred nanometer to a few micrometer— and is therefore of interest to study.[76] The initial motivation for this research was to investigate the self-assembly of both amine-terminated dendrimers into well-defined dendrimicelles. The goal was to investigate whether dendrimer-encapsulated nanoparticles can be used to determine the dendrimicelle aggregation numbers. PAMAM dendrimers generations 5 through 9 are presented in this thesis, and the formed dendrimicelles have been studied with light scattering and cryo-electron microscopy techniques. The micelle-embedded nanoparticles serve a dualistic purpose; besides providing contrast in the obtained cryoTEM images, they also reveal the dendrimer aggregation numbers —and variations thereof— inside the dendrimicelle cores. Additionally, the biconcave thin water film formed during cryoTEM sample is anticipated to serve as a template to induce the self-organization and size-sorting of dendrimicelles. A second goal was study the effect of a biconcave-shaped thin film template on the self-organization of dendrimicelles into superstructures. Using off-stoichiometric mixing ratios of the charged building blocks during dendrimicelle self-assembly is expected to increase the dendrimicelle polydispersity, which, in turn, could yield an increased size-sorting in the formed dendrimicelle superstructures. Lastly, the formed dendrimicelle superstructures are used to induce and follow the nanoscale rupture of thin films. Here, the dendrimicelle-embedded nanoparticles provide contrast and allow to follow and study the rupture process in great detail.

In **Chapter 2**, the formation of nanoparticle-containing dendrimicelles from PAMAM generation 7 dendrimers is presented. With cryoTEM, tuning of the dendrimicelle composition is studied by varying the mixing ratio of empty and nanoparticle-filled dendrimers. Using DLS, the stability of the formed dendrimicelles *versus* ionic strength, pH, and over time are investigated. CryoTEM is used to study exchange of dendrimers between individual dendrimicelles. The effect of the dendrimicelle molecular box on the thiol-induced degradation of dendrimer-encapsulated gold nanoparticles is studied.

In **Chapter 3**, PAMAM generations 7 through 9 are used to study the formation dendrimicelles at charge-stoichiometry and under off-stoichiometrical conditions; the dendrimicelles are investigated using DLS and cryoTEM. The self-organization into monolayer superstructures, and the effect of induced polydispersity on this self-organizing behavior is investigated. In some cases, the dendrimicelles organize into double-spiral patterns similar to those observed in macroscopic systems.

In **Chapter 4,** we use the dendrimicelle superstructures, formed during cryoTEM sample preparation, to investigate the rupture of thin films on the nanoscale upon prolonged exposure to an electron beam. We uniquely investigate the processes that take place before rupture, and use the gold nanoparticles as tracer, showing local as well as global migration of the individual dendrimicelles.

In **Chapter 5**, the formation of dendrimicelles from fifth generation based dendrimer-encapsulated and dendrimer-stabilized nanoparticles is studied, and the subsequent self-assembly into dendrimicelles is studied. The effect of induced polydispersity on the formation of dendrimicelles and dendrimicelle superstructures is studied by using off-stoichiometric block copolymer mixing ratios.

In **Chapter 6**, a general discussion on the investigation of self-assembling nanostructures as used throughout the chapters of this thesis is provided. The findings, limitations, some of the possibilities and implications are discussed and an outlook coming forth from the four experimental chapters is given. Suggestions for further research are provided and concluding statements and a conclusion are provided.

1.8 References

1. Thompson, D. A. W. *On Growth and Form*; Cambridge University Press: 1917.

2. Whitesides, G. M.; Grzybowski, B. Self-Assembly at All Scales. *Science* **2002**, 295, 2418-2421.

3. Timonen, J. V. I.; Latikka, M.; Leibler, L.; Ras, R. H. A.; Ikkala, O. Switchable Static and Dynamic Self-Assembly of Magnetic Droplets on Superhydrophobic Surfaces. *Science* **2013**, 341, 253-257.

4. Grzybowski, B. A.; Stone, H. A.; Whitesides, G. M. Dynamic Self-Assembly of Magnetized, Millimetre-Sized Objects Rotating at a Liquid-Air Interface. **2000**, 405, 1033-1036.

5. Ershov, D.; Sprakel, J.; Appel, J.; Cohen Stuart, M. A.; van der Gucht, J. Capillarity-Induced Ordering of Spherical Colloids on an Interface with Anisotropic Curvature. *Proceedings of the National Academy of Sciences* **2013**, 110, 9220-9224.

6. Grzelczak, M.; Vermant, J.; Furst, E. M.; Liz-Marzán, L. M. Directed Self-Assembly of Nanoparticles. *ACS Nano* **2010**, 4, 3591-3605.

7. Soligno, G.; Dijkstra, M.; van Roij, R. Self-Assembly of Cubic Colloidal Particles at Fluid-Fluid Interfaces by Hexapolar Capillary Interactions. *Soft Matter* **2017**.

8. McBride, J. M.; Avendano, C. Phase Behaviour and Gravity-Directed Self Assembly of Hard Convex Spherical Caps. *Soft Matter* **2017**, 13, 2085-2098.

9. Mehdizadeh Taheri, S.; Michaelis, M.; Friedrich, T.; Förster, B.; Drechsler, M.; Römer, F. M.; Bösecke, P.; Narayanan, T.; Weber, B.; Rehberg, I.*; et al.* Self-Assembly of Smallest Magnetic Particles. *Proceedings of the National Academy of Sciences* **2015**, 112, 14484-14489.

10. Studart, A. R. Towards High-Performance Bioinspired Composites. *Adv. Mater.* **2012**, 24, 5024-5044.

11. Fratzl, P.; Weinkamer, R. Nature's Hierarchical Materials. *Progress in Materials Science* **2007**, 52, 1263-1334.

12. Seidel, S. R.; Stang, P. J. High-Symmetry Coordination Cages Via Self-Assembly. *Accounts of chemical research* **2002**, 35, 972-83.

13. Wong, G. C. L.; Tang, J. X.; Lin, A.; Li, Y. L.; Janmey, P. A.; Safinya, C. R. Hierarchical Self-Assembly of F-Actin and Cationic Lipid Complexes: Stacked Three-Layer Tubule Networks. *Science* **2000**, 288, 2035-+.

14. Kataoka, K.; Harada, A.; Nagasaki, Y. Block Copolymer Micelles for Drug Delivery: Design, Characterization and Biological Significance. *Advanced Drug Delivery Reviews* **2001**, 47, 113-131.

15. Menger, F. M. Structure of Micelles. *Accounts of chemical research* **1979**, 12, 111-114.

16. Gaucher, G.; Dufresne, M. H.; Sant, V. P.; Kang, N.; Maysinger, D.; Leroux, J. C. Block Copolymer Micelles: Preparation, Characterization and Application in Drug Delivery. *Journal of Controlled Release* **2005**, 109, 169-188.

17. Shi, Y.; van Steenbergen, M. J.; Teunissen, E. A.; Novo, L. s.; Gradmann, S.; Baldus, M.; van Nostrum, C. F.; Hennink, W. E. Π–Π Stacking Increases the Stability and Loading Capacity of Thermosensitive Polymeric Micelles for Chemotherapeutic Drugs. *Biomacromolecules* **2013**, 14, 1826-1837.

18. Wang, J. Y.; Velders, A. H.; Gianolio, E.; Aime, S.; Vergeldt, F. J.; Van As, H.; Yan, Y.; Drechsler, M.; de Keizer, A.; Stuart, M. A. C.*; et al.* Controlled Mixing of Lanthanide(III) Ions in Coacervate Core Micelles. *Chemical Communications* **2013**, 49, 3736-3738.

19. Wang, J. Y.; de Keizer, A.; Fokkink, R.; Yan, Y.; Stuart, M. A. C.; van der Gucht, J. Complex Coacervate Core Micelles from Iron-Based Coordination Polymers. *Journal of Physical Chemistry B* **2010**, 114, 8313-8319.

20. Yang, C.; Ebrahim Attia, A. B.; Tan, J. P. K.; Ke, X.; Gao, S.; Hedrick, J. L.; Yang, Y.-Y. The Role of Non-Covalent Interactions in Anticancer Drug Loading and Kinetic Stability of Polymeric Micelles. *Biomaterials* **2012**, 33, 2971-2979.

21. Voets, I. K.; de Keizer, A.; Cohen Stuart, M. A. Complex Coacervate Core Micelles. *Advances in colloid and interface science* **2009**, 147-148, 300-18.

22. Wang, J.; Voets, I. K.; Fokkink, R.; van der Gucht, J.; Velders, A. H. Controlling the Number of Dendrimers in Dendrimicelle Nanoconjugates from 1 to More Than 100. *Soft Matter* **2014**, 10, 7337-7345.

23. Ding, J.; Chen, L.; Xiao, C.; Chen, L.; Zhuang, X.; Chen, X. Noncovalent Interaction-Assisted Polymeric Micelles for Controlled Drug Delivery. *Chemical Communications* **2014**, 50, 11274-11290.

24. Zhang, J.; Ma, P. X. Cyclodextrin-Based Supramolecular Systems for Drug Delivery: Recent Progress and Future Perspective. *Advanced Drug Delivery Reviews* **2013**, 65, 1215-1233.

25. Harada, A.; Kataoka, K. Formation of Polyion Complex Micelles in an Aqueous Milieu from a Pair of Oppositely-Charged Block Copolymers with Poly(Ethylene Glycol) Segments. *Macromolecules* **1995**, 28, 5294-5299.

26. Voets, I. K.; de Keizer, A.; de Waard, P.; Frederik, P. M.; Bomans, P. H. H.; Schmalz, H.; Walther, A.; King, S. M.; Leermakers, F. A. M.; Cohen Stuart, M. A. Double-Faced Micelles from Water-Soluble Polymers. *Angewandte Chemie* **2006**, 118, 6825-6828.

27. van der Kooij, H. M.; Spruijt, E.; Voets, I. K.; Fokkink, R.; Stuart, M. A. C.; van der Gucht, J. On the Stability and Morphology of Complex Coacervate Core Micelles: From Spherical to Wormlike Micelles. *Langmuir* **2012**, 28, 14180-14191.

28. Voets, I. K.; de Keizer, A.; Stuart, M. A. C. Complex Coacervate Core Micelles. *Advances in Colloid and Interface Science* **2009**, 147-48, 300-318.

29. Wang, J. Y.; Groeneveld, A.; Oikonomou, M.; Prusova, A.; Van As, H.; van Lent, J. W. M.; Velders, A. H. Revealing and Tuning the Core, Structure, Properties and Function of Polymer Micelles with Lanthanide-Coordination Complexes. *Soft Matter* **2016**, 12, 99-105.

30. Wang, J. Y.; Stuart, M. A. C.; Marcelis, A. T. M.; Colomb-Delsuc, M.; Otto, S.; van der Gucht, J. Stable Polymer Micelles Formed by Metal Coordination. *Macromolecules* **2012**, 45, 7179-7185.

31. Nolles, A.; Westphal, A. H.; de Hoop, J. A.; Fokkink, R. G.; Kleijn, J. M.; van Berkel, W. J. H.; Borst, J. W. Encapsulation of Gfp in Complex Coacervate Core Micelles. *Biomacromolecules* **2015**, 16, 1542-1549.

32. Hernandez-Garcia, A.; Velders, A. H.; Stuart, M. A. C.; de Vries, R.; van Lent, J. W. M.; Wang, J. Supramolecular Virus-Like Nanorods by Coassembly of a Triblock Polypeptide and Reversible Coordination Polymers. *Chem. Eur. J.* **2017**, 23, 239-243.

33. Nolles, A.; Westphal, A. H.; Kleijn, J. M.; van Berkel, W. J. H.; Borst, J. W. Colorful Packages: Encapsulation of Fluorescent Proteins in Complex Coacervate Core Micelles. *International Journal of Molecular Sciences* **2017**, 18.

34. Stapert, H. R.; Nishiyama, N.; Jiang, D.-L.; Aida, T.; Kataoka, K. Polyion Complex Micelles Encapsulating Light-Harvesting Ionic Dendrimer Zinc Porphyrins. *Langmuir* **2000**, 16, 8182-8188.

35. Liu, M.; Kono, K.; Frechet, J. M. Water-Soluble Dendritic Unimolecular Micelles: Their Potential as Drug Delivery Agents. *Journal of controlled release : official journal of the Controlled Release Society* **2000**, 65, 121-31.
36. Jansen, J. F.; de Brabander-van den Berg, E. M.; Meijer, E. W. Encapsulation of Guest Molecules into a Dendritic Box. *Science* **1994**, 266, 1226-9.
37. Ambade, A. V.; Savariar, E. N.; Thayumanavan, S. Dendrimeric Micelles for Controlled Drug Release and Targeted Delivery. *Molecular pharmaceutics* **2005**, 2, 264-272.
38. Tomalia, D. A.; Naylor, A. M.; Goddard, W. A. Starburst Dendrimers - Molecular-Level Control of Size, Shape, Surface-Chemistry, Topology, and Flexibility from Atoms to Macroscopic Matter. *Angewandte Chemie-International Edition in English* **1990**, 29, 138-175.
39. Newkome, G. R.; Shreiner, C. D. Poly(Amidoamine), Polypropylenimine, and Related Dendrimers and Dendrons Possessing Different 1→2 Branching Motifs: An Overview of the Divergent Procedures. *Polymer* **2008**, 49, 1-173.
40. Svenson, S.; Tomalia, D. A. Dendrimers in Biomedical Applications—Reflections on the Field. *Advanced Drug Delivery Reviews* **2005**, 57, 2106-2129.
41. Esfand, R.; Tomalia, D. A. Poly(Amidoamine) (Pamam) Dendrimers: From Biomimicry to Drug Delivery and Biomedical Applications. *Drug Discovery Today* **2001**, 6, 427-436.
42. Tomalia, D. A.; Baker, H.; Dewald, J.; Hall, M.; Kallos, G.; Martin, S.; Roeck, J.; Ryder, J.; Smith, P. A New Class of Polymers: Starburst-Dendritic Macromolecules. **1985**, 17, 117.
43. Maiti, P. K.; Çağın, T.; Wang, G.; Goddard, W. A. Structure of Pamam Dendrimers: Generations 1 through 11. *Macromolecules* **2004**, 37, 6236-6254.
44. Jevprasesphant, R.; Penny, J.; Jalal, R.; Attwood, D.; McKeown, N. B.; D'Emanuele, A. The Influence of Surface Modification on the Cytotoxicity of Pamam Dendrimers. *International Journal of Pharmaceutics* **2003**, 252, 263-266.
45. Tomalia, D. A. Birth of a New Macromolecular Architecture: Dendrimers as Quantized Building Blocks for Nanoscale Synthetic Polymer Chemistry. *Progress in Polymer Science* **2005**, 30, 294-324.
46. Crooks, R. M.; Zhao, M. Q.; Sun, L.; Chechik, V.; Yeung, L. K. Dendrimer-Encapsulated Metal Nanoparticles: Synthesis, Characterization, and Applications to Catalysis. *Accounts of chemical research* **2001**, 34, 181-190.
47. Zhao, M. Q.; Sun, L.; Crooks, R. M. Preparation of Cu Nanoclusters within Dendrimer Templates. *J. Am. Chem. Soc.* **1998**, 120, 4877-4878.
48. Grohn, F.; Bauer, B. J.; Akpalu, Y. A.; Jackson, C. L.; Amis, E. J. Dendrimer Templates for the Formation of Gold Nanoclusters. *Macromolecules* **2000**, 33, 6042-6050.
49. Scott, R. W. J.; Wilson, O. M.; Crooks, R. M. Synthesis, Characterization, and Applications of Dendrimer-Encapsulated Nanoparticles. *The Journal of Physical Chemistry B* **2005**, 109, 692-704.
50. Scott, R. W. J.; Wilson, O. M.; Oh, S. K.; Kenik, E. A.; Crooks, R. M. Bimetallic Palladium-Gold Dendrimer-Encapsulated Catalysts. *J. Am. Chem. Soc.* **2004**, 126, 15583-15591.
51. Kim, Y.-G.; Oh, S.-K.; Crooks*, R. M. Preparation and Characterization of 1−2 Nm Dendrimer-Encapsulated Gold Nanoparticles Having Very Narrow Size Distributions. *Chemistry of Materials* **2004**, 16, 167172.
52. Scott, R. W. J.; Datye, A. K.; Crooks, R. M. Bimetallic Palladium-Platinum Dendrimer-Encapsulated Catalysts. *J. Am. Chem. Soc.* **2003**, 125, 3708-3709.
53. Crooks, R. M.; Zhao, M.; Sun, L.; Chechik, V.; Yeung, L. K. Dendrimer-Encapsulated Metal Nanoparticles: Synthesis, Characterization, and Applications to Catalysis. *Accounts of Chemical Research* **2001**, 34, 181-190.

54. Gröhn, F.; Bauer, B. J.; Akpalu, Y. A.; Jackson, C. L.; Amis, E. J. Dendrimer Templates for the Formation of Gold Nanoclusters. *Macromolecules* **2000**, 33, 6042-6050.

55. Wilson, O. M.; Scott, R. W. J.; Garcia-Martinez, J. C.; Crooks, R. M. Synthesis, Characterization, and Structure-Selective Extraction of 1-3-Nm Diameter Auag Dendrimer-Encapsulated Bimetallic Nanoparticles. *J. Am. Chem. Soc.* **2005**, 127, 1015-1024.

56. Lemon, B. I.; Crooks, R. M. Preparation and Characterization of Dendrimer-Encapsulated Cds Semiconductor Quantum Dots. *J. Am. Chem. Soc.* **2000**, 122, 12886-12887.

57. Knecht, M. R.; Weir, M. G.; Myers, V. S.; Pyrz, W. D.; Ye, H.; Petkov, V.; Buttrey, D. J.; Frenkel, A. I.; Crooks, R. M. Synthesis and Characterization of Pt Dendrimer-Encapsulated Nanoparticles: Effect of the Template on Nanoparticle Formation. *Chemistry of Materials* **2008**, 20, 5218-5228.

58. Gomez, V. M.; Guerra, J.; Velders, A. H.; Crooks, R. M. Nmr Characterization of Fourth-Generation Pamam Dendrimers in the Presence and Absence of Palladium Dendrimer-Encapsulated Nanoparticles. *Journal of the American Chemical Society* **2009**, 131, 341-350.

59. Gomez, V. M.; Guerra, J.; Myers, S. V.; Crooks, R. M.; Velders, A. H. Nanoparticle Size Determination by (1)H NMR Spectroscopy. *J. Am. Chem. Soc.* **2009**, 131, 14634-14635.

60. Grohn, F. Soft Matter Nanoparticles with Various Shapes and Functionalities Can Form through Electrostatic Self-Assembly. *Soft Matter* **2010**, 6, 4296-4302.

61. Frankamp, B. L.; Boal, A. K.; Rotello, V. M. Controlled Interparticle Spacing through Self-Assembly of Au Nanoparticles and Poly(Amidoamine) Dendrimers. *Journal of the American Chemical Society* **2002**, 124, 15146-15147.

62. Düring, J.; Alex, W.; Zika, A.; Branscheid, R.; Spiecker, E.; Gröhn, F. Dendrimer–Dye Assemblies as Templates for the Formation of Gold Nanostructures. *Macromolecules* **2017**, 50, 6998-7009.

63. Reinhold, F.; Kolb, U.; Lieberwirth, I.; Grohn, F. Assemblies of Double Hydrophilic Block Copolymers and Oppositely Charged Dendrimers. *Langmuir* **2009**, 25, 1345-1351.

64. Beyond the Diffraction Limit. *Nature Photonics* **2009**, 3, 361.

65. Heintzmann, R.; Ficz, G. Breaking the Resolution Limit in Light Microscopy. *Briefings in Functional Genomics* **2006**, 5, 289-301.

66. Kisielowski, C.; Freitag, B.; Bischoff, M.; van Lin, H.; Lazar, S.; Knippels, G.; Tiemeijer, P.; van der Stam, M.; von Harrach, S.; Stekelenburg, M.*; et al.* Detection of Single Atoms and Buried Defects in Three Dimensions by Aberration-Corrected Electron Microscope with 0.5-Å Information Limit. *Microscopy and Microanalysis* **2008**, 14, 469-477.

67. Dubochet, J. Cryo-Em—the First Thirty Years. *Journal of Microscopy* **2012**, 245, 221-224.

68. Friedrich, H.; Frederik, P. M.; de With, G.; Sommerdijk, N. A. J. M. Imaging of Self-Assembled Structures: Interpretation of Tem and Cryo-Tem Images. *Angewandte Chemie International Edition* **2010**, 49, 7850-7858.

69. McKenzie, B. E.; Holder, S. J.; Sommerdijk, N. Assessing Internal Structure of Polymer Assemblies from 2d to 3d Cryotem: Bicontinuous Micelles. *Current Opinion in Colloid & Interface Science* **2012**, 17, 343-349.

70. Patterson, J. P.; Xu, Y. F.; Moradi, M. A.; Sommerdijk, N.; Friedrich, H. Cryotem as an Advanced Analytical Tool for Materials Chemists. *Accounts of chemical research* **2017**, 50, 1495-1501.

71. Dubochet, J.; Adrian, M.; Chang, J.-J.; Homo, J.-C.; Lepault, J.; McDowall, A. W.; Schultz, P. Cryo-Electron Microscopy of Vitrified Specimens. *Quarterly Reviews of Biophysics* **1988**, 21, 129-228.

72. Zheng, Y.; Lin, Z.; Zakin, J. L.; Talmon, Y.; Davis, H. T.; Scriven, L. E. Cryo-Tem Imaging the Flow-Induced Transition from Vesicles to Threadlike Micelles. *The Journal of Physical Chemistry B* **2000**, 104, 5263-5271.
73. Danino, D. Cryo-Tem of Soft Molecular Assemblies. *Current Opinion in Colloid & Interface Science* **2012**, 17, 316-329.
74. Frederik, P. M.; Stuart, M. C. A.; Bomans, P. H. H.; Busing, W. M. Phospholipid, Nature's Own Slide and Cover Slip for Cryo-Electron Microscopy. *Journal of Microscopy* **1989**, 153, 81-92.
75. Thompson, R. F.; Walker, M.; Siebert, C. A.; Muench, S. P.; Ranson, N. A. An Introduction to Sample Preparation and Imaging by Cryo-Electron Microscopy for Structural Biology. *Methods* **2016**, 100, 3-15.
76. Groschel, A. H.; Walther, A.; Lobling, T. I.; Schacher, F. H.; Schmalz, H.; Muller, A. H. E. Guided Hierarchical Co-Assembly of Soft Patchy Nanoparticles. **2013**, 503, 247-251.

Chapter 2

Dendrimer-Encapsulated Nanoparticle-Core Micelles as a Modular Strategy for [Particle-in-a-Box]-in-a-Box Nanostructures

The hierarchically controlled synthesis and characterization of self-assembling macromolecules and particles are key to explore and exploit new nanomaterials. Here we present a versatile strategy for constructing particle-in-a-box-in-a-box systems by assembling dendrimer-encapsulated gold nanoparticles (DENs) into dendrimicelles. This is realized by combining positively charged PAMAM dendrimers with a negative-neutral block copolymer. The number of particles per dendrimicelle can be controlled by mixing DENs with empty PAMAM dendrimers. The dendrimicelles are stable in solution for months and provide improved resistance for the nanoparticles against degradation. The dendrimicelle strategy provides a flexible platform with a plethora of options for variation in the type of nanoparticles, dendrimers and block copolymers used, and hence is tunable for applications ranging from nanomedicine to catalysis.

This chapter has been published in slightly adjusted form as: **Jan Bart ten Hove**, Junyou Wang, Fijs W.B. van Leeuwen and Aldrik H. Velders, *Nanoscale*, **2017**, 9(47):18619-18623. doi: 10.1039/c7nr06773a.

2.1 Introduction

The hierarchical organization of molecules, macromolecules, nanoparticles and self-assembled systems is at the heart of supramolecular and nanoscale chemistry, with nanocontainers being among the most appealing ones for applications ranging from drug delivery to catalysis.[1–4] Within the vast interest in obtaining well-defined nanoparticles in confined systems, micelles and dendrimers have proved to be excellent building blocks. Dendrimers are hyperbranched molecules and are archetypical soft nanoparticles in the 1–10 nanometer range with the potential to encapsulate molecules,[5] or nanoparticles.[6–8] Amis and Crooks and collaborators extensively studied the encapsulation of bare nanoparticles with polyamidoamino (PAMAM) dendrimers,[8–10] and via various NMR techniques we unambiguously proved that (palladium) nanoparticles are formed and reside inside these dendrimers, thus forming so-called dendrimer-encapsulated nanoparticles (DENs).[11,12] Micelles provide a method to self-assemble multiple, e.g., polymeric, molecular building blocks into well-defined structures typically in the 10–100 nanometer range.[13,14] In our investigations of coacervate core micellar systems for e.g. medical applications,[15,16] we recently showed the excellent control over the assembly of negatively charged, carboxylic acid-terminated, PAMAM dendrimers with a positive-neutral poly(vinylpyridine)-poly(ethylene oxide) diblock copolymer into well-defined micelles. These micelles contain 1–100 dendrimers per micelle, depending on the dendrimer generation used.[17] We here present a methodology in which gold nanoparticles in amine-terminated dendrimers, AuDENs, can form micelles by assembling with negative-neutral block copolymers to form a nanoparticle-in-a-box-in-a-box system (Scheme 2-1).

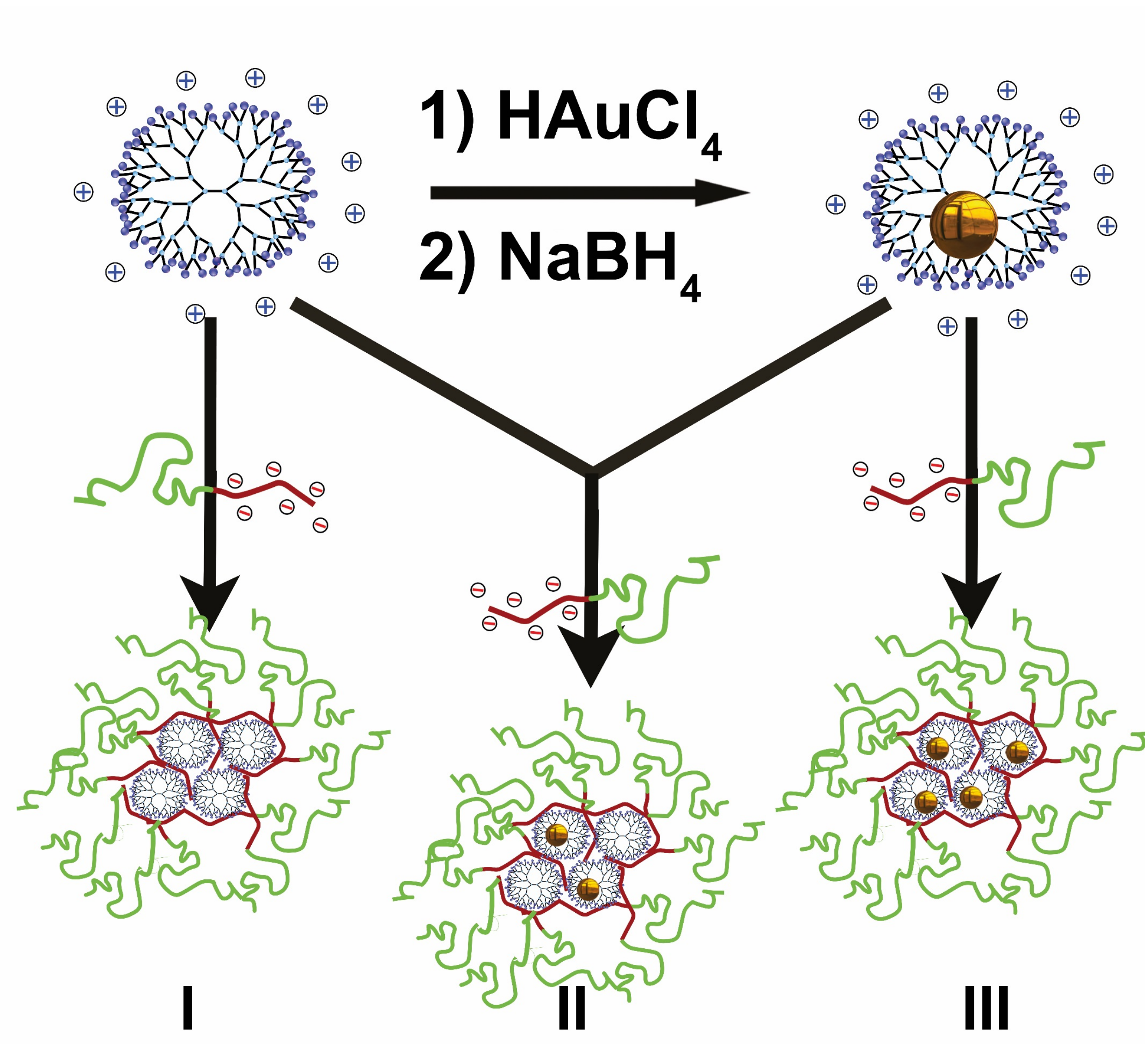

Scheme 2-1 The formation of (particle-in-)a-box-in-a-box. After synthesis of dendrimer-encapsulated Au_{256} *nanoparticles inside 7th generation, amine-terminated, PAMAM dendrimers, charge-stoichiometric addition of an anionic-neutral* $pMAA_{64}PEO_{885}$ *block copolymer results in the formation of dendrimicelles. The number of nanoparticles per dendrimer can be tuned by mixing empty with nanoparticle-filled dendrimers.*

2.2 Experimental

Materials

Amine-terminated polyamidoamino (PAMAM) dendrimers generation 7-9 were obtained from Dendritech Inc., MI, USA as 5 wt% methanolic solutions. $pMAA_{64}$-b-PEO_{885} (Mw/Mn = 1.15) was obtained from Polymer Sources Inc., Canada and used as a 5 mM solution based on carboxylic acid content. HAuCl4.3H2O was obtained from TCI. (3-(N-morpholino)-propanesulfonic acid) (MOPS), $NaBH_4$, 1M HCl and 1M NaOH solutions were obtained from Sigma Aldrich. NaOD, DCl and D2O with a purity of 99.96% D were obtained from Eurisotop, France.

Synthesis of Dendrimer Encapsulated Nanoparticles (DENs)

G7-Au_{256}DENs were made following established protocols.[10] Shortly, 50 µL (17 nmol) of 5 wt% PAMAM G7-NH_2 in methanol was transferred to a 5 mL vial and the solvent was evaporated under reduced pressure. Next, 2 mL of water was added to dissolve the PAMAM and the pH was adjusted to 3 using 1M HCl, after which 256 molar equivalents of Au^{3+} to PAMAM were added as 1 mL of a 4.4 mM aqueous solution of $HAuCl_4$ at pH 3. The resulting solution was then stirred for 20 minutes, after which 44 µL of a 1M solution of $NaBH_4$ in 0.3M NaOH (10 molar equivalents to Au^{3+}) were added. This resulted in the reduction of Au^{3+} to AuDENs, indicated by the change from colorless to a dark brown solution within seconds after addition. After reduction, the pH was set to 7 using HCl and the Au_{256}DENS were stored at 4 ^{o}C as a 5.6 µM solution. To prove that the formed AuNPs reside on the inside of the PAMAM dendrimer (e.g. DENs as opposed to DSNPs), 1H-NMR spectra were analyzed following the approach reported before.[11,12]

Dendrimer Encapsulated Nanoparticles in Micelles

To obtain dendrimicelles under charge stoichiometric conditions, 20 µL of G7-Au_{256} DENs (58 nmol positive charge based on surface groups) was dissolved in 149 µL water and 20 µL of 0.2M MOPS buffer at pH 7.0 was added. Then, 11 µL $pMAA_{64}$-b-PEO_{885} (55 nmol based on -COOH) was added and the sample was sonicated for two minutes. To obtain micelles at off-stoichiometric charge fractions, the amount of block copolymer and water added were adjusted accordingly, keeping the final volume constant at 200 µL. Samples were left to equilibrate for at least one day before characterization using cryoTEM. The nanoparticle-containing dendrimicelles used in this study are stable for at least months as concluded from high-resolution DLS and TEM analyses of fresh and aged solutions of dendrimicelles.

Characterization

Dynamic Light Scattering (DLS) was done on a Malvern Zetasizer Nano S equipped with a laser operating at 633 nm. Sample grids for electron microscopy were obtained from Electron Microscopy Sciences (EMS, Hatfield, PA, USA) and were rendered hydrophilic using a plasma cleaning setup (15 s at 10^{-1} Torr). For cryoTEM, samples were cast on Quantifoil R2/2 grids or 400 mesh Holey Carbon grids. After blotting, samples were plunged into liquid ethane using a Vitrobot system (FEI Company). Samples were imaged at ~ 90K in a JEOL 2100 TEM operating at 200 kV. For normal TEM, solutions were deposited on hydrophilic 400 mesh carbon-coated copper grids. TEM image analyses was done using FIJI (https://fiji.sc/). Nuclear Magnetic Resonance (NMR) spectra in D2O were obtained at 300K on a Bruker 14.1 T Avance III spectrometer operating at 600.13 MHz for 1H, equipped with a 5 mm TXI cryoprobe.

Critical Micelle Concentration (CMC) calculation

The CMC was calculated from plotting the excess Rayleigh ratio (R_θ) as a function of the total polymer concentration, following the approach used by Wang et al.[4] The excess Rayleigh ratio is defined as: $\mathrm{R}_\theta = \frac{\mathrm{I(sample)} - \mathrm{I(solvent)}}{I(toluene)} * R(toluene) * \frac{n^2(solvent)}{n^2(toluene)}$, where I_{sample}, $I_{solvent}$ and $I_{toluene}$ are the scattered light intensity of the sample, the solvent and of a toluene reference, as obtained from DLS experiments. $R_{toluene}$ is the Rayleigh ratio of toluene and $n_{solvent}$ and $n_{toluene}$ are the refractive indices of the solvent (1.333) respectively the toluene reference (1.497).

2.3 Results and Discussion

PAMAM dendrimers exist with a variety of terminating groups.[18,19] For the incorporation of AuNPs, the use of (amine-terminated) PAMAMs is preferred, as PAMAM dendrimers with carboxylic acid end groups tend to form dendrimer stabilized nanoparticles rather than DENS,[20,21] and hydroxyl-terminated dendrimers lack the required surface charge for self-assembly into coacervate core micelles. We synthesized Au_{256}DENs following the original work of Amis for the formation of well-defined single particles, focusing on amine-terminated 7th generation PAMAM.[10] To prove that the AuNPs reside inside the PAMAM dendrimers, *e.g.,* AuDENs as opposed to dendrimer-stabilized nanoparticles (Au-DSNPs), we used ^{1}H-NMR spectroscopy and DOSY (Fig. S1) to verify the complexation of metal ions in the interior of PAMAM and the consecutive formation of dendrimer-encapsulated nanoparticles.[11,12]

In addition, Transmission Electron Microscopy (TEM) showed that the AuDENs are ~1.7 nm in diameter, in agreement with the expected size of Au_{256} NPs (Fig. S2). Next, we assembled dendrimicelles by mixing the Au_{256}DENs at pH 7 with an anionic–neutral block copolymer having a 64-subunit polymethacrylic acid block and an 885-subunit polyethyleneoxide block, $pMAA_{64}pEO_{885}$. pH 7 was chosen since both the $pMAA_{64}pEO_{885}$ block copolymer as well as the PAMAM dendrimers are charged at this pH.[22,23] This allows electrostatic interactions of the positively charged amine-terminal groups of PAMAM to associate with the negatively charged methacrylic acid block of the $pMAA_{64}pEO_{885}$, forming a coacervate core. The neutral PEO block forms the corona of the micelle and stabilizes the resulting nanostructure. Dynamic light scattering, DLS, reveals this self-assembly as an increase in the scattered light intensity and, concurrently, as an increase in size (Fig. 2-1, S3). For the optimal building block ratios, i.e. the preferred micelle composition (PMC), we measured DLS at different mixing ratios of block copolymer to PAMAM, keeping the amount of positive charge (PAMAM) constant, and varying the amount of negative pMAA64pEO885 (Fig. S4). From this experiment, the PMC was determined to be at a mixing ratio of 0.92, corresponding to a slight excess of PAMAM to block copolymer.

This deviation from the theoretical molar charge neutrality might be attributed to the known presence of defects in higher generation PAMAM dendrimers, resulting in fewer charged end-groups and hence observed charge-stoichiometry at lower charge fraction.[17,24,25] To investigate whether or not the presence of a nanoparticle inside a dendrimer affects the formation of dendrimicelles, we mixed Au_{256}DENs with block copolymer at the previously determined PMC. DLS analysis showed that dendrimicelles formed and exhibited a similar size in solution as empty dendrimicelles. Additionally, we also prepared dendrimicelles by mixing a block copolymer with a dendrimer solution containing 50% Au_{256}DENs and 50% empty PAMAM dendrimers at the PMC.

Here, similarly sized dendrimicelles were again formed. DLS only indicates the formation of the dendrimicelles revealing the hydrodynamic diameter; however, it cannot discriminate whether dendrimicelles with only PAMAM and dendrimicelles with DENs were formed. Therefore, we characterized the obtained nanostructures in more detail and determined their stability under various conditions using both cryoTEM and DLS. CryoTEM allows for visualization of the obtained nanostructures in near-native state from which micelle properties such as shape, micelle core and corona size, and aggregation number can be derived. Representative CryoTEM micrographs and DLS data of the dendrimicelles discussed above are shown in Fig. 2-1 and S5–7, revealing the dendrimicelle structures for the PAMAM and DEN systems, and that mixing PAMAM and DENs result in mixed-core dendrimicelles. The dendrimicelle sample with empty PAMAM in the core can be visualized by cryoTEM (I, Fig. 2-1) since the dense coacervate core provides a higher electron-density, and hence contrast, in the cryoTEM images.[26] However, the presence of electron-dense AuNPs greatly improves the contrast and facilitates image analysis. In fact, Fig. 2-1 shows dendrimicelles made using 50% empty PAMAM mixed with 50% Au_{256}DENs (II), and shows the dendrimicelles made of 100% Au_{256}DENs (III). CryoTEM corroborates that the ~50 nm-sized structures observed with DLS are indeed well-defined nano-assemblies with a core–shell structure. Cryo-TEM micrographs of the micelles made from 100% Au_{256}DENs (III, Fig. 2-1, S8) show that the average core diameter is 27 ± 5 nm. DLS data show the hydrodynamic diameter of these micelles to be 52 nm.

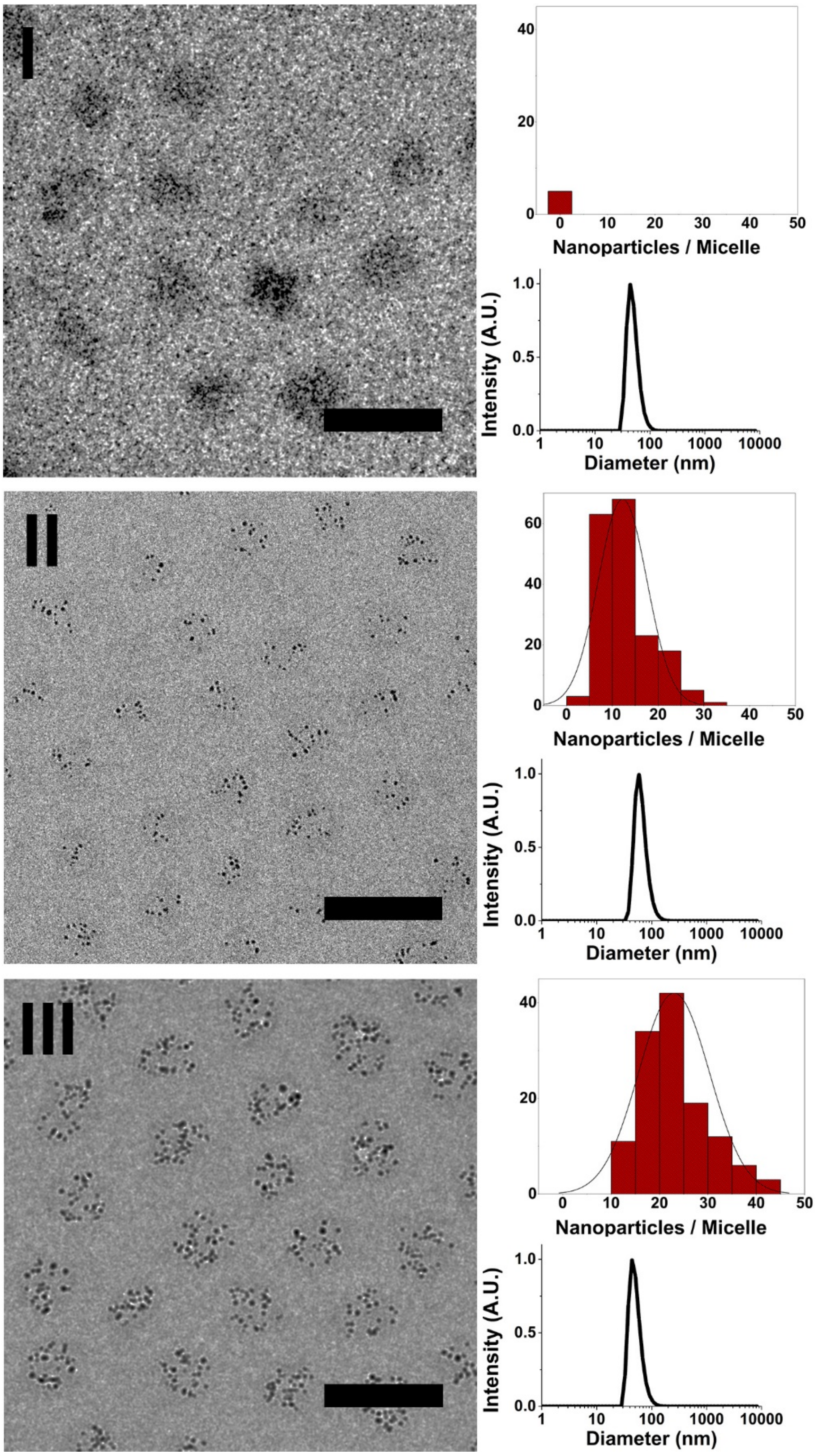

Figure 2-1 Dendrimicelle characterization. In each panel, the figure left shows a cryoTEM image, the figures right show the counted nanoparticles per micelle (upper), and number-averaged DLS size plot (lower). Dendrimicelles made from: top (I) empty dendrimers. The contrast observed originates from the dense dendrimicelle cores. Middle (II), from 50% Au_{256}-filled and 50% empty dendrimers; they contain 12 ± 5 AuNPs per micelle, and an equal amount of empty dendrimers which are not individually observable. Bottom (III), from Au_{256}-filled dendrimers. The dendrimicelles contain 23 ± 7 AuNPs per micelle. The AuNPs encapsulated inside the dendrimers greatly improve contrast of the TEM images (of II and III) and allow for determining aggregation numbers. Scale bars 50 nm.

The expected size for a PEO_{885} corona is ~14 nm,[27] hence showing the commensurability for the core size between the DLS (hydrodynamic radius minus corona) and cryoTEM (visible core) results. On the other hand, the micelle size (core + corona) obtained from the micelle core–core distance in the cryoTEM images is 39 ± 5 nm (Fig. S9), which indicates a corona thickness of ~6 nm. This difference is attributed to the compression of the PEG shell as a result of cryoTEM sample preparation and packing.[28] The formation of dendrimicelles straightforwardly allows for incorporation and tuning of the number of NPs per micelle by mixing DENs with empty, amine-terminated PAMAM. Moreover, the presence of only one AuNP per PAMAM allows for the direct determination of the aggregation number of the dendrimicelles by simply counting the number of nanoparticles per micelle. The number of Au_{256}DENs per micelle is 23 ± 7 for the dendrimicelle sample made using 100% Au_{256}DENs and 12 ± 5 for the sample made using 50% empty PAMAM and 50% Au_{256}DENs. Assuming a 1 : 1 association of positive and negative charges in the dendrimicelle core, this corresponds to an average micelle molecular weight of ~12MDa, roughly three times as heavy as the biggest proteins (Titins) found in nature.[29]

Using DLS, we further studied the stability of dendrimicelles formed at the PMC against different environmental conditions. Fig. S10 shows the observed scattering intensity and size of dendrimicelles versus pH. The dendrimicelles are stable between pH 6 and 8, in correspondence with the pKa values of the charged building blocks (~6 for methacrylic acid,[23] and ~9 for amine-terminated PAMAM[22]), supporting the hypothesis that the dendrimicelles are made by coacervation of the positively and negatively charged building blocks. The critical salt concentration (CSC), a measure of the salt stability of (dendri)micelles formed from the self-assembly of oppositely charged building blocks, is 1.5 M for NaCl (Fig. S11), and the critical micelle concentration (CMC) of these dendrimicelles is ~0.6 mg L−1 total polymer concentration (Fig. S12). Compared to dendrimicelles made from acid-terminated PAMAM dendrimers,[17] both CSC and CMC are slightly improved, and in line with other micelle systems.[14] DLS results obtained over time (Fig. S13) show that both the scattered light intensity as well as the obtained size remained virtually constant over a period of seven days.

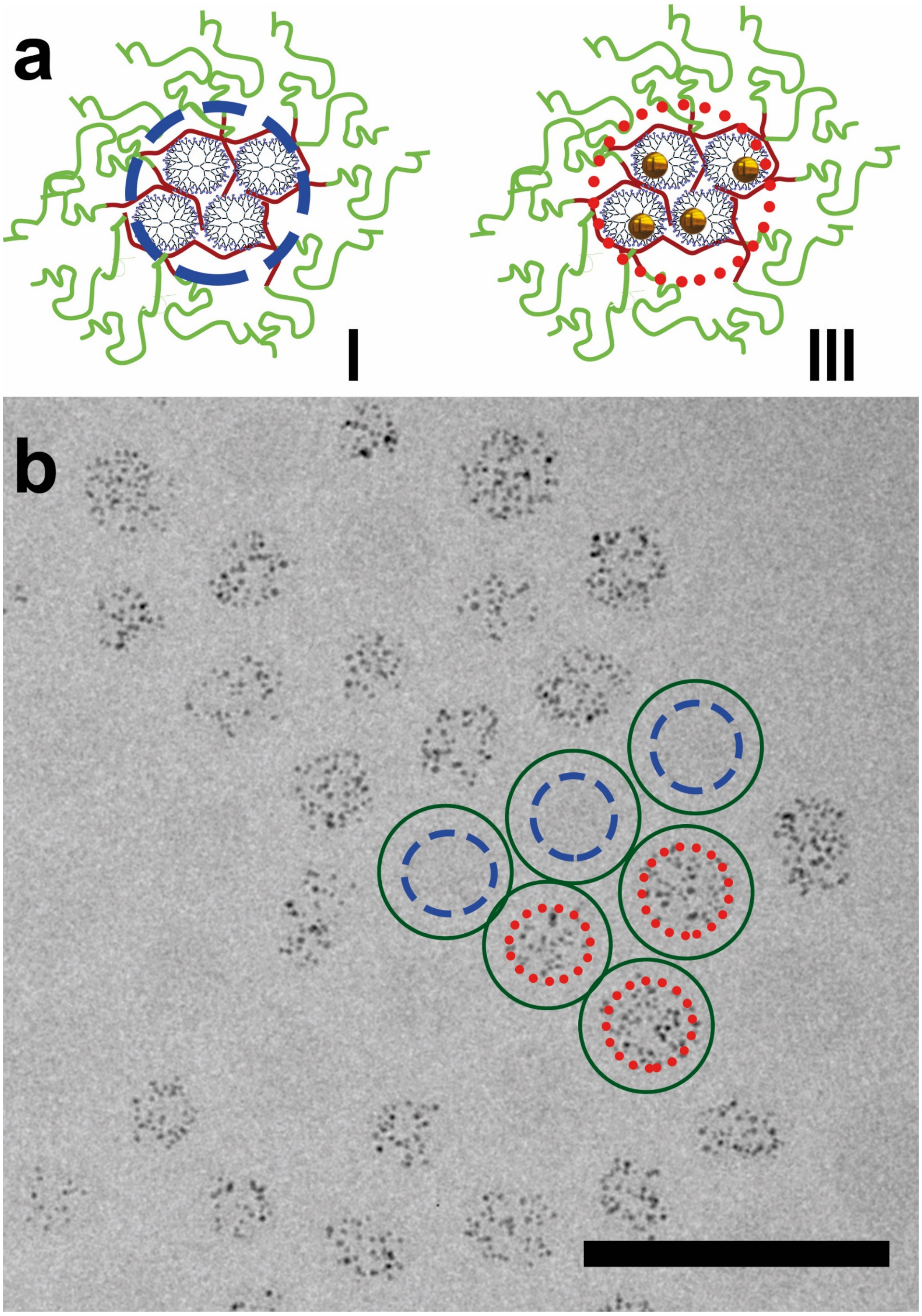

Figure 2-2 The effect of mixing dendrimicelles formed with empty dendrimers (I) and dendrimicelles formed with AuDENs, i.e. Au-nanoparticle filled dendrimers (III). a) Schematic representation of the two dendrimicelles that were mixed: the blue, dashed circle is drawn around the core of a selection of three empty dendrimicelles (I), and the red, dotted, circle is drawn around the nanoparticle-filled dendrimer core of another selection of three micelles (III). b) Cryo-TEM micrograph of a mix of dendrimicelles I and III, containing empty, respectively, Au_{256}-filled dendrimers; these were separately prepared and consecutively mixed, and measured after 30 days. As can be seen, mixing empty and filled micelles does not result in half-filled micelles, showing the high stability of the dendrimicelles. For visualization purposes, the blue circles are drawn around the micelle-core of three empty dendrimicelles, whereas red-dotted lines are drawn around the cores of three dendrimicelles containing Au-DENs. Additional images can be found in the Appendix. The scale bar is 100 nm.

To investigate whether the stability of the dendrimicelle as a whole also is representative of the stability of the micelle core, i.e. to see whether the dendrimicelle core is dynamic, we mixed dendrimicelles made from empty PAMAM with dendrimicelles containing Au_{256}DENS. Here cryo-TEM micrographs recorded one day (Fig. S14) or after 3 months at RT (Fig. 2-2 and S15/16) both show dendrimicelles either without any AuDENs, or completely filled with AuDENs. Analysis of the dendrimicelles containing AuDENs shows that these contain 26 ± 8 NPs per dendrimicelle, in agreement with the number of AuNPs per dendrimicelle found before (Fig. 2-1). Clearly, even at these timescales, no exchange between filled and empty dendrimicelles occurs. This implies that the dendrimer core is (kinetically) trapped and no exchange of dendrimers between the dendrimicelles takes place. Besides the conceptual value, the advantage of a nanocontainer lies in the fact that properties of the contained particle/molecule are altered, e.g. protected, activated, and selectively accessible. The presented AuDENs in dendrimicelles indeed have properties that are different from AuDENs in solution; we used thiol-induced etching of AuNPs to study the differences.[30] Upon adding two molar equivalents of mercaptoethanol (ME) to Au atoms the AuDENs are slowly degraded, the appearance of an absorption band at 395 nm (Fig. 2-3) being indicative of the formation of Au(I)–thiol complexes.[31,32] In the case of the dendrimicelle sample, it takes about six times as long before this peak appears. Additionally, the rate at which the peak appears, i.e. the slope in the intensity vs. time plots, is also higher for the sample with just the Au_{256}NPs than for the dendrimicelle sample. These observations suggest that the dendrimicelle forms a barrier that delays degradation.

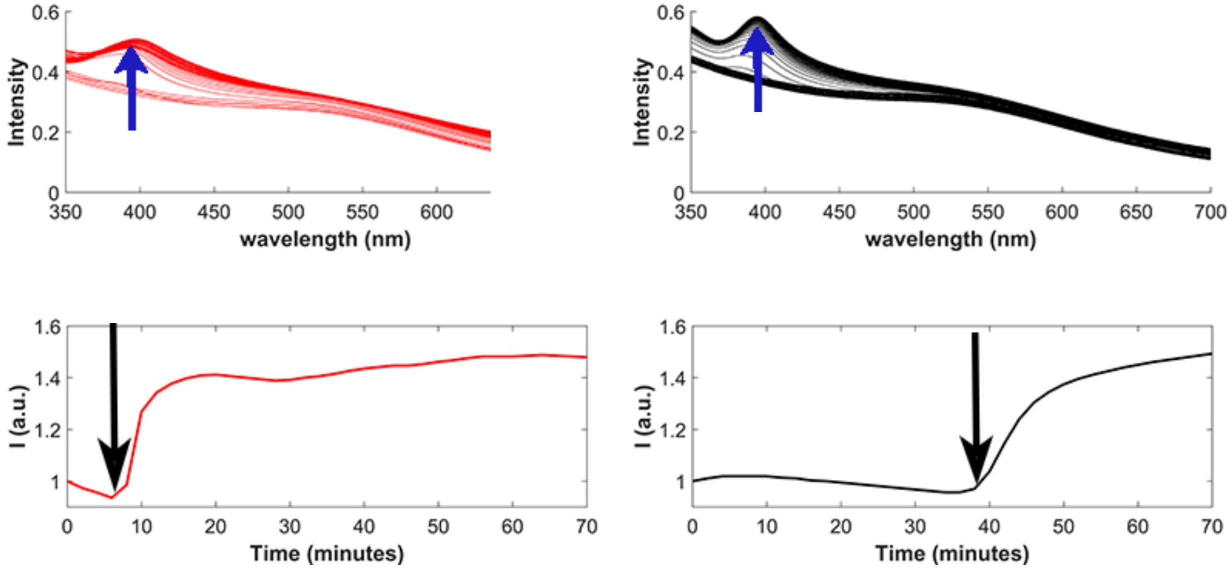

Figure 2-3 Stability against degradation of Au_{256}DENs in solution or encapsulated inside dendrimicelles. Top: UV-Visible absorption spectra of Au_{256}DENs (red) and Au_{256} dendrimicelles (black) after addition of two equivalents of mercaptoethanol. Bottom: normalized absorption plots, showing absorption at 395 nm versus time after addition of mercaptoethanol. For the Au_{256} dendrimicelles, a significant delay in the first appearance of the Au(I)-thiol complex peak (indicated by an arrow), as well as smaller slope, is observed.

2.4 Conclusion

Nanoparticles, dendrimers and micelles find wide applications in fields like nanomedicine, responsive materials and catalysis,[33] and the controlled assembly strategy presented here opens up a vast horizon of applications. It offers a great variety for generating box-in-a-box structures and nanoparticle/molecule-in-a-box-in-a-box structures. There is, first, the possibility of changing the AuNP size by tuning the metal–dendrimer ratio during the synthesis of the DENs. Second, the use of different dendrimer generations can be exploited. Third, the system allows for making dendrimicelles with different metal NPs or even mixed-metal NPs. Likewise, combinations can be made by mixing different generations, using different types of dendrimers, by encapsulating molecules inside the dendrimer, or even using other macromolecular systems. Finally, coacervate-core micelles form upon charge interactions, but other micellar strategies can be explored as well, e.g. based on hydrophobic or supramolecular interactions.

2.5 References

1. Koblenz, T. S.; Wassenaar, J.; Reek, J. N. H. Reactivity within a Confined Self-Assembled Nanospace. *Chemical Society Reviews* **2008**.

2. Chen, P.-C.; Liu, G.; Zhou, Y.; Brown, K. A.; Chernyak, N.; Hedrick, J. L.; He, S.; Xie, Z.; Lin, Q.-Y.; Dravid, V. P.*; et al.* Tip-Directed Synthesis of Multimetallic Nanoparticles. *Journal of the American Chemical Society* **2015**, 137, 9167-9173.

3. Mirtschin, S.; Slabon-Turski, A.; Scopelliti, R.; Velders, A. H.; Severin, K. A Coordination Cage with an Adaptable Cavity Size. *Journal of the American Chemical Society* **2010**, 132, 14004-14005.

4. Rosen, B. M.; Wilson, C. J.; Wilson, D. A.; Peterca, M.; Imam, M. R.; Percec, V. Dendron-Mediated Self-Assembly, Disassembly, and Self-Organization of Complex Systems. *Chemical Reviews* **2009**, 109, 6275-6540.

5. Jansen, J.; Debrabandervandenberg, E. M. M.; Meijer, E. W. Encapsulation of Guest Molecules into a Dendritic Box. *Science* **1994**, 266, 1226-1229.

6. Zhou, Z.; Wang, Y.; Yan, Y.; Zhang, Q.; Cheng, Y. Dendrimer-Templated Ultrasmall and Multifunctional Photothermal Agents for Efficient Tumor Ablation. *ACS Nano* **2016**, 10, 4863-4872.

7. Luo, L.; Zhang, L.; Duan, Z. Y.; Lapp, A. S.; Henkelman, G.; Crooks, R. M. Efficient Co Oxidation Using Dendrimer-Encapsulated Pt Nanoparticles Activated with <2% Cu Surface Atoms. *Acs Nano* **2016**, 10, 8760-8769.

8. Myers, S. V.; Weir, M. G.; Carino, E. V.; Yancey, D. F.; Pande, S.; Crooks, R. M. Dendrimer-Encapsulated Nanoparticles : New Synthetic and Characterization Methods and Catalytic Applications. *Chemical Science* **2011**, 2, 1632-1646.

9. Crooks, R. M.; Zhao, M.; Sun, L.; Chechik, V.; Yeung, L. K. Dendrimer-Encapsulated Metal Nanoparticles: Synthesis, Characterization, and Applications to Catalysis. *Accounts of Chemical Research* **2001**, 34, 181-190.

10. Gröhn, F.; Bauer, B. J.; Akpalu, Y. A.; Jackson, C. L.; Amis, E. J. Dendrimer Templates for the Formation of Gold Nanoclusters. *Macromolecules* **2000**, 33, 6042-6050.

11. Gomez, V. M.; Guerra, J.; Velders, A. H.; Crooks, R. M. Nmr Characterization of Fourth-Generation Pamam Dendrimers in the Presence and Absence of Palladium Dendrimer-Encapsulated Nanoparticles. *Journal of the American Chemical Society* **2009**, 131, 341-350.

12. Gomez, V. M.; Guerra, J.; Myers, S. V.; Crooks, R. M.; Velders, A. H. Nanoparticle Size Determination by (1)H NMR Spectroscopy. *Journal of the American Chemical Society* **2009**, 131, 14634-14635.

13. Riess, G. Micellization of Block Copolymers. *Progress in Polymer Science* **2003**, 28, 1107-1170.

14. Voets, I. K.; de Keizer, A.; Stuart, M. A. C. Complex Coacervate Core Micelles. *Advances in Colloid and Interface Science* **2009**, 147-48, 300-318.

15. Wang, J. Y.; Velders, A. H.; Gianolio, E.; Aime, S.; Vergeldt, F. J.; Van As, H.; Yan, Y.; Drechsler, M.; de Keizer, A.; Stuart, M. A. C.*; et al.* Controlled Mixing of Lanthanide(III) Ions in Coacervate Core Micelles. *Chemical Communications* **2013**, 49, 3736-3738.

16. Wang, J. Y.; Groeneveld, A.; Oikonomou, M.; Prusova, A.; Van As, H.; van Lent, J. W. M.; Velders, A. H. Revealing and Tuning the Core, Structure, Properties and Function of Polymer Micelles with Lanthanide-Coordination Complexes. *Soft Matter* **2016**, 12, 99-105.

17. Wang, J.; Voets, I. K.; Fokkink, R.; van der Gucht, J.; Velders, A. H. Controlling the Number of Dendrimers in Dendrimicelle Nanoconjugates from 1 to More Than 100. *Soft Matter* **2014**, 10, 7337-7345.

18. Balogh, L.; Valluzzi, R.; Laverdure, K. S.; Gido, S. P.; Hagnauer, G. L.; Tomalia, D. A. Formation of Silver and Gold Dendrimer Nanocomposites. *Journal of Nanoparticle Research* **1999**, 1, 353-368.

19. Esfand, R.; Tomalia, D. A. Poly(Amidoamine) (Pamam) Dendrimers: From Biomimicry to Drug Delivery and Biomedical Applications. *Drug Discovery Today* **2001**, 6, 427-436.

20. Scott, R. W. J.; Wilson, O. M.; Crooks, R. M. Synthesis, Characterization, and Applications of Dendrimer-Encapsulated Nanoparticles. *The Journal of Physical Chemistry B* **2005**, 109, 692-704.

21. Wilson, O. M.; Scott, R. W. J.; Garcia-Martinez, J. C.; Crooks, R. M. Synthesis, Characterization, and Structure-Selective Extraction of 1-3-Nm Diameter Auag Dendrimer-Encapsulated Bimetallic Nanoparticles. *Journal of the American Chemical Society* **2005**, 127, 1015-1024.

22. Niu, Y.; Sun, L.; Crooks, R. M. Determination of the Intrinsic Proton Binding Constants for Poly(Amidoamine) Dendrimers Via Potentiometric Ph Titration. *Macromolecules* **2003**, 36, 5725-5731.

23. Ruiz-Pérez, L.; Pryke, A.; Sommer, M.; Battaglia, G.; Soutar, I.; Swanson, L.; Geoghegan, M. Conformation of Poly(Methacrylic Acid) Chains in Dilute Aqueous Solution. *Macromolecules* **2008**, 41, 2203-2211.

24. Mullen, D. G.; Desai, A.; van Dongen, M. A.; Barash, M.; Baker, J. R.; Banaszak Holl, M. M. Best Practices for Purification and Characterization of Pamam Dendrimer. *Macromolecules* **2012**, 45, 5316-5320.

25. van Dongen, M. A.; Desai, A.; Orr, B. G.; Baker, J. R.; Holl, M. M. B. Quantitative Analysis of Generation and Branch Defects in G5 Poly(Amidoamine) Dendrimer. *Polymer* **2013**, 54, 4126-4133.

26. Zheng, Y.; Won, Y.-Y.; Bates, F. S.; Davis, H. T.; Scriven, L. E.; Talmon, Y. Directly Resolved Core-Corona Structure of Block Copolymer Micelles by Cryo-Transmission Electron Microscopy. *The Journal of Physical Chemistry B* **1999**, 103, 10331-10334.

27. Fee, C. J.; Van Alstine, J. M. Prediction of the Viscosity Radius and the Size Exclusion Chromatography Behavior of Pegylated Proteins. *Bioconjugate Chemistry* **2004**, 15, 1304-1313.

28. Zheng, Y.; Lin, Z.; Zakin, J. L.; Talmon, Y.; Davis, H. T.; Scriven, L. E. Cryo-Tem Imaging the Flow-Induced Transition from Vesicles to Threadlike Micelles. *The Journal of Physical Chemistry B* **2000**, 104, 5263-5271.

29. Labeit, S.; Kolmerer, B. Titins: Giant Proteins in Charge of Muscle Ultrastructure and Elasticity. *Science* **1995**, 270, 293-296.

30. Shichibu, Y.; Negishi, Y.; Tsunoyama, H.; Kanehara, M.; Teranishi, T.; Tsukuda, T. Extremely High Stability of Glutathionate-Protected Au25 Clusters against Core Etching. *Small* **2007**, 3, 835-839.

31. Schaaff, T. G.; Whetten, R. L. Controlled Etching of Au:Sr Cluster Compounds. *The Journal of Physical Chemistry B* **1999**, 103, 9394-9396.

32. Ye, H.; Crooks, R. M. Electrocatalytic O2 Reduction at Glassy Carbon Electrodes Modified with Dendrimer-Encapsulated Pt Nanoparticles. *Journal of the American Chemical Society* **2005**, 127, 4930-4934.

2.6 Appendix

Dendrimicelle aggregation number determination

Micelle aggregation numbers can be determined from static light scattering experiments, for example by constructing a (partial) Zimm plot.[17] For this, first the scattered light intensity is converted to the excess Rayleigh ratio following Equation 1. In this equation, R_θ is the excess Rayleigh ratio at scattering angle θ, with R_θ in m^{-1}, $R_{toluene}$ is the known Rayleigh scattering ratio of toluene (which is $1.35 * 10^{-3}$ m^{-1} following the Malvern Instruments documentation) and $n_{solvent}$ and $n_{toluene}$ are the refractive indeces of water (1.333) respective toluene (1.497). I_{sample},$I_{solvent}$, and $I_{toluene}$ are the scattering intensities of the sample, respectively the solvent, respectively that of the toluene scattering standard. Plotting the Rayleigh ratio *versus* total polymer concentration, and extrapolation to zero scattering intensity provides the critical micelle concentration. Plotting $\frac{K_R * C}{R_\theta}$ as a function of the polymer concentration C yields a Debije plot, in which the intercept with the y-axis is equal to 1/M, yielding the micelle molecular weight (See equation 3). K_r is a constant that is calculated using Equation 2, in which n is the refractive index, $N_{avagadro}$ is Avagadro's number, dn/dc is the refractive index increment (assumed to be $\sim 2 * 10^{-4}$ m^3/kg)[17] and λ is the wavelength of the light used (633 nm for the light scattering system used).

Equation 1)

$$R_\theta = \frac{I_{sample} - I_{solvent}}{I_{toluene}} * R_{toluene} * \frac{n_{solvent}^2}{n_{toluene}^2}$$

Equation 2)

$$K_R = \frac{4 * \pi^2 * n^2}{N_{Avagadro} * \lambda^4} * \left(\frac{dn}{dc}\right)^2$$

Equation 3)

$$\frac{K_r * C}{R_\theta} = \frac{1}{M} + 2B_2 * \frac{C}{M^2}$$

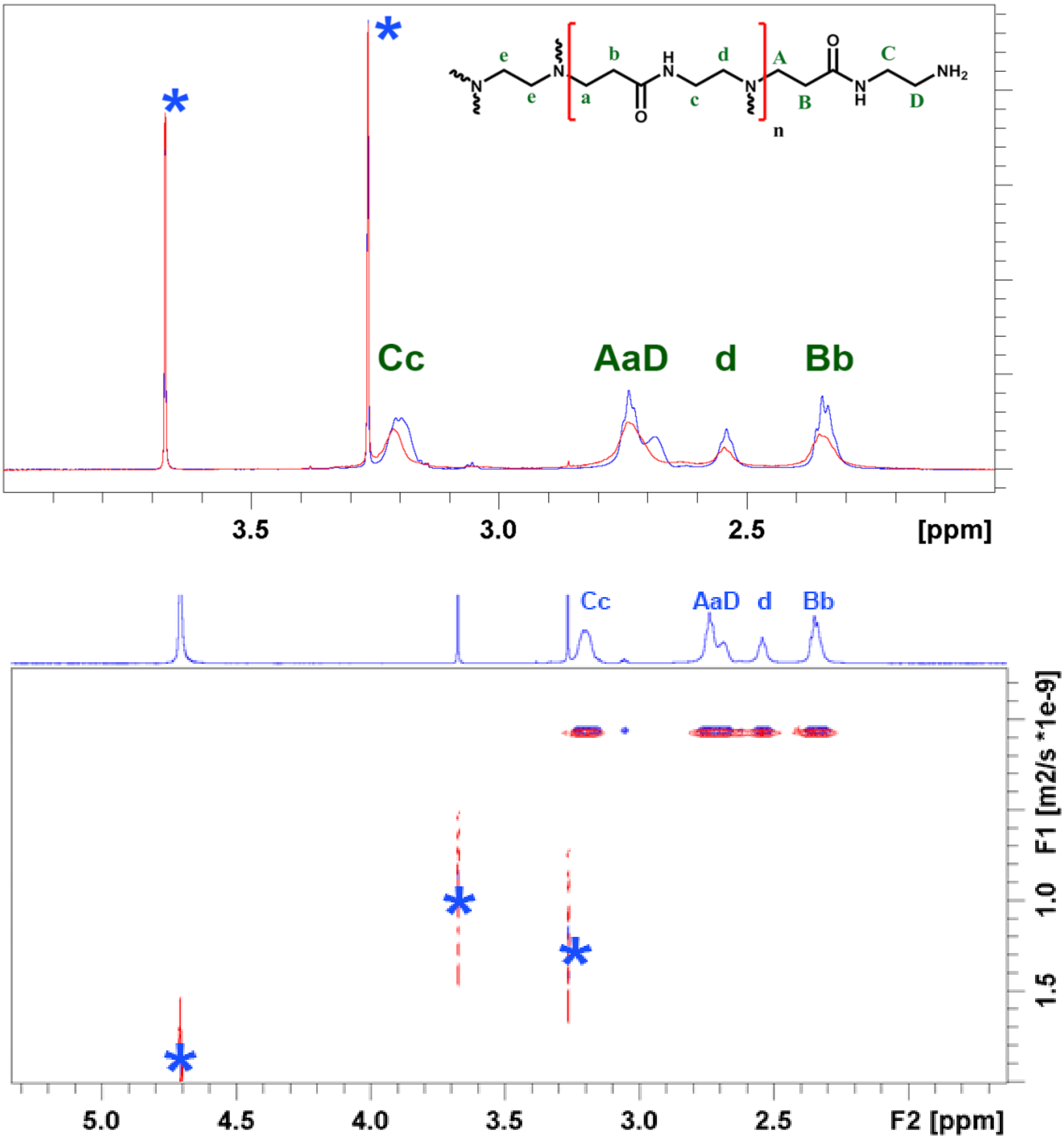

Fig. S1. NMR characterization of 7th generation PAMAM dendrimers. Top: overlay of the 1H-NMR spectra of PAMAM-G7-NH2 (blue) and PAMAM-G7-Au$_{256}$ (red) in D2O at pH 10. The increase of the ratio D/d from 1.0 to 1.2 for G7 to G7-Au$_{256}$ proves that the Au$_{256}$ nanoparticle resides inside the dendrimer cavity. The ratio D/d is calculated as the integral peak ratio of (AaD-Bb)/d. Bottom: Diffusion-Ordered Spectroscopy (DOSY) spectra of PAMAM G7-NH$_2$ in blue and PAMAM G7-Au$_{256}$ in red. The observed diffusion coefficient for G7 (D = 4.29*10^{-11}) corresponds to a hydrodynamic diameter of 9.8 nm. For G7-Au256, the observed diffusion coefficient (D = 4.41*10^{-11}) corresponds to a hydrodynamic diameter of 9.5 nm, indicating the absence of dendrimer stabilized nanoparticles. Peaks indicated with an asterisk belong to water (4.7 ppm), dioxane (internal standard, 3.7 ppm) and methanol (3.3 ppm). The pH of the samples was 10.

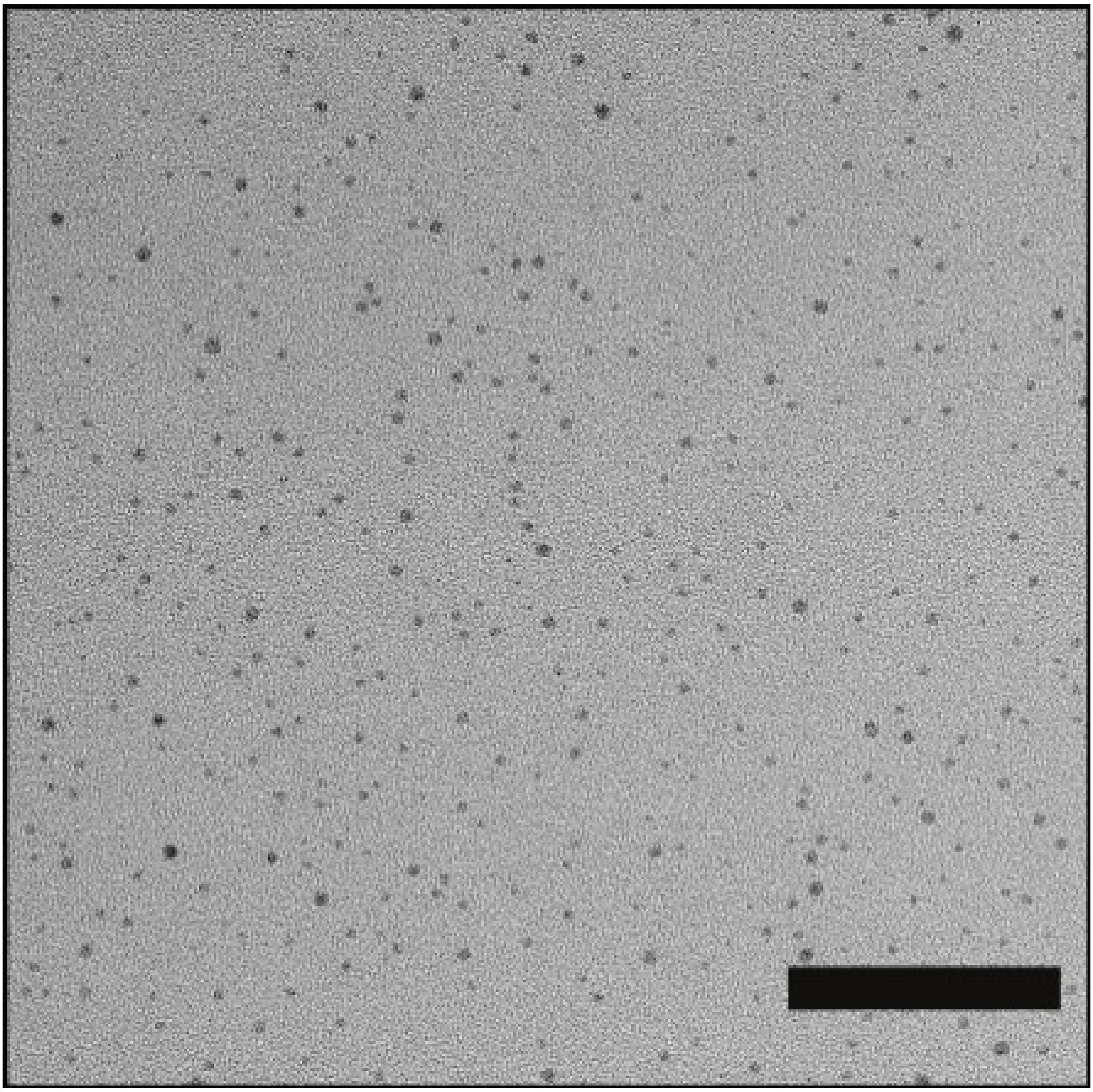

Fig. S2. TEM micrograph of PAMAM-G7 Dendrimer Encapsulated Nanoparticles (DENs). The G7-Au_{256} DENs are 1.8 ± 0.6 nm (226 particles analyzed). The scale bar in the figure corresponds to 50 nm.

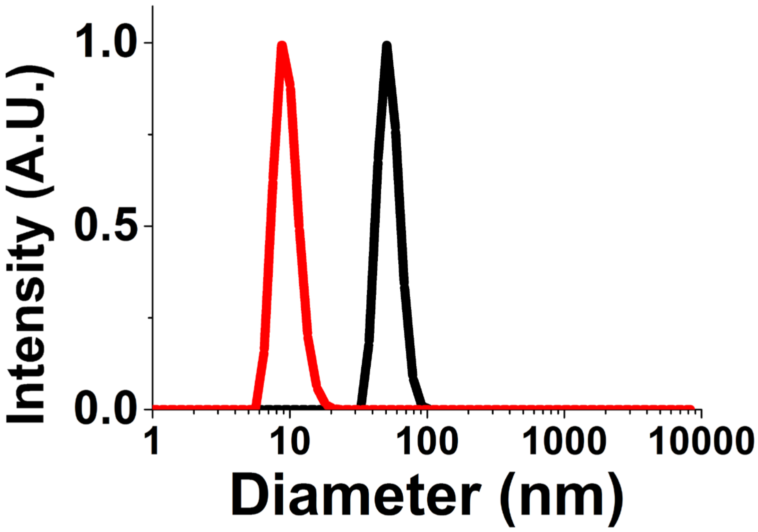

Fig. S3. DLS characterization of PAMAM G7 in solution and in dendrimicelles, showing the obtained number-averaged size plots. In red: the average hydrodynamic diameter of PAMAM in solution was about 10 nm. In black: the average hydrodynamic diameter of PAMAM dendrimicelles was about 50 nm.

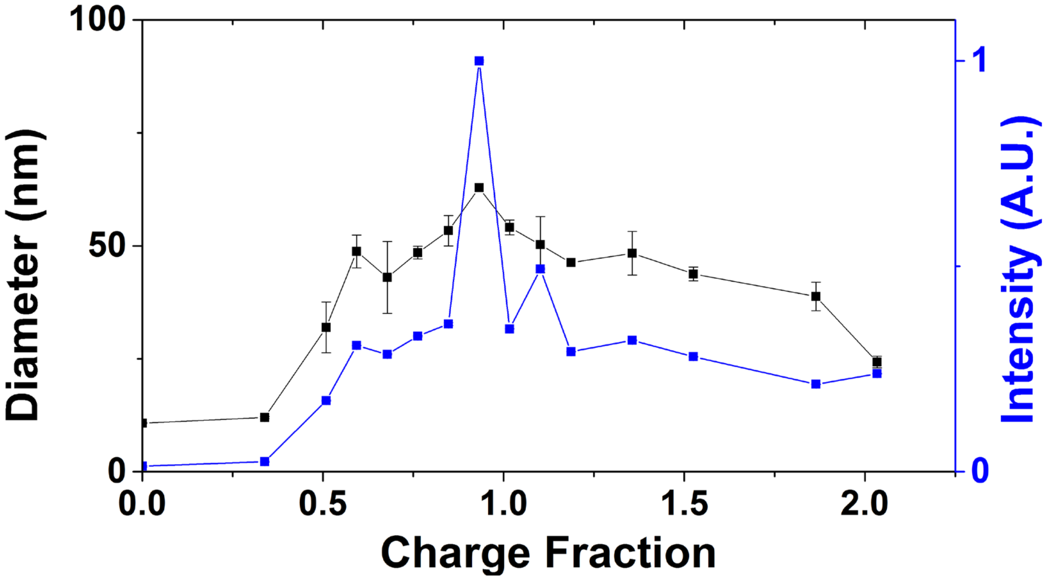

Fig. S4.DLS charge titration graph of PAMAM G7-NH_2 with $pMAA_{64}PEO_{885}$, showing the number-averaged dendrimicelle diameter in black and the normalized scattered light intensity in blue against the charge fraction. For every data point, the amount of positive charge (dendrimer-NH2) was kept constant at 59 nmoles, and the amount of negative block polymer was varied, while keeping total volume constant. The charge fraction was calculated as the ratio of (NH2/COOH).

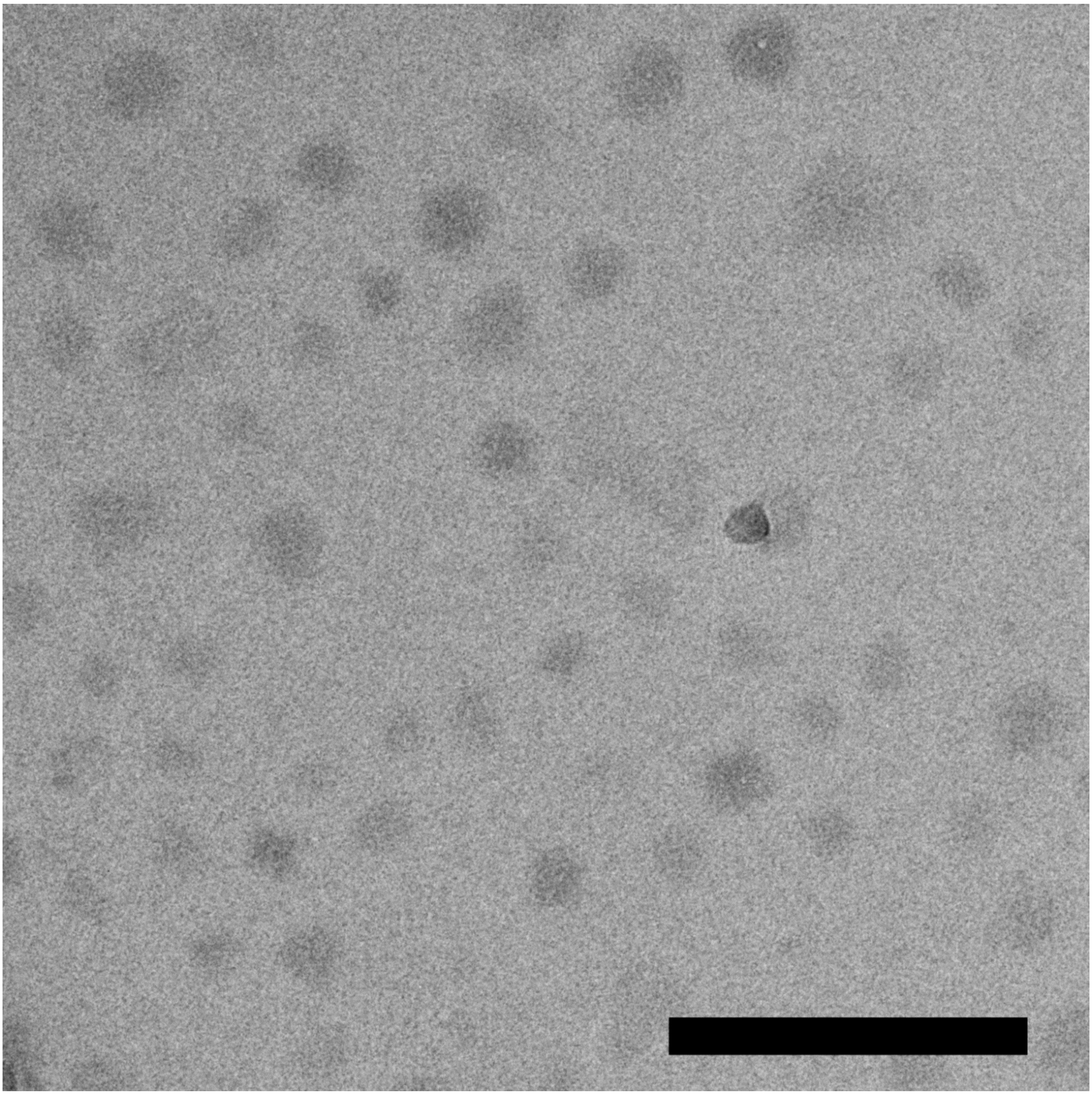

Fig. S5. CryoTEM micrograph of dendrimicelles made from empty, amine-terminated PAMAM G7. Scale bar is 200 nm.

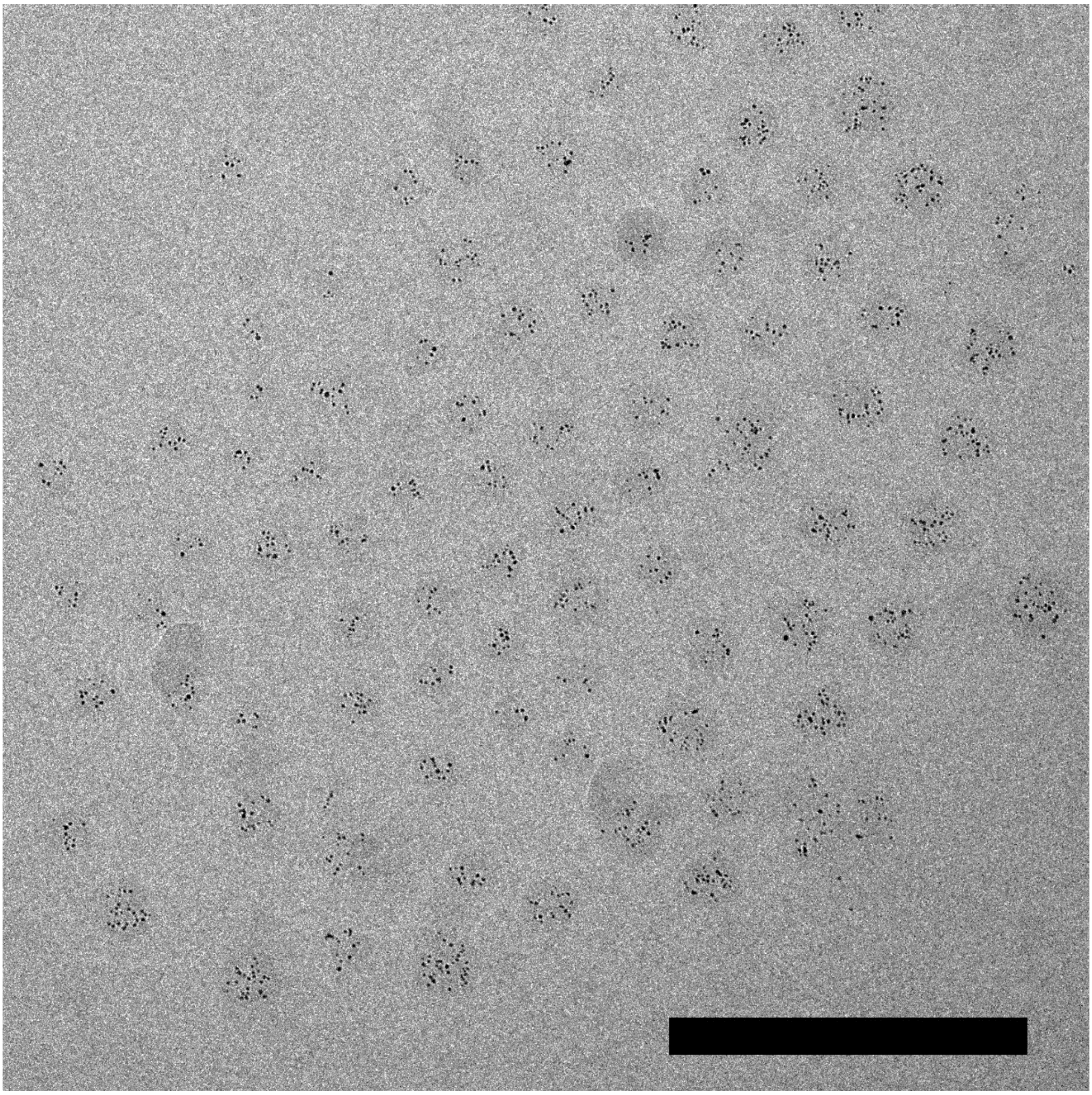

Fig. S6. CryoTEM micrograph of dendrimicelles made from 50% empty PAMAM G7 and 50% Au_{256}DENS. Scale bar is 200 nm.

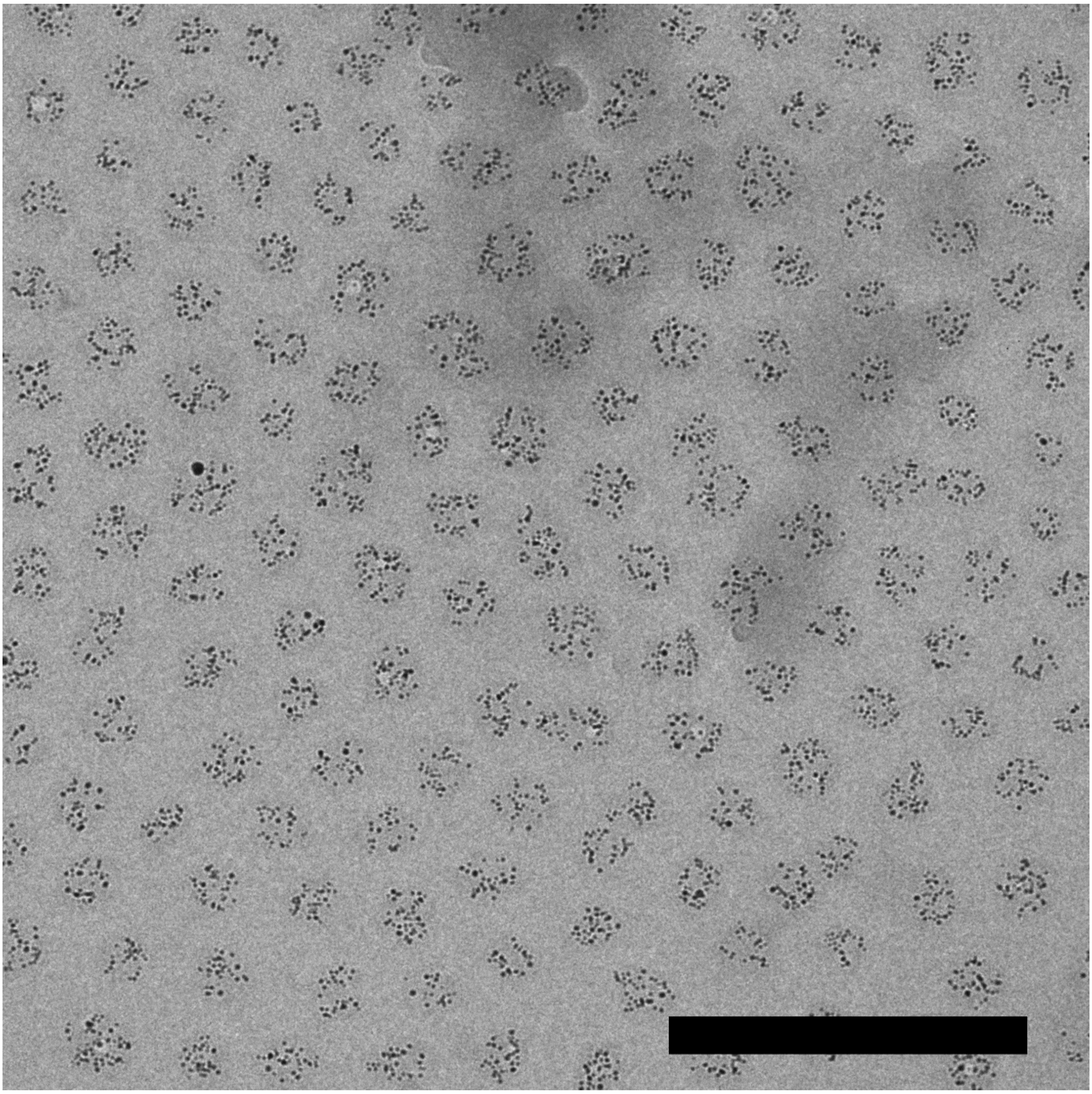

Fig. S7. CryoTEM micrograph of dendrimicelles made from Au_{256}DENS. Scale bar is 200 nm.

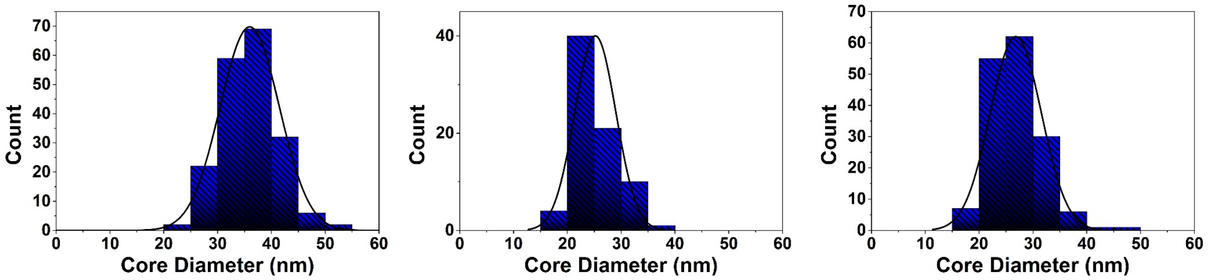

Fig. S8. CryoTEM characterization results of empty dendrimicelles, 50% empty / 50% Au_{256} dendrimicelles and Au_{256} dendrimicelles. Left: Histogram showing the average micellar core diameter as obtained from the cryoTEM micrographs, for G7 dendrimicelles made under charge-stoichiometric mixing conditions. The average core diameter is 36 ± 6 nm (193 micelles analyzed). Middle: Histogram showing the average micellar core diameter as obtained from the cryoTEM micrographs, for 50% empty / 50% Au_{256} dendrimicelles made under charge-stoichiometric mixing conditions. The average core diameter is 25 ± 4 nm (76 micelles analyzed). Right: Histogram showing the average micellar core diameter as obtained from the cryoTEM micrographs, for Au_{256} dendrimicelles made under charge-stoichiometric mixing conditions. The average core diameter is 27 ± 5 nm (162 micelles analyzed).

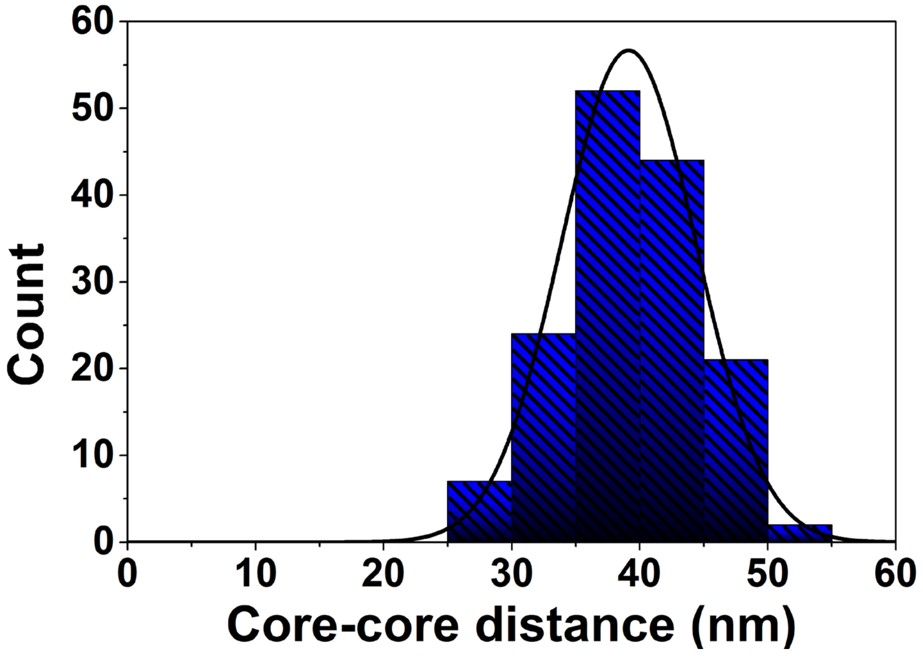

Fig. S9. Micellar size of G7-Au_{256} dendrimicelles as obtained from measuring the core-core distance of 150 randomly selected micelle pairs from the cryoTEM image in figure S6. The average core-core distance, and hence the micelle size (core+corona), is 39 ± 5 nm.

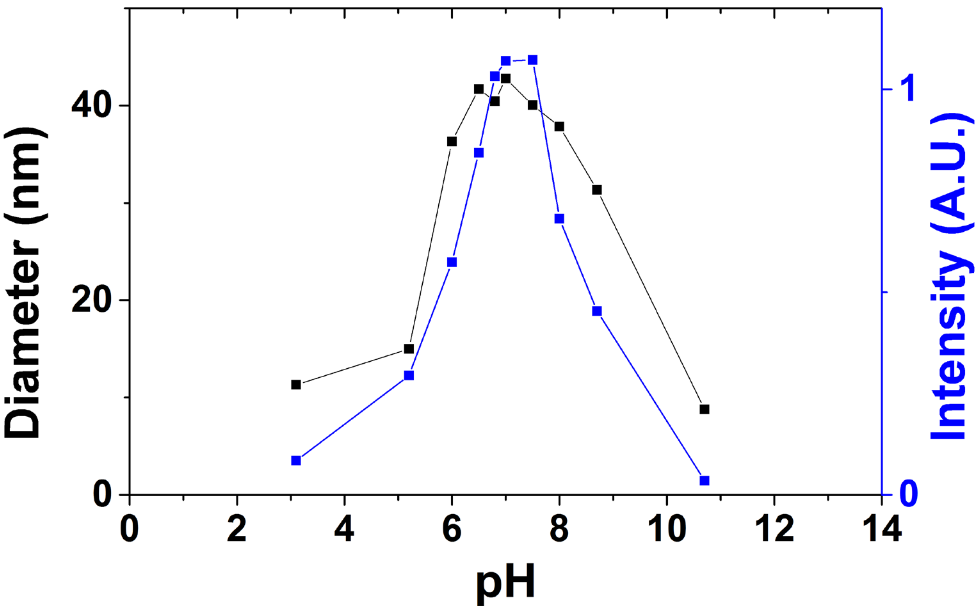

Fig. S10. The pH stability of G7 dendrimicelles. As can be seen, the formed dendrimicelles are stable between pH ~6 and ~8. In blue: Normalized average scattering intensity as obtained from DLS experiments. In black: number-averaged dendrimicelle size as obtained from DLS experiments. The dendrimicelles were made under charge-stoichiometric mixing conditions.

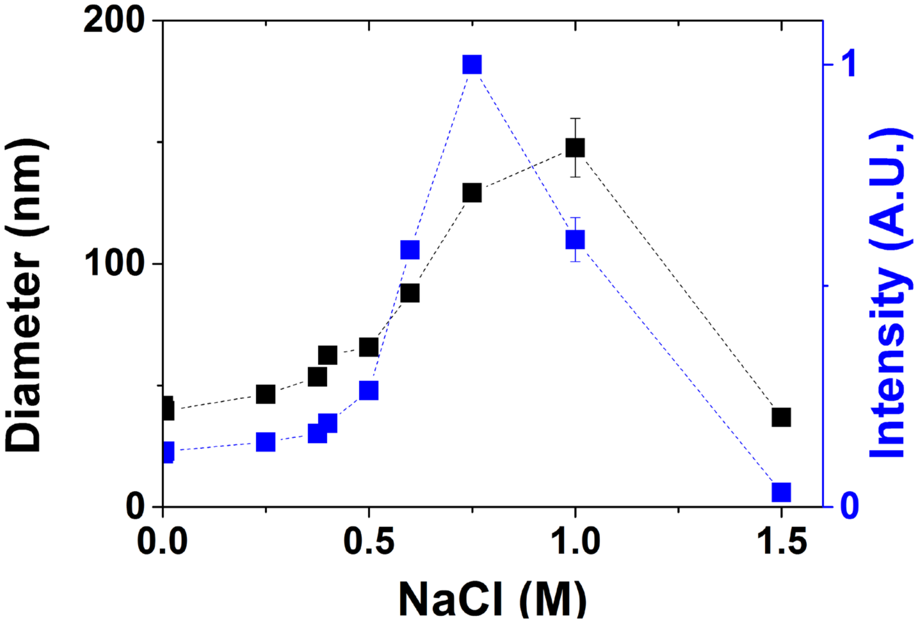

Fig. S11. Graph showing the stability of G7 dendrimicelles versus added NaCl. These dendrimicelles were made under charge-stoichiometric mixing conditions. In blue: Normalized average scattering intensity as obtained from DLS experiments. In black: number-averaged dendrimicelle size as obtained from DLS experiments. Up to ~0.5 M NaCl, both the scattered light intensity and the obtained size remain constant, indicating the stability of the dendrimicelles up to at least this salt concentration.

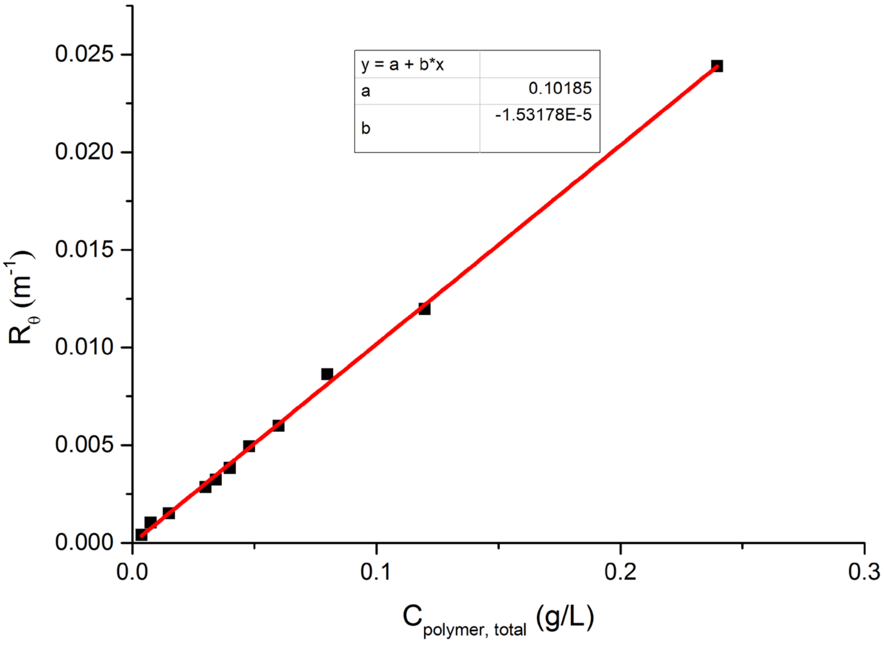

Fig. S12. CMC determination of G7 dendrimicelles. The excess Rayleigh ratio is plotted versus the total polymer concentration in gram per liter (e.g. the pMAApEO block copolymer concentration and dendrimer concentration). The data points were fitted linearly (see inset) and the CMC was obtained from the intersection with the x-axis.

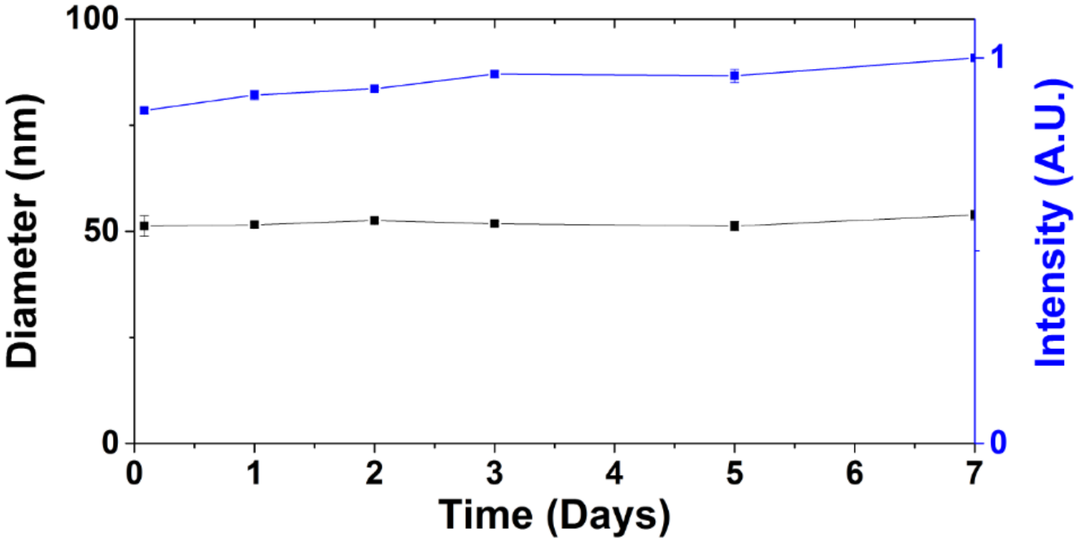

Fig. S13. The stability of G7-Au256 dendrimicelles over time. The average scattered light intensity and the average size remain virtually unchanged over time, indicating the stability of these dendrimicelles. In blue: Normalized average scattering intensity as obtained from DLS experiments. In black: number-averaged dendrimicelle size as obtained from DLS experiments. The dendrimicelles were made under charge-stoichiometric mixing conditions.

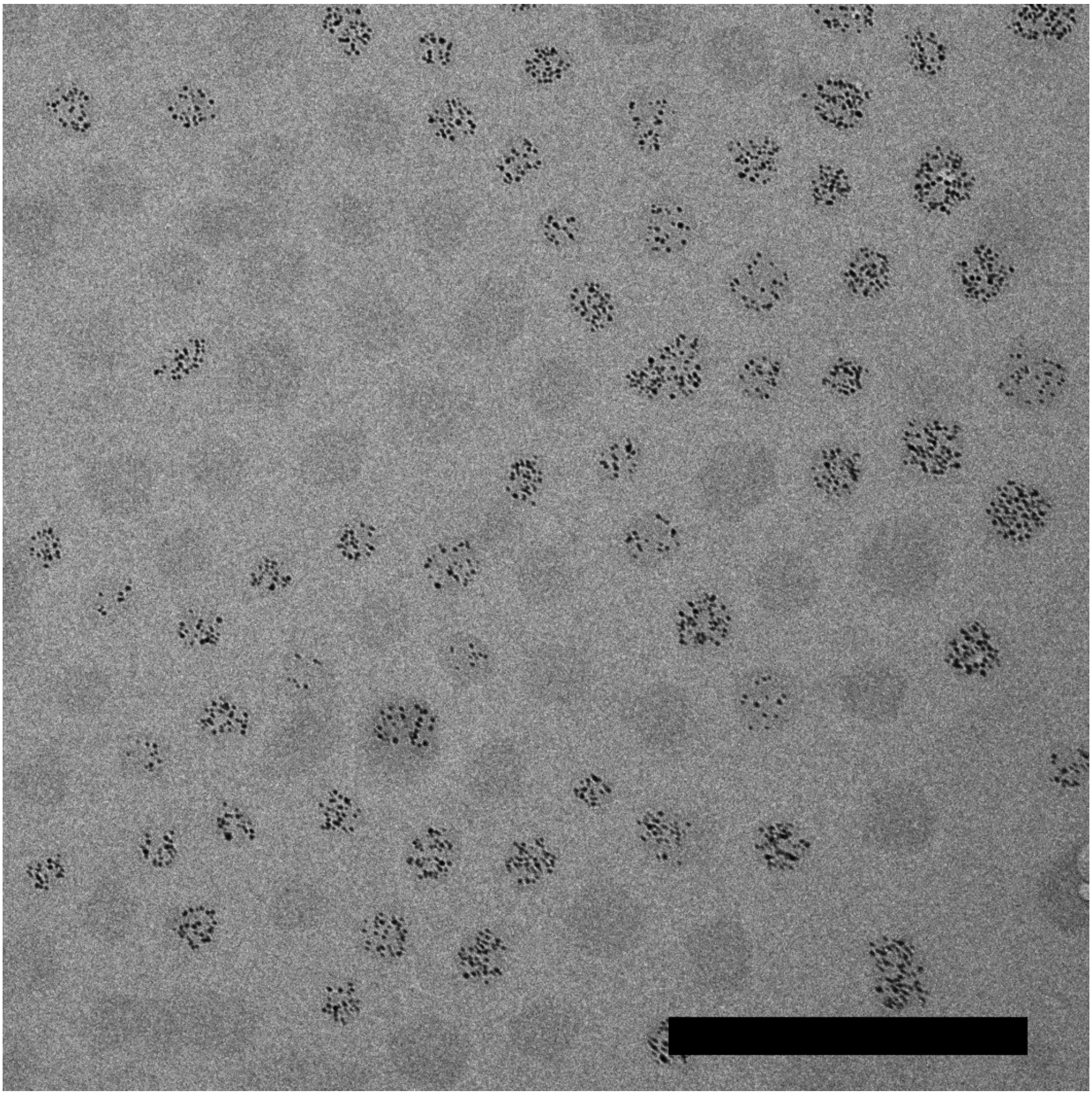

Fig. S14. Mixing empty and filled dendrimicelles does not result in half-filled micelles. This sample was made one day after mixing empty and filled dendrimers. As can be seen, the dendrimicelles did not exchange their core contents. The scale bar represents 200 nm.

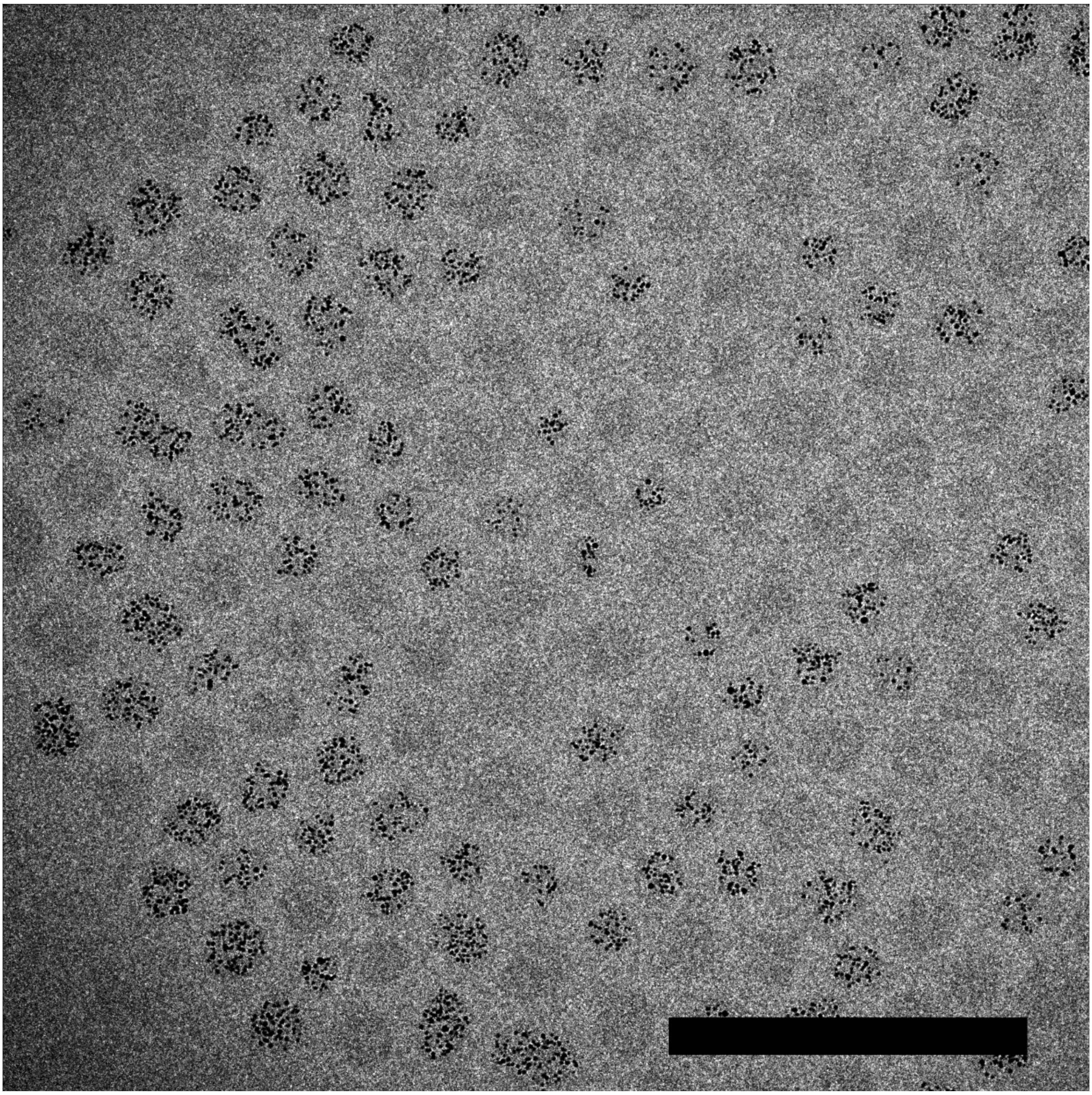

Fig. S15. Mixing empty and filled dendrimicelles does not result in half-filled micelles. This sample was made three months after mixing empty and filled dendrimers. The brightness and contrast in this image have been adjusted to better visualize the empty dendrimicelles. As can be seen, the dendrimicelles did not exchange their ‘core’ contents, even on extended timescales. The scale bar represents 200 nm.

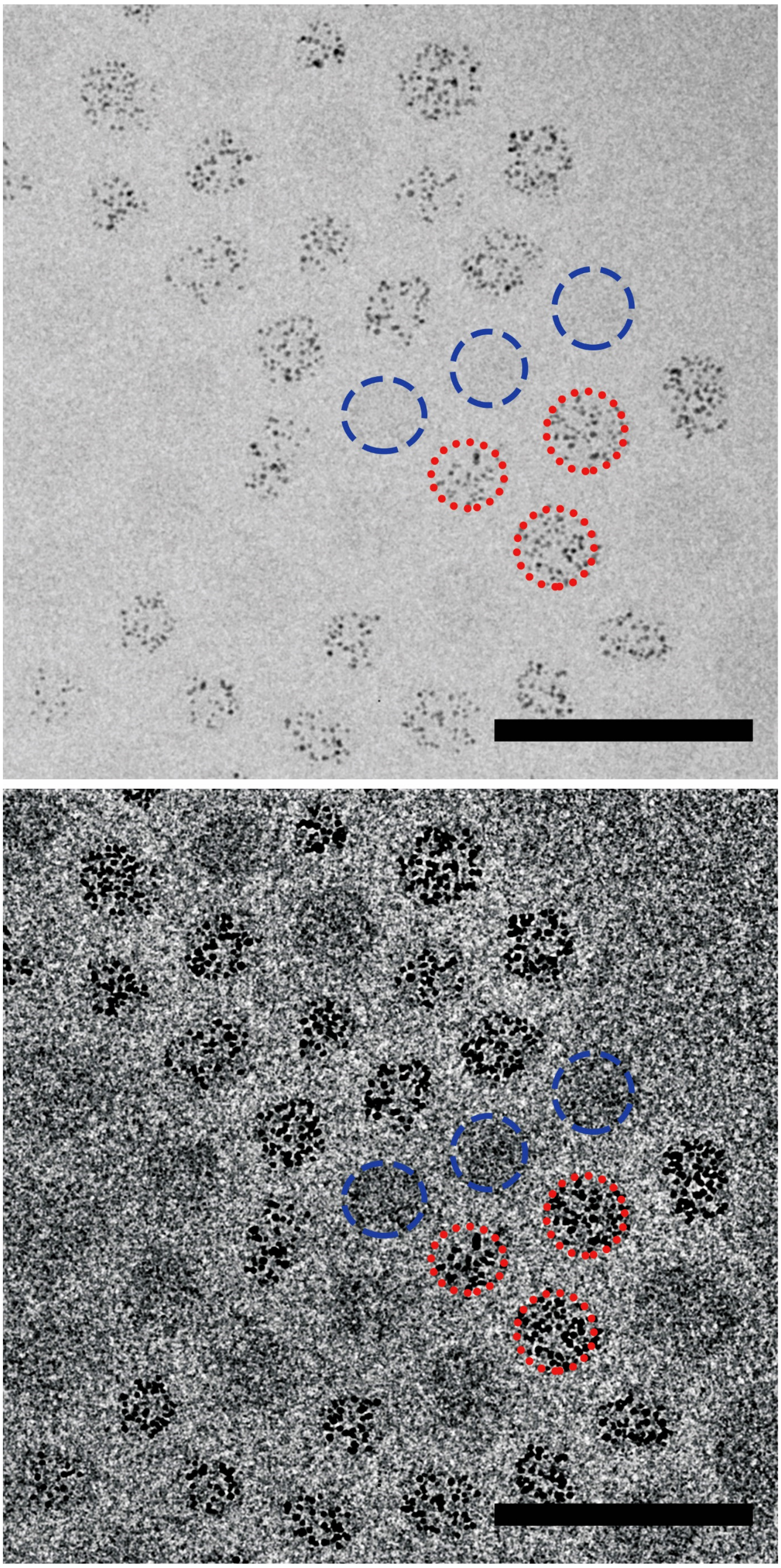

Fig. S16. Mixing empty and filled dendrimicelles does not result in half-filled micelles. Top: cryoTEM image with minimal post-processing. Bottom: The cryoTEM image has been corrected for uneven exposure by dividing the image by the Gaussian-blurred version (kernel size 15 nm) of the image, followed by linear adjustment of the brightness and contrast to such extent that the empty dendrimicelles are clearly visible as well. Scale bar in both images represents 100 nm.

Chapter 3

Size-Sorting and Pattern Formation of Nanoparticle-Loaded Micellar Superstructures in Biconcave Thin Films

Biconcave thin water layers represent a template to induce organization of supramolecular structures into ordered monolayers. Here we show how micelles form extensive micrometer-sized pseudo-2D superstructures that reveal size-sorting and geometric pattern formation, as shown by cryo-transmission electron microscopy (cryoTEM). Electron-rich gold particles inside the micelles facilitate direct visualization and determination of size, composition, and ordering of the micellar assemblies over multiple length scales. Some of the patterns observed show intriguing geometric patterns for superstructures, including Fibonacci-like, double-spiral domains that also appear in, for example, sunflower seed head patterns.

A slightly adjusted version of this chapter is published as: **Jan Bart ten Hove**, Junyou Wang, Matthias N. van Oosterom, Fijs W.B. van Leeuwen and Aldrik H. Velders, *ACS Nano*, **2017**, *11* (11), pp 11225–11231

3.1 Introduction

The enigmatic symmetry and ordering observed in biological systems has raised wonder and interest since mankind started observing nature, as described first in great detail by D'Arcy Thompson in 1917 in his seminal book *On Growth and Form*.[1] Order plays an important role at extreme length scales, also in nonbiological systems, from atomic ordering in crystals to spiral structures in galaxies light years in diameter.[2,3] Organization is also at the heart of sciences at the nanoscale, such as self-assembly of (macro)molecules and nanoparticles, where specific supramolecular interactions can generate complex yet discrete superstructures.[3-9] However, it is still a great challenge to control and investigate composition and ordering of hierarchically built-up systems over multiple length scales; micelles provide a versatile tool for such investigation.

Coacervate core micelles are nanoassemblies in which oppositely charged polymeric building blocks form the micelle core and neutral polymer blocks constitute the micelle corona. Many micelle building blocks have been reported, including proteins and dendrimers.[10,11] Dendrimers are well-defined hyperbranched macromolecules with the potential to encapsulate molecules or nanoparticles, with polyamidoamine (PAMAM) dendrimers being among the most studied.[12,13] In the past, we showed that carboxyl-terminated, negatively charged, PAMAM dendrimers are versatile and robust micellar building blocks,[14] and more recently we showed that amine-terminated, positively charged PAMAM dendrimers also form well-defined dendrimicelles through coacervation with charged block copolymers.[15] In PAMAM dendrimers small nanoparticles can be encapsulated,[16-18] which we managed to incorporate into dendrimicelles. The electron-rich, nanometer-sized, gold nanoparticles in the core of these micelles permit direct visualization and determination of size and composition of the 50-nm-sized nanoassemblies, by cryoTEM. We here present detailed cryoTEM analysis in which the micelles form extensive, ordered monolayer superstructures in the biconcave thin water layer.

Figure **3-1** shows this 4-fold organization of our dendrimicelle system, where nanometer-sized particles, templated in and residing inside dendrimers and assembled in micellar core structures, organize into well-defined micrometer-sized superstructures in biconcave thin water films. As dendrimers can be considered molecular boxes and micelles as nanoboxes, we coined the composite structure a [particle-in-a-box]-in-a-box nanostructure, reflecting back on the two separate levels of hierarchy of encapsulation. The first level concerns the nanoparticle encapsulation inside the dendrimer box, and the second level the encapsulation (of many of these dendrimer boxes) inside the micelle box. Our strategy allows for the straightforward variation of subcomponents, to tune size and polydispersity of the micelles. We here present superstructures from micelles obtained with three different generations of dendrimers and with two different subcomponent ratios to vary polydispersity. The use of the nanoparticles residing at the inside of one of the assembled components reveals composition, ordering, and patterns over multiple length scales. These superstructures reveal size sorting of the micelles within the superstructures and the formation of geometric patterns, including Fibonacci-like double-spiral domains resembling those that appear in, for example, sunflower seed heads and pine cones.[1,2,19,20] As the ordering in natural systems is called phyllotaxis, we coin the ordering of nanoparticles at the (sub)micrometer scale nanotaxis.

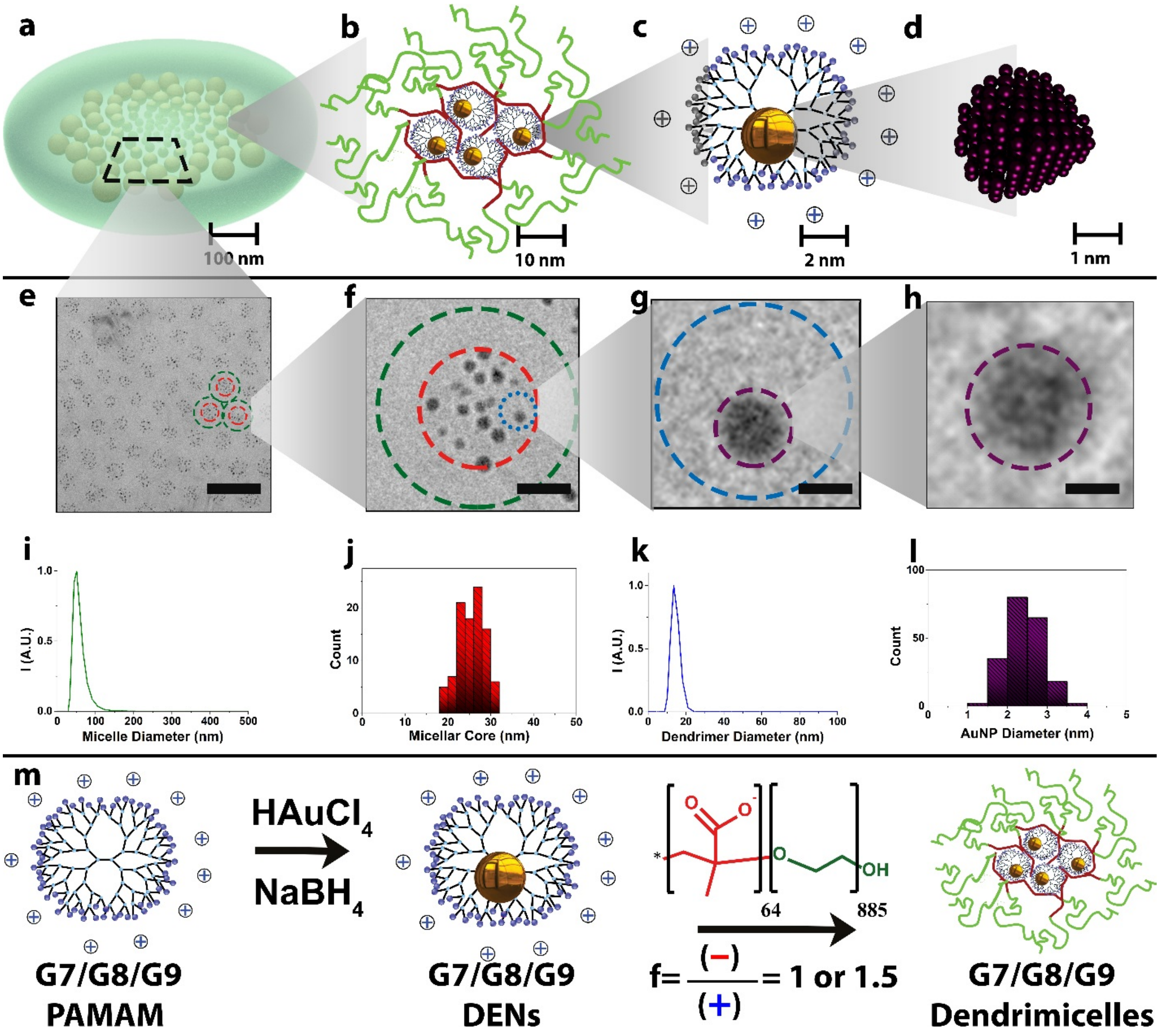

Figure **3-1** Organization and ordering over multiple length scales. (a) Illustration of a cryoTEM-grid hole consisting of a thin layer of water with patterns of assembled (b) complex coacervate core micelles, consisting of a negative(red)-neutral(green) pMAA$_{64}$-b-PEO$_{885}$ diblock copolymer and (c) a positively charged (blue) PAMAM core with an encapsulated (d) gold nanoparticle. The dendrimer encapsulated nanoparticles provide excellent contrast for cryoTEM (scale bars in e-h correspond to the ones in a-d, respectively). DLS reveals (i) micelles with a hydrodynamic diameter of about 50 nm, (j) with a core of about 25 nm as derived from TEM. In (e,f), the green circles indicate the dendrimicelle hydrodynamic diameter as determined by DLS, and the red circles in indicate the dendrimicelle core size as obtained from the cryoTEM micrographs. The hydrodynamic diameter of the 8th generation PAMAM is about 14 nm as determined by DLS (k), and the gold nanoparticles inside the dendrimer are about 2.4 nm (l). (m) Scheme showing the synthesis of nanoparticle-containing dendrimicelles. Complexation and reduction of gold(III) ions in PAMAM dendrimers yields dendrimer-encapsulated nanoparticles. Addition of pMAA$_{64}$-b-PEO$_{885}$ results in dendrimicelle formation. The blue circle in (g) indicates the dendrimer size as determined by DLS, and the purple circles in (g,h), indicates the AuNP.

3.2 Experimental

Materials

Amine-terminated PAMAM dendrimers generation 7–9 were obtained from Dendritech Inc., as 5 wt % methanolic solutions. pMAA$_{64}$-*b*-PEO$_{885}$ ($M_w/M_n = 1.15$) was obtained from Polymer Sources Inc., Canada, and used as a 5 mM solution based on carboxylic acid content. $HAuCl_4 \cdot 3H_2O$ was obtained from TCI. (3-(*N*-Morpholino)propanesulfonic acid) (MOPS), $NaBH_4$, 1 M HCl, and 1 M NaOH were obtained from Sigma-Aldrich.

Apparatus

DLS was done on a Malvern Zetasizer Nano S equipped with a laser operating at 633 nm. Sample grids for electron microscopy were obtained from Electron Microscopy Sciences (EMS, Hatfield, PA, USA) and were rendered hydrophilic using a plasma cleaning setup (15 s at 10^{-1} Torr). For cryoTEM, samples were cast on Quantifoil R2/2 grids or 400 mesh holey carbon grids. After blotting, samples were plunged into liquid ethane using a Vitrobot system (FEI Company). Samples were imaged at ~90 K in a JEOL 2100 TEM operating at 200 kV. For normal TEM, solutions were deposited on hydrophilic 400 mesh carbon-coated copper grids. The micrographs shown are representative for grid holes at different locations on the TEM grids and for samples made on different days. TEM image analyses were done using custom MATLAB scripts (The MathWorks Inc., Natick, MA, USA) and FIJI (https://fiji.sc/).

Synthesis of Dendrimer-Encapsulated Nanoparticles

G7-Au$_{256}$DENs were made following established protocols.[15] Briefly, 50 µL (17 nmol) of 5 wt % PAMAM G7-NH$_2$ in methanol was transferred to a 5 mL vial, and the solvent was evaporated under reduced pressure. Next, 2 mL of water was added to dissolve the PAMAM, and the pH was adjusted to 3 using 1 M HCl, after which 256 molar equiv of Au^{3+} to PAMAM were added as 1 mL of a 4.4 mM aqueous solution of $HAuCl_4$ at pH 3. The resulting solution was then stirred for 20 min, after which 44 µL of a 1 M solution of $NaBH_4$ in 0.3 M NaOH (10 molar equiv to Au^{3+}) was added. This resulted in the reduction of Au^{3+} to AuDENs, indicated by the change from colorless to a dark brown solution within seconds after addition. After reduction, the pH was set to 7 using HCl, and the Au$_{256}$DENS were stored at 4 °C as a 5.6 µM solution. G8/G9 DENs were made in a similar way, using 512, respectively, 1024 equivalents, of Au:PAMAM-NH$_2$.

Dendrimer-Encapsulated Nanoparticles in Micelles

To obtain dendrimicelles under charge stoichiometric conditions, 20 µL of GX DENs (~58 nmol positive charge based on surface groups, GX being generation 7, 8, or 9 PAMAM) was dissolved in 149 µL of water, and 20 µL of 0.2 M MOPS buffer at pH 7.0 was added. Then, 11 µL of $pMAA_{64}$-*b*-PEO_{885} (55 nmol based on −COOH) was added, and the sample was sonicated for 2 min. To obtain more polydisperse micelles off-stoichiometric charge fractions were used. Here, the ratio of block copolymer to dendrimer was adjusted accordingly, keeping the final volume constant at 200 µL. Samples were left to equilibrate for at least 1 day before characterization using cryoTEM.

Image Segmentation

To allow for an in-depth analysis of the individual micelle characteristics within the images, a semiautomatic micelle segmentation protocol was developed. This segmentation consisted of three main sections. First, an automatic intensity-based thresholding was applied to detect the gold nanoparticles, located within the micelles. Second, the detected features were filtered by size, excluding small noise structures, dilated, and connected based on *inter*-particle distance. This generated filled circular structures, approximating the actual micelles in the original image. Lastly, manual adjustment and verification of the created micelle segmentation with respect to the original microscopy image provided the final segmentation output.

After the segmentation, every segmented blob was digitally labeled and characterized for its individual properties, *e.g.*, micelle centroid location, micelle area in the image, and micelle diameter. These values were used to create heat map images, visualizing the micelle distributions based on their area. For these images, perfectly round circles, with the appropriate diameter, were drawn at the micelle centroid locations, using a linear color coding to depict the size distribution. Micelle coordinates were converted to polar coordinates using the approximated center of the pattern. The nearest neighbors of a dendrimicelle were defined as the particles that have their centroid coordinates located within a circle with a radius of 1.5 times the distance of a dendrimicelle and its closest neighbor.

Dendrimicelle Core Packing Density

The dendrimicelle core packing density was calculated by dividing the core volume by the total dendrimer volume inside the core. The total dendrimer volume inside the dendrimicelle core was calculated by multiplying the number of dendrimers per dendrimicelle by the dendrimer volume. The dendrimer volume was calculated from the manufacturer's specified diameter (8.1, 9.7, and 11.4 nm for G7, G8, and G9 PAMAM dendrimers, respectively), assuming the dendrimers to be spherical.

3.3 Results and Discussion

Dendrimer-encapsulated gold nanoparticles, Au-DENs, were synthesized following the original work of Amis by reduction of gold(III) ions residing inside PAMAM dendrimers[16,21] and as reported for generation 7 dendrimers elsewhere.[15] We focused on generations 7, 8, and 9 in order to have single particles of respectively Au_{256}, Au_{512}, and Au_{1024} per dendrimer and aggregation numbers in the dendrimicelles between 10 and 40, to allow straightforward discrimination and counting of individual nanoparticles. TEM analysis showed the formed Au-DENs to be about 2–3 nm in diameter, with the PAMAM ranging in hydrodynamic diameter (dynamic light scattering, DLS) from 9.6 to 17 nm for generation 7 to 9 (Figure **S1**). Consecutive mixing under charge stoichiometry conditions (Figure **S2**) of the Au-DENs with a $pMAA_{64}$-*b*-PEO_{885} block copolymer, consisting of a 64-subunit polymethacrylic acid block and an 885-subunit poly(ethylene oxide) (PEO) neutral block, resulted in coacervate-core micelle formation as shown by DLS.

The cryoTEM micrographs (Figure **3-1**) of a sample obtained from generation 8 Au-DENs clearly corroborate formation of dendrimicelles, with a core size of about 25 nm as deduced from the gold particles delineating the core; the PEO corona is not observed, but its size can be deduced from the *inter*-core distances to be about 7 nm. The average micelle diameter of about 40 nm, as determined from TEM, is slightly smaller than the about 50 nm hydrodynamic diameter obtained from DLS, which could indicate the PEO chains to be compressed or even interpenetrating with neighboring micelles upon packing in the superstructure.[22] Counting the Au-DENs per micelle core allows a straightforward determination of the aggregation number of the components and hence the size of the whole micelle. For the system shown in Figure **3-1**, on average 27 Au-DENs reside inside a micelle, corresponding to 27 PAMAM dendrimers and about 400 block copolymers at charge stoichiometric mixing conditions. The total molecular dry weight of such micelles is therefore on the order of about 25 MDa. We note that cryoTEM micrographs are the 2D representation (image) of the 3D system (the micelle), and therefore, particles that are overlapping in the micelle shown in Figure **3-1f** are not fused; they just have the same *x*,*y*-coordinates but are separated along the *z*-axis. The packing fraction of the DENs in the dendrimicelle core is ~0.9, indicating that the dendrimers are densely packed. Consequently, the *inter*-particle distances in the dendrimicelle core range between ~3 and ~15 nm (Figure **S3**). While analyzing the dendrimicelles in the cryoTEM micrograph, we observed ordering and organization on the micrometer scale, suggesting the formation of monolayer superstructures. To investigate the effect of the dendrimicelles on the higher-order organization, we prepared a series of dendrimicelles made from different dendrimer generations and studied these with cryoTEM. CryoTEM micrographs of the series of dendrimicelles based on Au-DENs of generation 7, 8, and 9 PAMAM are shown in Figure **3-2a–c**.

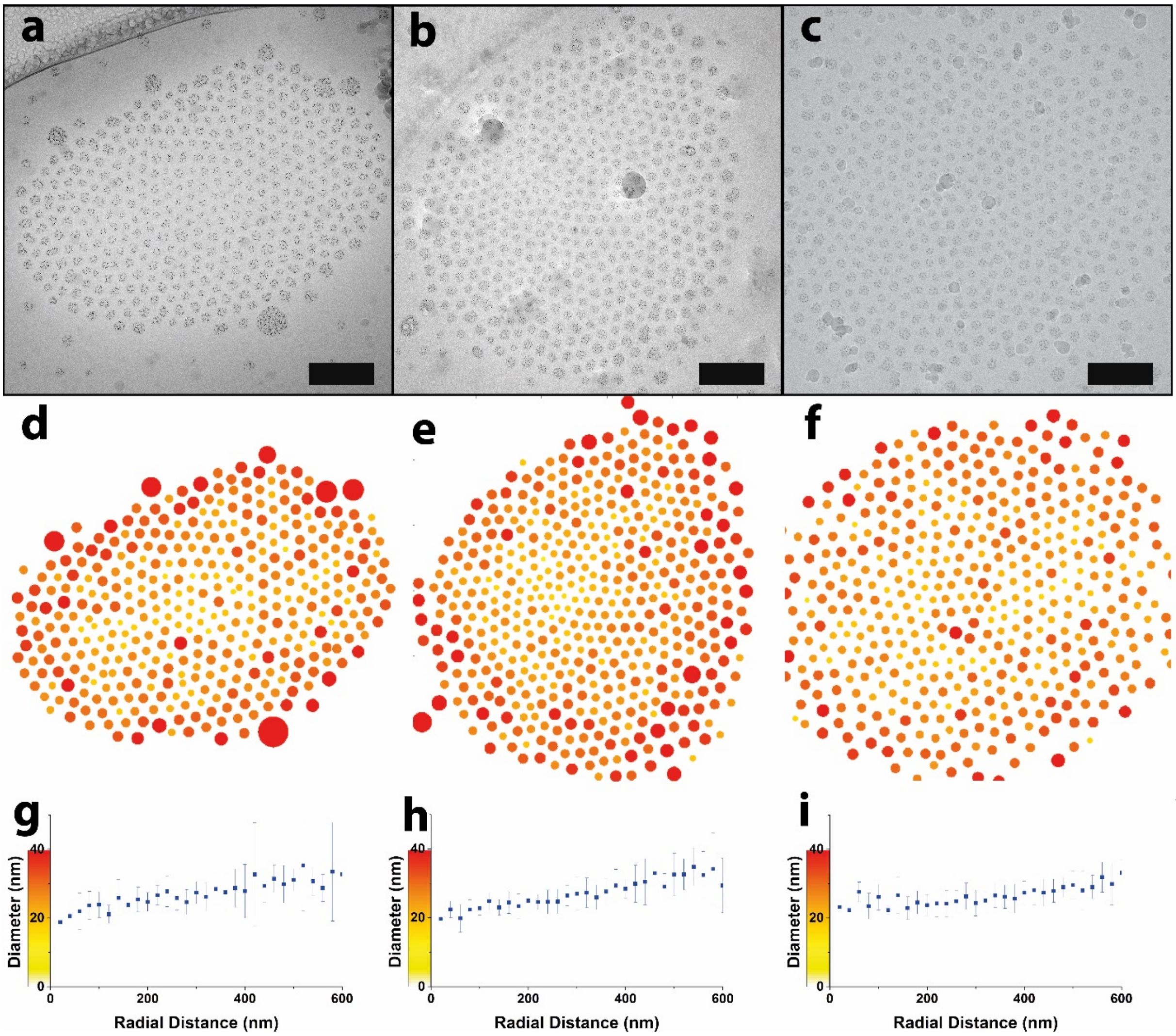

Figure **3-2** Ordering of 7th (left), 8th (middle) and 9th (right) generation PAMAM dendrimicelles. (a-c) The darker spots in the cryoTEM images are the 2-3 nm gold nanoparticles residing inside the dendrimers in the micelle core; scale bars correspond to 200 nm. (d-f) Image segmentation results in heat map plots with micelle cores color-coded according to their size. (g-i) Radial distance plots show micelle diameter versus distance to the center of the pattern.

The micrometer-sized grid holes contain several hundred micelles, which organize by size and into domains with discrete geometric patterns. Image analysis allowed for particle tracking and segmentation of individual micelles and was subsequently used to graphically display the positions and size of the micelles, with color coding highlighting the small size differences observed (Figure **3-2d–f**). The color coding also facilitates the discrimination of a clear size sorting in the patterns, with the smaller micelles being positioned more toward the center of the circular superstructures and the bigger ones more toward the outside. The vitreous ice layer formed in the holes of the TEM grid foil is biconcave shaped and thinner toward the center.[23-25] Figures **S4-6** show average image intensity plots as derived from the TEM micrographs, which are indicative for the thickness of the vitreous ice layer. These figures confirm that the ice layer is thinner toward the center of the dendrimicelle superstructure and give an estimate of the curvature of the biconcave thin film.

Plotting the determined micellar core diameter against the distance from the center of the superstructure further corroborates the size sorting (Figure **3-2g–i**) and shows the micelles evidently sort according to the thickness of the water layer. Also, clear domains with different geometric patterns are observed for all three different dendrimicelle systems (Figure **S7-9**) and appeared in samples prepared on different occasions and with different preparation protocols. CryoTEM provides snapshots of the micelle organization process during and after the blotting step, which does not necessarily represent a thermodynamic equilibrium state of the dendrimicelles in the thin film. The formation of the water layer in the blotting process prior to vitrification inflicts dramatic forces on the sample. In fact, the micrometer-size circular areas observed often consist of multiple domains (Figure **S7-9** for highlighted domains) and characteristic geometric patterns and five and seven nearest neighbor sites (Figure **S10-12**).

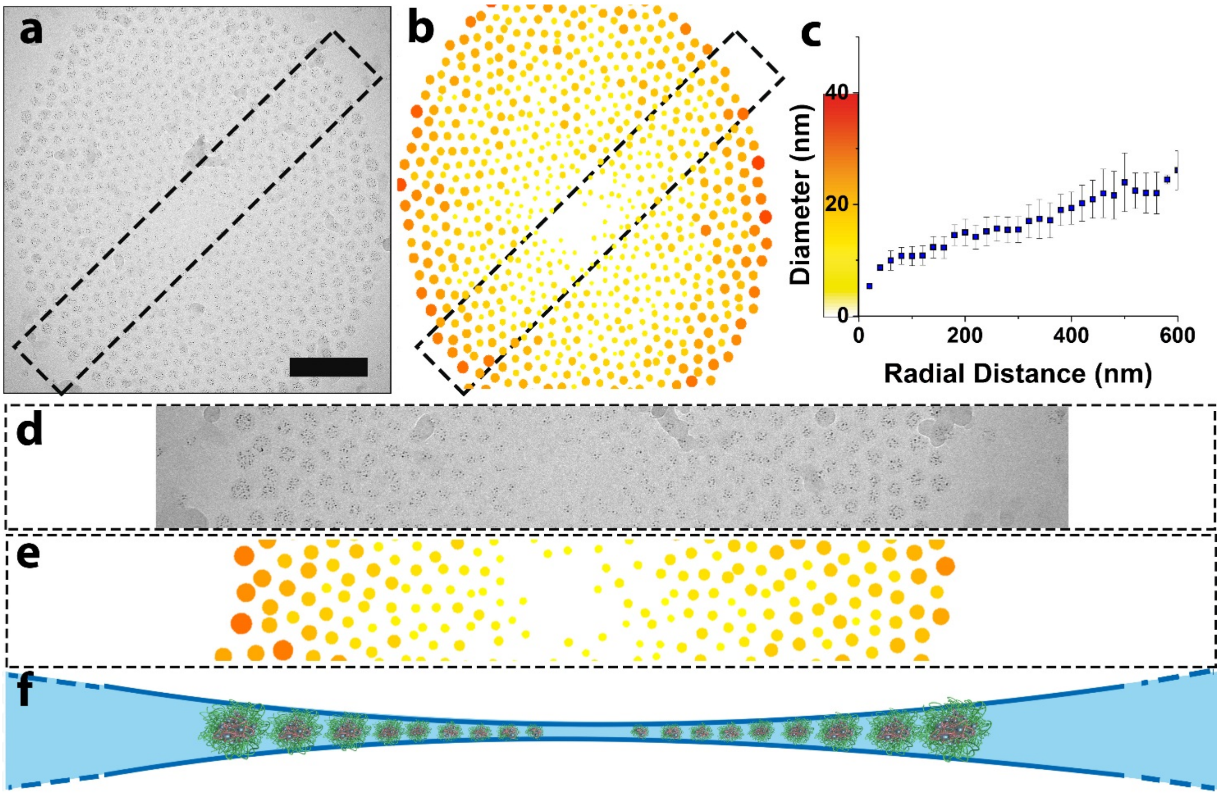

Figure 3-3 Extreme size sorting of dendrimicelles in biconcave thin films. CryoTEM micrograph (a) of a superstructure obtained from G7-based dendrimicelles obtained at non-charge stoichiometric conditions (f = 1.5). Color- and size-coded heatmap highlighting the size sorting (b). Core diameter of the dendrimicelles versus radial distance from the center of the superstructure. Slice from the cryoTEM micrograph (d) and corresponding heatmap (e) visualizing the extreme size-sorting. Side-view impression of the distribution of differently sized micelles in the thin biconcave water layer in a TEM-grid hole.

The size sorting of dendrimicelles in the biconcave thin water film was further investigated with dendrimicelle samples obtained under non-charge stoichiometric conditions, *i.e.*, with a 1.5 times excess of block copolymer. The resulting dendrimicelles were expected to be more polydisperse and show different packing and size sorting in the formed superstructures. Indeed, all three dendrimicelles, obtained from G7, G8, and G9 DENs, show increased size-sorting features (see Figures **S13-19**). The most prominent example was obtained from a G7 dendrimicelle, shown in Figure **3-3**. The TEM micrograph and the generated color-labeled heat map plot show a dramatic size sorting (Figure **3-3a–c**). A cross section of the superstructure further highlights this sorting of dendrimicelles with sizes that range in the core diameter from 10 to 20 nm. The size sorting is most likely templated by the thickness of the thin water film formed during sample preparation, which is a double, biconcave, air–water interface that becomes thinner toward the center (see Figure **3-3f**).

We note that when this layer is too thick, we do not detect the formation of the superstructures nor observe size sorting and only witness dendrimicelles that are randomly distributed throughout the TEM grid hole. Monolayer superstructures typically form as real 2D structures on flat surfaces, at solvent–-air interfaces, or on curved surfaces.[26-31] The biconcave thin water layer formed in the cryoTEM preparation provides a double air–water curved interface where the micelles are likely arranging symmetrically in the layer, touching both interfaces. Interestingly, the thin water layer in the center of the superstructure shown in Figure **3-3** does not contain any dendrimicelles, indicating the layer to be thinner than 20 nm and possibly just a few nanometers in the center. Figure **S14** shows the average intensity plot over the superstructure, corroborating the size sorting observed with the ice layer thickness.

The size-sorting and pattern formation have been further investigated in detail for a generation 7 PAMAM-based dendrimicelle with particularly large domains. Figure **3-4a** shows a cryoTEM image with Au-DENs revealing domains hundreds of nanometers across containing multiple spiral geometries (see Supplementary Figures **S20–22** for enlarged figures). Segmentation of the TEM micrograph allowed reconstruction of the image, showing interesting double-spiral domains, of which a few have been highlighted (Figure **3-4b**). Similar Fibonacci-related spiral patterns and symmetry are commonly observed in nature at millimeter, centimeter, or even larger scales,[1-3] *e.g.*, the archetypical sunflower seed head (Figure **3-4c**). More recently, such geometries have been discovered to form in stress-induced micrometer-sized core–shell particles[28] and Fibonacci-related ordering is observed also in 2D quasicrystals.[32] The spiral patterning features observed for the micelle superstructures in the biconcave thin water layer template is further extending this extraordinary symmetry into the nanoscale.

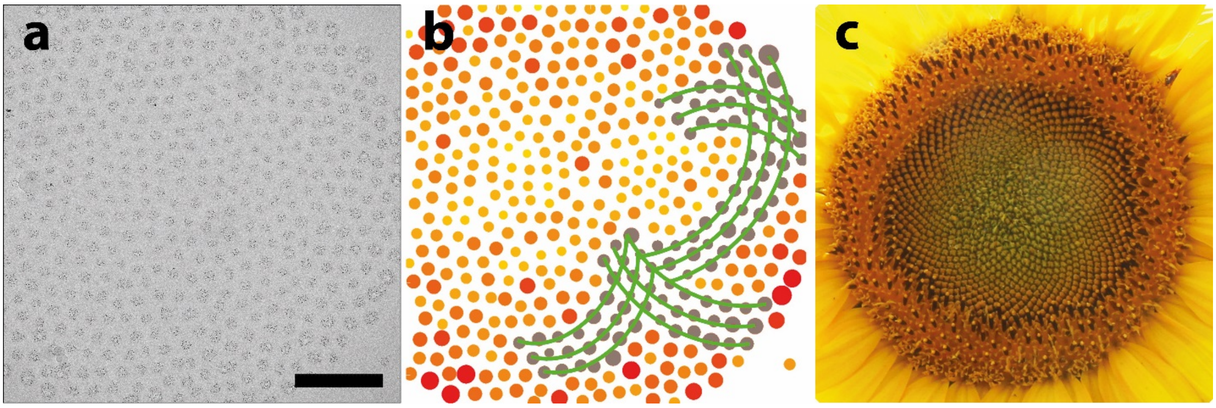

Figure **3-4** Double-spiral sunflower-like patterns in dendrimicelles superstructures. (a) CryoTEM shows large multiple spiral domains; scale bar corresponds to 200 nm. (b) Corresponding color coded heat maps highlight geometric features such as intersecting spirals, a feature commonly observed in nature, e.g., (c) sunflower heads, with Fibonacci related symmetry.

3.4 Conclusion

The micelle strategy presented here offers stable structures (Figure **S23**) with a great potential for further generating and understanding hierarchically orchestrated [particle-in-a-box]-in-a-box superstructures, *via* changing the nanoparticle or dendrimer loading, using different types of dendrimers or micelles, or with different or even mixed components. Finally, the ordering is not expected to be limited to micelle structures, but might be well observed for other macromolecular/supramolecularly assembled systems. The biconcave water layer that progressively becomes thinner in the cryoTEM sample preparation induces physical stress on the sample, which together with the complex interplay of attractive and repulsive forces between the micelles, solvent, and air at the water–air interfaces eventually results in assembly and formation of the superstructures. For 3D systems, the packing of soft nanoparticles has been investigated and modeled in great detail.[33] Paradoxically, 2D systems are of a very different complexity, in which not only *inter*-particle forces play a role,[34] but also polydispersity and size gradients, air–solvent interfaces, and reciprocal template effects play crucial roles. In addition, the deformability of micelles under stress could also play a role, as particle shape has shown to influence packing as well.[27] Finally, large domains are observed, yet the presence of multiple domains within one superstructure implies the photos obtained are snapshots of out-of-equilibrium situations. It is experimentally a challenge control all parameters involved in the cryoTEM sample preparation, which is currently one of our interest areas for further research. Nanoparticles, dendrimers, and micelles all find wide applications in fields such as optically or magnetically active materials, and the superstructures presented here might provide 2D super lattices with emerging properties related to the ordering of the nanoscale building blocks, for which in nature occurring patterns can serve as inspiration. The presented strategy offers a plethora of variations in supramolecular building blocks to investigate hierarchical organization, pattern formation, size sorting, and ordering mechanisms at the nanoscale, and we anticipate our work will inspire exploration of alternative avenues for fabrication of metamaterials, *e.g.*, thin film non-periodic super lattices with concomitant emerging properties.[31,35-41] The parallels with the study of ordered structures found in nature,[1,2,19,20] in botany described as phyllotaxis, inspired us to define the current field of study as nanotaxis.

References

1. Thompson, D. W. *On Growth and Form*; University Press: Cambridge, 1917.
2. Ball, P. *Shapes- Nature's Patterns* Oxford University Press Inc., New York: 2009.
3. Whitesides, G. M.; Grzybowski, B. Self-Assembly at All Scales. *Science* **2002**, 295, 2418-2421.
4. Boles, M. A.; Engel, M.; Talapin, D. V. Self-Assembly of Colloidal Nanocrystals: From Intricate Structures to Functional Materials. *Chemical Reviews* **2016**, 116, 11220-11289.
5. Li, M.; Schnablegger, H.; Mann, S. Coupled Synthesis and Self-Assembly of Nanoparticles to Give Structures with Controlled Organization. *Nature* **1999**, 402, 393-395.
6. Zeng, C. J.; Chen, Y. X.; Kirschbaum, K.; Lambright, K. J.; Jin, R. C. Emergence of Hierarchical Structural Complexities in Nanoparticles and Their Assembly. *Science* **2016**, 354, 1580-1584.
7. Zeng, X. B.; Ungar, G.; Liu, Y. S.; Percec, V.; Dulcey, S. E.; Hobbs, J. K. Supramolecular Dendritic Liquid Quasicrystals. *Nature* **2004**, 428, 157-160.
8. Wang, Y. Z.; Zeiri, O.; Raula, M.; Le Ouay, B.; Stellacci, F.; Weinstock, I. A. Host-Guest Chemistry with Water-Soluble Gold Nanoparticle Supraspheres. *Nature Nanotechnology* **2017**, 12, 170-176.
9. Zeng, X. B.; Kieffer, R.; Glettner, B.; Nurnberger, C.; Liu, F.; Pelz, K.; Prehm, M.; Baumeister, U.; Hahn, H.; Lang, H.*; et al.* Complex Multicolor Tilings and Critical Phenomena in Tetraphilic Liquid Crystals. *Science* **2011**, 331, 1302-1306.
10. Hernandez-Garcia, A.; Kraft, D. J.; Janssen, A. F. J.; Bomans, P. H. H.; Sommerdijk, N.; Thies-Weesie, D. M. E.; Favretto, M. E.; Brock, R.; de Wolf, F. A.; Werten, M. W. T.*; et al.* Design and Self-Assembly of Simple Coat Proteins for Artificial Viruses. *Nature Nanotechnology* **2014**, 9, 698-702.
11. Voets, I. K.; de Keizer, A.; Stuart, M. A. C. Complex Coacervate Core Micelles. *Advances in Colloid and Interface Science* **2009**, 147-48, 300-318.
12. Astruc, D.; Boisselier, E.; Ornelas, C. Dendrimers Designed for Functions: From Physical, Photophysical, and Supramolecular Properties to Applications in Sensing, Catalysis, Molecular Electronics, Photonics, and Nanomedicine. *Chemical Reviews* **2010**, 110, 1857-1959.
13. Tomalia, D. A.; Khanna, S. N. A Systematic Framework and Nanoperiodic Concept for Unifying Nanoscience: Hard/Soft Nanoelements, Superatoms, Meta-Atoms, New Emerging Properties, Periodic Property Patterns, and Predictive Mendeleev-Like Nanoperiodic Tables. *Chemical Reviews* **2016**, 116, 2705-2774.
14. Wang, J. Y.; Velders, A. H.; Gianolio, E.; Aime, S.; Vergeldt, F. J.; Van As, H.; Yan, Y.; Drechsler, M.; de Keizer, A.; Stuart, M. A. C.*; et al.* Controlled Mixing of Lanthanide(Iii) Ions in Coacervate Core Micelles. *Chemical Communications* **2013**, 49, 3736-3738.
15. Ten Hove, J. B.; Wang, J.; Van Leeuwen, F. W. B.; Velders, A. H. Dendrimer-Encapsulated Nanoparticle-Core Micelles as Versatile Strategy for Particle-in-a-Box-in-a-Box Nanostructures.
16. Crooks, R. M.; Zhao, M. Q.; Sun, L.; Chechik, V.; Yeung, L. K. Dendrimer-Encapsulated Metal Nanoparticles: Synthesis, Characterization, and Applications to Catalysis. *Accounts Chem. Res.* **2001**, 34, 181-190.
17. Gomez, M. V.; Guerra, J.; Myers, V. S.; Crooks, R. M.; Velders, A. H. Nanoparticle Size Determination by H-1 Nmr Spectroscopy. *Journal of the American Chemical Society* **2009**, 131, 14634-14635.

18. Gomez, M. V.; Guerra, J.; Velders, A. H.; Crooks, R. M. Nmr Characterization of Fourth-Generation Pamam Dendrimers in the Presence and Absence of Palladium Dendrimer-Encapsulated Nanoparticles. *Journal of the American Chemical Society* **2009**, 131, 341-350.

19. Mitchison, G. J. Phyllotaxis and Fibonacci Series. *Science* **1977**, 196, 270-275.

20. Vogel, H. Better Way to Construct the Sunflower Head. *Mathematical Biosciences* **1979**, 44, 179-182.

21. Grohn, F.; Bauer, B. J.; Akpalu, Y. A.; Jackson, C. L.; Amis, E. J. Dendrimer Templates for the Formation of Gold Nanoclusters. *Macromolecules* **2000**, 33, 6042-6050.

22. Ungar, G.; Zeng, X. B. Frank-Kasper, Quasicrystalline and Related Phases in Liquid Crystals. *Soft Matter* **2005**, 1, 95-106.

23. Danino, D. Cryo-Tem of Soft Molecular Assemblies. *Current Opinion in Colloid & Interface Science* **2012**, 17, 316-329.

24. Friedrich, H.; Frederik, P. M.; de With, G.; Sommerdijk, N. Imaging of Self-Assembled Structures: Interpretation of Tem and Cryo-Tem Images. *Angewandte Chemie-International Edition* **2010**, 49, 7850-7858.

25. Glaeser, R. M.; Han, B. G.; Csencsits, R.; Killilea, A.; Pulk, A.; Cate, J. H. D. Factors That Influence the Formation and Stability of Thin, Cryo-Em Specimens. *Biophysical Journal* **2016**, 110, 749-755.

26. Ershov, D.; Sprakel, J.; Appel, J.; Stuart, M. A. C.; van der Gucht, J. Capillarity-Induced Ordering of Spherical Colloids on an Interface with Anisotropic Curvature. *Proceedings of the National Academy of Sciences of the United States of America* **2013**, 110, 9220-9224.

27. Iacovella, C. R.; Keys, A. S.; Glotzer, S. C. Self-Assembly of Soft-Matter Quasicrystals and Their Approximants. *Proceedings of the National Academy of Sciences of the United States of America* **2011**, 108, 20935-20940.

28. Li, C.; Zhang, X.; Cao, Z. Triangular and Fibonacci Number Patterns *Science* **2005**, 309, 909-911.

29. Lin, Y.; Boker, A.; Skaff, H.; Cookson, D.; Dinsmore, A. D.; Emrick, T.; Russell, T. P. Nanoparticle Assembly at Fluid Interfaces: Structure and Dynamics. *Langmuir* **2005**, 21, 191-194.

30. Mueggenburg, K. E.; Lin, X. M.; Goldsmith, R. H.; Jaeger, H. M. Elastic Membranes of Close-Packed Nanoparticle Arrays. *Nature Materials* **2007**, 6, 656-660.

31. Vanmaekelbergh, D. Self-Assembly of Colloidal Nanocrystals as Route to Novel Classes of Nanostructured Materials. *Nano Today* **2011**, 6, 419-437.

32. Dotera, T.; Oshiro, T.; Ziherl, P. Mosaic Two-Lengthscale Quasicrystals. *Nature* **2014**, 506, 208-211.

33. Ziherl, P.; Kamien, R. D. Maximizing Entropy by Minimizing Area: Towards a New Principle of Self-Organization. *The Journal of Physical Chemistry B* **2001**, 105, 10147-10158.

34. Glaser, M. A.; Grason, G. M.; Kamien, R. D.; Košmrlj, A.; Santangelo, C. D.; Ziherl, P. Soft Spheres Make More Mesophases. *EPL (Europhysics Letters)* **2007**, 78, 46004.

35. Bigioni, T. P.; Lin, X. M.; Nguyen, T. T.; Corwin, E. I.; Witten, T. A.; Jaeger, H. M. Kinetically Driven Self Assembly of Highly Ordered Nanoparticle Monolayers. *Nature Materials* **2006**, 5, 265-270.

36. Boneschanscher, M. P.; Evers, W. H.; Geuchies, J. J.; Altantzis, T.; Goris, B.; Rabouw, F. T.; van Rossum, S. A. P.; van der Zant, H. S. J.; Siebbeles, L. D. A.; Van Tendeloo, G.*; et al.* Long-Range Orientation and Atomic Attachment of Nanocrystals in 2d Honeycomb Superlattices. *Science* **2014**, 344, 1377-1380.

37. Cargnello, M.; Johnston-Peck, A. C.; Diroll, B. T.; Wong, E.; Datta, B.; Damodhar, D.; Doan-Nguyen, V. V. T.; Herzing, A. A.; Kagan, C. R.; Murray, C. B. Substitutional Doping in Nanocrystal Superlattices. *Nature* **2015**, 524, 450-+.
38. Dong, A. G.; Chen, J.; Vora, P. M.; Kikkawa, J. M.; Murray, C. B. Binary Nanocrystal Superlattice Membranes Self-Assembled at the Liquid-Air Interface. *Nature* **2010**, 466, 474-477.
39. Huang, X. Q.; Tang, S. H.; Mu, X. L.; Dai, Y.; Chen, G. X.; Zhou, Z. Y.; Ruan, F. X.; Yang, Z. L.; Zheng, N. F. Freestanding Palladium Nanosheets with Plasmonic and Catalytic Properties. *Nature Nanotechnology* **2011**, 6, 28-32.
40. Parker, G. J. Biomimetically-Inspired Photonic Nanomaterials. *Journal of Materials Science-Materials in Electronics* **2010**, 21, 965-979.
41. Ungar, G.; Liu, Y. S.; Zeng, X. B.; Percec, V.; Cho, W. D. Giant Supramolecular Liquid Crystal Lattice. *Science* **2003**, 299, 1208-1211.

3.6 Appendix

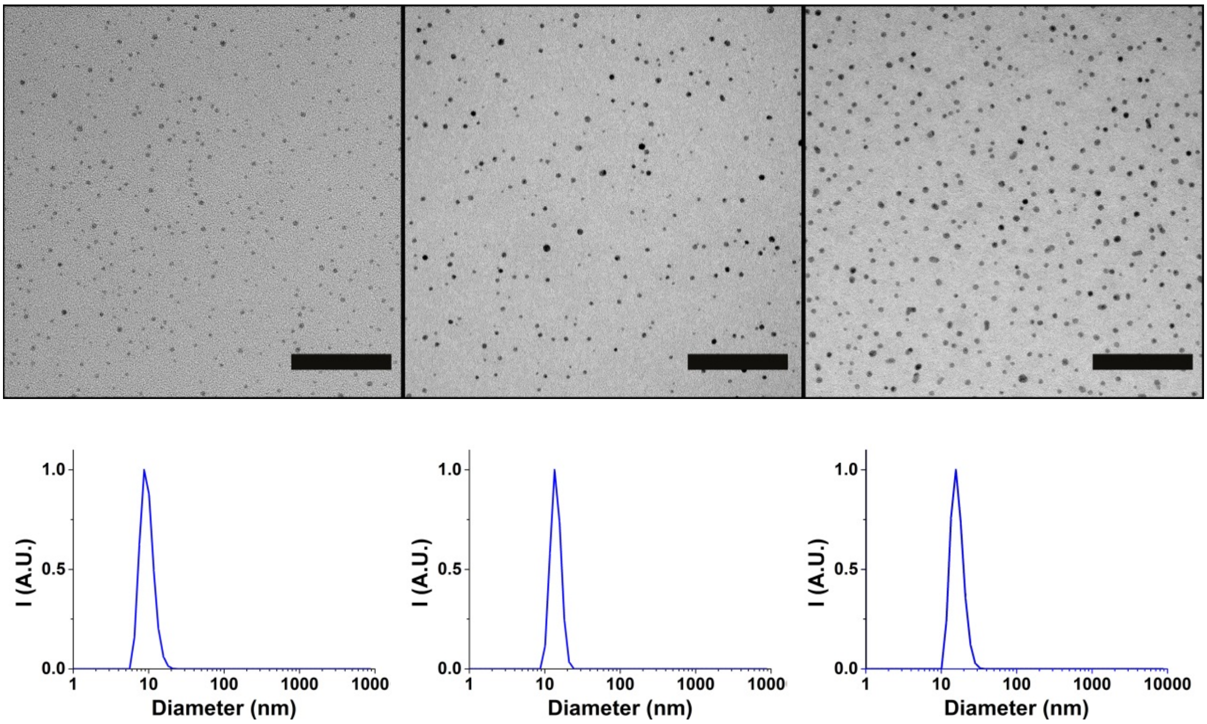

Fig. S1 Characterization of PAMAM G7-9 AuDENs Top: TEM micrographs of PAMAM-G7, -G8 and -G9 Dendrimer Encapsulated Nanoparticles. Left: G7-Au$_{256}$ DENs are 1.8 ± 0.6 nm (226 particles analyzed). Middle: G8-Au$_{512}$ DENs are 2.0 ± 0.9 nm (190 particles analyzed). Right: G9-Au$_{1024}$ DENs are 2.3 ± 0.8 nm (295 particles analyzed). The scale bars in the figures correspond to 50 nm. Bottom: Number-averaged DLS size plots of G7-Au$_{256}$ (left), G8-Au$_{512}$ (middle) and G9-Au$_{1024}$ (right). The average hydrodynamic diameter was (from left to right) 9.6, 14, 17 nm for G7-Au$_{256}$, G8-Au$_{512}$ and G9-Au$_{1024}$ respectively.

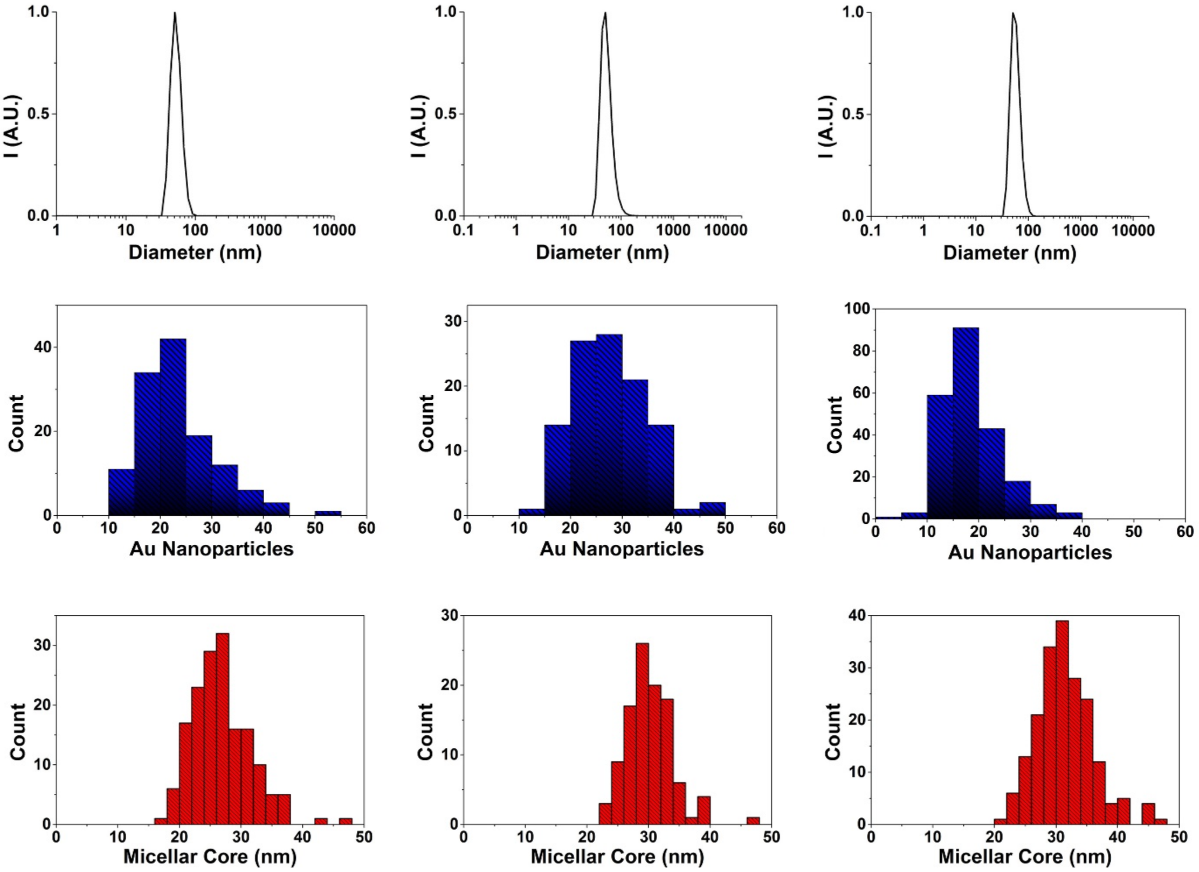

Fig. S2 Characterization of PAMAM G7-9 dendrimicelles. Top: Number-averaged DLS size plots of G7 (left), G8 (middle) and G9 (right) dendrimicelles made under charge-stoichiometric mixing conditions, using G7-Au$_{256}$ respectively G8-Au$_{512}$ respectively G9-Au$_{1024}$ DENs. The determined average hydrodynamic diameter was 52, 51, 55 nm for G7, G8, G9 respectively. Middle: Histograms showing the counted number of AuNPs per micelle for the G7-Au$_{256}$ (left), G8-Au$_{512}$ (middle) and G9-Au$_{1024}$ (right) dendrimicelles. The average number of AuNPs per micelle is 23 ± 7 for G7-Au$_{256}$ (128 micelles analyzed), 27 ± 7 for G8-Au$_{512}$ (108 micelles analyzed) and 18 ± 6 for G9-Au$_{1024}$ dendrimicelles (225 micelles analyzed). Bottom: Histograms showing the average micellar core diameter as obtained from the cryoTEM micrographs, for G7-Au$_{256}$ (left), G8-Au$_{512}$ (middle) and G9-Au$_{1024}$ (right) dendrimicelles made under charge-stoichiometric mixing conditions. The average core diameter is 27 ± 5 nm for G7-Au$_{256}$ (162 micelles analyzed), 30 ± 4 nm for G8-Au$_{512}$ (105 micelles analyzed) and 32 ± 5 nm for G9-Au$_{1024}$ (192 micelles analyzed). The dendrimicelle core packing density is ~0.6 for the G7 dendrimicelles, ~0.9 for the G8 dendrimicelles, and ~0.8 for the G9 dendrimicelles, indicating that the dendrimicelle core is densely packed.

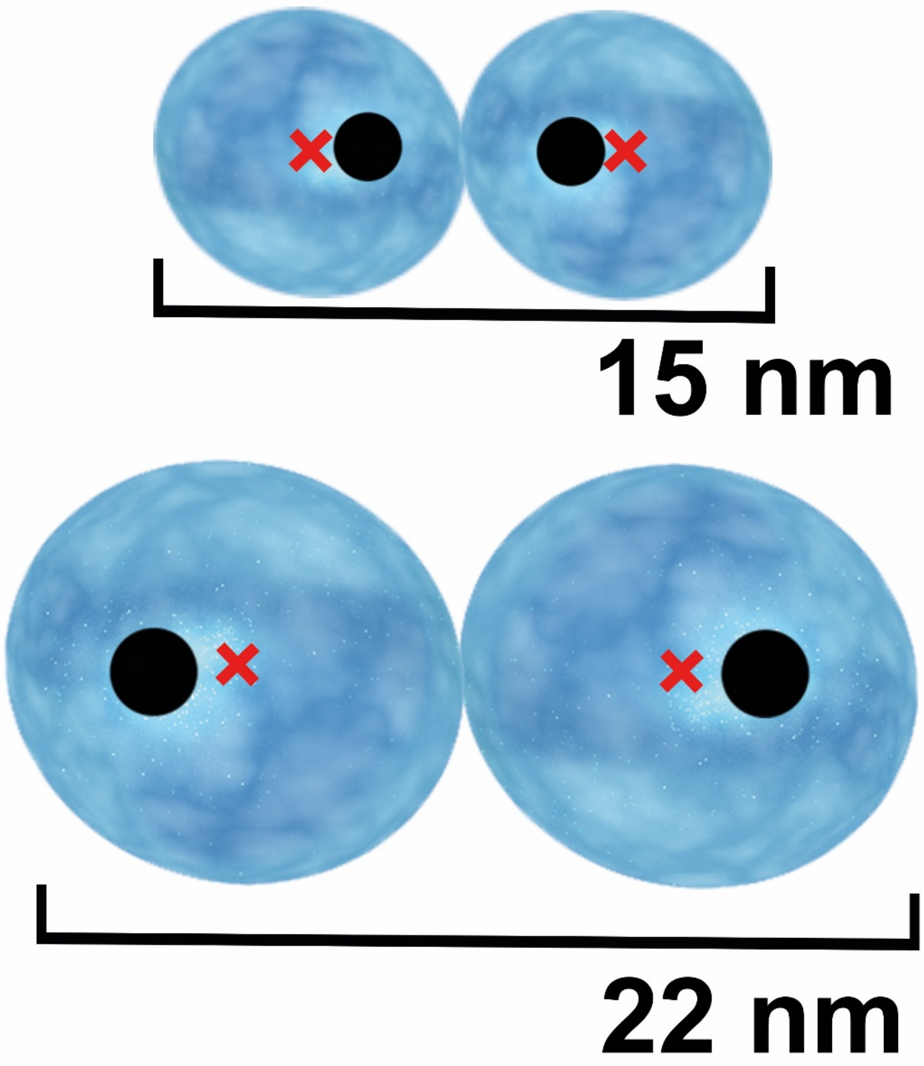

Fig. S3 Schematic drawing illustrating the minimum and maximum distance between dendrimer encapsulated nanoparticles inside the dendrimicelle core. The blue spheres represent the dendrimer, and the black circle the encapsulated nanoparticle. The red cross indicates the center of the dendrimer. Top: the minimum separation distance is ~3 nm, as depicted for the generation 7-based dendrimer-encapsulated nanoparticles. Bottom: the maximum nanoparticle separation distance is ~15 nm, as depicted for the generation 9-based dendrimer-encapsulated nanoparticles. Image is drawn to scale.

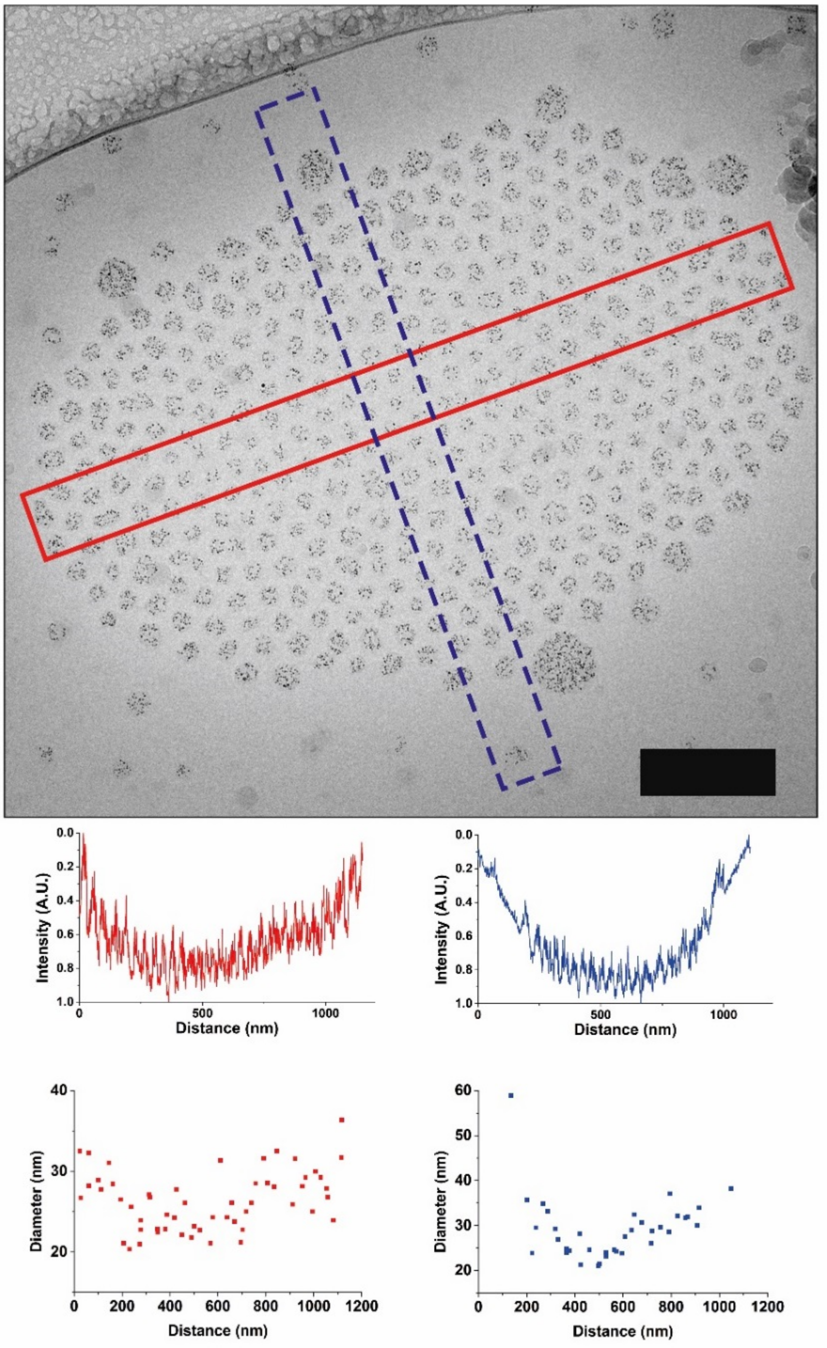

Fig. S4 Quantification of the vitreous ice film thickness and curvature in the G7-based dendrimicelle superstructure sample in Fig 2. **Top**: cryoTEM micrograph of the superstructure. **Middle**: normalized average intensity plots. The left, red, graph shows the average image intensity as determined from the solid, red box and the right, blue, graph shows the average image intensity as obtained from the dashed, blue, box in the TEM micrograph. **Bottom:** The left, red, graph shows the micelle core diameter as determined from the solid, red box and the right, blue, graph shows the micelle core diameter as determined from the dashed, blue, box in the TEM micrograph. The image intensity plots show the curvature of the vitrified water layer, and the dendrimicelle core size plots show that the dendrimicelle sizes follow the same trend, indicating the local thickness of the vitrified water film.

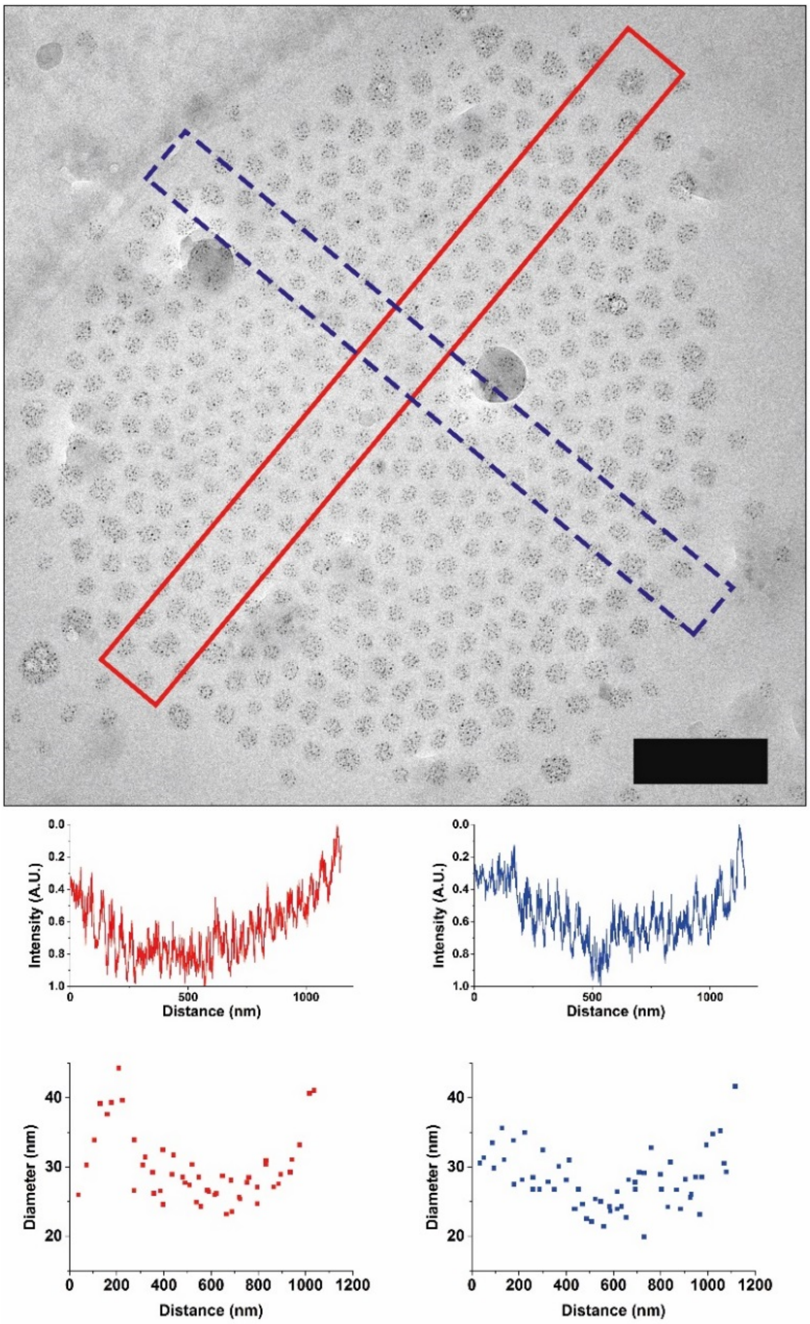

Fig. S5 Quantification of the vitreous ice film thickness and curvature in the G8-based dendrimicelle superstructure sample (Fig 2). **Top**: cryoTEM micrograph of the superstructure. **Middle**: normalized average intensity plots. The left, red, graph shows the average image intensity as determined from the solid, red box and the right, blue, graph shows the average image intensity as obtained from the dashed, blue, box in the TEM micrograph. **Bottom:** The left, red, graph shows the micelle core diameter as determined from the solid, red box and the right, blue, graph shows the micelle core diameter as determined from the dashed, blue, box in the TEM micrograph. The image intensity plots show the curvature of the vitrified water layer, and the dendrimicelle core size plots show that the dendrimicelle sizes follow the same trend, indicating the local thickness of the vitrified water film.

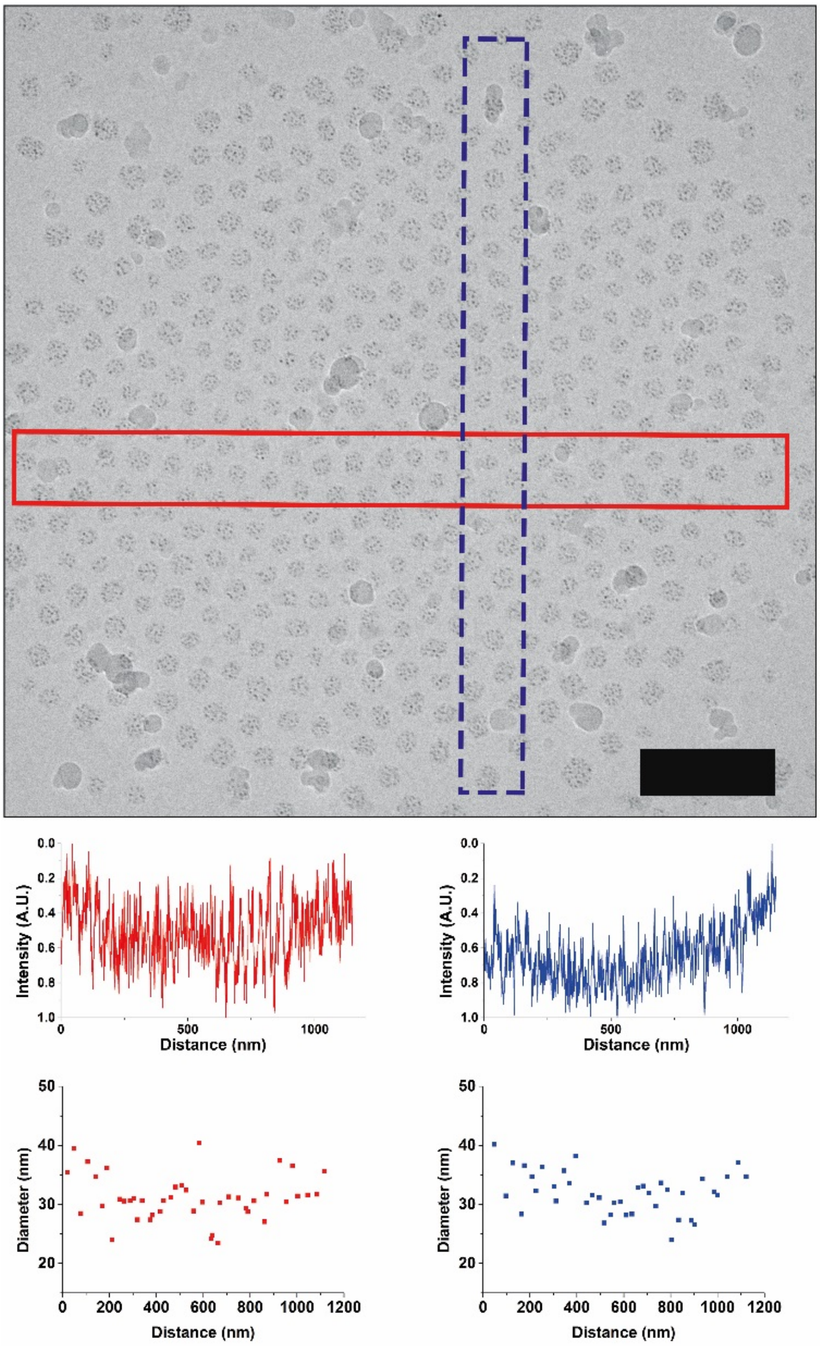

Fig. S6 Quantification of the vitreous ice film thickness and curvature in the G9-based dendrimicelle superstructure sample (Fig 2). **Top**: cryoTEM micrograph of the superstructure. **Middle**: normalized average intensity plots. The left, red, graph shows the average image intensity as determined from the solid, red box and the right, blue, graph shows the average image intensity as obtained from the dashed, blue, box in the TEM micrograph. **Bottom:** The left, red, graph shows the micelle core diameter as determined from the solid, red box and the right, blue, graph shows the micelle core diameter as determined from the dashed, blue, box in the TEM micrograph. The image intensity plots show the curvature of the vitrified water layer, and the dendrimicelle core size plots show that the dendrimicelle sizes follow the same trend, indicating the local thickness of the vitrified water film.

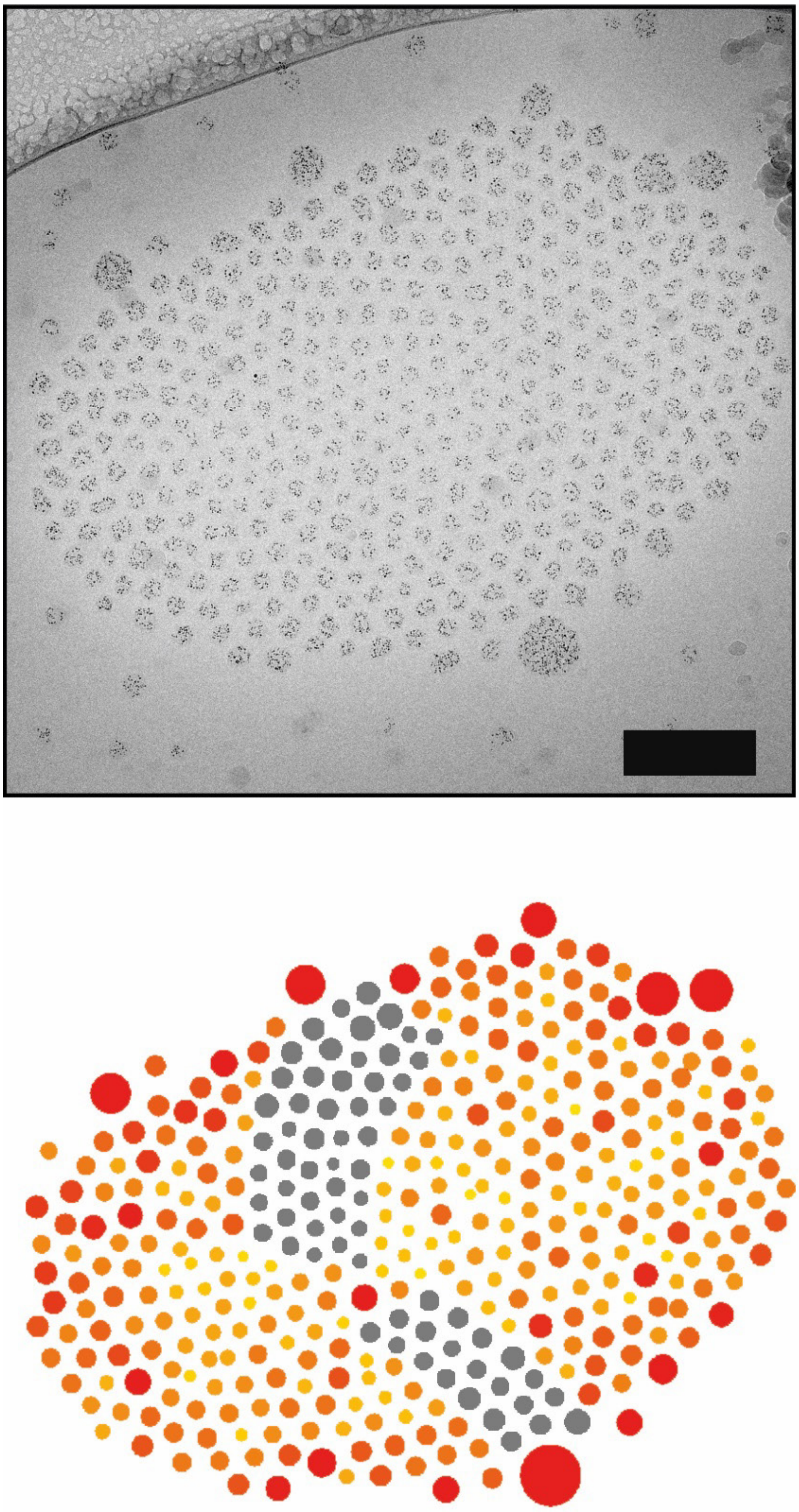

Fig. S7 Characterization of G7 dendrimicelles Top: CryoTEM micrograph of G7 dendrimicelles obtained from charge-stoichiometric mixing with pMAA$_{64}$PEO$_{885}$ block copolymer (Figure 2). The scale bar represents 200 nm. Bottom: Image segmentation and analysis of G7 dendrimicelles, highlighting geometric features such as spiral domains.

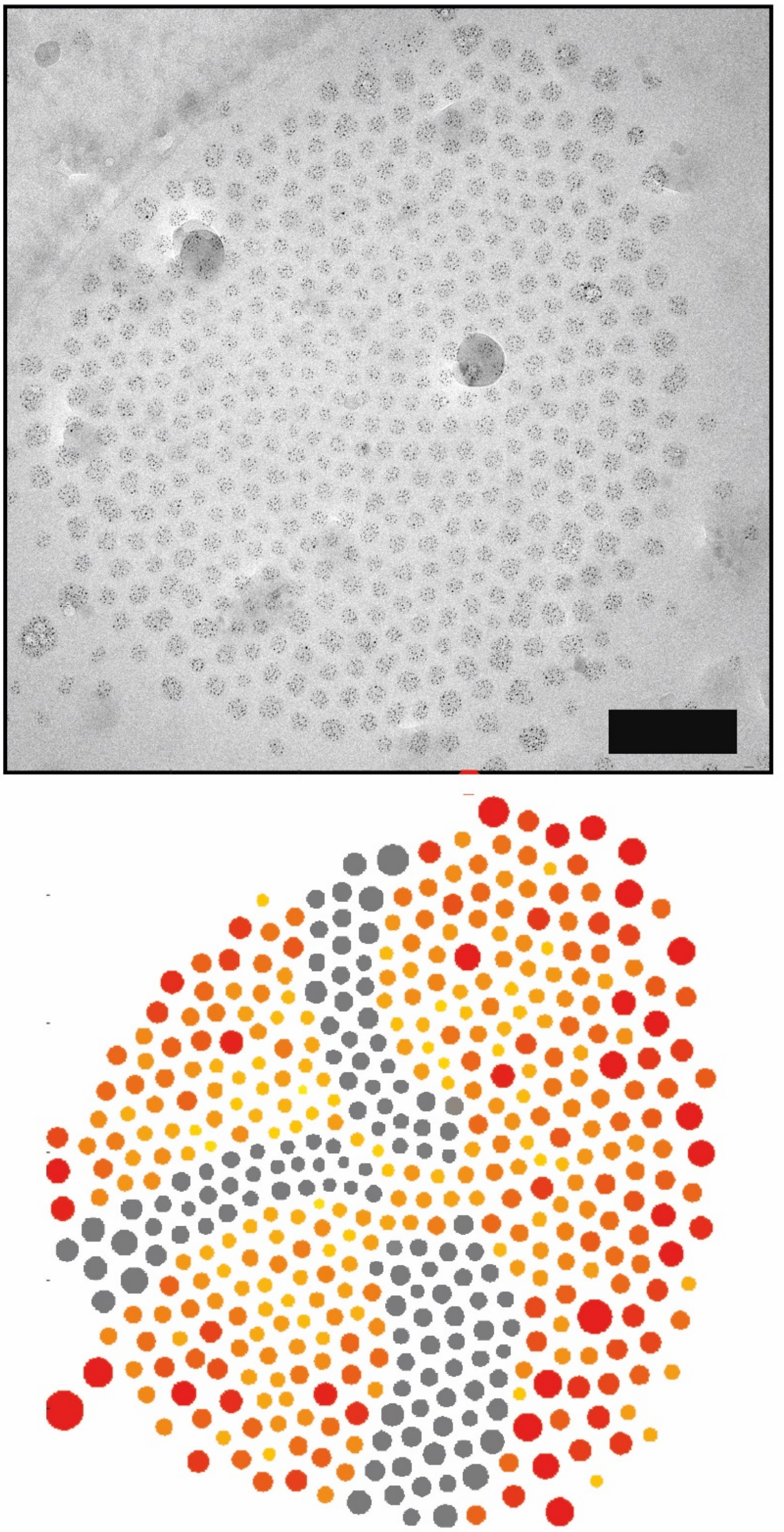

Fig. S8 Characterization of G8 dendrimicelles. Top: CryoTEM micrograph of G8 dendrimicelles obtained from charge-stoichiometric mixing with pMAA$_{64}$PEO$_{885}$ block copolymer (Figure 2). The scale bar represents 200 nm. Bottom: Image segmentation and analysis of G8 dendrimicelles, highlighting geometric features such as spiral domains.

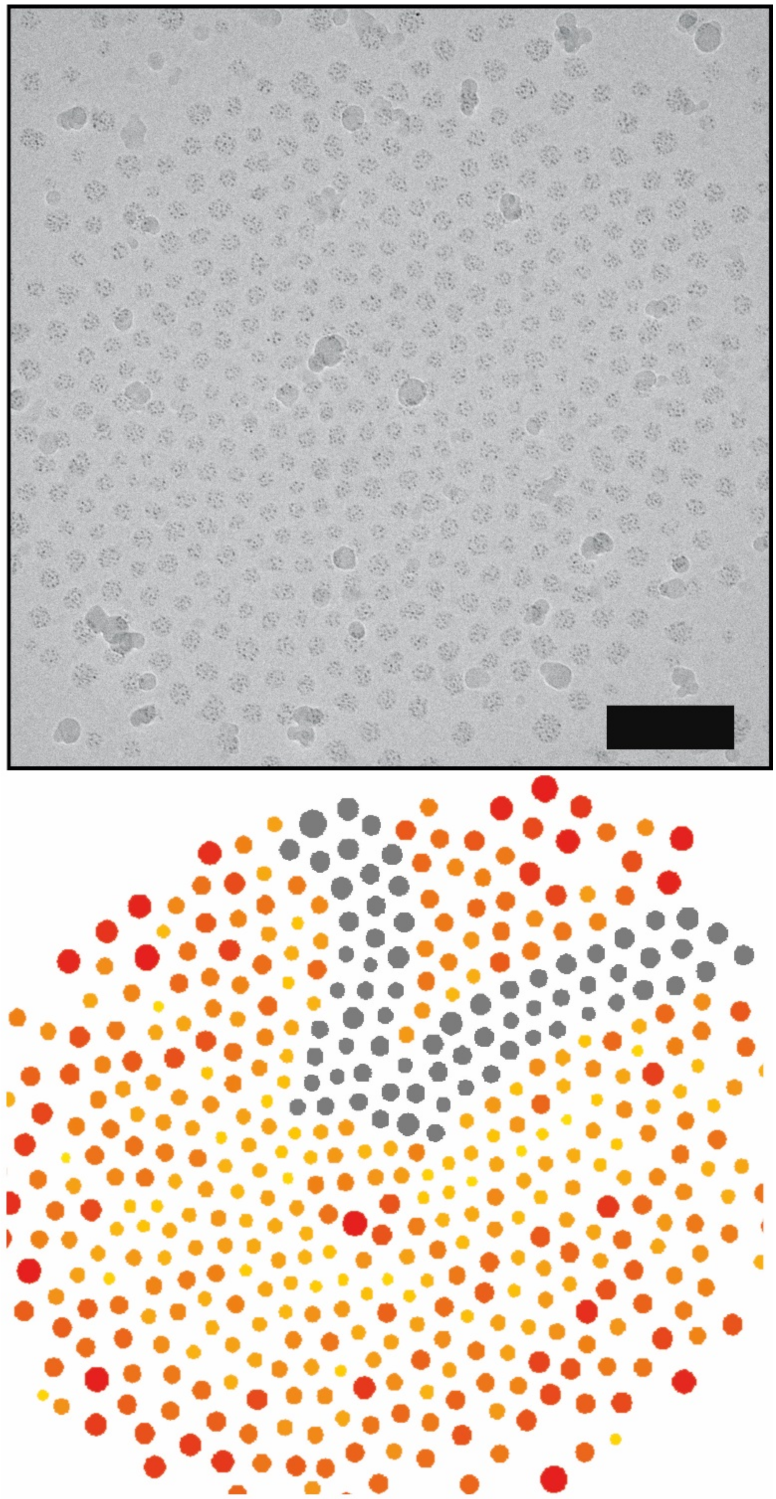

Fig. S9 Characterization of G9 dendrimicelles. Top: CryoTEM micrograph of G9 dendrimicelles obtained from charge-stoichiometric mixing with pMAA$_{64}$PEO$_{885}$ block copolymer (Figure 2). The scale bar represents 200 nm. Bottom: Image segmentation and analysis of G9 dendrimicelles, highlighting geometric features such as spiral domains.

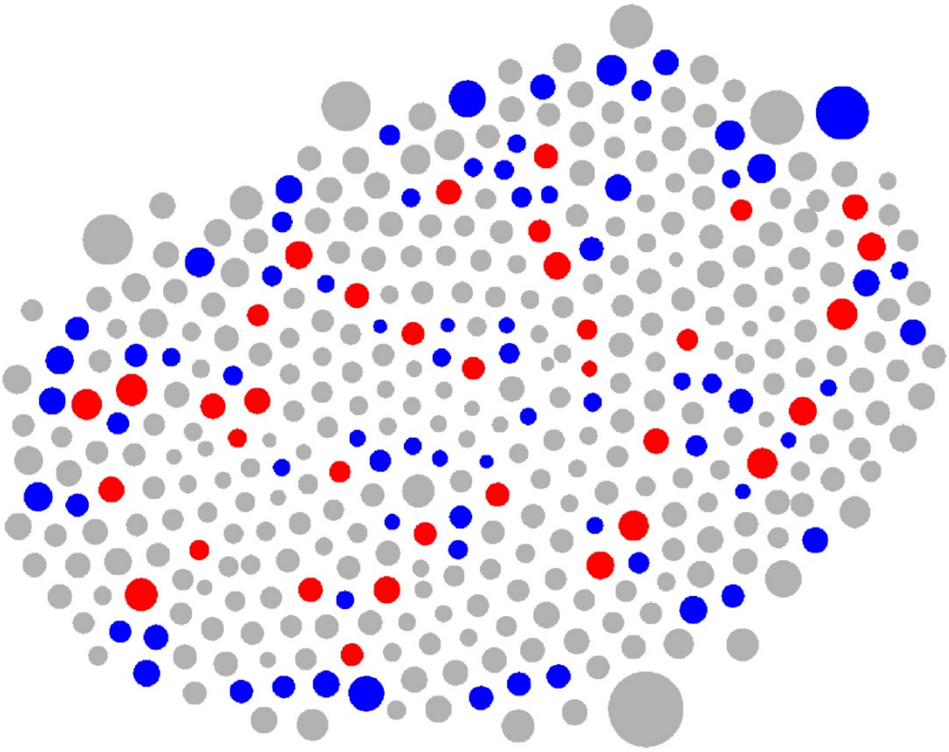

Fig. S10 Analysis of the number of nearest neighbors in a dendrimicelle superstructure and their location. Here, the superstructure obtained for seventh generation-based dendrimicelles made at charge-stoichiometry (Figure 2) is shown. In blue are the dendrimicelles with five nearest neighbors, and in red are the dendrimicelles with seven nearest neighbors. Dendrimicelles with another number of nearest neighbors are shown as grey.

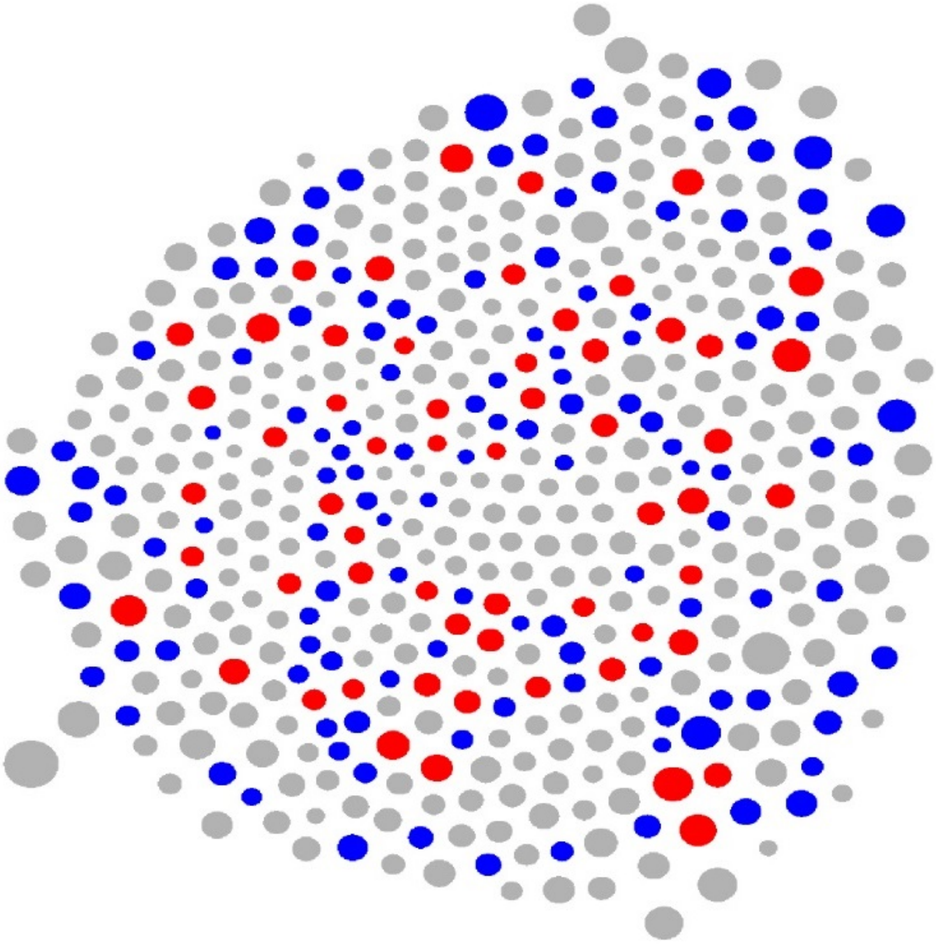

Fig. S11 Analysis of the number of nearest neighbors in a dendrimicelle superstructure and their location. Here, the superstructure obtained for eighth generation-based dendrimicelles made at charge-stoichiometry (Figure 2) is shown. In blue are the dendrimicelles with five nearest neighbors, and in red are the dendrimicelles with seven nearest neighbors. Dendrimicelles with another number of nearest neighbors are shown as grey.

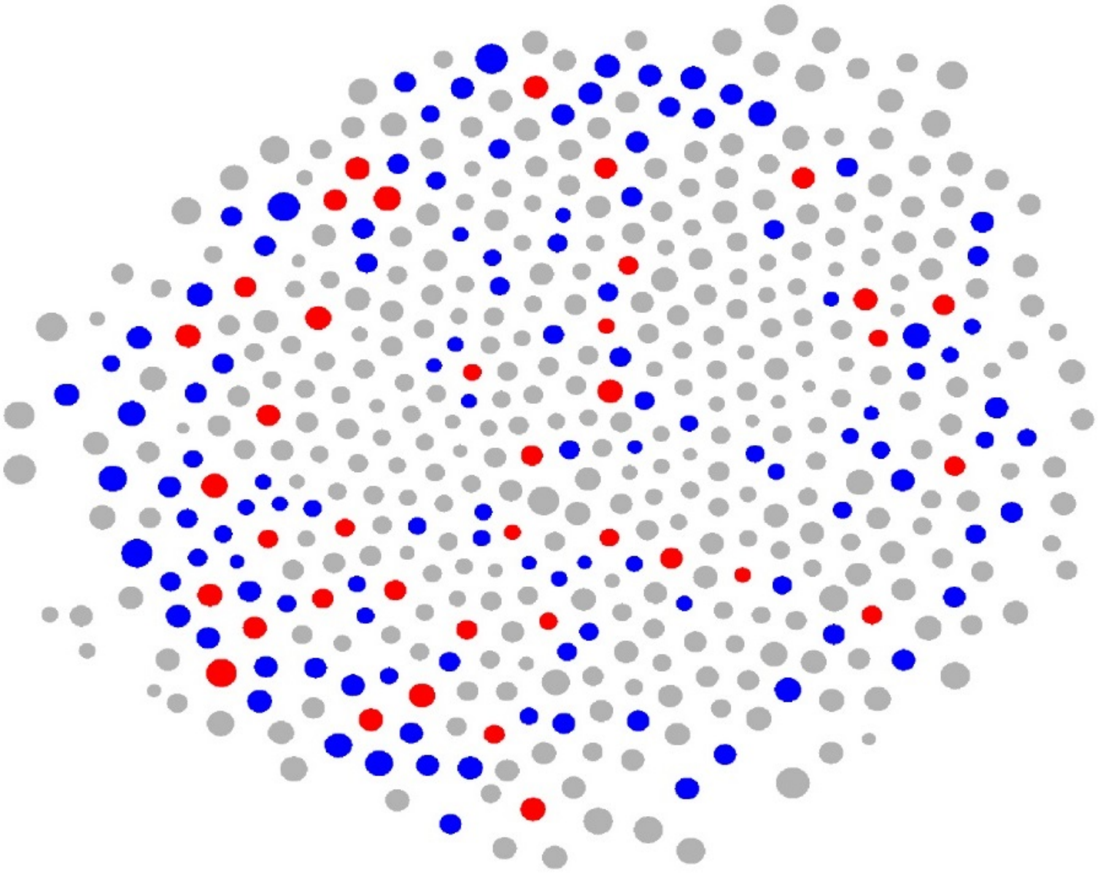

Fig. S12 Analysis of the number of nearest neighbors in a dendrimicelle superstructure and their location. Here, the superstructure obtained for ninth generation-based dendrimicelles made at charge-stoichiometry (Figure 2) is shown. In blue are the dendrimicelles with five nearest neighbors, and in red are the dendrimicelles with seven nearest neighbors. Dendrimicelles with another number of nearest neighbors are shown as grey.

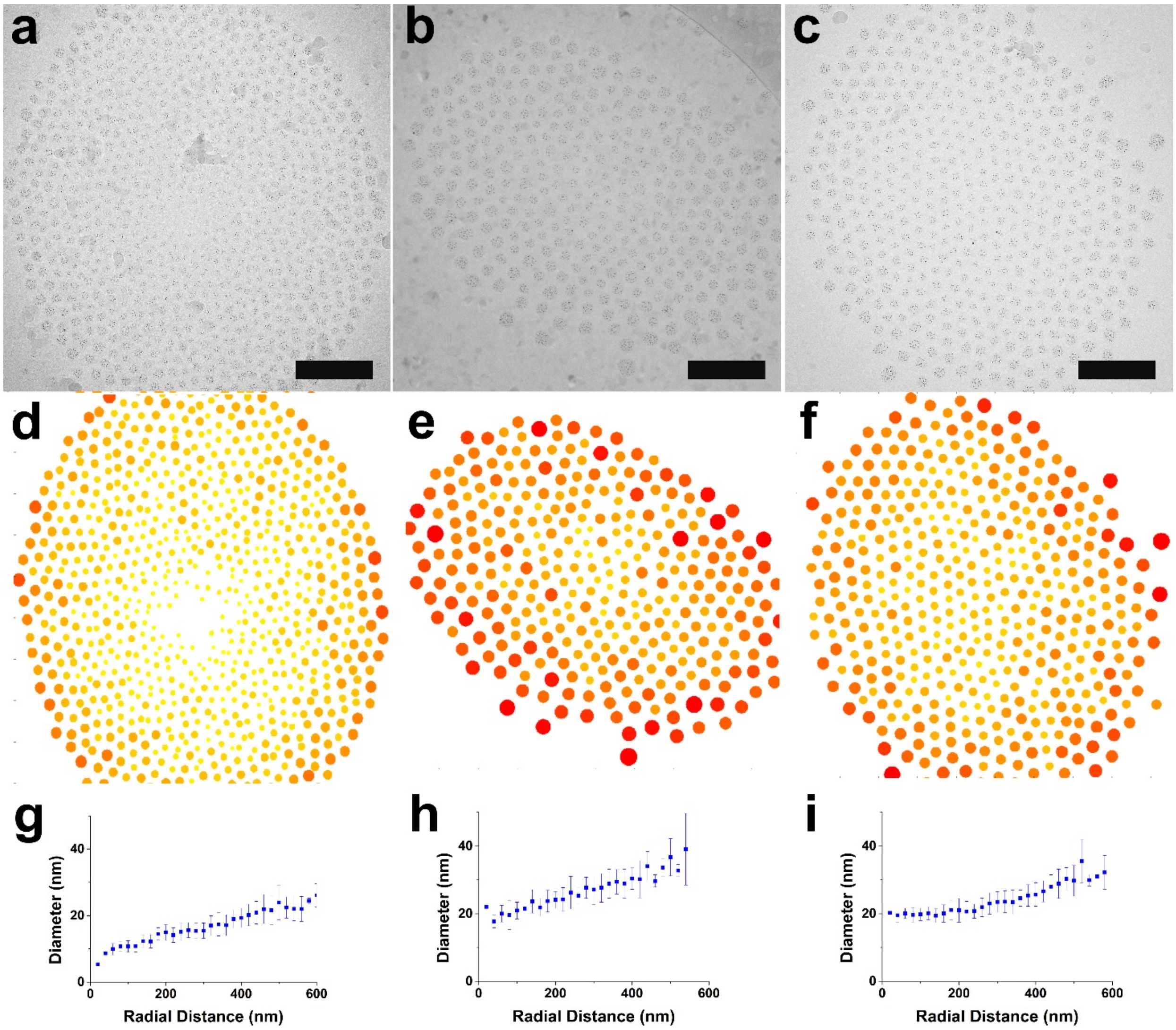

Figure S13. Ordering of 7th (left), 8th (middle) and 9th (right) generation PAMAM dendrimicelles obtained with a non-stoichiometric mixing ratio of 1.5. (**a-c**) The darker spots in the cryoTEM image are the 2-3 nm gold nanoparticles residing inside the dendrimers in the micelle core; scale bars correspond to 200 nm. (**d-f)** Image segmentation results in heat map plots with micelle cores color-coded according to their size. (**g-i)** Radial distance plots show micelle diameter versus distance to the center of the pattern.

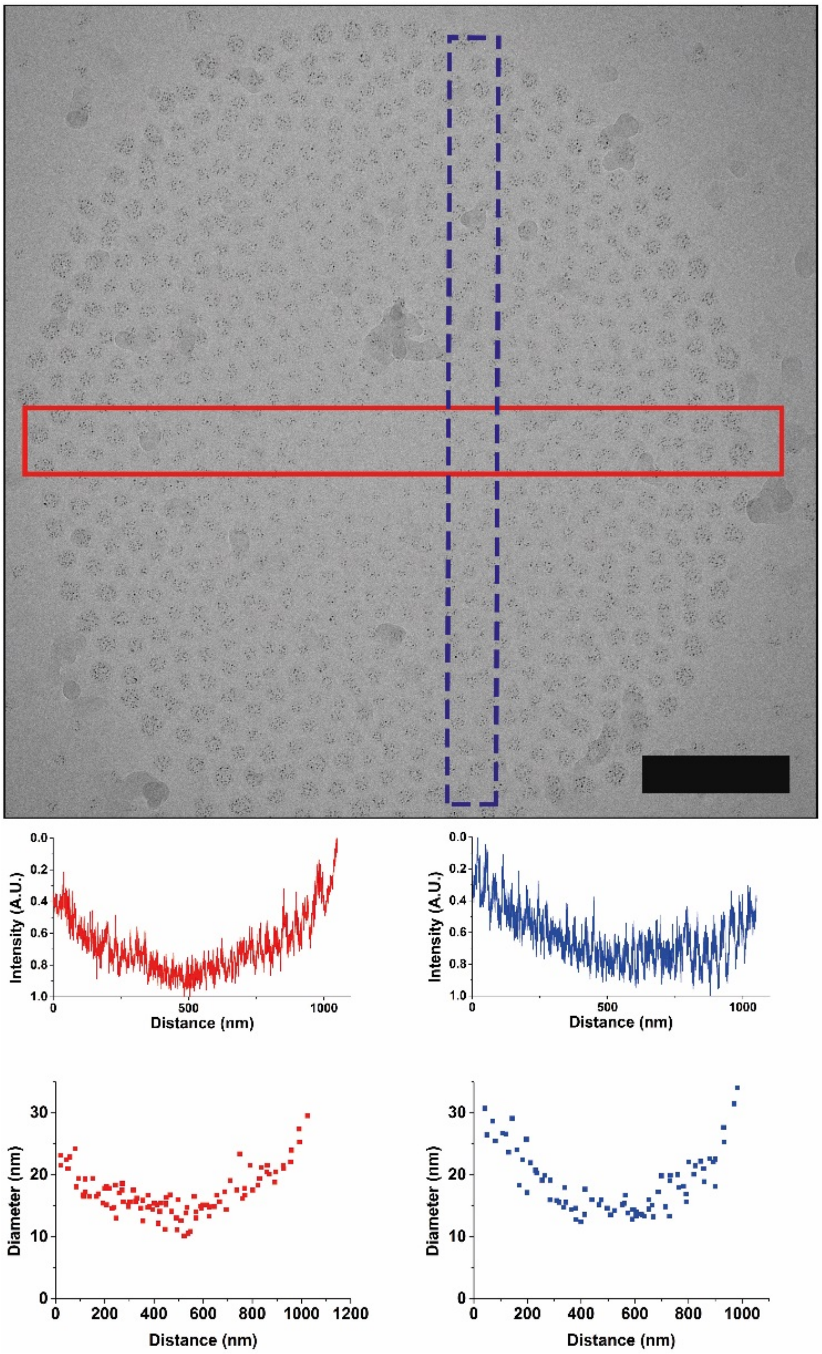

Fig. S14 Quantification of the vitreous ice film thickness and curvature in the G7-based dendrimicelle superstructure sample made using 1.5 times excess block copolymer (Fig **S13a**). **Top**: cryoTEM micrograph of the superstructure. **Middle**: normalized average intensity plots. The left, red, graph shows the average image intensity as determined from the solid, red box and the right, blue, graph shows the average image intensity as obtained from the dashed, blue, box in the TEM micrograph. **Bottom:** The left, red, graph shows the micelle core diameter as determined from the solid, red box and the right, blue, graph shows the micelle core diameter as determined from the dashed, blue, box in the TEM micrograph. The image intensity plots show the curvature of the vitrified water layer, and the dendrimicelle core size plots show that the dendrimicelle sizes follow the same trend, indicating the local thickness of the vitrified water film.

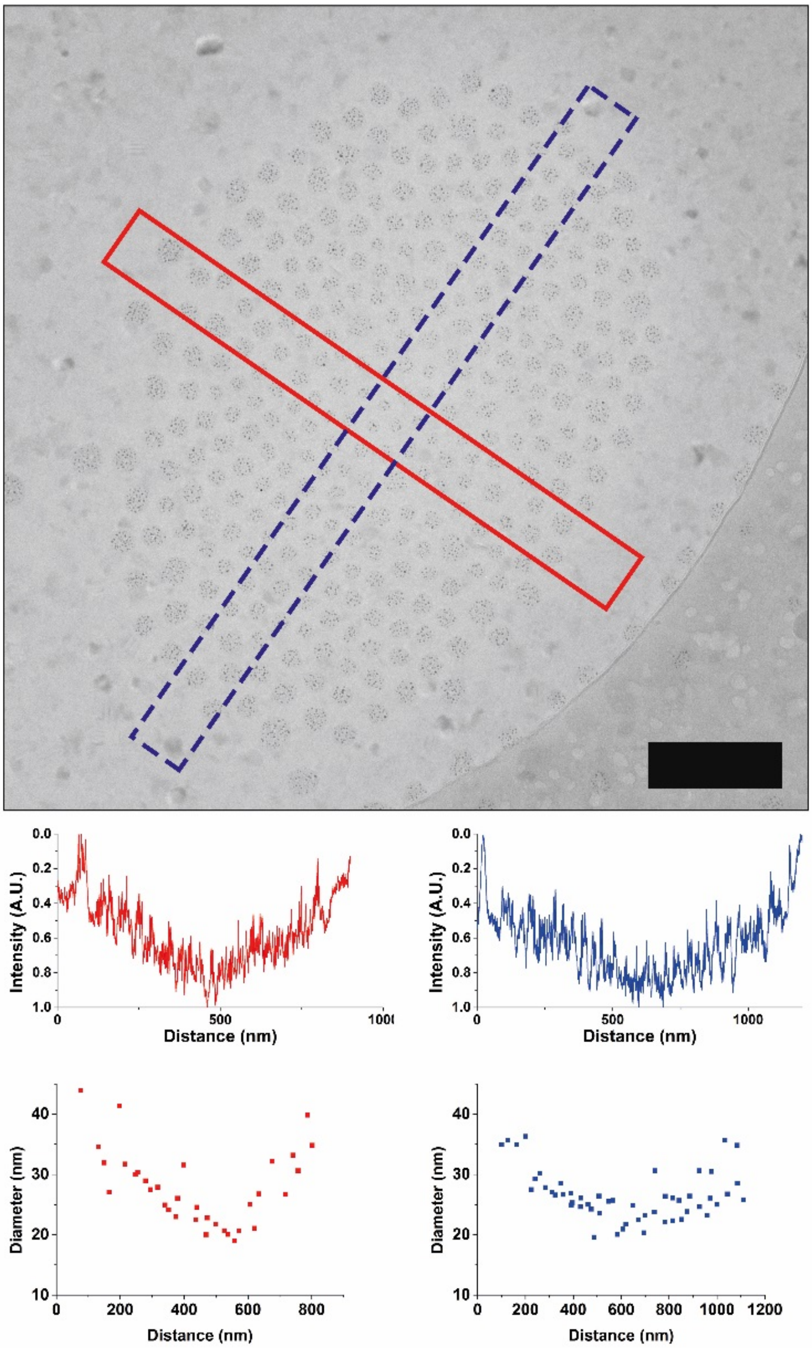

Fig. S15 Quantification of the vitreous ice film thickness and curvature in the G8-based dendrimicelle superstructure sample made using 1.5 times excess block copolymer (Fig **S13b**). **Top**: cryoTEM micrograph of the superstructure. **Middle**: normalized average intensity plots. The left, red, graph shows the average image intensity as determined from the solid, red box and the right, blue, graph shows the average image intensity as obtained from the dashed, blue, box in the TEM micrograph. **Bottom:** The left, red, graph shows the micelle core diameter as determined from the solid, red box and the right, blue, graph shows the micelle core diameter as determined from the dashed, blue, box in the TEM micrograph. The image intensity plots show the curvature of the vitrified water layer, and the dendrimicelle core size plots show that the dendrimicelle sizes follow the same trend, indicating the local thickness of the vitrified water film.

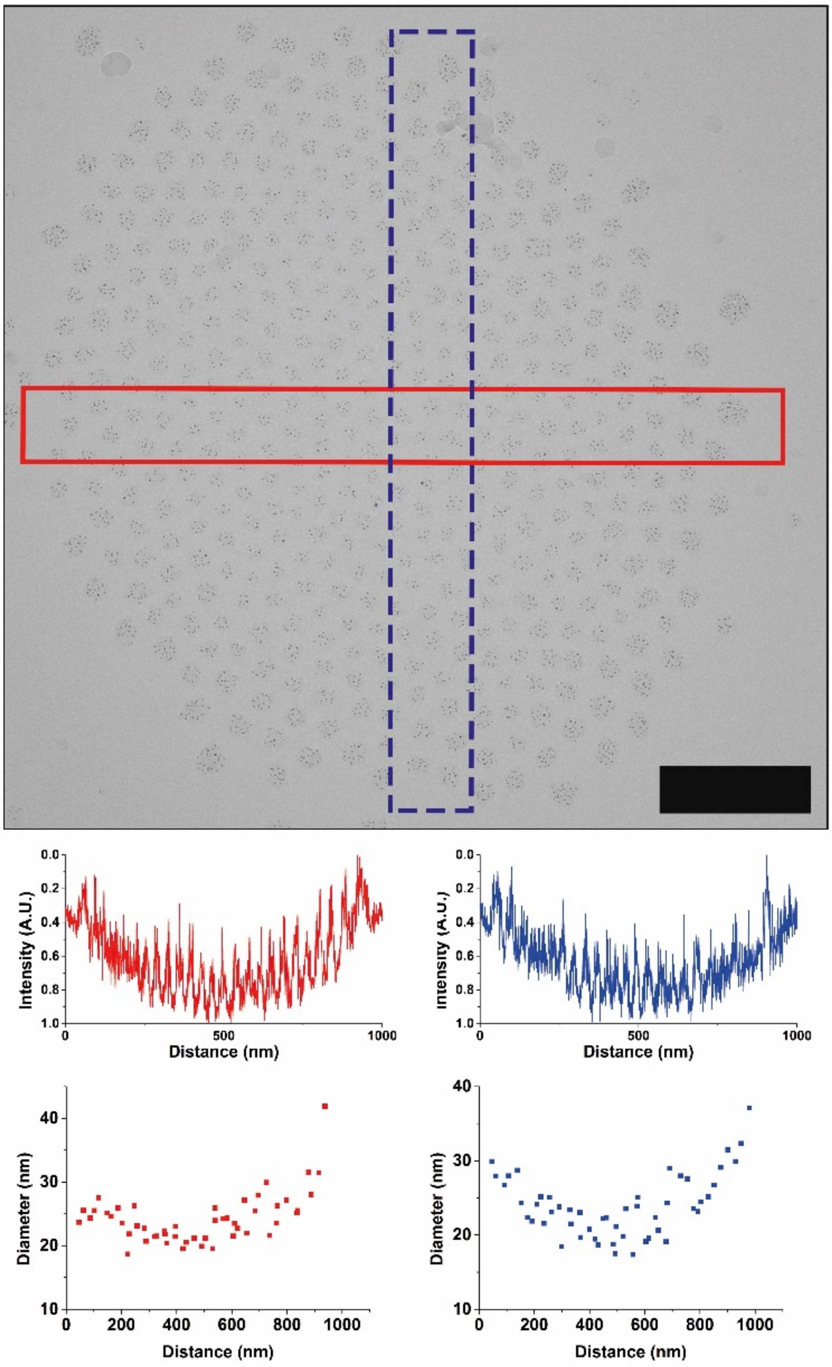

Fig. S16 Quantification of the vitreous ice film thickness and curvature in the G9-based dendrimicelle superstructure sample made using 1.5 times excess block copolymer (Fig **S13c**). **Top**: cryoTEM micrograph of the superstructure. **Middle**: normalized average intensity plots. The left, red, graph shows the average image intensity as determined from the solid, red box and the right, blue, graph shows the average image intensity as obtained from the dashed, blue, box in the TEM micrograph. **Bottom:** The left, red, graph shows the micelle core diameter as determined from the solid, red box and the right, blue, graph shows the micelle core diameter as determined from the dashed, blue, box in the TEM micrograph. The image intensity plots show the curvature of the vitrified water layer, and the dendrimicelle core size plots show that the dendrimicelle sizes follow the same trend, indicating the local thickness of the vitrified water film.

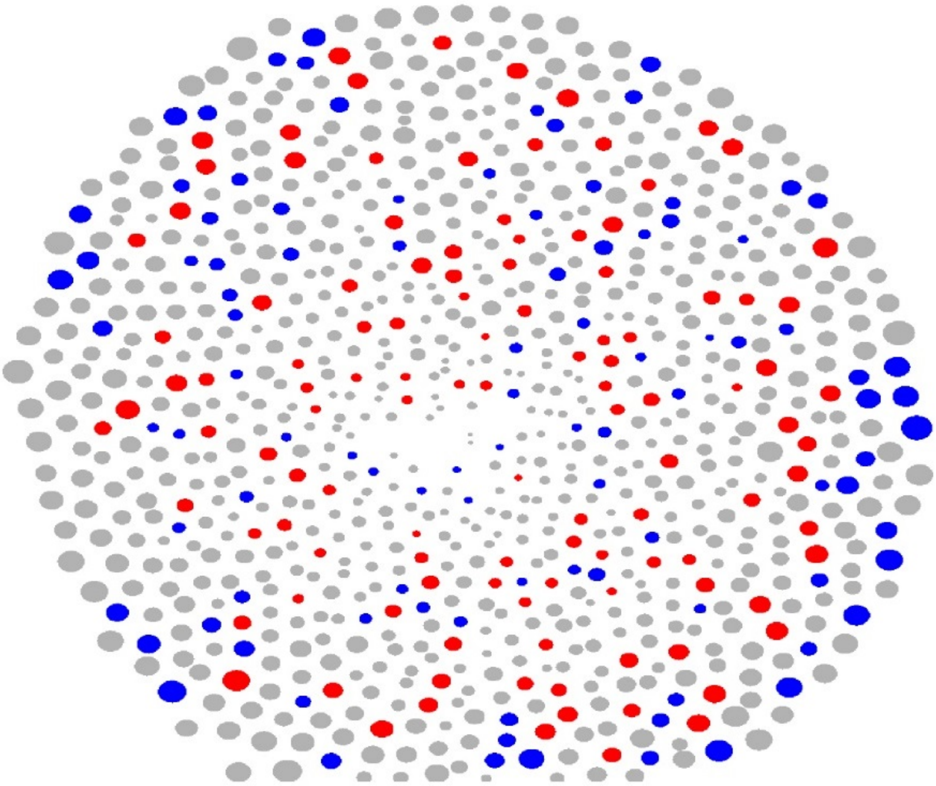

Fig. S17 Analysis of the number of nearest neighbors in a dendrimicelle superstructure and their location. Here, the superstructure obtained for seventh generation-based dendrimicelles made at charge fraction f=1.5 (**Fig S13a**) is shown. In blue are the dendrimicelles with five nearest neighbors, and in red are the dendrimicelles with seven nearest neighbors. Dendrimicelles with another number of nearest neighbors are shown as grey.

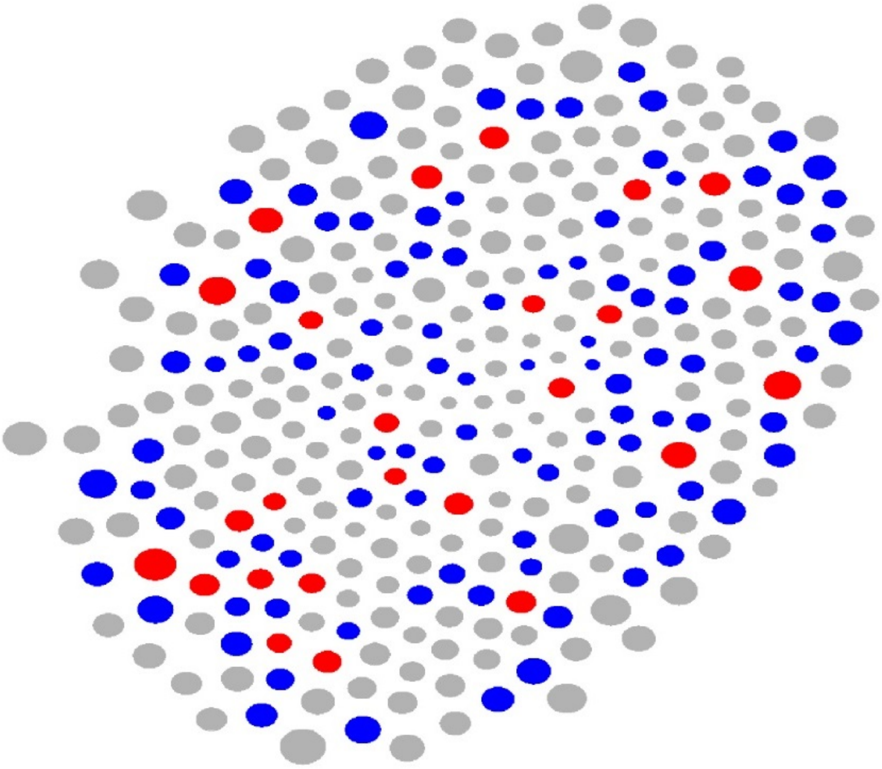

Fig. S18 Analysis of the number of nearest neighbors in a dendrimicelle superstructure and their location. Here, the superstructure obtained for eighth generation-based dendrimicelles made at charge fraction f=1.5 (**Fig S13b**) is shown. In blue are the dendrimicelles with five nearest neighbors, and in red are the dendrimicelles with seven nearest neighbors. Dendrimicelles with another number of nearest neighbors are shown as grey.

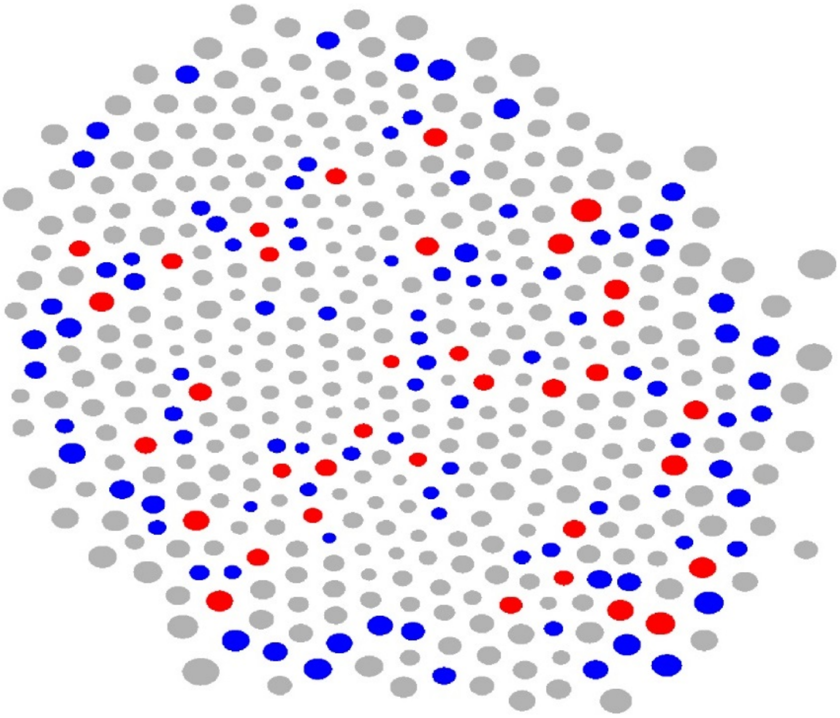

Fig. S19 Analysis of the number of nearest neighbors in a dendrimicelle superstructure and their location. Here, the superstructure obtained for ninth generation-based dendrimicelles made at charge fraction f=1.5 (**Fig S13c**) is shown. In blue are the dendrimicelles with five nearest neighbors, and in red are the dendrimicelles with seven nearest neighbors. Dendrimicelles with another number of nearest neighbors are shown as grey.

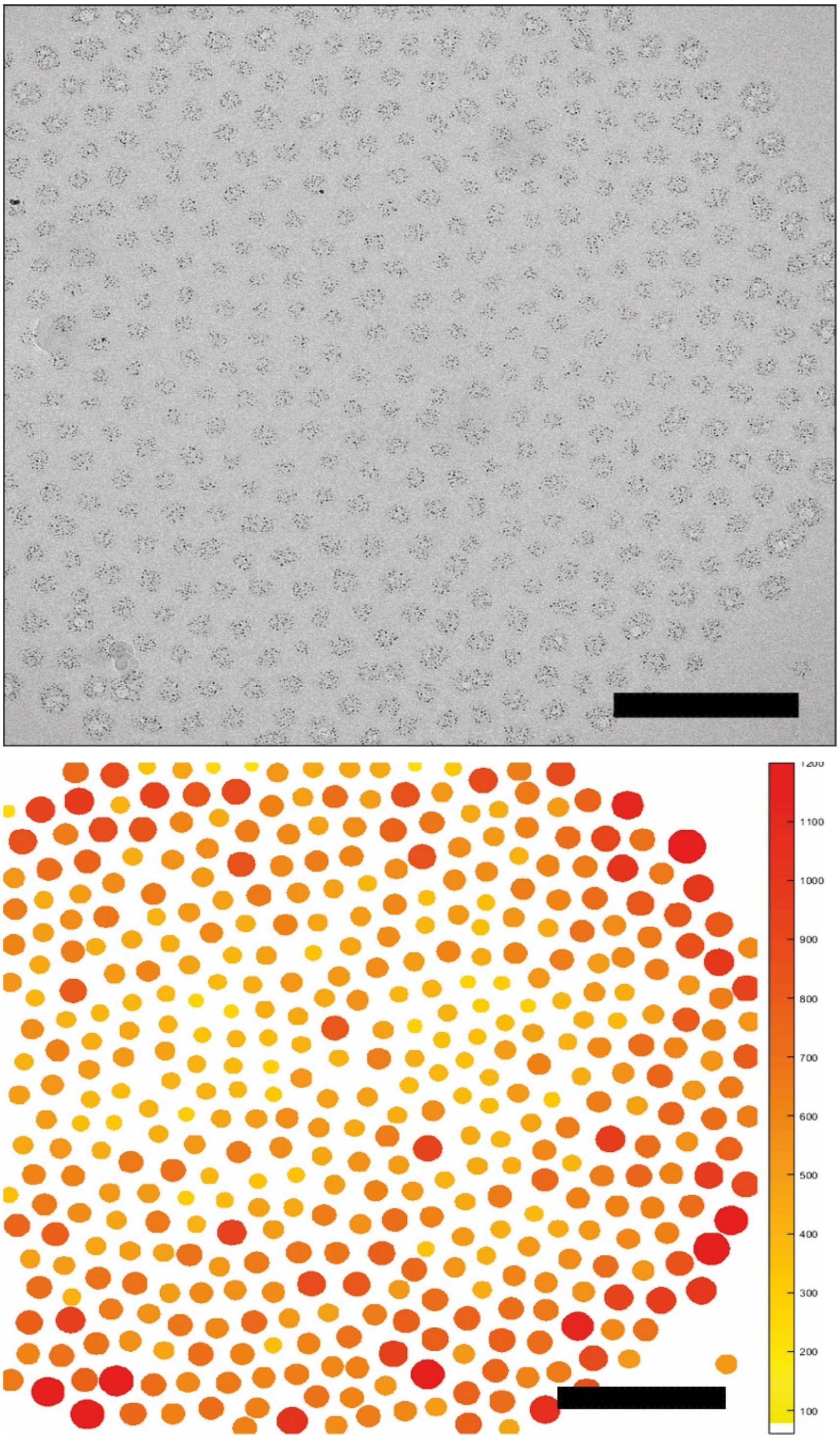

Fig. S20 Characterization of G7 dendrimicelles. Top: CryoTEM micrograph of G7-Au_{256} dendrimicelles made under charge-stoichiometric mixing conditions. Scale bar represents 200 nm. Bottom: Heat map of G7-Au_{256} dendrimicelles made under charge-stoichiometric mixing conditions. The color-coding represents the dendrimicelle core area as obtained from the image analysis, and ranges from 0-1200 nm^2. The scale bar represents 200 nm.

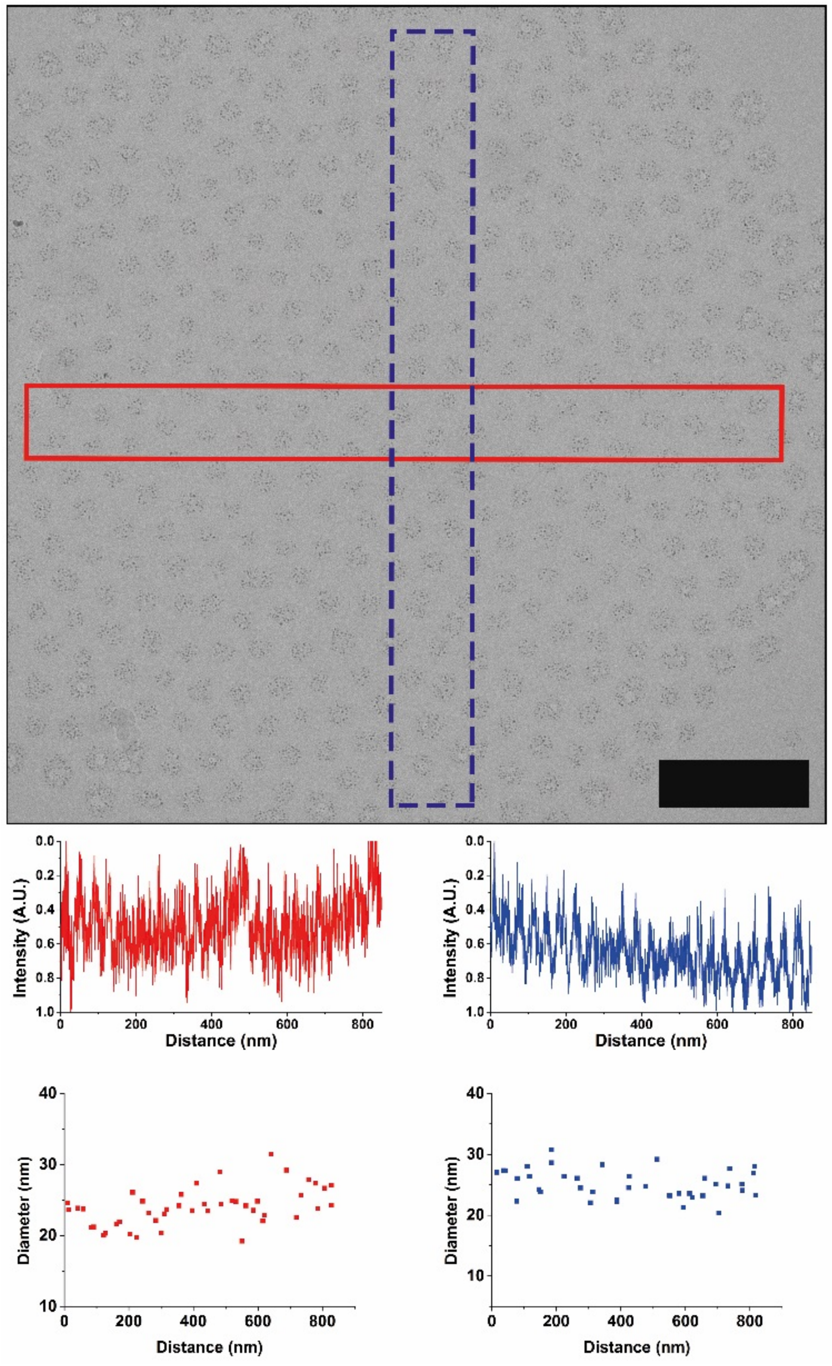

Fig. S21 Quantification of the vitreous ice film thickness and curvature in the G7-based dendrimicelle superstructure sample made at charge-stoichiometry (Fig **S20**). **Top**: cryoTEM micrograph of the superstructure. **Middle**: normalized average intensity plots. The left, red, graph shows the average image intensity as determined from the solid, red box and the right, blue, graph shows the average image intensity as obtained from the dashed, blue, box in the TEM micrograph. **Bottom:** The left, red, graph shows the micelle core diameter as determined from the solid, red box and the right, blue, graph shows the micelle core diameter as determined from the dashed, blue, box in the TEM micrograph. The image intensity plots show the curvature of the vitrified water layer, and the dendrimicelle core size plots show that the dendrimicelle sizes follow the same trend, indicating the local thickness of the vitrified water film.

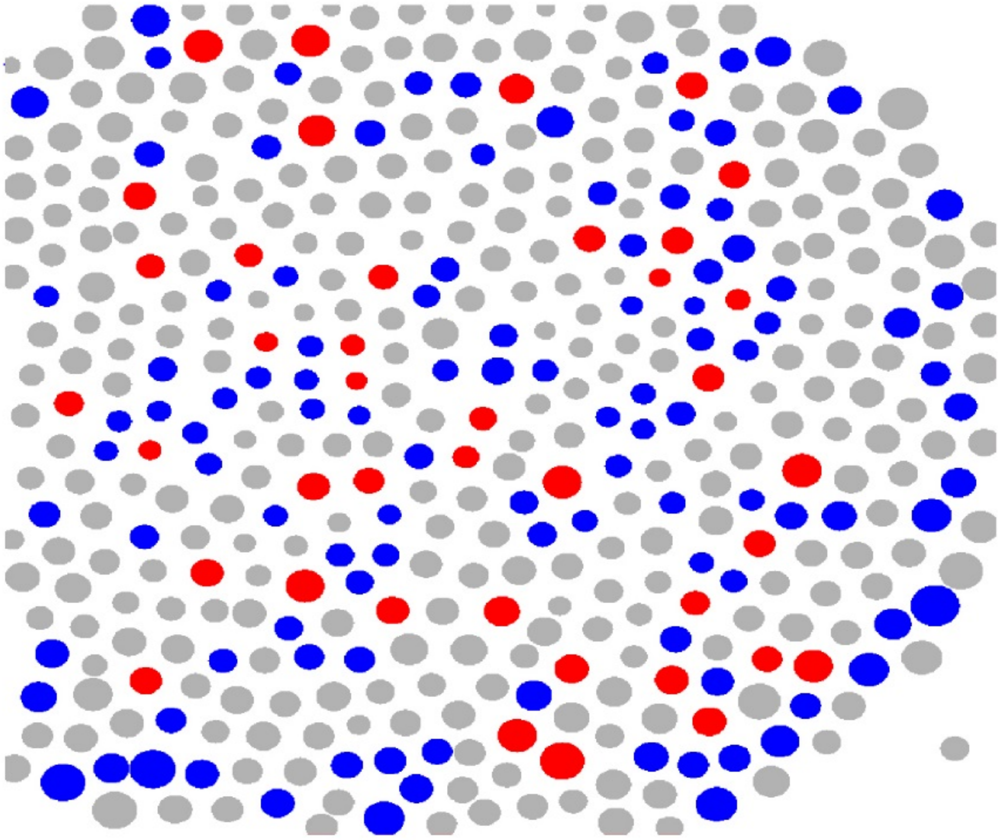

Fig. S22 Analysis of the number of nearest neighbors in a dendrimicelle superstructure and their location. Here, the superstructure obtained for the seventh generation-based dendrimicelles made at charge stoichiometry (**Fig 20**) is shown. In blue are the dendrimicelles with five nearest neighbors, and in red are the dendrimicelles with seven nearest neighbors. Dendrimicelles with another number of nearest neighbors are shown as grey.

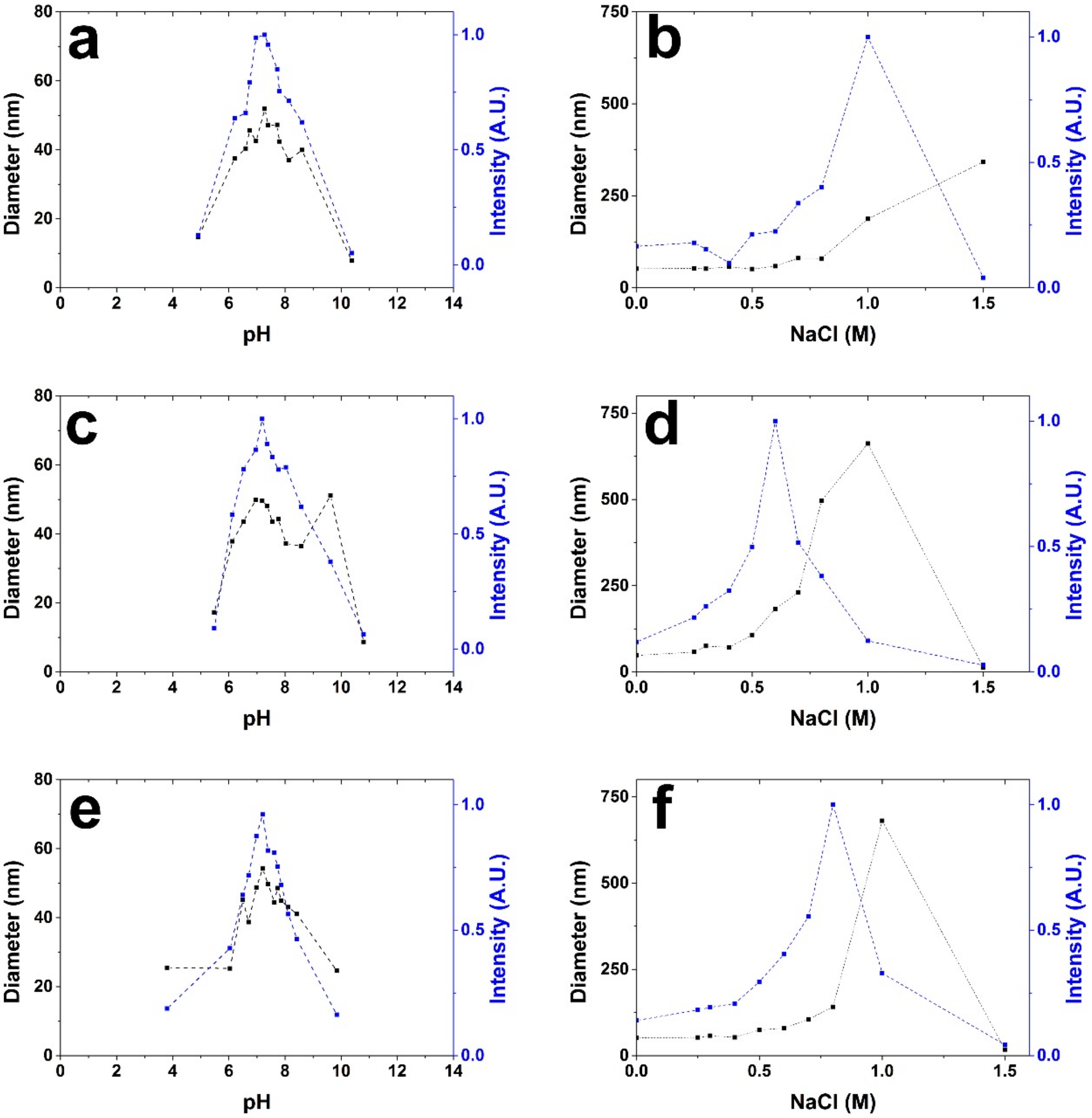

Fig. S23 pH and salt stability of generation 7-based dendrimicelles (**a**,**b**), of generation 8-based dendrimicelles (**c**,**d**) and of generation 9-based dendrimicelles (**e**,**f**).

Chapter 4

Monitoring Global and Local Motion in Biconcave Thin Films with Gold Nanoparticle Containing Superstructures

Understanding the dynamics of discrete self-assembled structures under influence of external triggers is of importance to harvest the potential of nano- and mesoscale materials. In particular controlling the hierarchical organization of (macro)molecular and nanoparticle building blocks in monolayer superstructures is of paramount importance for properties and characteristics. Here we use cryo-Transmission Electron Microscopy, (cryoTEM), to follow local migration of building blocks and global migration of micellar aggregates inside micrometer-sized superstructures. We use the electron beam to induce the controlled local evaporation of water, eventually leading to rupture of the monolayer superstructure. Dendrimer-encapsulated gold nanoparticles indicate both the global movement of individual coacervate dendrimicelles, and local migration of the nanoparticles inside the micellar core — before and during the nanoexplosion— which proceeds with speeds around ~50, respectively 1 nm.s^{-1}. The nanoparticles prove a powerful tool to manipulate and study complex hierarchically built-up system, consisting of a monolayer superstructure of micelles. The electron beam can heat up superstructures, controlling the release of embedded particles and converting vitreous ice samples into organic liquid thin films at cryogenic temperatures.

This chapter is based on: **Jan Bart ten Hove**, Fijs W.B. van Leeuwen and Aldrik H. Velders, *Manuscript submitted*.

4.1 Introduction

The assembly of well-defined building blocks into superstructures is of widespread interest because of the emerging properties of such materials, in for example, catalysis,[1] storage,[2] optics,[3] and drug delivery.[4,5] Although three-dimensional self-assembled materials are studied most, such as gels and metal-organic frameworks, their two-dimensional counterparts are of interest too, and include monolayers of atomic, molecular, self-assembled, and colloidal building blocks.[6-13] Among the strategies reported to engineer two-dimensional self-assembled materials, interfaces have proven to be a versatile tool to do so.[14-19] Recently, we showed how micrometer-sized, freestanding dendrimicelle monolayer superstructures could be made from nanometer-sized building blocks, bridging three levels of hierarchy during the self-assembly and organization.[20,21] We hypothesized that the micelle-embedded nanoparticles could be used to study the dynamics of the superstructure under electron beam-induced heating. The nanoparticles having a dualistic purpose: In addition to revealing dendrimicelle characteristics such as aggregation numbers and core size, their contrast also allows for use as tracer to follow the dynamics of the superstructure under extended electron irradiation.[22] Moreover, the gold nanoparticles —with their high electron density— prove to increase homogenously the local heating of the superstructures under irradiation, leading to the concomitant evaporation of water in the thin film and finally to rupture of the liquid-like remaining superstructure. Interestingly, the electron beam allows manipulation of the building blocks of the aggregates at the lower nanometer length scales, including the removal of the gold particles from the dendrimer host. Here, we use stroboscopic cryoTEM to observe movements inside monolayers of nanoparticle-containing superstructures, revealing the nanoscale processes that take place just before and during the thin film rupture.

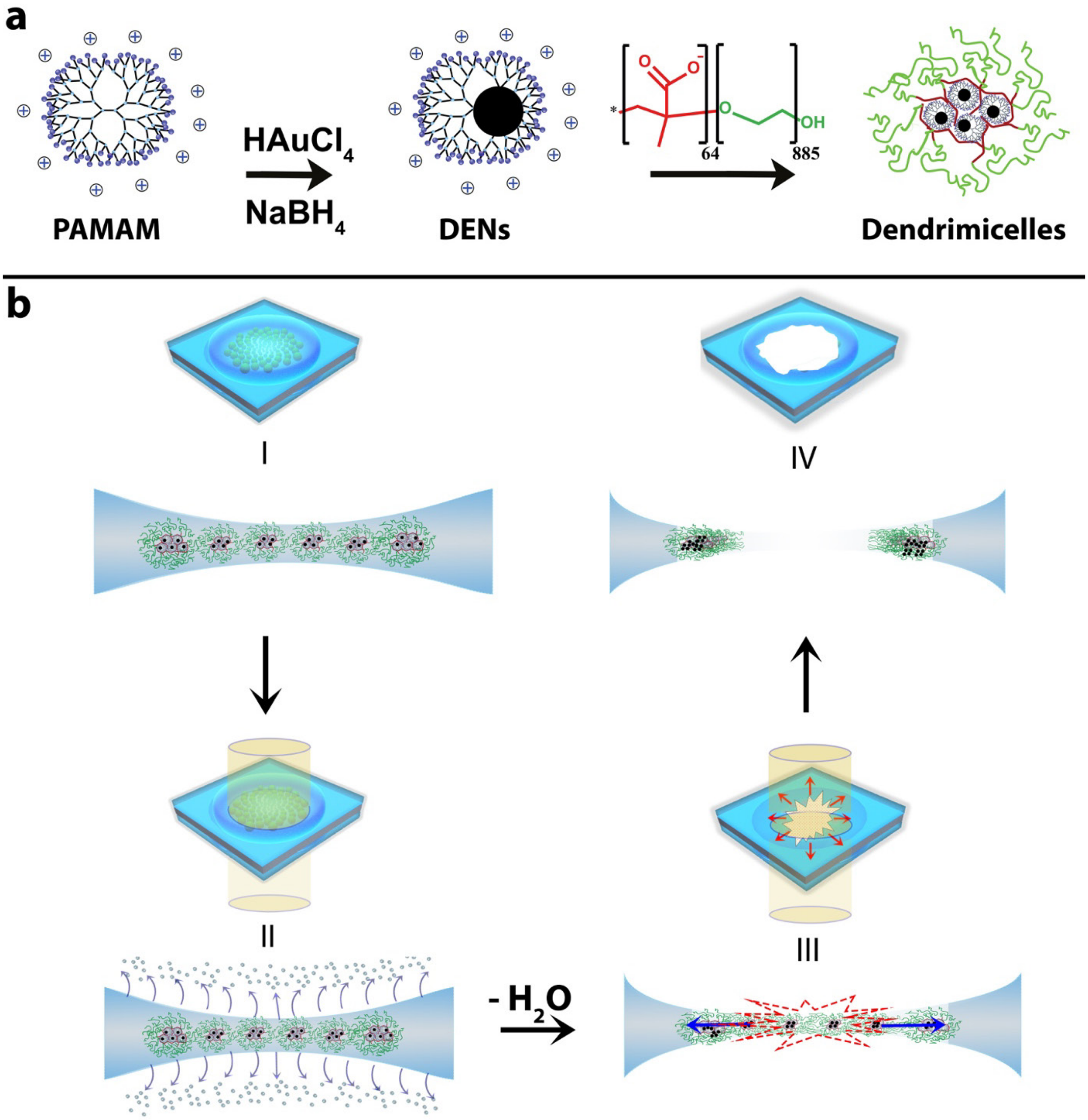

Scheme 4-1) Synthesis of dendrimicelles and subsequent cryoTEM analysis of monolayer dendrimicelle superstructures. **a**: Complexation and reduction of Au(III) ions inside PAMAM dendrimers provides dendrimer-encapsulated gold nanoparticles (AuDENs). Mixing of these AuDENs with a negative-neutral $pMAA_{64}PEO_{885}$ block copolymer results in ~50 nm dendrimicelles. The AuNPs embedded reveal local building block movements as wells as the global rupture of the dendrimicelle superstructure. **b**: For cryoTEM analysis, the micron-sized grid holes are filled with an aqueous thin dendrimicelle film, with the biconcave shape of the layer acting as a template for the organization of dendrimicelles into (sub-) micron-sized monolayer superstructures (**I**). Exposure of the superstructure to an electron beam results in evaporation of water (**II**). Prolonged exposure results in the rupture of the superstructure (**III**). After the nanoexplosion, a hole similar in size to the superstructure is left behind. (**IV**)

4.2 Experimental Section

Materials and Methods

Sixth generation, amine-terminated polyamidoamine (PAMAM) dendrimers, (3-(N-morpholino)-propanesulfonic acid) (MOPS), $NaBH_4$, 1M NaOH and 1M HCl solutions were obtained from Sigma Aldrich. $pMAA_{64}$-b-PEO_{885} (Mw/Mn = 1.15) was obtained from Polymer Sources Inc., Canada and used as 5 mM solution based on carboxylic acid content. $HAuCl_4.3H_2O$ was obtained from TCI. Ninth generation, amine-terminated PAMAM was obtained from Dendritech, Inc., USA.

Apparatus

Dynamic Light Scattering (DLS) was done on a Malvern Zetasizer Nano S equipped with a laser operating at 633 nm. For cryoTEM, samples were cast on Quantifoil R2/2 grids or 400 mesh Holey Carbon grids. After blotting, samples were plunged into liquid ethane using a Vitrobot system (FEI Company). Samples were then imaged at ~ 90-100 K in a JEOL 2100 TEM operating at 200 kV or JEOL 1400Plus TEM operating at 120 kV. Sample grids for electron microscopy were obtained from Electron Microscopy Sciences (EMS, Hatfield, PA, USA) and were rendered hydrophilic using a plasma cleaning setup (15 s at 10^{-1} Torr).

Dendrimer Encapsulated Nanoparticles

G6-Au_{128}DENS were made following established protocols.[36] Shortly, 50 µL (35 nmol) of 5 wt% PAMAM G6-NH_2 in methanol was transferred to a 5 mL vial and the solvent was evaporated under reduced pressure. Next, 2 mL of water was added to dissolve the PAMAM and the pH was adjusted to 3 using 1M HCl, after which 128 molar equivalents of Au^{3+} to PAMAM were added. The resulting solution was then stirred for 20 minutes, after which 44 µL of a 1M solution of $NaBH_4$ in 0.3M NaOH (10 molar equivalents to Au^{3+}) were added. This resulted in the reduction of Au^{3+} to AuDENs, indicated by the change from colorless to a dark brown solution within seconds after addition. Following reduction, the pH was set to 7 using HCl and the AuDENS were stored at 4 °C. Generation 9 AuDENS were made in a similar way, using 1024 equivalents of Au^{3+} to PAMAM.

Dendrimer Encapsulated Nanoparticles in Micelles

To obtain dendrimicelles under charge stoichiometric conditions, 20 µL of 2.89 mM dendrimer solution (charge concentration, 57 nmol positive charge based on surface groups) was dissolved in 149 µL water and 20 µL of 0.2M MOPS buffer at pH 7.0 was added. Then, 11 µL $pMAA_{64}$-b-PEO_{885} (55 nmol based on -COOH) was added and the sample was sonicated for 2 minutes. Generation 9 dendrimicelles were made using 1.5 charge equivalents of $pMAA_{64}PEO_{885}$ to $G9_{1024}DENS$ to decrease the average number of nanoparticles per dendrimicelle. Samples were left to equilibrate for at least one day before characterization using cryoTEM.

4.3 Results and Discussion

Our strategy, as depicted in Scheme **1a**, is as follows: Dendrimer-encapsulated gold nanoparticles (AuDENs) were synthesized inside positively-charged sixth-generation (G6) PAMAM dendrimers, yielding Au_{128}DENs. Coacervation with anionic-neutral $pMAA_{64}pEO_{885}$ block copolymers yielded highly-stable dendrimicelles as indicated by cryoTEM and DLS (Figures **S1-3**) which prove that these are indeed well-defined dendrimicelles (Figure **S4**). The dendrimicelles host an average of 30 ± 10 nanoparticles in the micelle core, which —based on a 1:1 association of positive and negative charges— implies that the average micelle molecular weight is ~8 MDa. These dendrimicelles organize into superstructures, located in the thinnest part of the thin water film spanning across the TEM grid hole (Figure **S5**). The formation of these superstructures is the result of the complex interplay between the poly(ethyleneglycol) of the dendrimicelle corona and the templating effect of the biconcave thin film.[23-26] Next, we studied the effect of prolonged electron beam irradiation on these self-organized superstructures of self-assembled micelles. During cryo-electron microscopy, inelastic scattering of electrons by the sample causes evaporation of the vitreous ice layer, which can result in the destruction sample and the thin water film in which the sample is embedded.[27-30]

Figure **4-2** shows that prolonged electron beam exposure results in the rupture of the dendrimicelle superstructure. The combination of the exposure time (2 seconds) and the velocity at which the rupture propagated, results in the rupture being captured as streaks, similar to motion blur observed in *e.g.* long exposure photography. The observed streaks originate from the gold nanoparticles inside the dendrimicelles; their electron density clearly provides enough contrast to visualize the rupture of the thin film, whilst the macromolecular building blocks of the dendrimicelles are not providing enough contrast. The red arrows in Figure **4-2** are drawn parallel to the gold nanoparticle streaks, and extrapolation indicates these to originate from the center of the superstructure. The center of this image lacks visible streaks, despite dendrimicelles being present before rupture. The rupture therefore likely started right before the cryoTEM micrograph was recorded, or the contrast provided by the micelle-embedded nanoparticles was attenuated over too large an area, and effectively merged with the background signal. Therefore, we can only obtain a minimum value for the rupture propagation speed, as determined from the nanoparticle streaks visible.

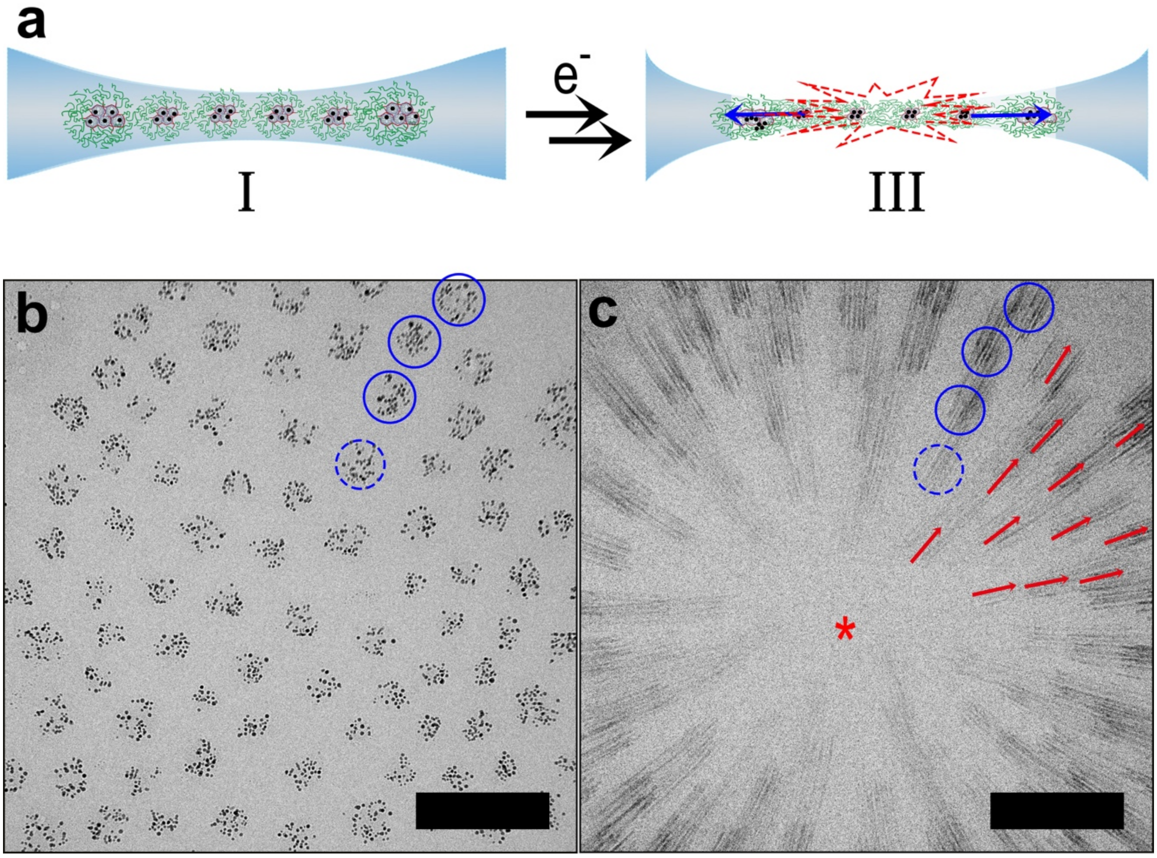

Figure 4-2 **a**) Prolonged exposure of G6-Au_{128}-based dendrimicelles results in the rupture of the thin film in which they are embedded. CryoTEM micrographs of the dendrimicelles superstructure before (**b**) and during explosion (**c**). Because of the relatively long exposure time and the contrast provided by the gold nanoparticles, the rupture process is captured as streaks. The rupture starts from the center of the dendrimicelle superstructures (as indicated with an asterisk), and radially propagates outwards. The blue circles are drawn as a guide to the eye around four dendrimicelles before and after rupture. The red arrows are drawn as a guide to the eye to show the directionality of the nanoparticle streaks. Scale bars are 100 nm.

Assuming the particles moved for the full 2 seconds of exposure time, the length of the streaks in the center of the figure indicates that dendrimicelles moved at an average speed of ~50 nm.s^{-1} during the exposure; the dendrimicelles at the edges of the superstructure appear to have moved at an average speed of ~25 nm.s^{-1}. These observations point to the rupture starting from the center of the superstructure, followed by a radially-outward propagation of the rupture front. Figures **S6-7** show more examples of dendrimicelle superstructure ruptures, supporting this hypothesis. Because of the visual similarities between this nanoscale rupture and an explosion (*i.e.*, the sudden, destructive, outward migration), we coined this rupture ‘nanoexplosion’. Most thin film rupture studies regard thin soap films, but contrary to aerosol studies, in our case we do not observe formation of smaller bubbles in the process.[31]

To investigate the processes that take place inside the thin film just before and during the nanoexplosion, we use the micelle-embedded nanoparticles as tracer to follow the rupture of thin film under stroboscopic exposure (i.e. by taking pictures successively).[30] Figure **4-3a** shows a (~4x4 µm) cryoTEM micrograph, in which a 2.4 µm circular TEM grid hole is present. Inside this grid hole, a ~500 nm diameter dendrimicelle superstructure is residing in the center. Figure **4-3b** shows the dendrimicelle, acquired at higher magnification and at higher electron flux (~41 $e^-/Å^2$ per micrograph, acquired with a ~2 µm electron beam spot size). After a series of 14 micrographs and a total electron exposure dose of ~600 $e^-/Å^2$ (Figures **4-3b-d** and Figure **S8** for the full series), the dendrimicelle superstructure exploded, leaving a hole behind roughly similar in size to the original dendrimicelle superstructure (Figure **4-3d&e**).

The stroboscopic TEM micrographs allow for detailed analysis. Figure **4-3b-d** shows three representative figures of the fourteen cryoTEM micrographs taken during the stroboscopic exposure, with Figure **4-3b** showing the first image of the exposure series, in which the individual dendrimicelle cores in the superstructure are clearly visible. In the last frame before the nanoexplosion (Figure **4-3c**), the superstructure area appears as a smooth film, which suggests that the majority of the water that was present has evaporated, leaving a thin polymeric film behind with groups of DENs of the original micelle cores. The next frame, Figure **4-3d**, shows the superstructure just at the final stage of the nanoexplosion. Figure **4-3e** shows that after the nanoexplosion, the exposed area (*i.e.* the area exposed to the ~2 µm circular electron beam) appears lighter-colored, implying the exposure resulted in a thinning of the vitrified thin film, also outside of the superstructure area. Plotting the intensity average image intensity over the dendrimicelle superstructure (Figure **4-3g** and **S9**) indicates that during the exposure series the image transmission steadily increased, corresponding to a thinning of the film. Figure **S10** indicates a linear relationship between the image intensity and the exposure dose, corresponding to the well-defined evaporation of water during each exposure. The observed thinning and the homogenous intensity of the superstructure layer just before nanoexplosion suggest a phase transition occurs with the thin vitreous ice layer formed during sample preparation, converting into an even thinner liquid-like layer of organic, nanoparticle containing, material.

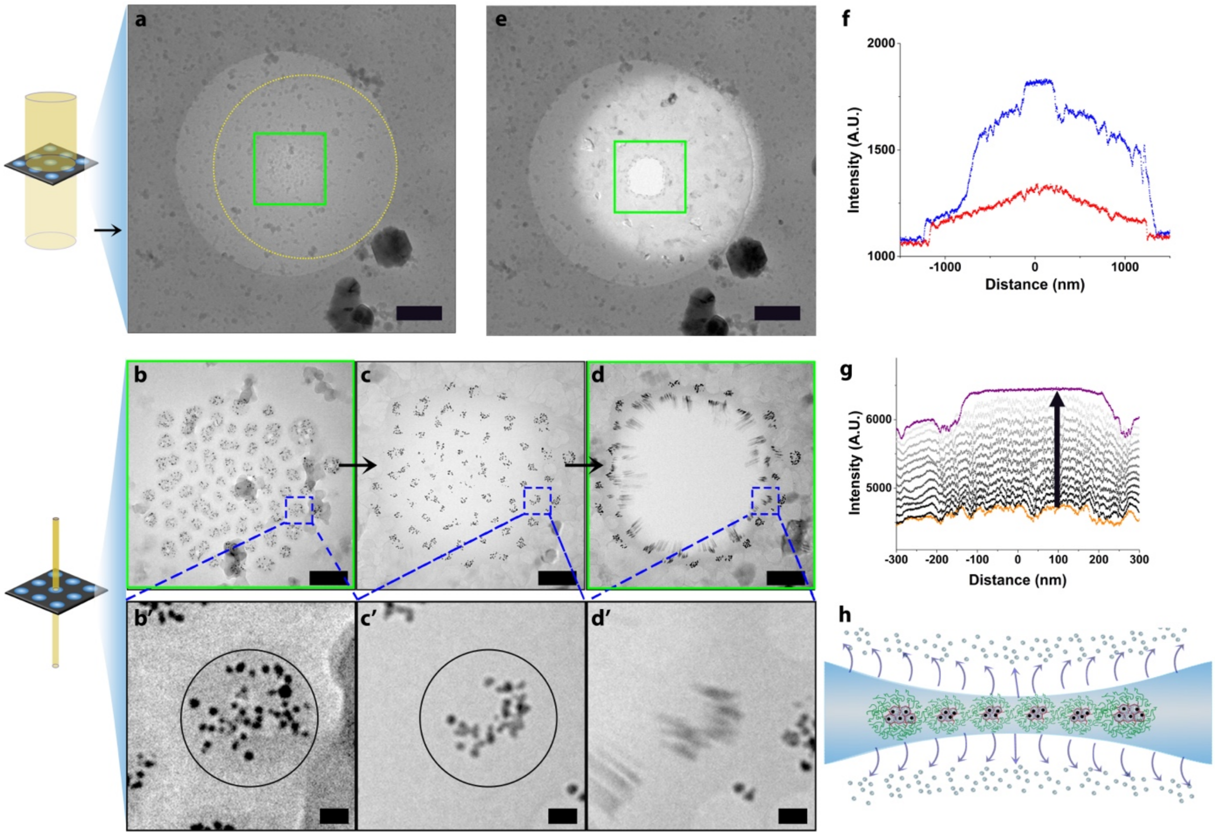

Figure **4-3** The effect of stroboscopic electron exposure on a nanoparticle-containing dendrimicelle superstructure. a) CryoTEM micrograph of a generation-six based dendrimicelle superstructure obtained at low electron flux. b-d) CryoTEM micrographs during high electron flux stroboscopic irradiation, showing: (b) the superstructure at the start of irradiation, (c) just before the nanoexplosion, and (d) right after the nanoexplosion, as indicated by the green sqaure in **e**. The yellow circle in **a** indicates the size of the electron beam used for the exposure series, and the green sqaure in **a** and **e** show the area of the superstructure that is captured by the microscope's camera. b'-d') Enlarged micrographs showing a single dendrimicelle during the stroboscopic exposure series. e) Micrograph obtained after high electron flux irradiation series. The high flux irradiation resulted in the evaporation of water from the irradiated area, decreasing the local thickness of the water film. f) Image intensity plot over the cryoTEM gridholes shown in a (red) and e (blue), showing that the exposure series resulted in an increase in the image intensity, corresponding to a decrease in thickness. g) Image intensity plot during the high flux irradiation. This figure shows that exposure yielded a gradual decrease of the water film thickness in the irradiated area. h) Cartoon showing the induced water evaporation during the stroboscopic exposure. The scale bars are 500 nm in (a, e), 100 nm in (b-d) and 10 nm in (b'-d').

The image intensity plot (Figure **4-3f**) confirms that before the stroboscopic exposure series (in red, corresponding to Figure **4-3a**), the dendrimicelle superstructure is located at the thinnest part of the biconcave thin film. After the stroboscopic exposure series, (in blue, corresponding to Figure **4-3e**), the average image intensity has increased over the exposed area, implying that the electron beam transmission has increased, corresponding to a decreased thickness of the thin film (See also Figure **S9/10**). These observations support our claim that the stroboscopic exposure resulted in a thinning of the film and indicate that specifically the exposed part of the vitreous ice layer decreased in thickness, with the thickness of the unexposed part of the vitreous water film remaining virtually unchanged. The increased electron scattering of the micelle-embedded gold nanoparticles likely serves to aggravate heating and evaporation of water. Inelastic scattering (*i.e.,* of electrons) transfers about 20 eV to the sample[32], and dissipated as heat, this can increase the local specimen temperature and leading to evaporation of the irradiated area.[29,30] Moreover, the hole present after the nanoexplosion allows to estimate the amount of water that evaporated during the exposure series. By assuming that the dendrimicelle superstructure was a 50-nm thick monolayer before exposure *(i.e.,* the size of the dendrimicelles), the image intensity over the induced hole (Figure **4-3f)** can be converted to a thickness in nm. This translates to a thickness of the remaining vitreous water film of about 10 nm at the edge of the hole after the nanoexplosion, suggesting that a ~3 nm thick layer of water evaporated over the irradiated area during every exposure. Taking the height of a single 'layer' of water to be the size of a water molecule (~0.3 nm), this infers that the water evaporation rate was on the order of ~10 layers of water per exposure. Given the electron exposure rate of ~41 $e^-/Å^2$ per exposure, this corresponds to a dose of ~30 electrons required for the evaporation of each molecule of water.

Figures **4-3b'-d'** show enlarged sections of the cryoTEM micrographs shown in Figures **4-3b-d**, highlighting an individual dendrimicelle, with the dendrimicelle core area indicated in Figure **4-3b'** by the black circle surrounding the gold nanoparticles. Surprisingly, Figure **4-3c'** seems to indicate that right before the nanoexplosion, the gold nanoparticles are located closer together than they were in Figure **4-3b'**. This observation suggests that the dendrimicelle core shrunk during the electron irradiation. Measurements of the dendrimicelle core area between these figures confirmed that the core area shrunk by about 40% during the stroboscopic exposure (Figure **S11**). Since the interior of PAMAM dendrimers,[33] as well as the cores of complex coacervate micelles[34] are known to contain substantial amounts of water, this contraction is likely due to the evaporation of dendrimer- and micelle-entrapped water. Alternatively, or in addition, it also might be that the gold nanoparticles simply have been pushed out of the shrinking dendrimer cavities, and therefore appear closer together, possibly surrounded by dendrimer material and hence forming so-called dendrimer-stabilized nanoparticles.

To study the apparent dendrimicelle core shrinkage in more detail, we prepared a dendrimicelle sample from ninth-generation (G9) Au_{024}DENs at off-stoichiometric mixing ratio. Not only does the increased dendrimer generation allow for the encapsulation of larger nanoparticles inside, it also leads to fewer dendrimers per dendrimicelles, enlarging contrast and facilitating visualization of the contents of the micelle core. Figure **4-4a** shows the obtained dendrimicelle superstructure before stroboscopic exposure, with the dendrimicelles in the center of the superstructure containing ~9 nanoparticles per dendrimicelle. The enlarged cryoTEM micrographs in Figure **4-4c-e** show the same location at various time points during the exposure series, with the whole exposure series shown in Figure **S12**. These figures show the appearance of gas bubbles, (Figure **4-4c**), that consecutively disappear (Figure **4-4d**), followed by the shrinkage of the core (i.e., the clustering of the AuNPs, Figure **4-4e**). Plotting the average image intensity against total exposure dose (See Figure **S13-14**) shows again the controlled decrease in thickness of the irradiated area. Plotting the dendrimicelle core area, *i.e. as* defined by the circle encompassing the nanoparticles, *versus* the exposure dose (Figure **S15**) indicates that the average core volume decreased from ~10^4 to ~$2*10^3$ nm^3. As the volume of a generation nine dendrimer is already about ~10^3 nm^3, this indicates that the dendrimicelle core has shrunk significantly during the exposure series. In fact, the appearance of gas bubbles during TEM irradiation (Figure **S16**), has been attributed to the evolution of hydrogen gas derived from the radiolysis of organic matter.[27-29] The apparent shrinking of the micelle core and the gas bubbles suggest that the dendrimicelle core has been —at least partially— damaged; making it plausible that the gold nanoparticles have ceased to be dendrimer-encapsulated-nanoparticles. The grouping of the gold nanoparticles in this process might be related to the magnetic properties attributed to gold nanoparticles.[35]

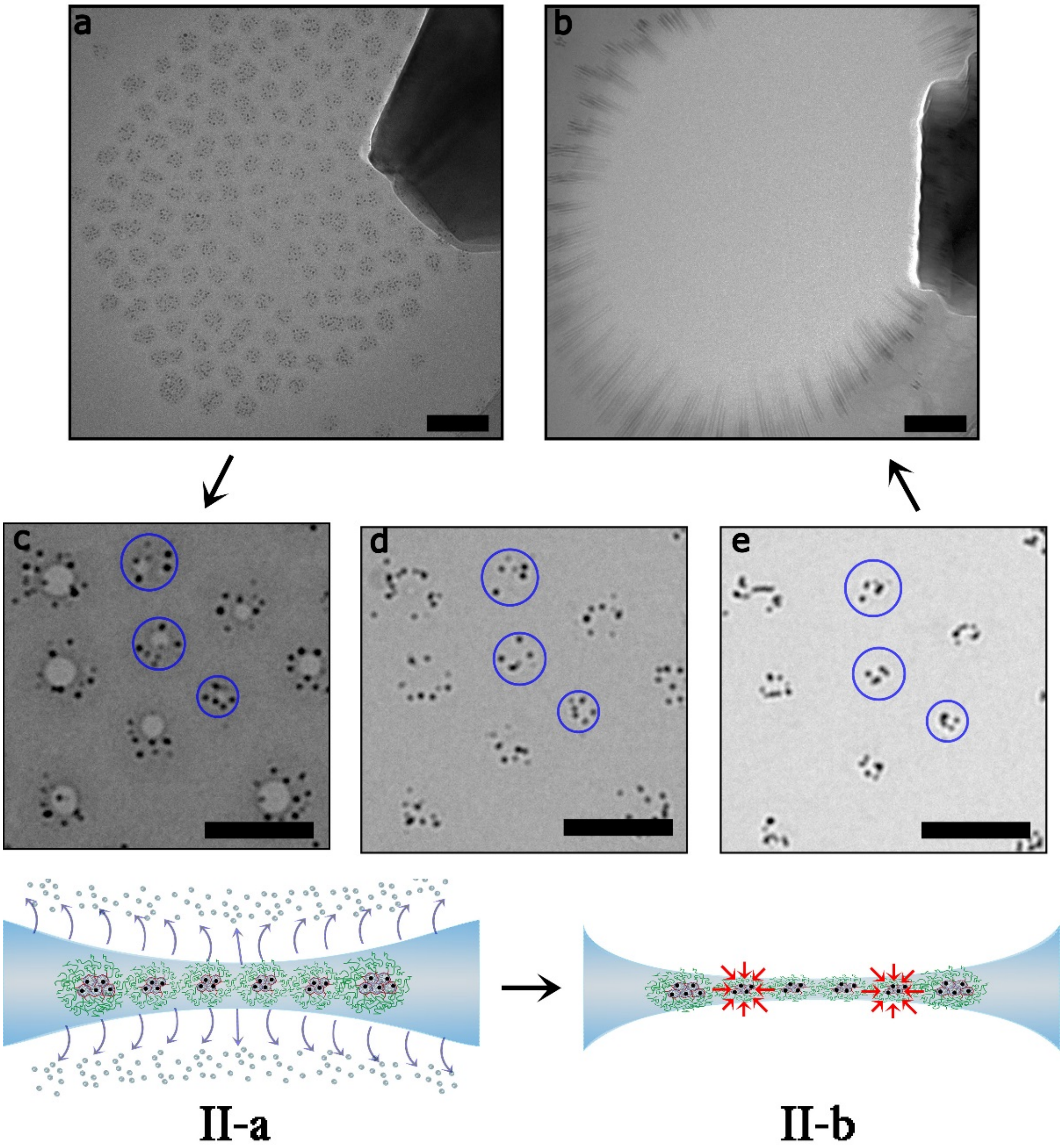

Figure **4-4** **a)** CryoTEM micrograph of a dendrimicelle superstructure obtained from dendrimicelles encapsulating ninth-generation PAMAM dendrimers in their core, with an Au_{1024} nanoparticle encapsulated inside every dendrimer. **b)** CryoTEM micrograph after the electron beam-induced nanoexplosion of the dendrimicelle superstructure. **c-e)** Enlarged sections of the superstructure at various time points during the electron beam irradiation, showing that upon prolonged irradiation, the contrast provided by the dendrimicelle core is reduced, and the gold nanoparticles appear closer together. **f)** Schematic illustration of the different stages during the nanoexplosion. CryoTEM sample preparation provides a dendrimicelle superstructure located at the thinnest part of the biconcave water film. Extensive electron irradiation results in the evaporation of water from the biconcave thin film (II-a), leading to the formation of a freestanding polymer film in the center of the grid hole, in which the dendrimicelle cores seems to have shrunk, but more likely the gold particles have been excreted from the dendrimer voids and group together (II-b).

The processes that take place during the clustering of the nanoparticles and the final nanoexplosion include the following: Extended electron beam irradiation results in heating of the exposed area, with the density of the nanoparticle-containing dendrimicelle core likely providing additional local heating. The “increase in temperature” of the vitreous ice layer results in the evaporation of water, from both the water layer and from the dendrimicelle core (Figure **4-4f**, **II-a**); in addition, the partial radiolysis of hydrocarbons inside the dendrimicelle core generates gas bubbles. At the start of the exposure series, the dendrimicelle corona is still visible, and there is contrast between dendrimicelle coronas. Just before the nanoexplosion, however, this contrast disappears, and a smooth, dendrimicelle superstructure is observed (as shown in Figure **4-3c & 4-4e**). Since both PAMAM as well as the complex coacervate micelle cores are hydrated,[32,33] evaporation of water could cause the shrinkage of the core (Figure **4-4f**, **II-b**), applying a stress on the thin film. Further evaporation of water likely amplifies the stress inside the superstructure, leading to the rupture starting from the thinnest point, the superstructure center. Apart from observing a (global) radially outward-directed movement of the micelles during the nanoexplosion and the shrinkage of the dendrimicelle prior to the nanoexplosion, we also observed local migration of dendrimicelles (Figure **S17)**. These results show that the dendrimicelle superstructures become viscous, liquid-like thin films rather than the solid vitreous structures as obtained from the cryoTEM sample preparation.

4.4 Conclusion

Here, we exploited gold nanoparticles embedded inside dendrimicelle superstructures to study local and global processes that take place before and during electron beam-induced rupture of vitrified thin films containing self-organized superstructures of self-assembled micelles. The micelle-embedded nanoparticles act as tracer by providing contrast in the cryoTEM micrographs and allow for visualizing the superstructure rupture, which we coined 'nanoexplosion'. The gold nanoparticles not only provide information on the global migration patterns during the nanoexplosion, they also visualize local migration of individual dendrimicelles and show movement inside individual dendrimicelles. For future work, the highly modular dendrimicelles allows to systematically investigate relevant parameters for thin film rupture at the nanoscale. It not only allows for varying the type, size and number of nanoparticles per dendrimicelle, but also allows for changing the number of nanoparticles-containing dendrimicelles and the dendrimicelle polydispersity per superstructure. This study opens up thin film physics at the nanometer scale, of relevance for novel materials that are being developed for, *e.g.,* medicinal, catalytic, magnetic or optical properties.

4.5 References

1 Shenhar, R., Norsten, T. B. & Rotello, V. M. Polymer-Mediated Nanoparticle Assembly: Structural Control and Applications. *Adv. Mater.* **17**, 657-669, doi:10.1002/adma.200401291 (2005).

2 Wang, Y. *et al.* Host–guest chemistry with water-soluble gold nanoparticle supraspheres. **12**, 170 (2016).

3 Blanco, A. *et al.* Large-scale synthesis of a silicon photonic crystal with a complete three-dimensional bandgap near 1.5 micrometres. **405**, 437 (2000).

4 Bae, Y., Fukushima, S., Harada, A. & Kataoka, K. Design of Environment-Sensitive Supramolecular Assemblies for Intracellular Drug Delivery: Polymeric Micelles that are Responsive to Intracellular pH Change. *Angewandte Chemie International Edition* **42**, 4640-4643, doi:10.1002/anie.200250653 (2003).

5 Mura, S., Nicolas, J. & Couvreur, P. Stimuli-responsive nanocarriers for drug delivery. **12**, 991 (2013).

6 Bonaccorso, F., Sun, Z., Hasan, T. & Ferrari, A. C. Graphene photonics and optoelectronics. *Nature Photonics* **4**, 611-622, doi:10.1038/nphoton.2010.186 (2010).

7 Grabar, K. C., Freeman, R. G., Hommer, M. B. & Natan, M. J. Preparation and Characterization Au Colloid Monolayers. *Analytical Chemistry* **67**, 735-743, doi:10.1021/ac00100a008 (1995).

8 Butler, S. Z. *et al.* Progress, Challenges, and Opportunities in Two-Dimensional Materials Beyond Graphene. *Acs Nano* **7**, 2898-2926, doi:10.1021/nn400280c (2013).

9 Geim, A. K. & Novoselov, K. S. The rise of graphene. *Nature Materials* **6**, 183-191, doi:10.1038/nmat1849 (2007).

10 Radisavljevic, B., Radenovic, A., Brivio, J., Giacometti, V. & Kis, A. Single-layer MoS2 transistors. *Nature Nanotechnology* **6**, 147-150, doi:10.1038/nnano.2010.279 (2011).

11 Schreiber, F. Structure and growth of self-assembling monolayers. *Progress in Surface Science* **65**, 151-256, doi:10.1016/s0079-6816(00)00024-1 (2000).

12 Novoselov, K. S. *et al.* Two-dimensional atomic crystals. *Proceedings of the National Academy of Sciences of the United States of America* **102**, 10451-10453, doi:10.1073/pnas.0502848102 (2005).

13 Aveyard, R., Binks, B. P. & Clint, J. H. Emulsions stabilised solely by colloidal particles. *Advances in colloid and interface science* **100**, 503-546, doi:10.1016/s0001-8686(02)00069-6 (2003).

14 Vogel, N., Retsch, M., Fustin, C.-A., del Campo, A. & Jonas, U. Advances in Colloidal Assembly: The Design of Structure and Hierarchy in Two and Three Dimensions. *Chemical Reviews* **115**, 6265-6311, doi:10.1021/cr400081d (2015).

15 McGorty, R., Fung, J., Kaz, D. & Manoharan, V. N. Colloidal self-assembly at an interface. *Materials Today* **13**, 34-42, doi:10.1016/s1369-7021(10)70107-3 (2010).

16 Boles, M. A., Engel, M. & Talapin, D. V. Self-Assembly of Colloidal Nanocrystals: From Intricate Structures to Functional Materials. *Chemical Reviews* **116**, 11220-11289, doi:10.1021/acs.chemrev.6b00196 (2016).

17 Reincke, F., Hickey, S. G., Kegel, W. K. & Vanmaekelbergh, D. Spontaneous assembly of a monolayer of charged gold nanocrystals at the water/oil interface. *Angewandte Chemie-International Edition* **43**, 458-462, doi:10.1002/anie.200352339 (2004).

18 Reincke, F. *et al.* Understanding the self-assembly of charged nanoparticles at the water/oil interface. *Physical Chemistry Chemical Physics* **8**, 3828-3835, doi:10.1039/b604535a (2006).

19 Li, M., Schnablegger, H. & Mann, S. Coupled synthesis and self-assembly of nanoparticles to give structures with controlled organization. **402**, 393 (1999).

20 ten Hove, J. B., Wang, J., van Leeuwen, F. W. B. & Velders, A. H. Dendrimer-Encapsulated Nanoparticle-Core Micelles as Modular Strategy for Particle-in-a-Box-in-a-Box Nanostructures. *Nanoscale* **9**, 18619-18623, doi:DOI: 10.1039/c7nr06773a (2017).

21 ten Hove, J. B., Wang, J., van Oosterom, M. N., van Leeuwen, F. W. B. & Velders, A. H. Size-Sorting and Pattern Formation of Nanoparticle-Loaded Micellar Superstructures in Biconcave Thin Films. *ACS Nano* **11**, 11225–11231, doi:10.1021/acsnano.7b05541 (2017).

22 Evers, L. J., Nijman, E. J. & Frens, J. The role of structure in rupturing Newton-black soap films: dynamics of a molecular bilayer. *Colloids and Surfaces a-Physicochemical and Engineering Aspects* **149**, 521-527, doi:10.1016/s0927-7757(98)00582-2 (1999).

23 Glaeser, R. M. *et al.* Factors that Influence the Formation and Stability of Thin, Cryo-EM Specimens. *Biophysical Journal* **110**, 749-755, doi:10.1016/j.bpj.2015.07.050 (2016).

24 Frederik, P. M., Stuart, M. C. A., Bomans, P. H. H. & Busing, W. M. Phospholipid, Nature's own slide and cover slip for cryo-electron microscopy. *Journal of Microscopy* **153**, 81-92, doi:10.1111/j.1365-2818.1989.tb01469.x (1989).

25 Glaser, M. A. *et al.* Soft spheres make more mesophases. *Epl* **78**, doi:10.1209/0295-5075/78/46004 (2007).

26 Ziherl, P. & Kamien, R. D. Maximizing entropy by minimizing area: Towards a new principle of self-organization. *Journal of Physical Chemistry B* **105**, 10147-10158, doi:10.1021/jp010944q (2001).

27 Mishyna, M. *et al.* Effects of radiation damage in studies of protein-DNA complexes by cryo-EM. *Micron* **96**, 57-64, doi:http://dx.doi.org/10.1016/j.micron.2017.02.004 (2017).

28 Leapman, R. D. & Sun, S. Cryo-electron energy loss spectroscopy: observations on vitrified hydrated specimens and radiation damage. *Ultramicroscopy* **59**, 71-79, doi:http://dx.doi.org/10.1016/0304-3991(95)00019-W (1995).

29 Egerton, R. F., Li, P. & Malac, M. Radiation damage in the TEM and SEM. *Micron* **35**, 399-409, doi:http://dx.doi.org/10.1016/j.micron.2004.02.003 (2004).

30 Karuppasamy, M., Nejadasl, F. K., Vulovic, M., Koster, A. J. & Ravelli, R. B. G. Radiation damage in single-particle cryo-electron microscopy: effects of dose and dose rate. *Journal of Synchrotron Radiation* **18**, 398-412, doi:10.1107/s090904951100820x (2011).

31 Henderson, R. Realizing the potential of electron cryo-microscopy. *Quarterly Reviews of Biophysics* **37**, 3-13, doi:10.1017/s0033583504003920 (2004).

32 Kéri, M., Peng, C., Shi, X. & Bányai, I. NMR Characterization of PAMAM_G5.NH2 Entrapped Atomic and Molecular Assemblies. *The Journal of Physical Chemistry B* **119**, 3312-3319, doi:10.1021/acs.jpcb.5b00272 (2015).

33 Spruijt, E., Westphal, A. H., Borst, J. W., Cohen Stuart, M. A. & van der Gucht, J. Binodal Compositions of Polyelectrolyte Complexes. *Macromolecules* **43**, 6476-6484, doi:10.1021/ma101031t (2010).

34 Gröhn, F., Bauer, B. J., Akpalu, Y. A., Jackson, C. L. & Amis, E. J. Dendrimer Templates for the Formation of Gold Nanoclusters. *Macromolecules* **33**, 6042-6050, doi:10.1021/ma000149v (2000).

4.6 Appendix

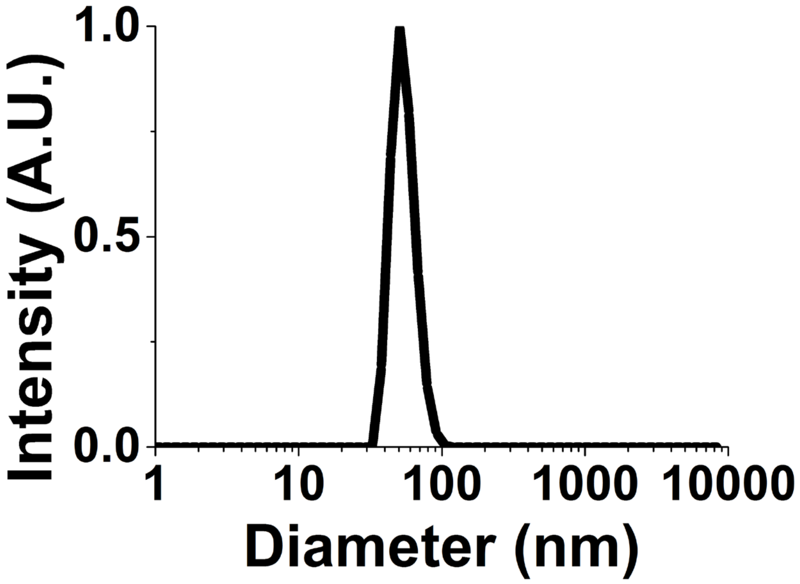

Figure **S1** Number-averaged DLS size plot of dendrimicelles made (at charge-stoichiometry) from sixth generation poly(amidoamine) dendrimers hosting an Au_{128} nanoparticle within. The average hydrodynamic diameter was found to be 52 nm.

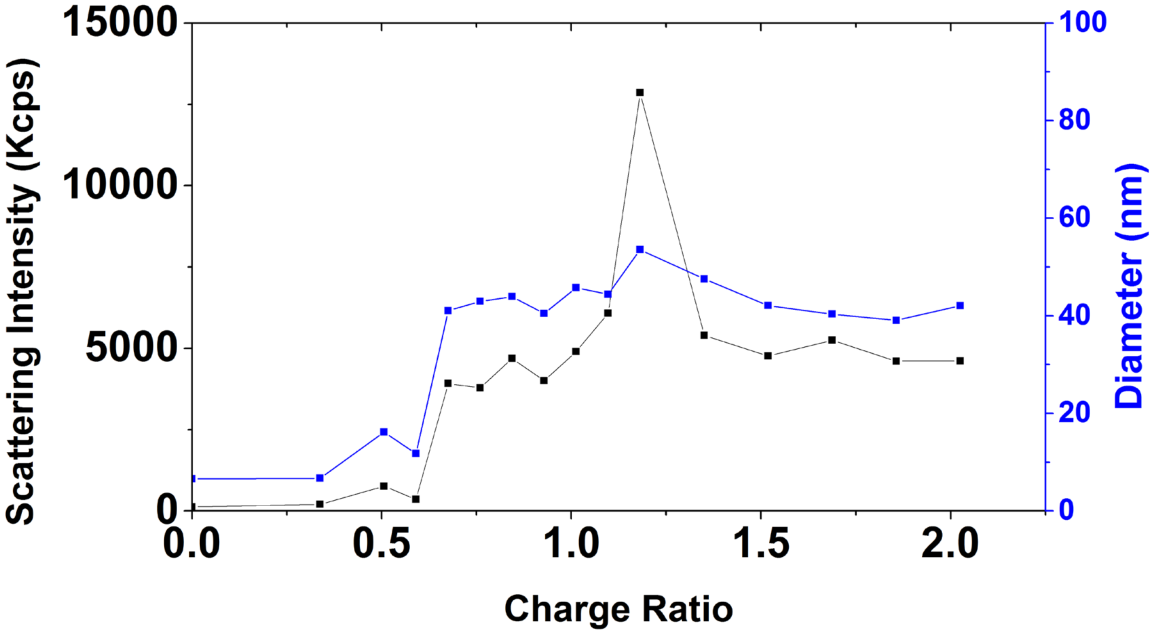

Figure **S2** DLS charge titration graph of PAMAM G6-NH_2 with $pMAA_{64}PEO_{885}$, showing the number-averaged dendrimicelle diameter in blue and the normalized scattered light intensity in black against the charge fraction. The amount of positive charge (dendrimer-NH2) was kept constant at 59 nmoles, and the amount of negative block polymer was varied, while keeping total volume constant. The charge fraction was calculated as the ratio of (NH_2/COOH).

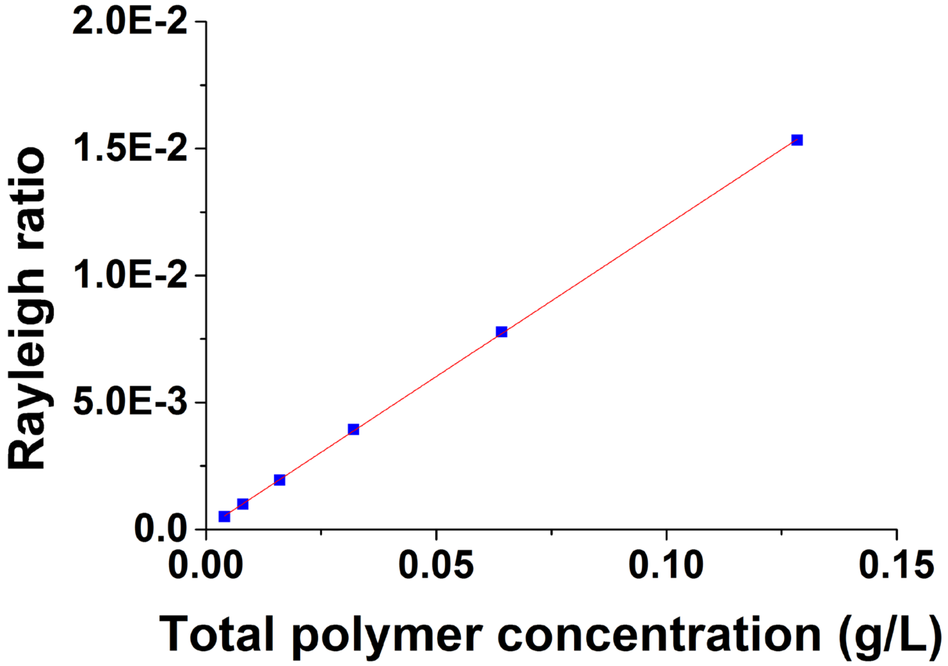

Figure **S3** CMC determination of dendrimicelles made from sixth generation poly(amidoamine) dendrimers. The intensity (as the excess Rayleigh ratio in m^{-1}) is plotted versus the total concentration of polymer (dendrimer + block copolymer). Fitting the data points with a linear fitting formula, and extrapolating to zero intensity gives the CMC. The thus-determined CMC is found at a negative polymer concentration (~ -1 $mg.L^{-1}$), indicating the stability of the dendrimicelles. Since the linear fitting formula almost perfectly fits the data points (R^2>0.999), we attribute the negative sign of the CMC to experimental error, likely because the CMC lays below the limit of detection of our setup. Therefore, the CMC is lower than 4 $mg.L^{-1}$.

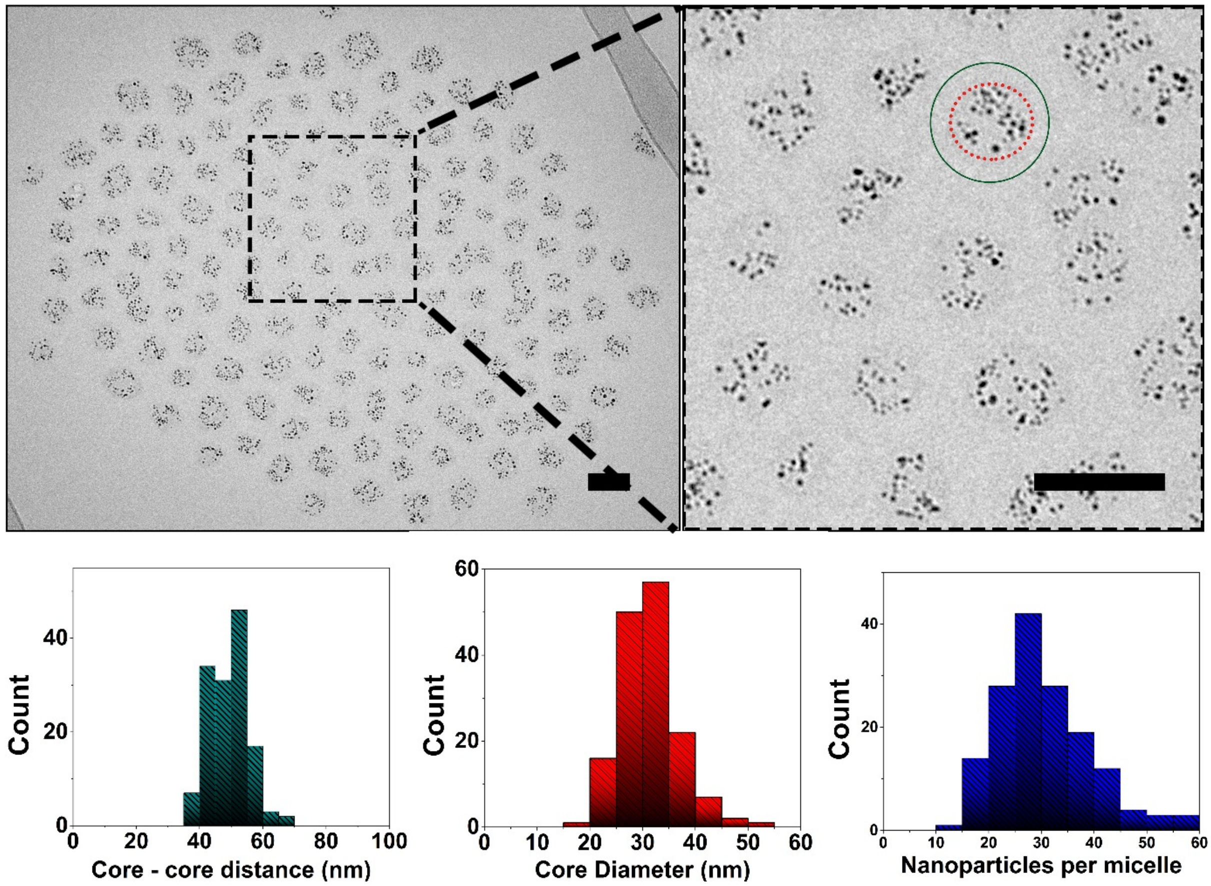

Figure **S4** Characterization of sixth generation-based dendrimicelles. **Top**: cryoTEM micrograph of the formed dendrimicelle superstructure. Inset: Magnification of the superstructure. In this micrograph, the nanoparticles residing inside the dendrimicelle core (the black spots) reveal the location and size of the dendrimicelle core, as indicated with the red, dotted box. The green, solid, circle indicates the size of the total dendrimicelle (core+corona), as determined by DLS. **Bottom**: Characterization of the cryoTEM images by measuring the core-core distances (**left**) shows that the average micelle is ~50 nm, has a core diameter that is ~30 nm (**middle**), and contains about 30 ± 10 nanoparticles per dendrimicelle (**right**).

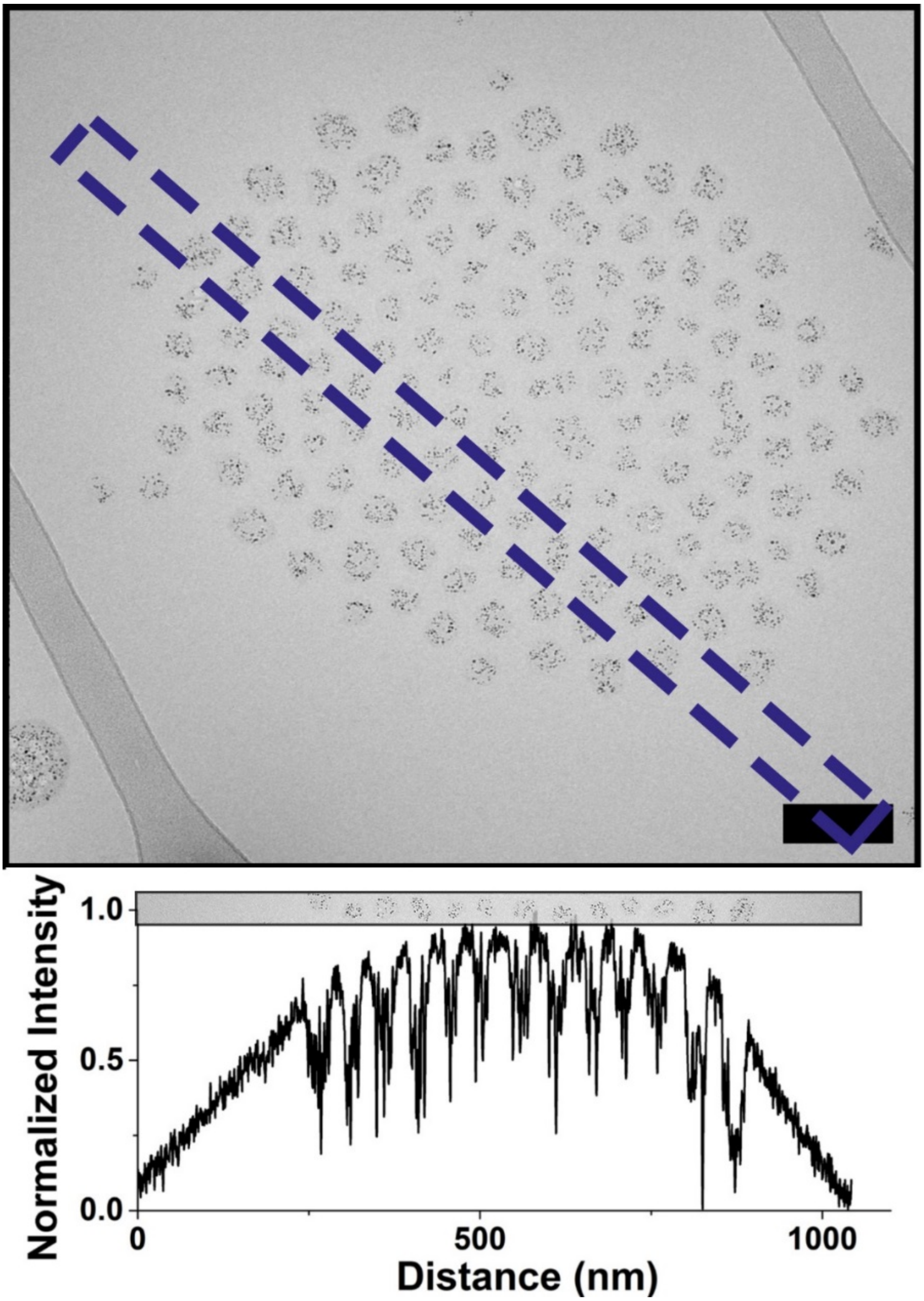

Figure **S5**) top: TEM micrograph showing a PAMAM G6-based dendrimicelle superstructure. The blue, dotted, rectangle indicates the location in the micrograph where the normalized Intensity plot has been calculated for. The scale bar represents 100 nm. Bottom: By plotting the (normalized) image intensity versus distance, it is apparent that the amount of transmitted light is increased towards the center of the dendrimicelle superstructure, implying that the thickness of the water layer is thinner towards the center of the superstructure.

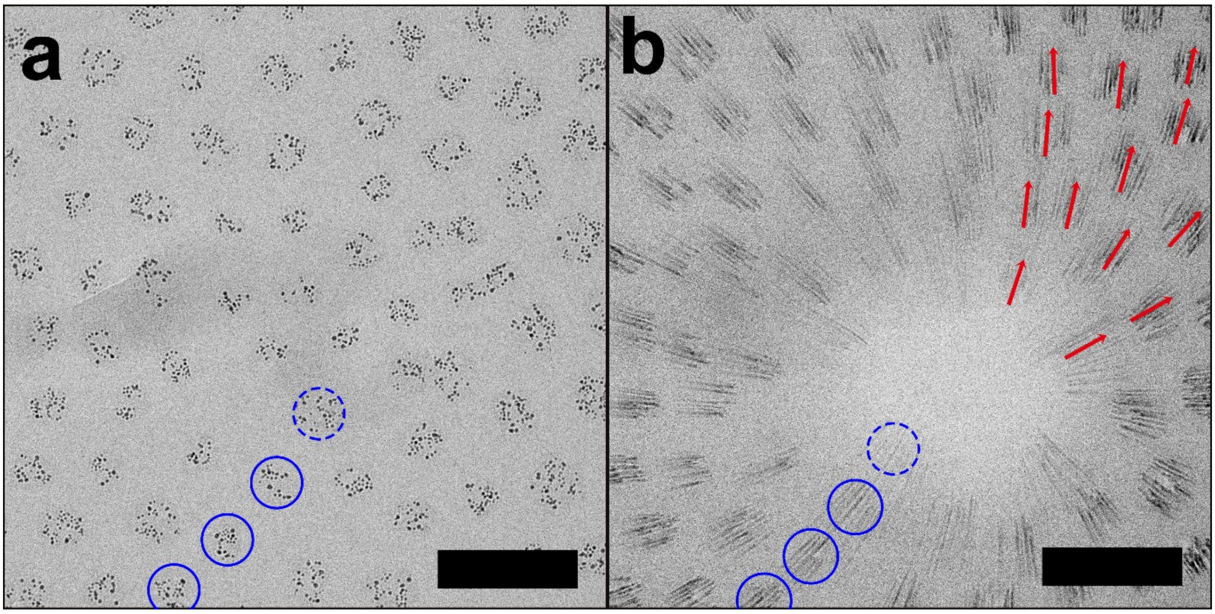

Figure **S6** Electron beam-induced thin film rupture of a sixth-generation PAMAM-based dendrimicelle superstructure. TEM micrographs showing: a dendrimicelle superstructure and b) the rupture of the thin water film. Film rupture appears to start from the center of the superstructure, anisotropically radiating outwards. Scale bars are 100 nm.

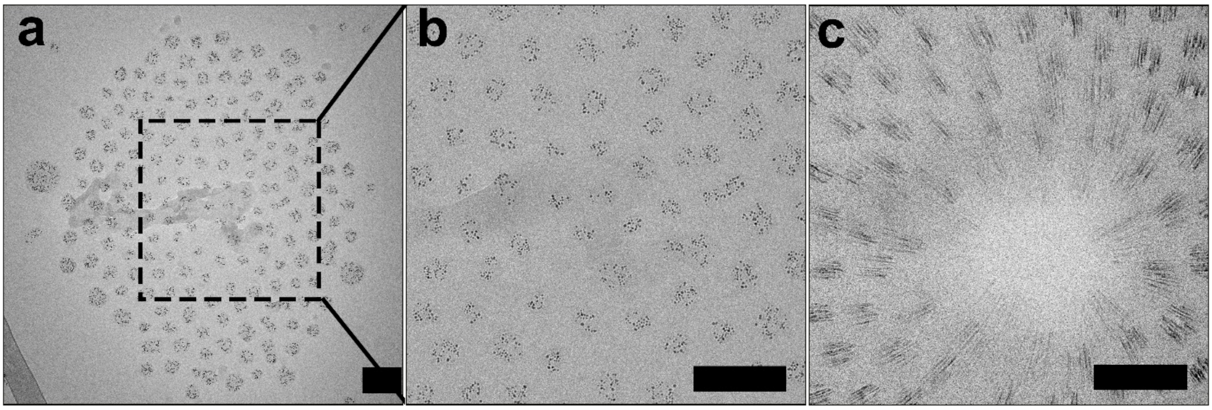

Figure **S7**: Electron beam-induced thin film rupture of a sixth-generation PAMAM-based dendrimicelle superstructure. TEM micrographs showing: a) the dendrimicelle superstructure. b) Zoom-in on the center of the superstructure. c) electron-beam induced radiation damage, and d) the rupture of the thin water film. Although the structures toward the edge of the superstructure show the most signs of radiation damage, the film ruptures from the center of the superstructure. Scale bars are 100 nm.

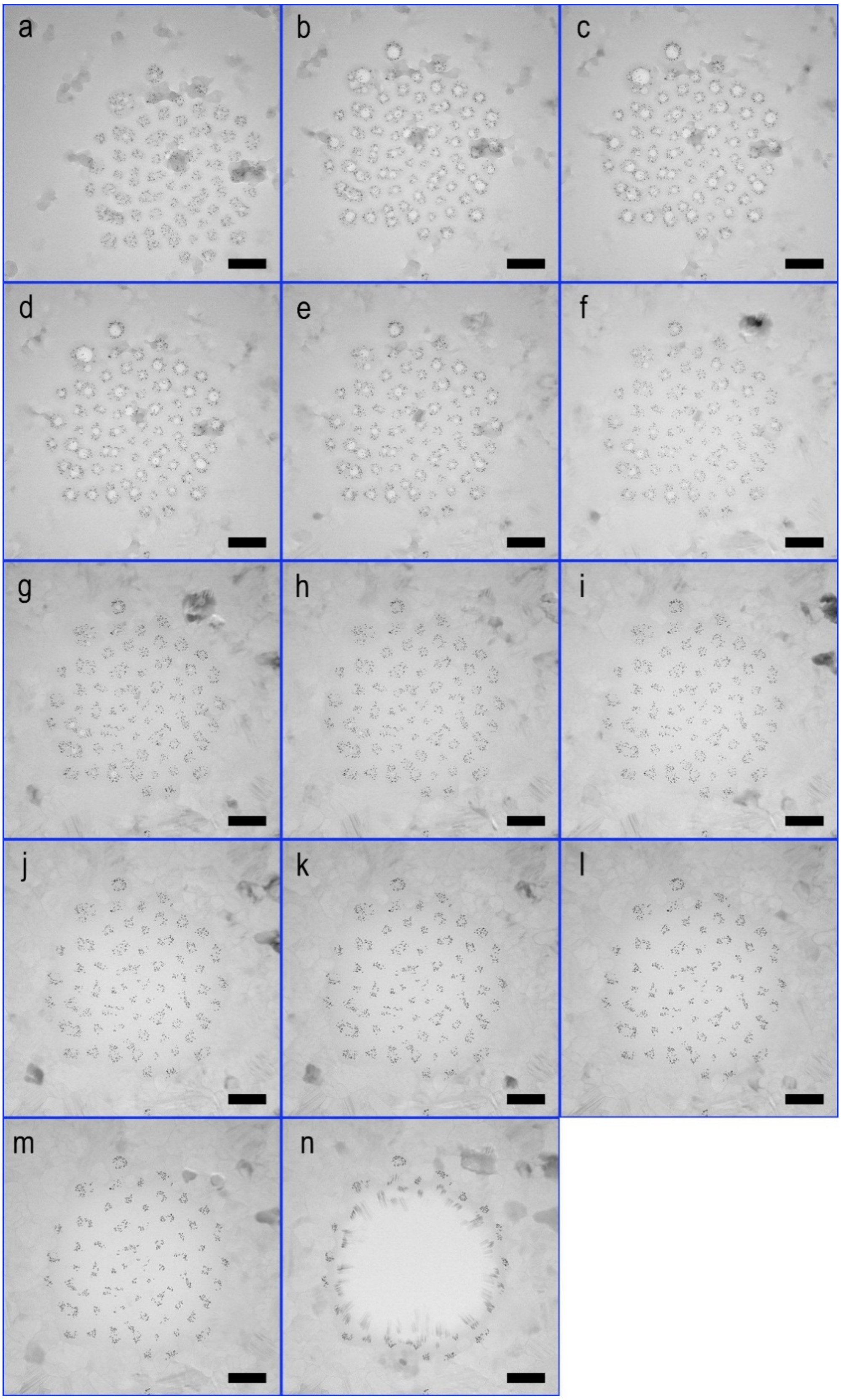

Figure **S8**) Stroboscopic exposure series of a generation six-based dendrimicelle superstructure. First (b-d), radiation damage appears in the form of gas bubbles, followed by the slow disappearance of the gas bubbles (e-h) and further evaporation of water (i-m). Finally, the superstructure ruptures, leaving a hole behind (n).

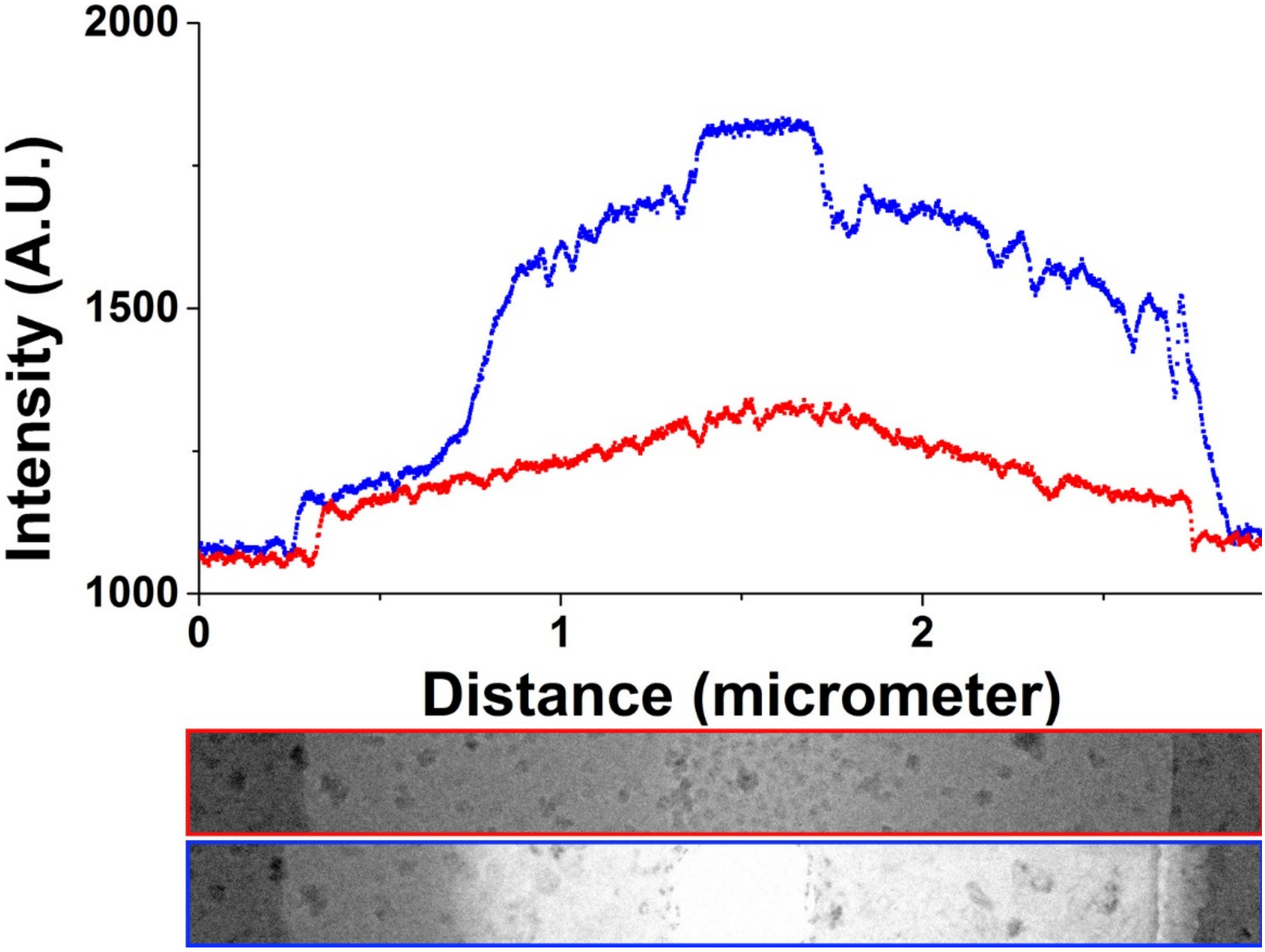

Figure **S9**) Average image intensity profile plot and corresponding cryoTEM micrographs before (red) and after (blue) the electron beam induced nanoexplosion. The TEM micrographs are 3 * 0.3 μm, and the average intensity plots show the averaged image intensity over the 0.3 μm tall box. The location of the dendrimicelle superstructure coincides with the thinnest part of the biconcave thin film.

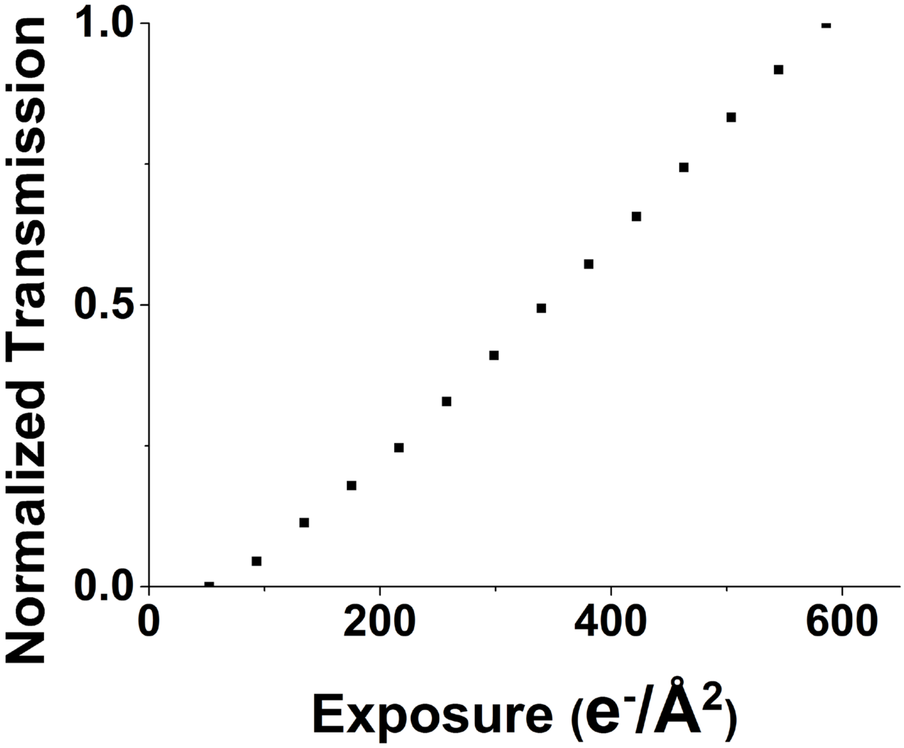

Figure **S10**) Normalized image intensity during the stroboscopic exposure series as shown in Figure **S8**, indicating a linear relationship between the exposure dose and number of transmitted electrons.

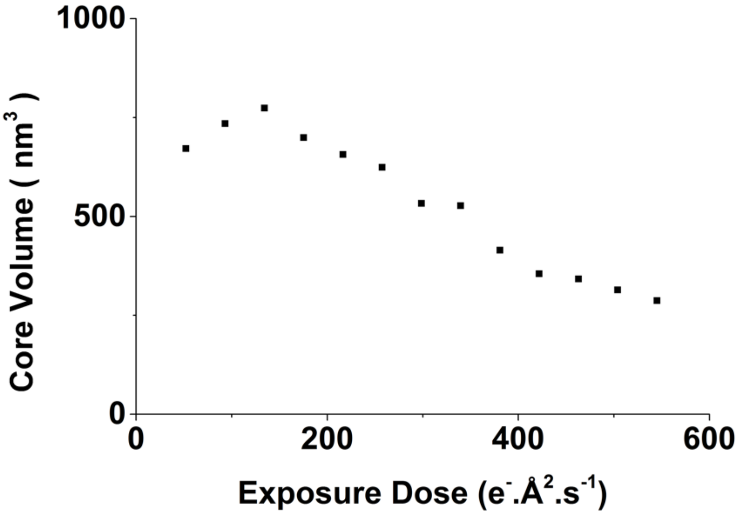

Figure **S11**) Measuring the dendrimicelle core area, –as indicated by the gold nanoparticles embedded within– of 10 dendrimicelles indicates that the dendrimicelle core area decreases by ~40 percent during the during stroboscopic exposure.

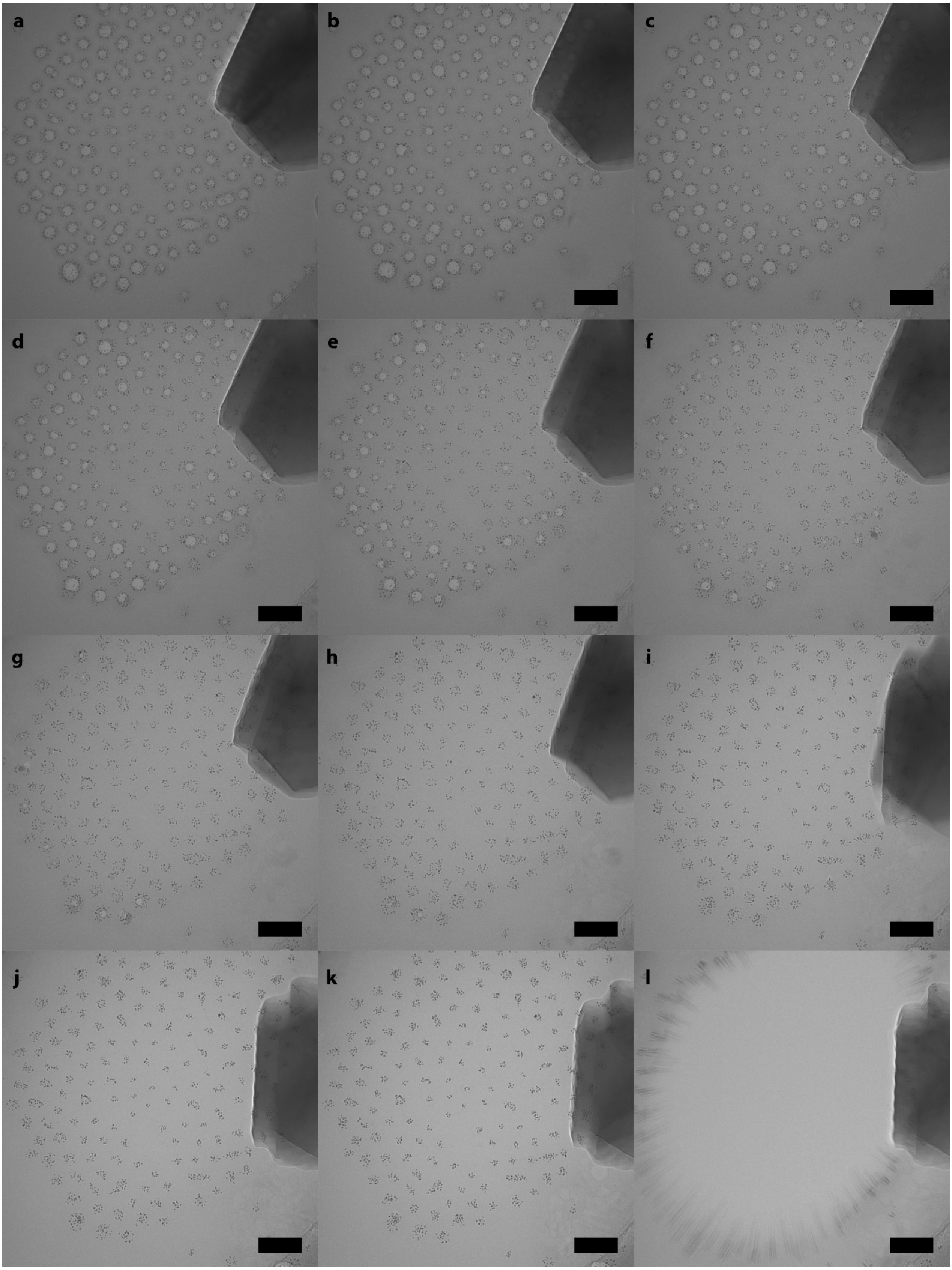

Figure **S12**) Stroboscopic exposure series of a generation nine-based dendrimicelle superstructure. First (a-c), radiation damage appears in the form of gas bubbles, followed by the slow disappearance of the gas bubbles (d-g) and further evaporation of water (g-k). Finally, the superstructure ruptures, leaving a hole behind (l).

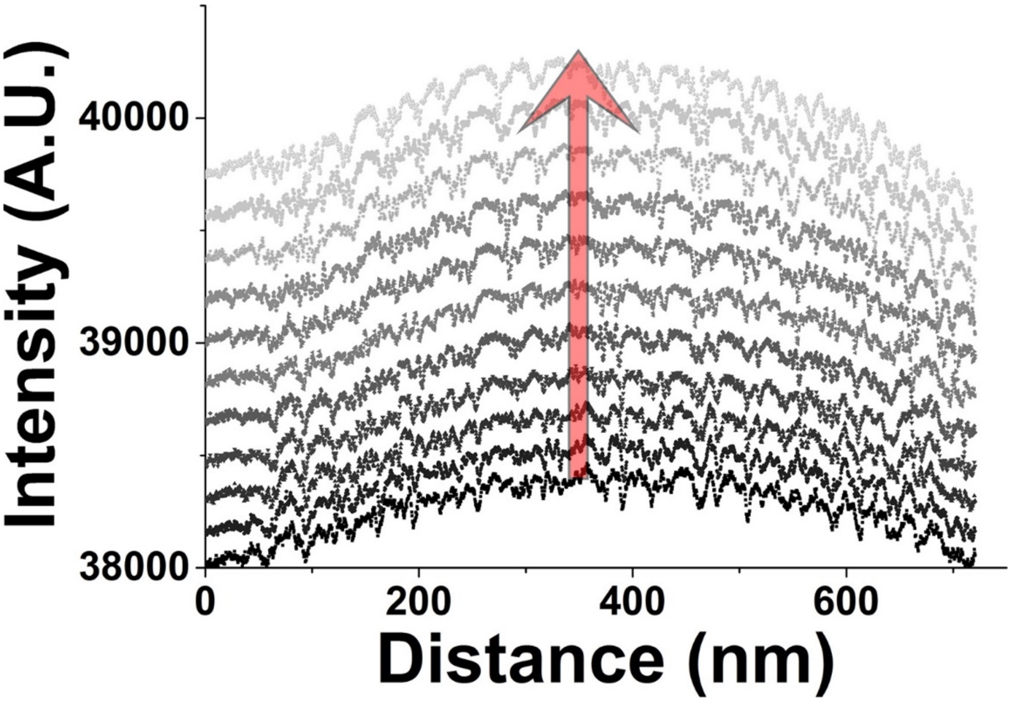

Figure **S13**) Average intenity of the G9 dendrimicelle superstructure during the stroboscopic exposure. During the exposure series, the average intensity increases, corresponding an increased transmission, and hence a decrease in thin film thickness.

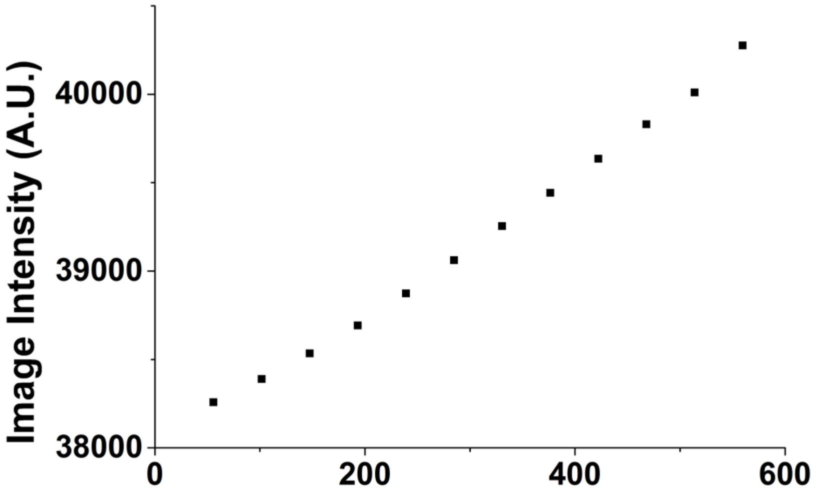

Figure **S14**) Graph showing the average intenity of the G9 dendrimicelle superstructure versusthe total accumulated electron dose, confirming that during the exposure series, the average intensity increases, implying an increased transmission, and hence a decrease in thin film thickness.

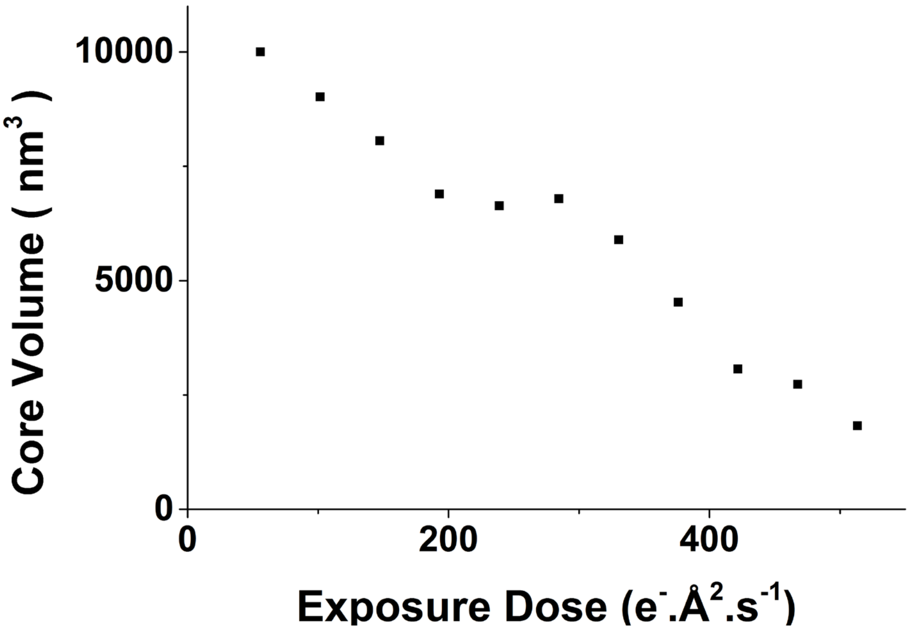

Figure **S15)** Analysis of the dendrimicelle core area –as indicated by the gold nanoparticles embedded within–shows that the core area decreases with increasing total exposure dose, suggesting the shrinkage of the dendrimicelle cores.

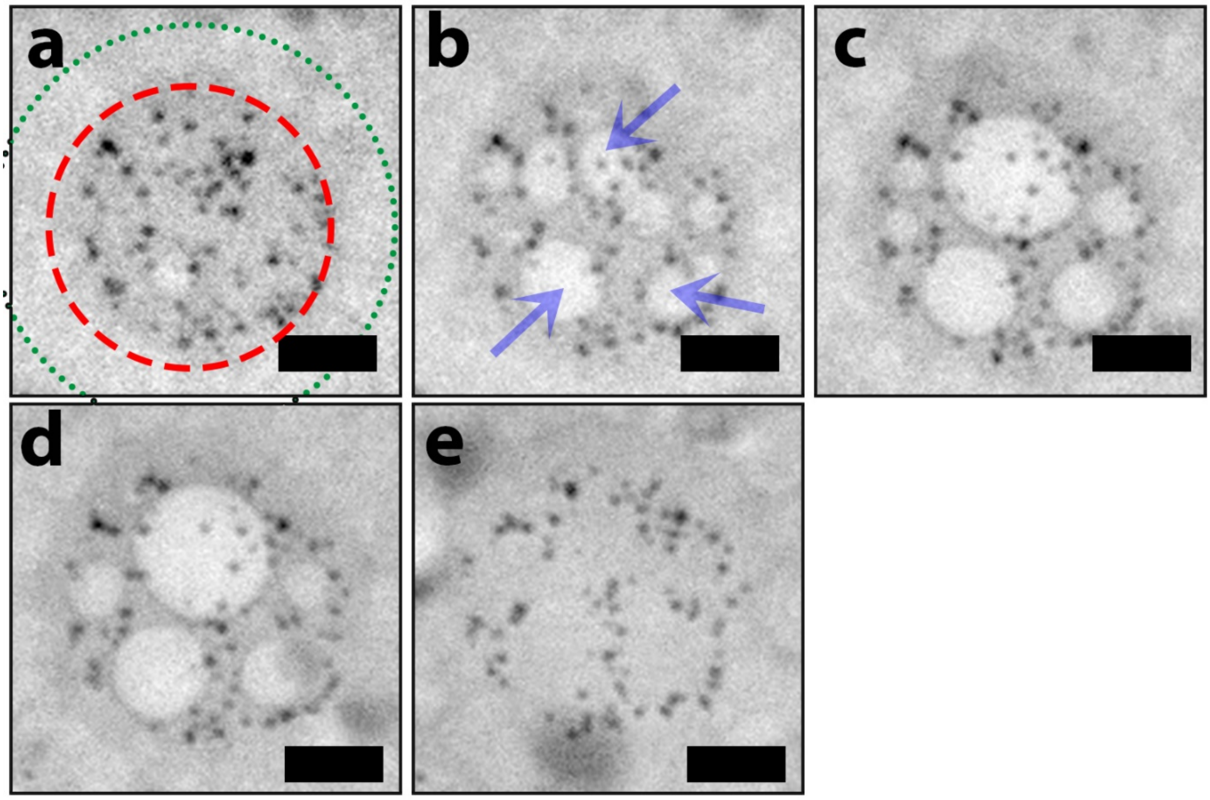

Figure **S16** Progressive electron beam-induced radiation damage to a PAMAM G6 dendrimicelle. The cryoTEM micrograph (**a**) shows the dendrimicelle core. Radiation damage appears as gas bubbles (**b**) (indicated with the blue arrows), that increase in size (**c-d**), and finally disappear (**e**). Upon further irradiation, the dendrimicelle superstructure ruptures, leaving a hole behind.

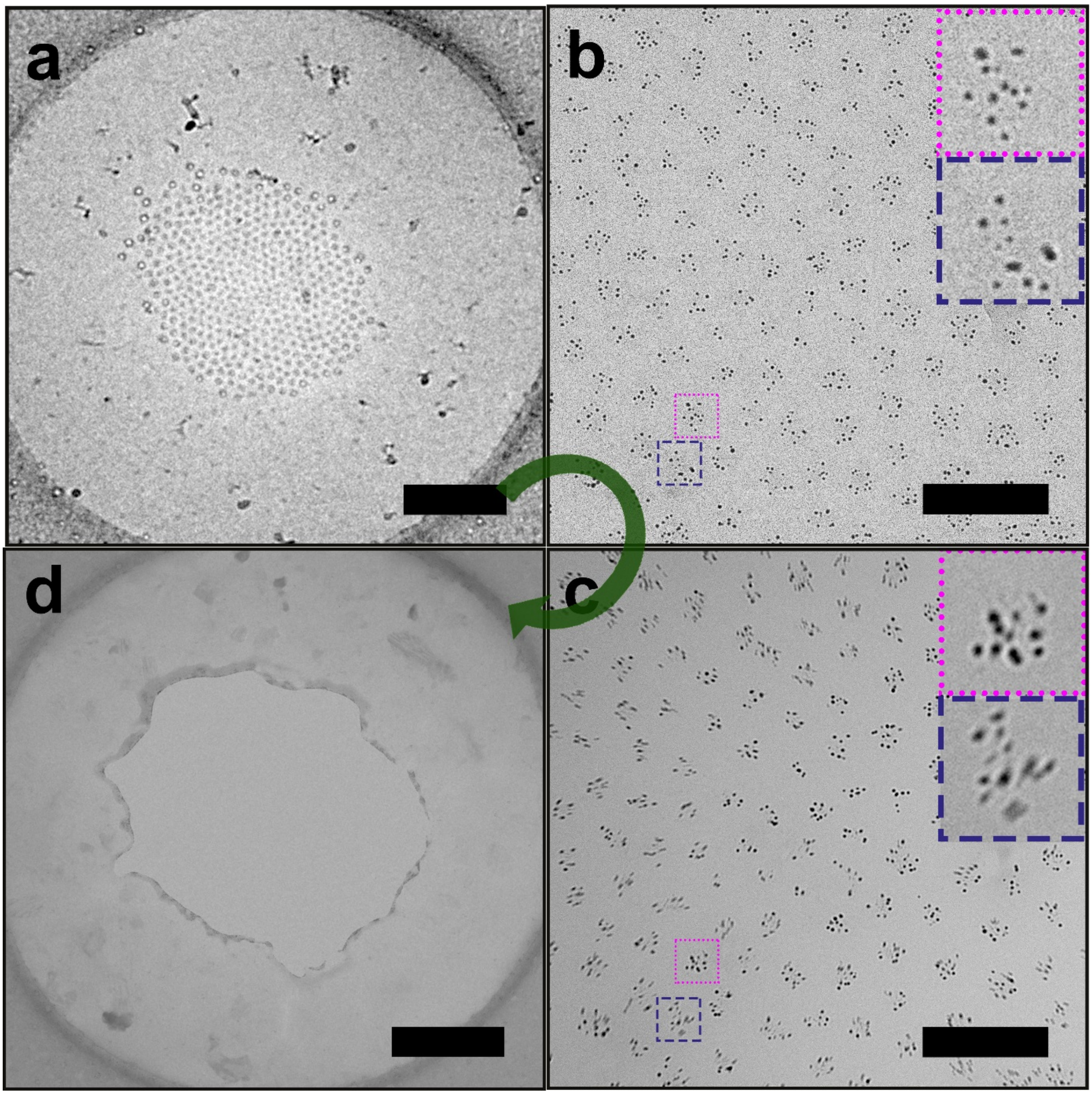

Figure **S17** Electron beam-induced rupture of biconcave thin water films containing a G9 dendrimicelle superstructure. a) Micron-sized hole in a circular grid hole, containing a vitrified, biconcave water film. b) Enlarged view of the dendrimicelle superstructure embedded in the biconcave thin film. c) the dendrimicelles just before rupture, with some of the dendrimicelles already showing local migration during acquisition in the form of motion blur. The pink, dotted inset box shows a dendrimicelle that remained static, and the purple, dashed, box shows a dendrimicelle that migrated during image acquisition, as indicated by the motion blur streaks. d) View of the TEM grid, showing the hole after electron beam-induced rupture. Scale bars are 500 nm (**a**/**d**), respectively 100 nm (**b**/**c**).

Chapter 5

Nanoparticles Reveal Extreme Size-Sorting and Phase-Transition of Dendrimicelles in Biconcave Thin Films

We here show provide detailed insight in self-assembled dendrimicelle systems exploiting gold nanoparticles for cryoTEM contrast. The nanoparticle-containing dendrimicelles are formed from fifth-generation dendrimer-encapsulated (DENs) and dendrimer-stabilized nanoparticles (DSNs). The dendrimicelles self-organize in biconcave thin water layers into size-sorted monolayer superstructures. The micelle embedded nanoparticles are a straightforward tool to determine the micelle aggregation number, and the polydispersity of the dendrimicelles can be tuned providing superstructures with extreme size-sorting patterns. Contrary to related systems with higher generation dendrimers, these fifth-generation structures form not only dendrimicelles but also other nanoassemblies, such as vesicles.

This chapter is based on: **Jan Bart ten Hove**, Matthias N. van Oosterom, Fijs W.B. van Leeuwen and Aldrik H. Velders. *Manuscript submitted*.

5.1 Introduction

Hierarchical assembly allows for sophisticated and well-defined ordering of molecular building blocks into complex materials that exhibit unique properties.[1-3] Among the many different self-assembled nanomaterials that have been created, e.g, metal-organic frameworks,[4] molecular boxes,[5,6] and vesicles,[7] micelles have proven to be most versatile supramolecular structures.[8] Complex coacervate core micelles, (C3Ms), form upon the combination of oppositely-charged polymeric building blocks and have been formed using a plethora of macromolecules, ranging from proteins to linear-, coordination-, branched-, and hyper-branched polymers.[1,9-12] Well-defined polymers such as dendrimers allow for detailed investigations on structure, composition, shape and stability of C3Ms as we showed before.[13] Dendrimers are known for their ability to encapsulate small molecules and nanoparticles,[14,15] Poly(AmidoAmine), PAMAM, dendrimers are among the most studied dendrimers.[16-18] From the original work of Amis and Crooks, it is known that only the higher generations amine-terminated PAMAM (*i.e.*, generations six through nine) can effectively encapsulate a nanoparticle (*i.e.*, Au, Pd, Cu, etc.) inside their interior cavities, yielding DENs.[14,19] In fact, PAMAM generations 0-3 tend to form dendrimer-stabilized nanoparticles, DSNs, instead, where a nanoparticle is stabilized by multiple dendrimers rather than being encapsulated in a single, individual, dendrimer. As a result, DSNs are considerably larger than DENs. Fourth- and fifth-generation PAMAM dendrimers can be considered ‘hybrids’ in the sense that both DENs as well as DSNs can form.[14,20] By incorporating dendrimers into the micelles, the unique encapsulation property of dendrimers can be used to “load” complex coacervate core micelles, as we recently showed by combining block copolymers together with DENs,[21,22] forming well-defined dendrimicelles that carried ~20-30 nanoparticles/dendrimicelle depending on the generation used. These nanoparticle-containing dendrimicelles self-organized into distinct disk-like monolayer superstructures inside ~0.1 μm thick biconcave ice films formed during cryoTEM sample preparation.[21]

The dendrimicelles arranged following the thickness of the thin, biconcave-shaped, ice film, related to the increased size-sorting to an increased dendrimicelle polydispersity caused by a decreased micelle stability, corroborating with previous work by Wang et al. on carboxylic acid-terminated PAMAM dendrimers that showed a generation-dependent dendrimicelle stability.[13] To better understand the properties of dendrimicelles formed from dendrimer generations <6, we reasoned that gold particles embedded in the micellar core could reveal details on composition shape, and stability of the micellar subcomponents with unprecedented detail. The decreased stability of lower generation-based dendrimicelles is expected to lead to an increased dendrimicelle polydispersity at off-stoichiometric charge mixing fractions. In turn, the increased polydispersity is expected to lead to a more pronounced size sorting of dendrimicelle inside dendrimicelle superstructures formed during cryoTEM sample preparation.

We here present dendrimicelles formed from generation five-based PAMAM dendrimers at various charge stoichiometries, and analyze the formed dendrimicelles and superstructures using cryoTEM and Dynamic Light Scattering techniques. The synchronous formation of DSNs as well as DENs is shown, which co-assembled into well-defined dendrimicelles at charge-stoichiometry. Using off-stoichiometric mixing conditions yields samples with a high polydispersity, in which an amplified size-sorting inside the formed superstructures is observed and in which additional nanoaggregates –too large to be dendrimicelles– form.

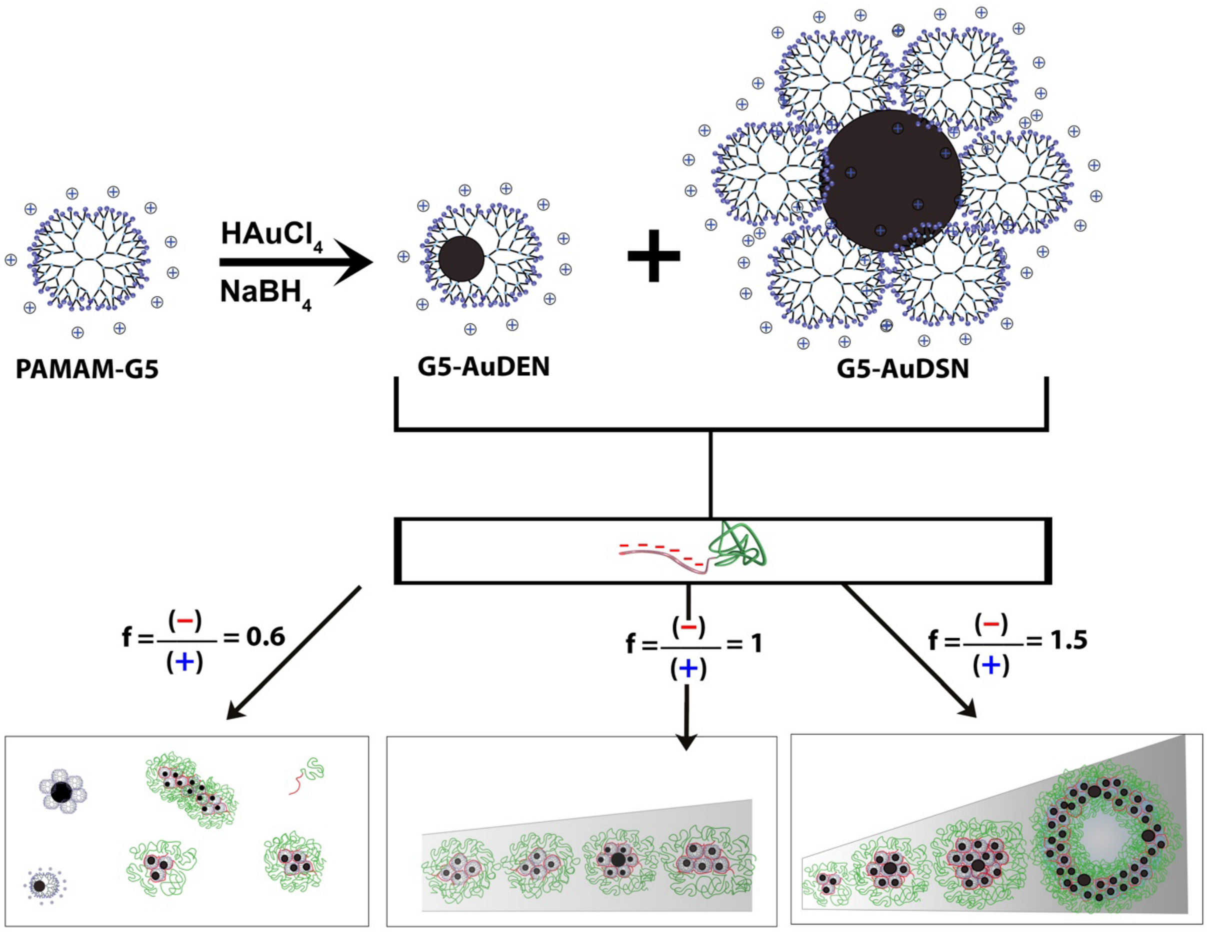

Scheme ***5-1:*** *Preparation of dendrimicelles from amine-terminated fifth generation PAMAM dendrimers. Complexation and reduction of* Au^{3+} *ions inside fifth-generation PAMAM results in DENs as well as DSNs. Addition of a negative-neutral block copolymer,* $pMAA_{64}pEO_{885}$ *results in formation of dendrimicelles, depending on the charge fraction f, where f = (negative charge from the block copolymers)/(positive charge from the dendrimers). Charge stoichiometric mixing (f=1) yields well-defined dendrimicelles. Using excess block copolymer to dendrimer (f=1.5) results in micelles with an increased polydispersity as well as in the formation of additional nanostructures, such as complex coacervate vesicles.*

5.2 Experimental Section

Materials

Amine-terminated polyamidoamine (PAMAM) dendrimers, (3-(N-morpholino)-propanesulfonic acid) (MOPS), $NaBH_4$, 1M NaOH and 1M HCl solutions were obtained from Sigma Aldrich. $pMAA_{64}$-b-PEO_{885} (Mw/Mn = 1.15) was obtained from Polymer Sources Inc., Canada and used as 5 mM solution based on carboxylic acid content. $HAuCl_4.3H_2O$ was obtained from TCI.

Dendrimer Encapsulated Nanoparticles

G5-Au_{64}DENs were made following established protocols.[14] Shortly, 50 μL (69 nmol) of 5 wt% PAMAM G5-NH_2 in methanol was transferred to a 5 mL vial and the methanol was evaporated under reduced pressure. Next, 2 mL of water was added to dissolve the PAMAM and the pH was adjusted to 3 using 1M HCl, after which 64 molar equivalents of Au^{3+} to PAMAM were added. This solution was stirred for 20 minutes, after which 44 μL of a 1M solution of $NaBH_4$ in 0.3M NaOH (10 molar equivalents to Au^{3+}) were added. This resulted in the reduction of Au^{3+} to AuDENs, indicated by the change from colorless to a dark brown solution within seconds after addition. After reduction, pH was set to 7 using HCl; the DENs were stored at 4 ^{o}C.

Dendrimer-Encapsulated-Nanoparticle Micelles

To obtain dendrimicelles under charge stoichiometric conditions, 20 μL of 2.9 mM dendrimer solution (charge concentration, corresponding to 59 nmol positive charge based on surface groups) was dissolved in 149 μL water and 20 μL of 0.2M MOPS buffer at pH 7 was added. Then, 11 μL $pMAA_{64}$-b-PEO_{885} (55 nmol based on -COOH) was added under sonication, and the sample was sonicated for 2 minutes total. Dendrimicelles at off-stoichiometric charge mixing fractions were made by adjusting the amount of $pMAA_{64}PEO_{885}$ added, keeping the total volume constant at 200 μL.

Methods

Dynamic Light Scattering (DLS) was done on a Malvern Zetasizer Nano S equipped with a laser operating at 633 nm. Sample grids for electron microscopy were obtained from Electron Microscopy Sciences (EMS, Hatfield, PA, USA) and were rendered hydrophilic using a plasma cleaning setup (~15 s at 10^{-1} Torr). CryoTEM samples were cast on Quantifoil R2/2 grids. After blotting, samples were plunged into liquid ethane using a Vitrobot system (FEI Company). Samples were then imaged at ~ 90-100 K in a JEOL 2100 TEM operating at 200 kV or JEOL 1400Plus TEM operating at 120 kV.

Image Analysis

CryoTEM images were analyzed using ImageJ and custom Matlab particle micelle tracking script, as reported before.[21] The average core-core distance was calculated by measuring 100 randomly selected neighboring dendrimicelles. Dendrimicelle core areas were determined from measuring the area of the circle surrounding core, as indicated by the AuNPs embedded within.

5.3 Results and Discussion

Au_{64}DENs were synthesized inside fifth-generation poly(amidoamine) (PAMAM) dendrimers by complexation and subsequent reduction of Au^{3+} inside the PAMAM dendrimer.[14] TEM analysis showed the formed nanoparticles to be 2.5 ± 1.5 nm (Figures **S1/S2**), slightly bigger than the expected size of Au_{64}DENs.[23] The polydispersity and the observation of large nanoparticles in Figure **S1**, suggests the formation of DSNs as well as DENs. Following the strategy that we reported before,[22] we mixed the AuDENs with an anionic–neutral block copolymer, consisting of a 64-subunit polymethacrylic acid and a 885-subunit polyethyleneoxide block, $pMAA_{64}pEO_{885}$. Coacervation of the cationic dendrimer with the anionic-neutral block copolymer resulted in the formation of a complex coacervate core micelle, as indicated by Dynamic Light Scattering, DLS. Charge-stoichiometry was found at a ~1:1 combination of positive charge to negative charge (Figure **S3**), and the CMC of the formed dendrimicelles was determined to be ~2 $mg.L^{-1}$ (Figure **S4**). Cryo-Transmission Electron Microscopy, cryoTEM, confirmed that the structures observed with DLS are indeed well-defined dendrimicelles (Figure **5-2** & **S5-6**), and revealed the dendrimicelle core diameter, as indicated by the gold nanoparticles, to be 26 ± 6 nm (Figure **5-2c**). The dendrimicelle diameter, as determined by measuring core-core distances, is 45 ± 5 nm (Figure **5-2d**), in good agreement with the size as determined by DLS (Figure **S5**). The inset in the cryoTEM image in Figure **5-2**, however, illustrates that next to the many ~1-2 nm-sized nanoparticles, also a 6 nm gold particle is encapsulated in the dendrimicelle core. Since the diameter of a fifth-generation PAMAM dendrimer is about 5 nm, such a 6 nm gold nanoparticle does not fit inside a single dendrimer, and therefore has to be considered a DSN rather than a DEN. Interestingly, the data discussed above infer that both DSNs and DENs can be encapsulated inside dendrimicelles. DSNs consist of a gold nanoparticle with multiple dendrimers passivating the surface, but still a great part of the dendrimer, including its charged groups, is exposed to the solution and are available for charge interactions to allow C3M formation. The unknown number of dendrimers surrounding a DSN, as well as the large number of AuDENs inside every dendrimicelle hinder quantification of the micelle aggregation numbers by simply counting the number of nanoparticles per dendrimicelle. Counting of the number of nanoparticles per dendrimicelles indicated ~27 ± 11 nanoparticles per dendrimicelle (Figure **S7**).

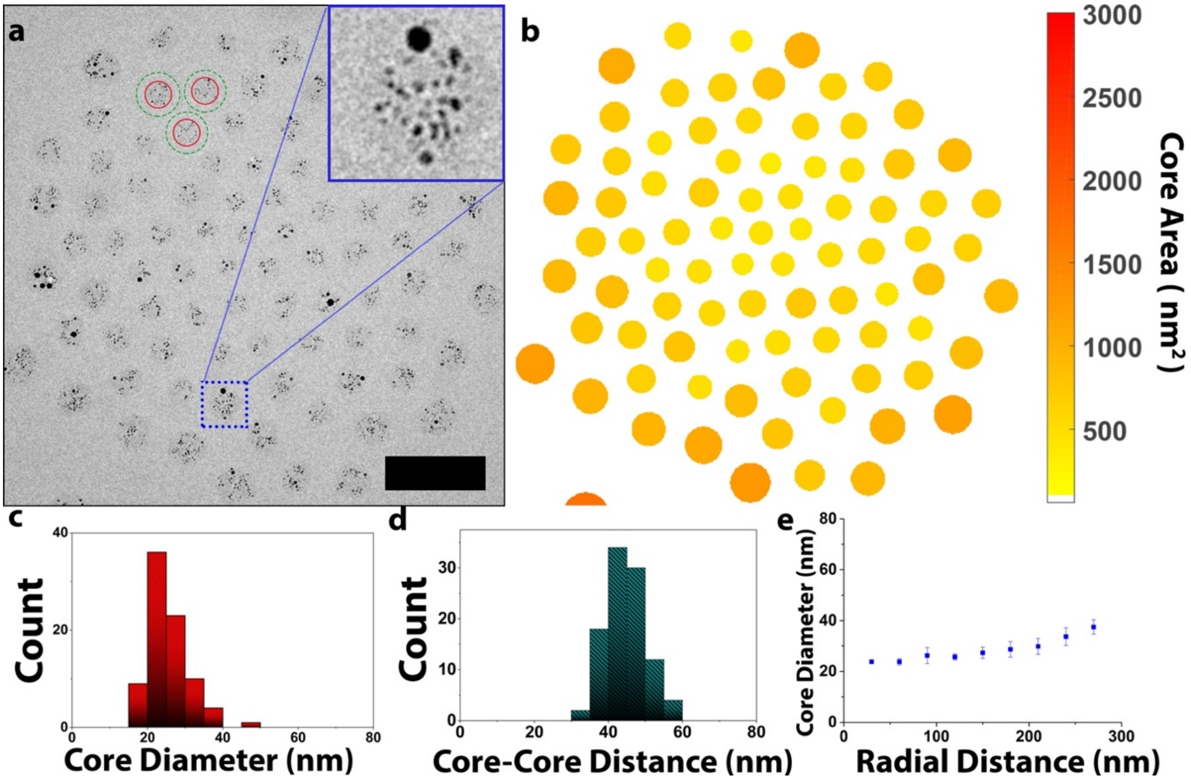

Figure 5-2. PAMAM generation 5-based dendrimicelles made at charge-stoichiometry. **a)** cryoTEM micrograph of the dendrimicelle superstructure, with the (40 x 40 nm) inset showing a single dendrimicelle; here, the core clearly reveals smaller gold particles (DENs) as well as ~6 nanometer big particles (DSNs) The red, solid circles in this figure indicate the dendrimicelle core, as identified by the embedded nanoparticles. The green, dotted circle indicates the total dendrimicelle size, as determined from DLS. The scale bar is 100 nm. **b)** Heat map plot of dendrimicelle superstructure, with the individual dendrimicelles color-coded according to the core area as determined from the cryoTEM micrograph in **a**. **c)** The average dendrimicelle core diameter, as determined from the cryoTEM micrograph, is 26 ± 6 nm. d) The average dendrimicelle diameter, as determined from measuring dendrimicelle core-core distances is 45 ± 5 nm. **e)** Plotting the micelle core area versus the radial distance to the center of the dendrimicelle superstructure shows a slight size-sorting of the dendrimicelles over the superstructure.

Assuming AuNPs >3.5 nm to be DSNs indicated that about 16% of the AuNPs observed in Figure **S1/S2** are DSNs, from which the average nanoparticle size inside a DSN was deduced to be ~5 nm, suggesting that ~11 dendrimers surround a DSN. Correcting the observed number of nanoparticles per dendrimicelle (e.g., both DENs and DSNs) for the number of dendrimers surrounding a DSN suggests an average of 70 dendrimers per dendrimicelle. Assuming that 50% of the dendrimer terminal amines of a DSN is available for coacervating, and the 1:1 association of (available) positive and negative charges, the average micelle molecular weight can be guestimated to be ~7 MDa (See Supporting Info for calculations).

Analysis of the formed dendrimicelles superstructure using image segmentation, and color-coding of the determined dendrimicelle core area suggests a slight size-sorting present in the dendrimicelle superstructure (See Figure **5-2b**). We quantified the size sorting by plotting the average dendrimicelle core diameter versus the radial distance to the center of the dendrimicelle superstructure, as shown in Figure **5-2e**. This figure indicates that dendrimicelles located at a radial distance of ~60 nm from the center have an average core diameter of ~24 nm, whereas the dendrimicelles located at a radial distance of ~240 nm have a core diameter of ~34 nm, endorsing the size-sorting of dendrimicelles inside the biconcave-shaped ice layer.

By forming generation five-based dendrimicelles using an excess of one of the building blocks, we attempted to increase the polydispersity. Initially, we prepared a dendrimicelle sample at a charge fraction f=0.6 (i.e. 40% less block copolymer than needed to achieve charge-stoichiometry). At this mixing fraction, however, the scattered light intensity is considerably lower, indicating that despite some dendrimicelles form (Figure **S3/8**), they are likely ill-defined. Indeed, Figure **S9** depicts a representative cryoTEM micrograph of this sample, corroborating that the structures observed with DLS are ill-defined and non-spherical. Next, we prepared a generation five-based sample using excess block copolymer to dendrimer (i.e., at charge fraction f=1.5). Analysis of this sample using DLS indicated that dendrimicelles with a hydrodynamic diameter of ~50 nm formed (Figure **S10**). CryoTEM micrographs of these dendrimicelles (Figure **5-3** and **S11**) show that the polydispersity of the sample increased with respect to the charge-stoichiometrically prepared sample. The average dendrimicelle core diameter, as determined from the cryoTEM images, was 36 ± 18 nm for the f=1.5 sample, compared to 26 ± 6 nm for the f=1 sample, demonstrating that both the average size, as well as the standard deviation are increased in the f=1.5 sample.

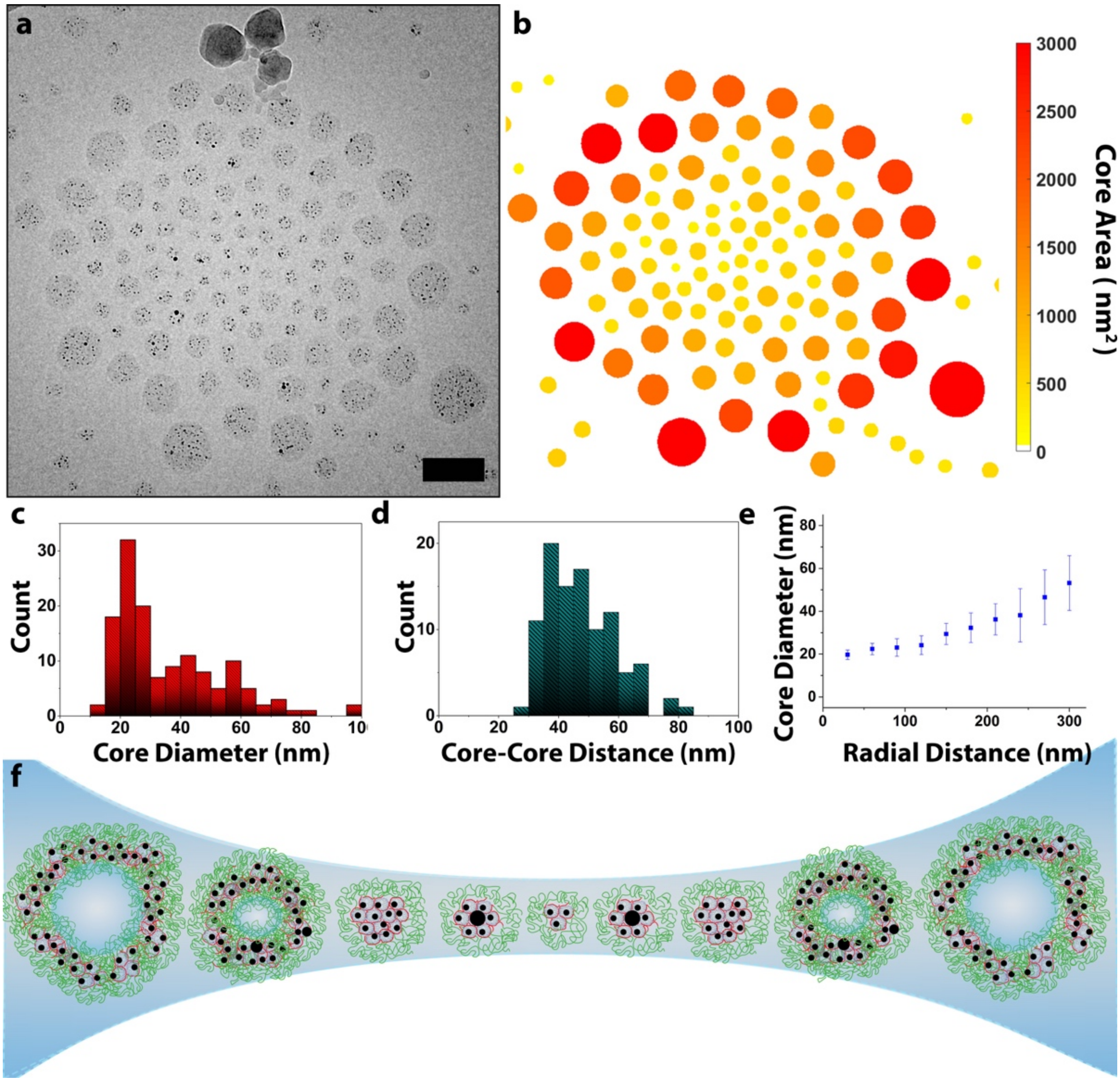

Figure **5-3**. Extreme size-sorting of dendrimicelles made under off-stoichiometric conditions. a) CryoTEM micrograph of the formed dendrimicelle superstructure. b) Heat map plot of dendrimicelle superstructure, with the individual dendrimicelles color-coded according to the core area as determined from the cryoTEM micrograph in a, emphasizing the size-sorting present. c) The average micelle core diameter is 36 ± 18 nm. d) The average micelle size, as determined from the micelle core-core distances is 48 ± 12 nm. e) Plotting the micelle core area versus the radial distance to the center of the dendrimicelle superstructure confirms the size-sorting of the dendrimicelles. f) Schematic illustration of the amplified thin film-templated size sorting. Scale bar is 100 nm.

Analysis of the cryoTEM micrographs showed the largest nano-assemblies in Figure **5-3** have a “core” diameter of ~90 nm. As the methacrylic acid block of the block copolymer we use here, $pMAA_{64}pEO_{885}$, has a contour length of well under 20 nm,[24] and the “core” radius is about 50 nm, the charged block of the block copolymer is not long enough to fill and form the core of such a size complex coacervate core micelle. Furthermore, the core size distribution plot, as shown in Figure **5-3c**, indicates there are multiple populations present. This supports our claim that the in Figure **5-3** observed nanostructures with a ‘core’ >40 nm are some other form of nano-assembly rather than dendrimicelles. The presence of a second type of nano-assemblies besides dendrimicelles would also explain the two populations that appear to be present in Figure **5-3c**. Therefore, these large structures observed are likely not dendrimicelles, but rather vesicles, as shown in Figure **1**.[25]

The cryoTEM micrograph (Figure **5-3a**) shows that the increased polydispersity in this sample translated into more distinctive size-sorting in the dendrimicelle superstructures. This effect is visually emphasized when dendrimicelle core-size based color-coding is applied (See Figure **5-3b**). We quantified the size sorting by plotting the average core diameters versus the radial distance to the center of the superstructure (Figure **5-3e**). Interestingly, the slope of the radial distribution plot also suggests the presence of two separate nanoaggregate populations. Dendrimicelles in the center of the superstructure have a core diameter of about 20 nm, whereas the nano-assemblies residing at the edge of the superstructure reach ‘core’ diameters up to ~100 nm. In this plot, a doubling of the core diameter occurs over a radial distance of ~250 nm, demonstrating that here the increased polydispersity leads to amplified size-sorting in the formed superstructures.

5.4 Conclusion

We demonstrate here how gold nanoparticles, synthesized inside fifth-generation PAMAM dendrimers, form DENs as well as DSNs, which both are embedded inside well-defined dendrimicelles upon charge-stoichiometric mixing with an oppositely-charged block copolymer. We show that ill-defined nanostructures form in the case of excess dendrimer to block copolymer, whereas excess block copolymer to dendrimer provides more explicitly defined nanostructures with an increased polydispersity. This increased polydispersity translates into an amplified size sorting inside formed superstructures. The combination of cryoTEM with the nanoparticle-loaded dendrimicelles is a powerful tool to investigate the formed structures in great detail. We here showed that besides well-defined dendrimicelles, also nanostructures were observed that are too large to be dendrimicelles, and contained fewer nanoparticles than expected for dendrimicelles, were observed. This observation strongly suggests that these structures are not complex coacervate core micelles, but likely vesicles. The incorporation of both DENs and DSNs inside the complex coacervate core dendrimicelles is, for example, of interest for catalytic applications, as the catalytic activity of nanoparticles is dependent on, among others, the nanoparticle size.[26,27] Both the catalytic activity inside dendrimicelles as well as the formed vesicles are currently investigated.

5.5 References

1. Mai, Y. Y.; Eisenberg, A. Self-Assembly of Block Copolymers. *Chemical Society Reviews* **2012**, 41, 5969-5985.
2. Whitesides, G. M.; Grzybowski, B. Self-Assembly at All Scales. *Science* **2002**, 295, 2418-2421.
3. Rosen, B. M.; Wilson, C. J.; Wilson, D. A.; Peterca, M.; Imam, M. R.; Percec, V. Dendron-Mediated Self-Assembly, Disassembly, and Self-Organization of Complex Systems. *Chemical Reviews* **2009**, 109, 6275-6540.
4. Li, J. R.; Kuppler, R. J.; Zhou, H. C. Selective Gas Adsorption and Separation in Metal-Organic Frameworks. *Chemical Society Reviews* **2009**, 38, 1477-1504.
5. Andersen, E. S.; Dong, M.; Nielsen, M. M.; Jahn, K.; Subramani, R.; Mamdouh, W.; Golas, M. M.; Sander, B.; Stark, H.; Oliveira, C. L. P.*; et al.* Self-Assembly of a Nanoscale DNA Box with a Controllable Lid. *Nature* **2009**, 459, 73-76.
6. Corbellini, F.; Knegtel, R. M. A.; Grootenhuis, P. D. J.; Crego-Calama, M.; Reinhoudt, D. N. Water-Soluble Molecular Capsules: Self-Assembly and Binding Properties. *Chemistry-a European Journal* **2005**, 11, 298-307.
7. Broz, P.; Driamov, S.; Ziegler, J.; Ben-Haim, N.; Marsch, S.; Meier, W.; Hunziker, P. Toward Intelligent Nanosize Bioreactors: A Ph-Switchable, Channel-Equipped, Functional Polymer Nanocontainer. *Nano Letters* **2006**, 6, 2349-2353.
8. Savić, R.; Luo, L.; Eisenberg, A.; Maysinger, D. Micellar Nanocontainers Distribute to Defined Cytoplasmic Organelles. *Science* **2003**, 300, 615-618.
9. Voets, I. K.; de Keizer, A.; Cohen Stuart, M. A. Complex Coacervate Core Micelles. *Advances in colloid and interface science* **2009**, 147-148, 300-18.
10. Hernandez-Garcia, A.; Velders, A. H.; Stuart, M. A. C.; de Vries, R.; van Lent, J. W. M.; Wang, J. Y. Supramolecular Virus-Like Nanorods by Coassembly of a Triblock Polypeptide and Reversible Coordination Polymers. *Chemistry-a European Journal* **2017**, 23, 239-243.
11. Wang, J. Y.; Groeneveld, A.; Oikonomou, M.; Prusova, A.; Van As, H.; van Lent, J. W. M.; Velders, A. H. Revealing and Tuning the Core, Structure, Properties and Function of Polymer Micelles with Lanthanide-Coordination Complexes. *Soft Matter* **2016**, 12, 99-105.
12. Wang, J. Y.; Velders, A. H.; Gianolio, E.; Aime, S.; Vergeldt, F. J.; Van As, H.; Yan, Y.; Drechsler, M.; de Keizer, A.; Stuart, M. A. C.*; et al.* Controlled Mixing of Lanthanide(Iii) Ions in Coacervate Core Micelles. *Chemical Communications* **2013**, 49, 3736-3738.
13. Wang, J.; Voets, I. K.; Fokkink, R.; van der Gucht, J.; Velders, A. H. Controlling the Number of Dendrimers in Dendrimicelle Nanoconjugates from 1 to More Than 100. *Soft Matter* **2014**, 10, 7337-7345.
14. Gröhn, F.; Bauer, B. J.; Akpalu, Y. A.; Jackson, C. L.; Amis, E. J. Dendrimer Templates for the Formation of Gold Nanoclusters. *Macromolecules* **2000**, 33, 6042-6050.
15. Tomalia, D. A. Birth of a New Macromolecular Architecture: Dendrimers as Quantized Building Blocks for Nanoscale Synthetic Polymer Chemistry. *Progress in Polymer Science* **2005**, 30, 294-324.
16. Tomalia, D. A.; Naylor, A. M.; Goddard, W. A. Starburst Dendrimers - Molecular-Level Control of Size, Shape, Surface-Chemistry, Topology, and Flexibility from Atoms to Macroscopic Matter. *Angewandte Chemie-International Edition in English* **1990**, 29, 138-175.
17. D'Emanuele, A.; Attwood, D. Dendrimer-Drug Interactions. *Advanced Drug Delivery Reviews* **2005**, 57, 2147-2162.

18. Kojima, C.; Kono, K.; Maruyama, K.; Takagishi, T. Synthesis of Polyamidoamine Dendrimers Having Poly(Ethylene Glycol) Grafts and Their Ability to Encapsulate Anticancer Drugs. *Bioconjugate Chemistry* **2000**, 11, 910-917.

19. Scott, R. W. J.; Wilson, O. M.; Crooks, R. M. Synthesis, Characterization, and Applications of Dendrimer-Encapsulated Nanoparticles. *The Journal of Physical Chemistry B* **2005**, 109, 692-704.

20. Gomez, V. M.; Guerra, J.; Velders, A. H.; Crooks, R. M. Nmr Characterization of Fourth-Generation Pamam Dendrimers in the Presence and Absence of Palladium Dendrimer-Encapsulated Nanoparticles. *Journal of the American Chemical Society* **2009**, 131, 341-350.

21. ten Hove, J. B.; Wang, J.; van Oosterom, M. N.; van Leeuwen, F. W. B.; Velders, A. H. Size-Sorting and Pattern Formation of Nanoparticle-Loaded Micellar Superstructures in Biconcave Thin Films. *ACS Nano* **2017**, 11, 11225–11231.

22. ten Hove, J. B.; Wang, J.; van Leeuwen, F. W. B.; Velders, A. H. Dendrimer-Encapsulated Nanoparticle-Core Micelles as Modular Strategy for Particle-in-a-Box-in-a-Box Nanostructures. *Nanoscale* **2017**, 9, 18619-18623.

23. Mori, T.; Hegmann, T. Determining the Composition of Gold Nanoparticles: A Compilation of Shapes, Sizes, and Calculations Using Geometric Considerations. *Journal of Nanoparticle Research* **2016**, 18, 295.

24. Cranford, S. W.; Buehler, M. J. Variation of Weak Polyelectrolyte Persistence Length through an Electrostatic Contour Length. *Macromolecules* **2012**, 45, 8067-8082.

25. Holder, S. J.; Sommerdijk, N. A. J. M. New Micellar Morphologies from Amphiphilic Block Copolymers: Disks, Toroids and Bicontinuous Micelles. *Polymer Chemistry* **2011**, 2, 1018-1028.

26. Laoufi, I.; Saint-Lager, M. C.; Lazzari, R.; Jupille, J.; Robach, O.; Garaudée, S.; Cabailh, G.; Dolle, P.; Cruguel, H.; Bailly, A. Size and Catalytic Activity of Supported Gold Nanoparticles: An in Operando Study During Co Oxidation. *The Journal of Physical Chemistry C* **2011**, 115, 4673-4679.

27. Johnson, J. A.; Makis, J. J.; Marvin, K. A.; Rodenbusch, S. E.; Stevenson, K. J. Size-Dependent Hydrogenation of P-Nitrophenol with Pd Nanoparticles Synthesized with Poly(Amido)Amine Dendrimer Templates. *The Journal of Physical Chemistry C* **2013**, 117, 22644-22651.

5.6 Appendix

Guestimation of the dendrimicelle molecular weight: Since the dendrimicelles contain both dendrimer-encapsulated (DENs) and –stabilized nanoparticles (DSs), calculation of the average molecular weight is hindered. To calculate the average micelle molecular weight, the ratio between DSNs:DENs should be known. Based on Figure S1/S2, nanoparticles >3.5 nm are assumed to be DSNs. This indicates that 16% of the nanoparticles are DSNs, with an average DSN size of 5 nm. Assuming the dendrimer radius to be 2.5 nm and its packing area to be $\pi * r^2$, the DSNs to be spherical, with a surface area of $4\pi*(rDSN,avg+rPAMAM)^2$ and the packing density of dendrimers per DSN of 0.7, this infers an average of 11 dendrimers per DSN. cryoTEM indicated an average of 27 nanoparticles per dendrimicelle, of which 16% are DSN, and 84% are DENs. Correcting the number of counted nanoparticles by the number of dendrimers/DSN suggests the actual number of dendrimers per micelle to be ~70. Since dendrimers in DSNs only expose part of their terminal amines to the solution, we assume 50% the dendrimer terminal amines to play a role in the complex coacervate core of the micelle. The other 50% charge is assumed to be inaccessible by the block copolymer or to interact with the gold nanoparticle. Taking a 1:1 interaction of available dendrimer charger (of the DSNs and DENs) with the block copolymer suggests the presence of ~90 block copolymers per dendrimicelle. The average size of a gold particle per dendrimer is presumed to be Au_{64}. Finally, the micelle molecular weight is calculated from the molecular weight of the polymer (~45 kDa), the dendrimer (~30 kDa) and of the average gold nanoparticle (13 kDa), yielding an average dendrimicelle molecular weight of ~7 MDa.

Guestimation of dendrimicelle volume per dendrimer: The core diameter of PAMAM generation five-based dendrimicelles was determined to be ~26 nm (Figure 2c), corresponding to a core volume of ~$9*10^3$ nm^3. Division of the dendrimicelle core volume by the actual number of dendrimers per dendrimicelle suggests ~$1.3*10^2$ nm^3 per dendrimer present in the complex coacervate core. Note: This volume is not the volume that a single dendrimer occupies, but rather the sum of the contributions of (dendrimer + charged block copolymer + water). As the volume of a single fifth generation PAMAM dendrimer is ~$7*10^1$ nm^3, this indicates that about 50% of the dendrimicelle core consists of dendrimer.

Calculation of the number of dendrimers per vesicle: By assuming the thickness of the complex coacervate vesicle 'wall' to be 13 nm, and the diameter of the complex coacervate part of the vesicle to be 50 nm, this gives a vesicle core radius of 12 nm. The volume of the complex coacervate part of the vesicle is then given by $V = (\frac{4}{3}\pi r_{vesicle\ wall}{}^{3} - \frac{4}{3}\pi r_{vesicle\ core}{}^{3}$, corresponding to a volume of ~$6*10^4$ nm^3. Assuming the dendrimer volume in the complex coacervate part to be ~$1.3*10^2$ nm^3 —as determined in the section above—, this infers that complex coacervate vesicles should contain ~400 dendrimers / vesicle.

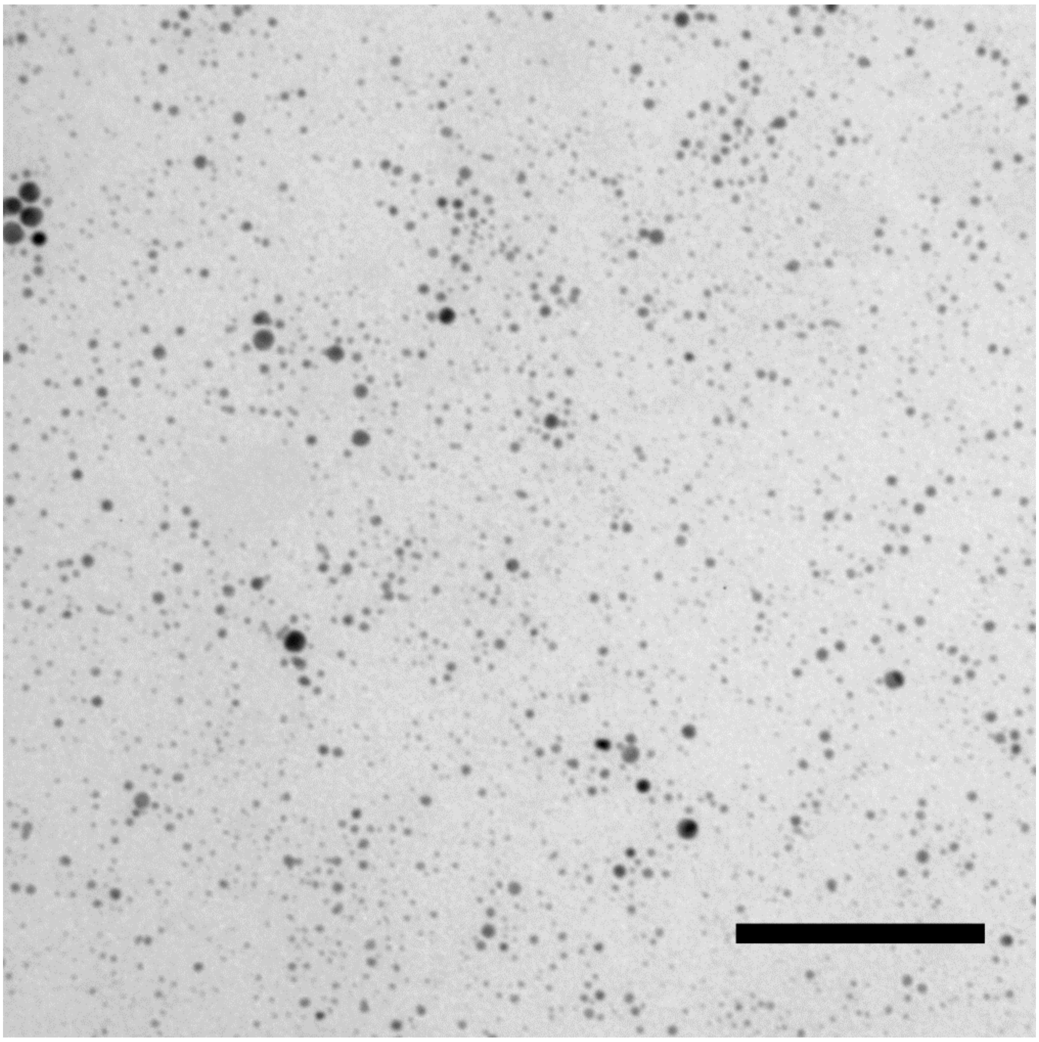

Figure S1. TEM micrograph of PAMAM G5-Au_{64} dendrimer-encapsulated nanoparticles. The many ~1 nm-sized nanoparticles are dendrimer-encapsulated nanoparticles, and the few large nanoparticles are likely dendrimer-stabilized nanoparticles (DSNs). The scale bar represents 100 nm.

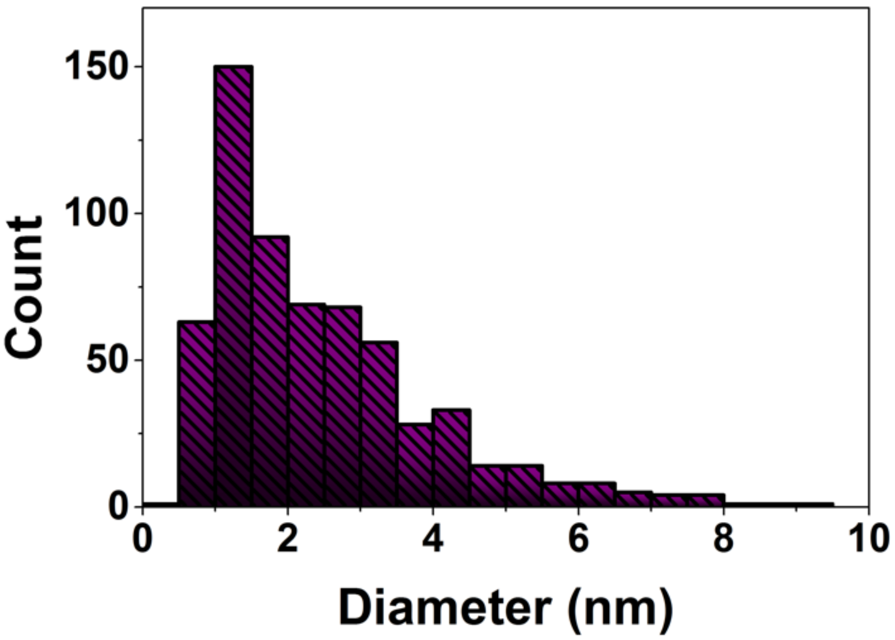

Figure S2. Histogram showing the mean diameter of the obtained G5-Au_{64} DENs as shown in Figure S1. The average diameter was determined to be 2.5 ± 1.5 nm, indicating the presence of both Au_{64} DENs as well as DSNs.

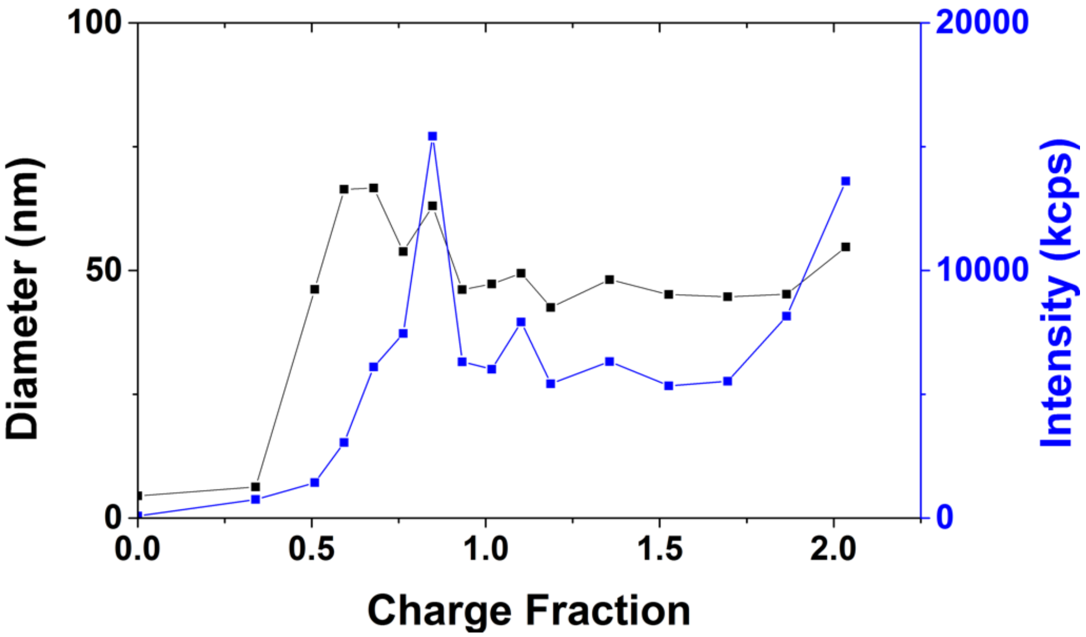

Figure S3. DLS charge titration graph of PAMAM G5-NH_2 with $pMAA_{64}PEO_{885}$, showing the number-averaged dendrimicelle diameter in blue and the normalized scattered light intensity in black against the charge fraction. The amount of positive charge (dendrimer-NH_2) was kept constant at 59 nmoles, and the amount of negative block polymer was varied, while keeping total volume constant. The charge fraction was calculated as the ratio of (NH2/COOH).

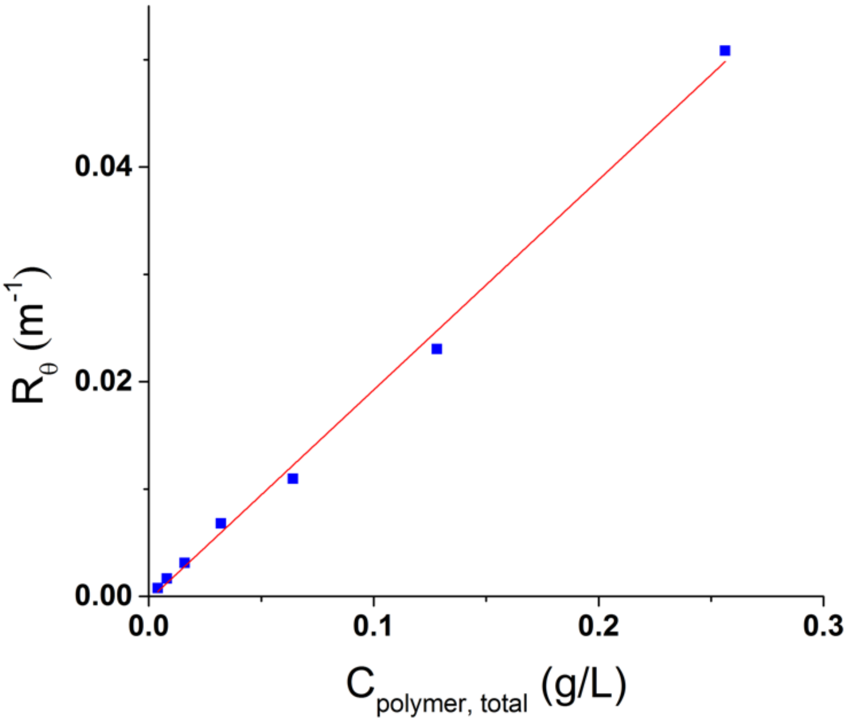

Figure S4. CMC determination of dendrimicelles made from fifth generation poly(amidoamine) dendrimers. The intensity (as the Rayleigh ratio) is plotted versus the total concentration of polymer (dendrimer + block copolymer). Fitting the data points with a linear fitting formula (R^2=0.996), and extrapolating to zero intensity gives a CMC of ~2 mg.L^{-1}.

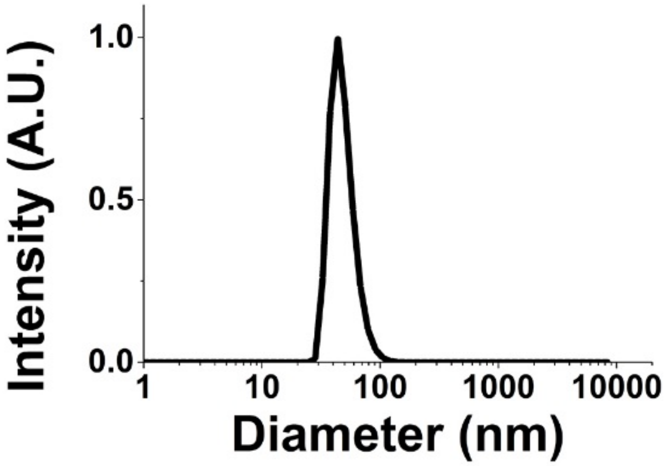

Figure S5. The number-weighed DLS size plot indicates an average micelle hydrodynamic diameter of 48 nm for dendrimicelles made at charge-stoichiometry (f=1).

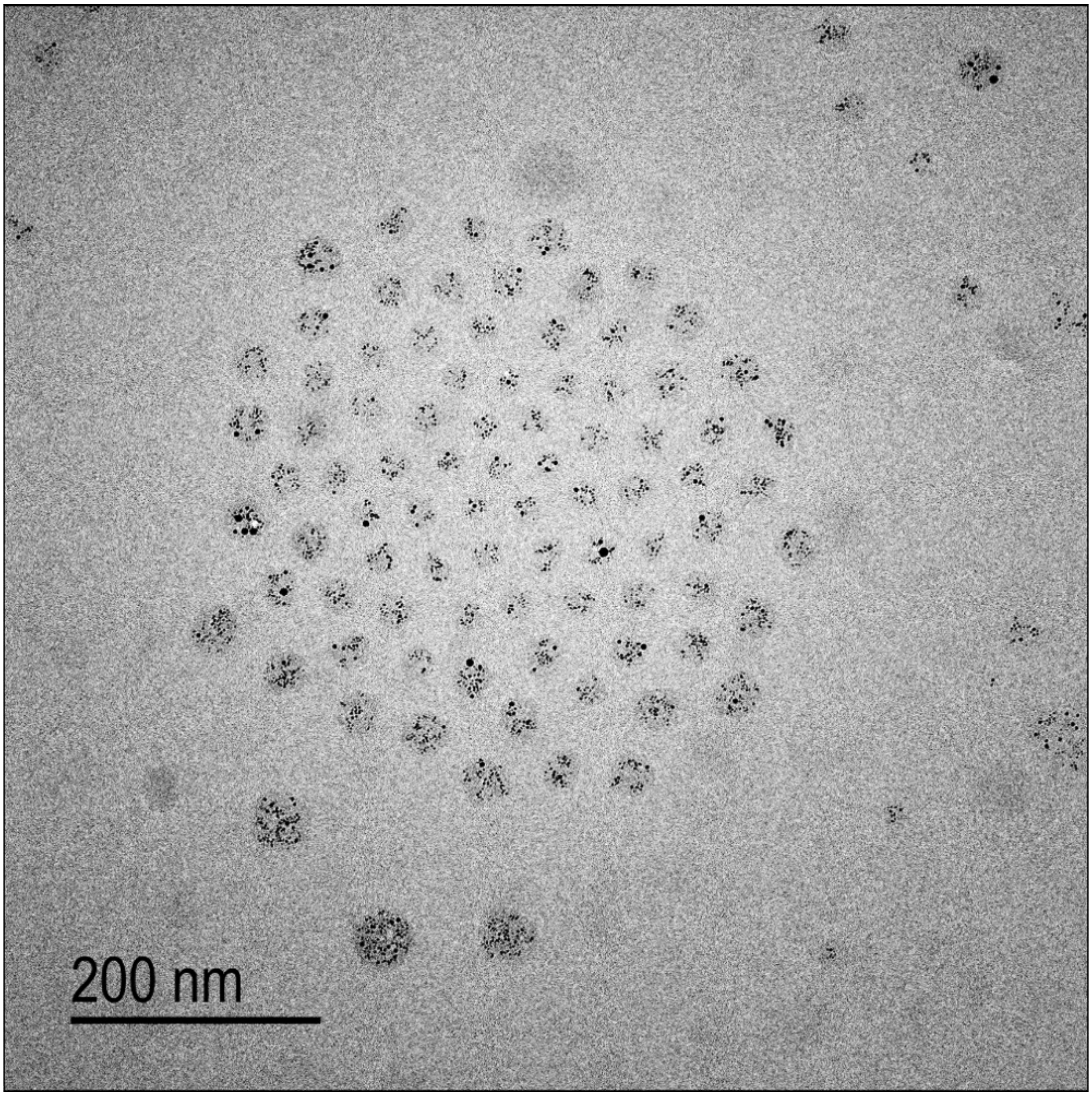

Figure S6. cryoTEM micrograph of PAMAM-G5 dendrimicelles prepared at charge-stoichiometry.

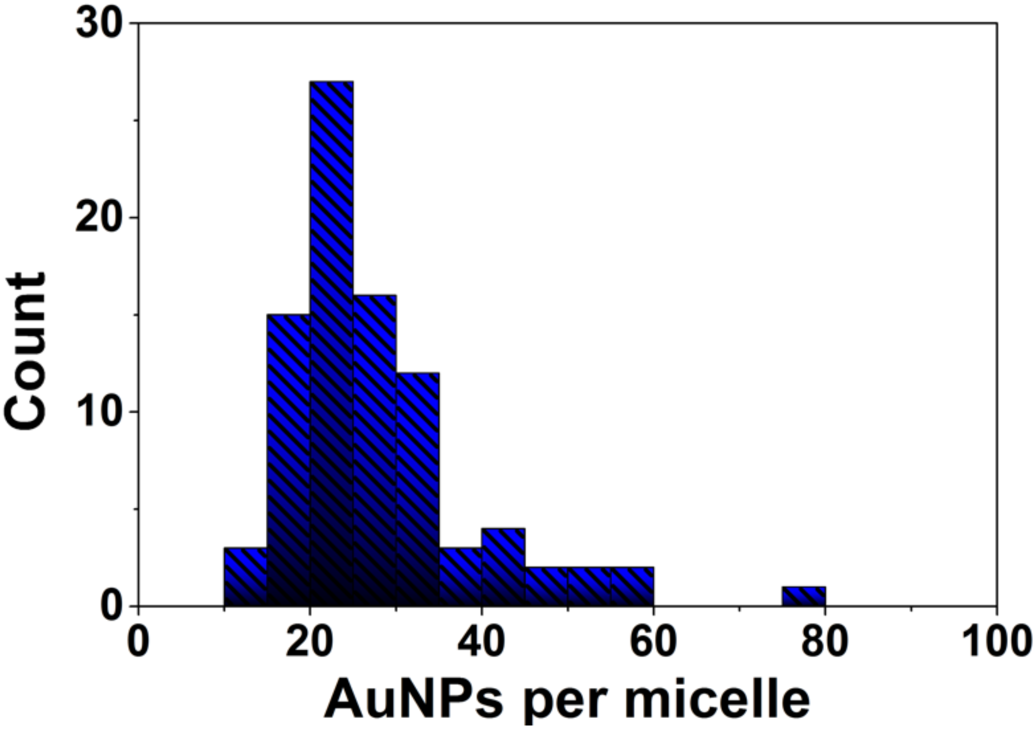

Figure S7. Size histogram showing the number of AuNPs per dendrimicelle for fifth-generation based dendrimicelles made at charge-stoichiometry. The average counted number of gold nanoparticles per dendrimicelles is 27 ± 11. We do note that here the large number of nanoparticles per micelle, together with the presence of DSNs among the DENs hindered the accurate determination of the dendrimicelle aggregation numbers.

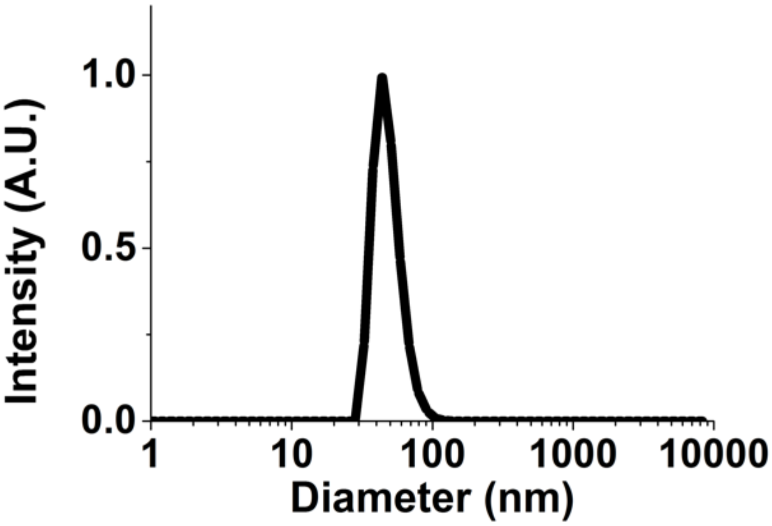

Figure S8. Number-weighed DLS characterization of generation five-based dendrimicelles made at off-stoichiometric mixing conditions (f=0.6). The average hydrodynamic size is 48 nm.

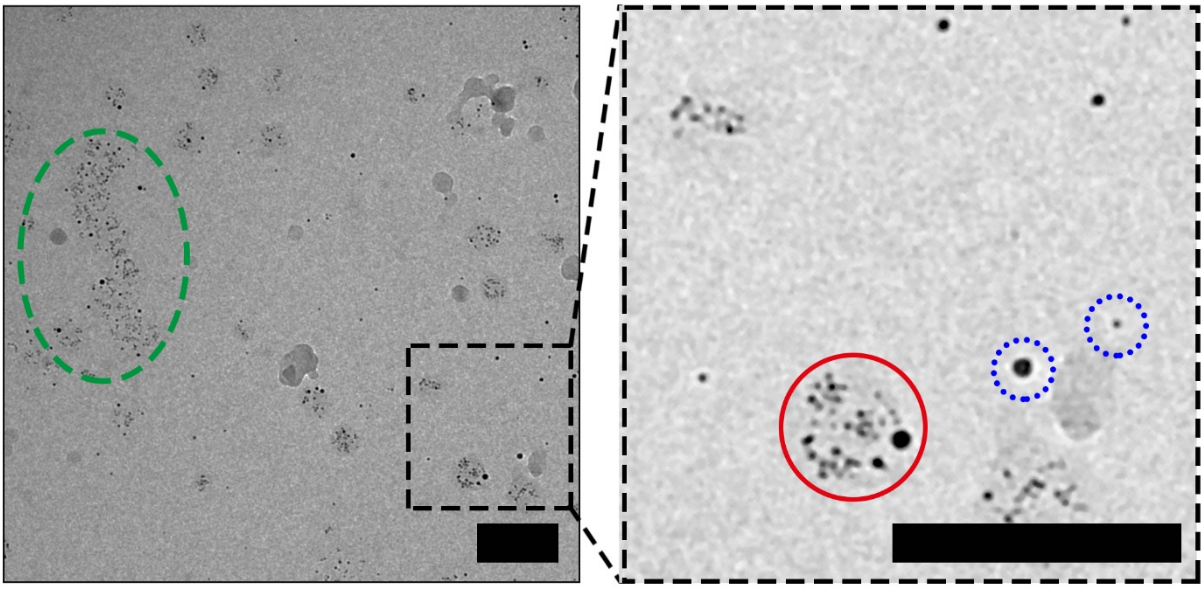

Figure S9. Representative cryoTEM micrograph of generation five-based dendrimicelles prepared at a charge mixing fraction f=0.6, corresponding to excess an excess of dendrimer to block copolymer. Clearly, the solution contains a mixture of large aggregates (dashed, green, oval), dendrimicelles (solid, red, circles) and individual nanoparticles (DENs and DSNs, indicated with the dotted, blue, circles). The scale bars represent 100 nm.

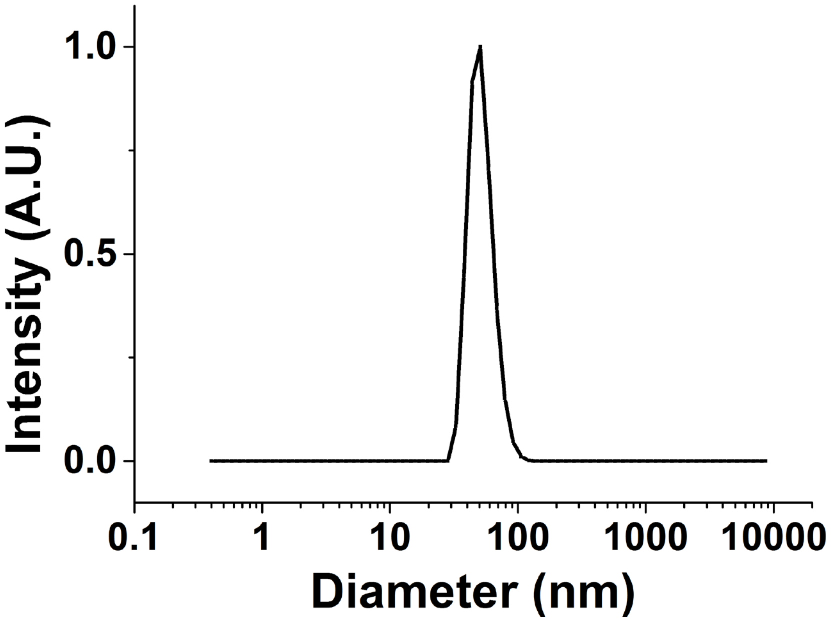

Figure S10. Number-weighed DLS characterization plots generation five-based dendrimicelles made under off-stoichiometric mixing conditions (f=1.5). The average hydrodynamic size is ~52 nm.

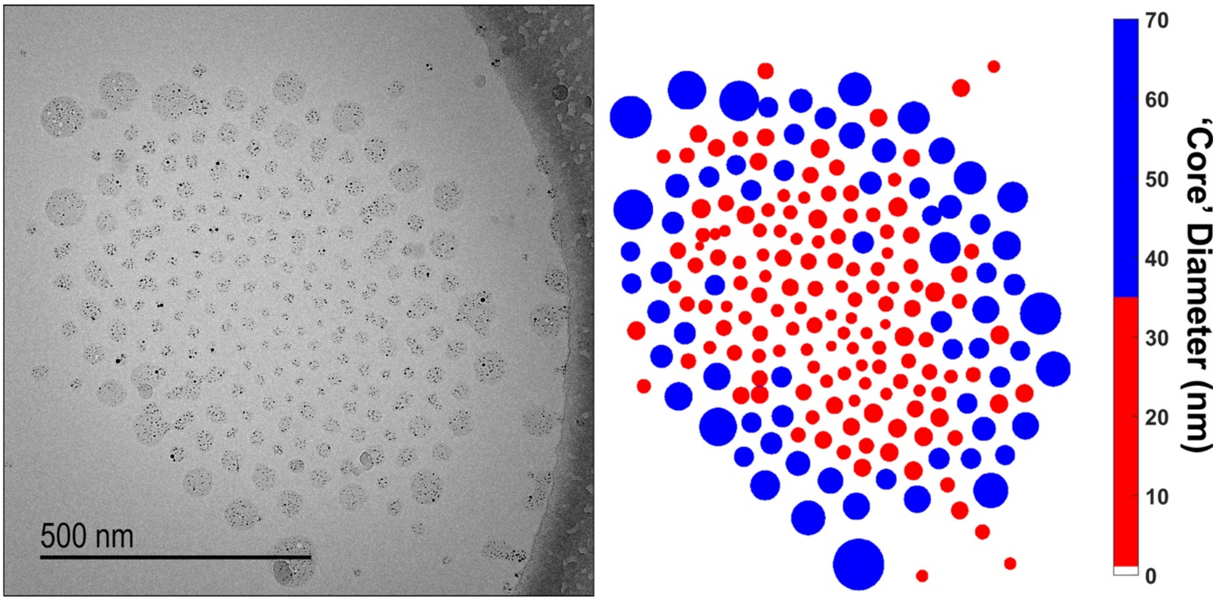

Figure S11. Left: cryoTEM micrograph of PAMAM-G5 dendrimicelles prepared using 1.5 times excess block copolymer. This off-stoichiometric amount results in a polydisperse dendrimicelle sample. Right: Color-coded heat map plot, showing the dendrimicelles with a core diameter (as indicated by the embedded gold nanoparticles) smaller than 35 nm in red, and the nanoaggregates with a ‘core’ diameter bigger than 35 nm in blue.

Chapter 6

General Discussion

This chapter provides a general discussion on the results from and implications of the different experimental chapters of this thesis. An outlook for follow-up as well as spin-off research topics, coming forth from the four different experimental chapters, is provided at the end of the sections, and the chapter finishes with concluding statements.

6.1 Gold Nanoparticles for the Investigation of Self-Assembled Nanostructures and Superstructures

For this thesis work, the initial motivation was to study the self-assembly of dendrimers into well-defined complex coacervate core dendrimicelles using light scattering techniques and cryo-Transmission Electron Microscopy (cryoTEM). To this end, the encapsulation of nanometer-sized gold nanoparticles was exploited. The contrast provided by the micelle-embedded nanoparticles allowed for obtaining detailed information on the micelle subcomponents at an unprecedented level. As emerging and concomitant benefit, the gold nanoparticles also allowed for unprecedented observation and investigation of mesoscale superstructures formed from the dendrimicelles.

In section **6.2**, two methods for determining micelle aggregation numbers are compared: The use of dendrimer-encapsulated nanoparticles in cryoTEM is compared to light scattering methods for determining micelle aggregation numbers. Several theories to explain deviations between the results obtained with cryoTEM and light scattering are explored. In section **6.3**, the formation of micelle superstructures, and the interactions that play a role therein are discussed. Potential future directions and applications of the superstructures, and the use of thin film templating are discussed. Section **6.4** discusses the effects of prolonged electron beam irradiation on dendrimicelle superstructures and reflects on several processes that are identified to play a role in the global and local migration of dendrimicelles under sustained electron beam irradiation. Several factors to consider are discussed and options worth investigated are discussed. Section **6.5** discusses the high modularity of the dendrimicelle concept, and addresses the co-assembly of dendrimer-encapsulated and –stabilized nanoparticles. Also, the use of cryoTEM to identify and analyze dendrimicelle (sub)composition is considered. Section **6.6** provides an outlook and reflects on the modular dendrimicelle system reported in this thesis. Suggestions for improving and extending dendrimicelle stability, for introducing different functionalities, and for extending the modular dendrimicelle toolbox are given. Implications and potential applications of both the dendrimicelles and the thin film-templated size-sorting are discussed and suggestions for future research are provided. This section ends with some concluding remarks. Finally, section **6.7** summarizes the main conclusions of this thesis work.

6.2 Dendrimicelle Aggregation Numbers

Micelle aggregation numbers can be determined from static light scattering experiments, for example by constructing a (partial) Zimm plot (See Chapter 2, Appendix).[1] Table 1 shows that the, with light scattering determined, micelle molecular weights for PAMAM generation five through nine-based dendrimicelles are on the order of ~10^5 g.mol^{-1}. By assuming the charge-stoichiometric combination of dendrimers and block copolymers in the micelle, the micelle molecular weights are converted to micelle aggregation numbers (**Table 6-1**). The light scattering data indicate that the dendrimer aggregation numbers decrease exponentially with increasing dendrimer generation. Interestingly, the results obtained here show the same trend that Wang *et al.* also observed with light scattering, namely an exponential decrease in dendrimer aggregation number with increased dendrimer generation used. However, the aggregation numbers —as we here determined with cryoTEM— do not match those observed with light scattering. For example, for generation 9-based dendrimicelles made at charge-stoichiometry (Chapter 03), cryoTEM showed an average of 18 nanoparticle per micelle, whereas light scattering data indicates that only 1-2 dendrimers and hence 1-2 nanoparticles should be present inside a dendrimicelle. Possible explanations for the difference in aggregation numbers derived from light scattering experiments and observed with cryoTEM could be, for example, due to the presence of multiple nanoparticles per dendrimer or due to deviations between the determined and actual charge stoichiometry.

Table ***6-1*** *Dendrimicelle molecular weight and derived number of dendrimers per dendrimicelle as determined using light scattering techniques and cryoTEM. *For generation 5 dendrimers, the coexisting of dendrimer-stabilized and –encapsulated nanoparticles hinder accurate determination of the dendrimer aggregation number per dendrimicelle using cryoTEM.*

PAMAM	Dendrimicelle Mw (Light Scattering)	PAMAM Mw (g.mol^{-1})	End Groups per PAMAM	Ratio dendrimer: $pMAA_{64}pEO_{885}$	Dendrimers per micelle	
					Light Scattering	cryoTEM
G5	7.2E+06	2.9E+04	128	2	61	~27 ± 11*
G6	4.7E+06	5.8E+04	256	4	20	30 ± 10
G7	4.8E+06	1.2E+05	512	8	10	23 ± 7
G8	4.6E+06	2.3E+05	1024	16	5	27 ± 7
G9	3.6E+06	4.7E+05	2048	32	2	18 ± 6

At first glance, the presence of multiple nanoparticles per dendrimicelle would be an explanation for the observed deviations in micelle aggregation numbers. However, the original work of Grohn *et al.* showed that only for PAMAM generation ten, multiple smaller nanoparticles instead of a single nanoparticle form per dendrimer.[2] For nanoparticles synthesized in dendrimer generations six through nine, we observed an increase in nanoparticle size with increasing dendrimer generation. All dendrimer-encapsulated nanoparticles used in this thesis were made at a fixed ratio of (Au^{3+}:dendrimer end groups). Therefore, if only one nanoparticle per dendrimer forms, the nanoparticle size should increase with increasing dendrimer generation. Indeed, (cryo-)TEM micrographs obtained from generation six through nine-based dendrimer-encapsulated nanoparticles showed an increase in average size with increasing generation. Moreover, cryoTEM micrographs of generation seven-based dendrimer-encapsulated nanoparticles did not indicate the presence of significant numbers of dendrimers containing multiple particles per dendrimer (based on the spacing in between individual nanoparticle). Therefore, it is not likely that the aggregation numbers, as observed in this thesis with cryoTEM, are skewed by the presence of multiple nanoparticles per dendrimer.

Another explanation for the deviations in dendrimicelle aggregation numbers in **Table 6-1** could be related to a difference between assumed and 'actual' charge of the micelle subcomponents. Both the dendrimer as well as the block copolymer are 'soft' polyelectrolytes that contain many charged groups, and therefore have a pKa that spans over a range.[3] Literature indicates the pKa of pMAA to be around pH ~6, corresponding to a deprotonation degree at pH 7 of about 90%.[4] A lower deprotonation degree of the pMAA block would imply that the ratio block copolymer:dendrimer in a micelle increases for forming a charge-neutral micelle. As the micelle size is mainly determined by the size of the neutral block copolymer, this should result in less nanoparticles per dendrimicelle and therefore does not satisfactorily explain the observed difference in aggregation numbers. Considering that the pKa of amine-terminated dendrimers is ~9, the protonation degree of the dendrimer terminal amines is expected to be around 99% at pH 7.[5] However, if only part of the dendrimer charge is available for interacting with the $pMAA_{64}pEO_{885}$ block copolymer, this would —given a constant micelle size and charge— infer that more dendrimers can be encapsulated per dendrimicelle.

Throughout this thesis, both cryoTEM and DLS showed that a 1:1 charge mixing ratio of block copolymer to dendrimer yields ~50 nm-sized dendrimicelles, irrespective of the dendrimer generation. Division of the micelle corona volume by the volume that a single PEO_{885} chain implies that about 100 block copolymers are present per 50 nm-sized dendrimicelle. Assuming full deprotonation of the block copolymer, this suggests that the amount of negative charge per dendrimicelle is $\sim 6*10^3$. Taking the average number of dendrimers per dendrimicelle as determined with cryoTEM (**Table 6-1**), and multiplying by the number dendrimer end groups yields a theoretical amount of positive charge in the core that ranges from $6*10^3$ for G6, to $4*10^4$ for generation 9. This strongly suggests that not all PAMAM end groups are charged, or participate in the coacervation with the block copolymer. Literature shows that higher generation PAMAM dendrimers are known to contain defects, like missing branches, presence of dimers and trimers, which could result in a lower actual charge per dendrimer than expected based on the number of theoretical end groups.[6,7] In addition, the dendrimer branches can 'back fold' into the dendrimer interior. However, this is mostly associated with the use of poor solvents (*e.g.* dichloromethane) or increased pH.[8-10] Lastly, the micelle-embedded gold nanoparticle could play an active role in interacting with the dendrimer branches, as amines are known to have an affinity for gold, effectively reducing the actual surface charge of a dendrimer, and resulting in the encapsulation of more dendrimers per dendrimicelle. Although charge screening is the most likely explanation for the deviations in micelle aggregation numbers as observed with light scattering and cryoTEM, it should be investigated further. It could be of interest to investigate the effect of partial charge screening by, for example, acetylation on the formation of dendrimicelles and on the corresponding aggregation numbers as found with cryoTEM. Alternatively, an investigation with cryoTEM and DLS on the dendrimicelle aggregation numbers in a range of charge mixing fractions, could elucidate the effect of the dendrimer-encapsulated nanoparticles on the 'actual' charge-stoichiometry. The dendrimicelle system reported by Wang *et al.*[1] used a carboxylic acid-terminated dendrimers and a block copolymer with a pH independent charge, yet still similar-sized dendrimicelles to those formed throughout this thesis were obtained. Unfortunately, dendrimer-encapsulated nanoparticles cannot be synthesized inside carboxyl-terminated dendrimers. This infers that the nanoparticle-embedding and counting strategy reported in this thesis cannot be extended to determine aggregation numbers in the dendrimicelles as reported by Wang *et al.* [1]

6.3 Size-Sorting and Pattern Formation

Superstructure analysis

In Chapter 3, the templated self-organization of dendrimicelles into mesoscale superstructures is discussed. The biconcave-shape of the thin water film, formed during cryoTEM sample preparation, was identified as the driving force for the self-organization and self-sorting of the dendrimicelles into the micrometer-sized ‘2D’-superstructures. The observation that some of the dendrimicelle superstructures did not contain any dendrimicelles in the center of the superstructure was attributed to a film thickness that was too thin for a single dendrimicelle to fit inside. Together with the absence of overlapping dendrimicelles in the observed superstructures, and the size-sorting profile that followed the thickness profile over the thin water film, this led to the hypothesis that the dendrimicelles inside these superstructures are “touching both interfaces” of the biconcave thin film. The above-mentioned observations, however, only provide indirect evidence for the hypothesis. Direct evidence for this claim might be obtained by, for example, energy-filtering TEM or cryo-electron tomography.[11] Whereas during conventional cryo-transmission the micrographs are acquired at a single sample tilt angle —yielding a projection of the 2D or 3D structures present—, with cryo-electron tomography the micrographs are acquired over a range of tilting angles, allowing the spatial reconstruction of the sample using software processing. As a result, tomography experiments should provide information on the superstructure thickness, shape, and on the distribution of the dendrimicelles inside the superstructures. Moreover, tomography experiments would also provide information about the complex coacervate core of the dendrimicelles, for example, it would show the nanoparticle distribution and density inside a single dendrimicelle core.

Although dendrimicelles obtained at charge-stoichiometric mixing of the building blocks are fairly monodisperse, we do not observe the formation of large hexagonally packed assemblies as commonly observed for nanoparticles with a low polydispersity. Likely, the size gradient induced by the biconcave layer hinders ‘crystallization’ into a closely-packed, hexagonally-ordered structure. Instead, a slightly offset structure is formed, leading to the observed spiral domains. In nature, spiral domains also appear in systems where a size gradient is present, for example, in sunflower seed heads, pineapples, pine cones, and in succulents. The effect of polydispersity on the packing of spheres subjected to a size-sorting gradient would be interesting to study using the modular dendrimicelle system used in this thesis. By tuning the polydispersity of the dendrimicelles carefully, new periodic or non-periodic micelle packings might be observed. The use of mathematical modelling would be of interest here, to predict the effect of a size-sorting gradient of the packing of polydisperse spheres inside a biconcave film. Lastly, the superstructures obtained are likely derived from a non-equilibrium situation as, shortly after blotting away excess sample, the formed thin films are rapidly frozen. Investigating a more controlled formation of superstructures, for example by sample equilibration after blotting, would be of interest to investigate.

Size-sorting as a novel self-assembly tool for mesoscale materials

The bottom-up synthesis of nanomaterials with a controlled and well-defined size in the micrometer scale is challenging. The biconcave-shaped thin film-induced self-organization and size-sorting of dendrimicelles into superstructures could be a versatile tool to design and obtain well-defined monolayer superstructures. Chapter 2 showed that the nanoparticle loading per dendrimicelle can be controlled by mixing ‘nanoparticle-filled’ dendrimers with ‘empty’ dendrimers, yielding ‘half-full’ dendrimicelles. Likewise, the density of nanoparticle-containing dendrimicelles per superstructure can be controlled by mixing ‘half-full’ dendrimicelles with ‘empty’ dendrimicelles. **Figure 6-1** illustrates this, and shows the cryoTEM micrograph of a superstructure obtained from an equivolumetric mix of ‘half-full’ and ‘empty’ PAMAM generation six-based dendrimicelles. Analysis of this figure shows that in the formed superstructure, about 40% of the dendrimicelles contain at least one nanoparticle, with the remaining 60% containing no nanoparticles at all. This example illustrates that— as expected— the number of nanoparticle-containing dendrimicelles per superstructure can be controlled by changing the ratio of ‘empty’ and ‘nanoparticle-containing’ dendrimicelles. Interestingly, although this dendrimicelle superstructure was made from a 1:1 mix of ‘empty’ and ‘nanoparticle-filled’ dendrimicelles, the number of nanoparticle-containing dendrimicelles is slightly lower than 50%. Additionally, by eye, it also appears that the superstructure formation resulted in the separation of the dendrimicelles based on their content. It appears that the ‘empty’ dendrimicelles are located more often toward the center of the superstructure, whereas the nanoparticle-filled dendrimicelles are located more often toward the edge of the superstructure. Possibly, a difference in size between the two dendrimicelle populations, combined with the induced size sorting, is responsible for this. The thin-film induced size-sorting might find applications to obtain, for example, “core-shell”-type superstructures where the dendrimicelles in the center contain one payload, and those at the superstructure edge contain another.

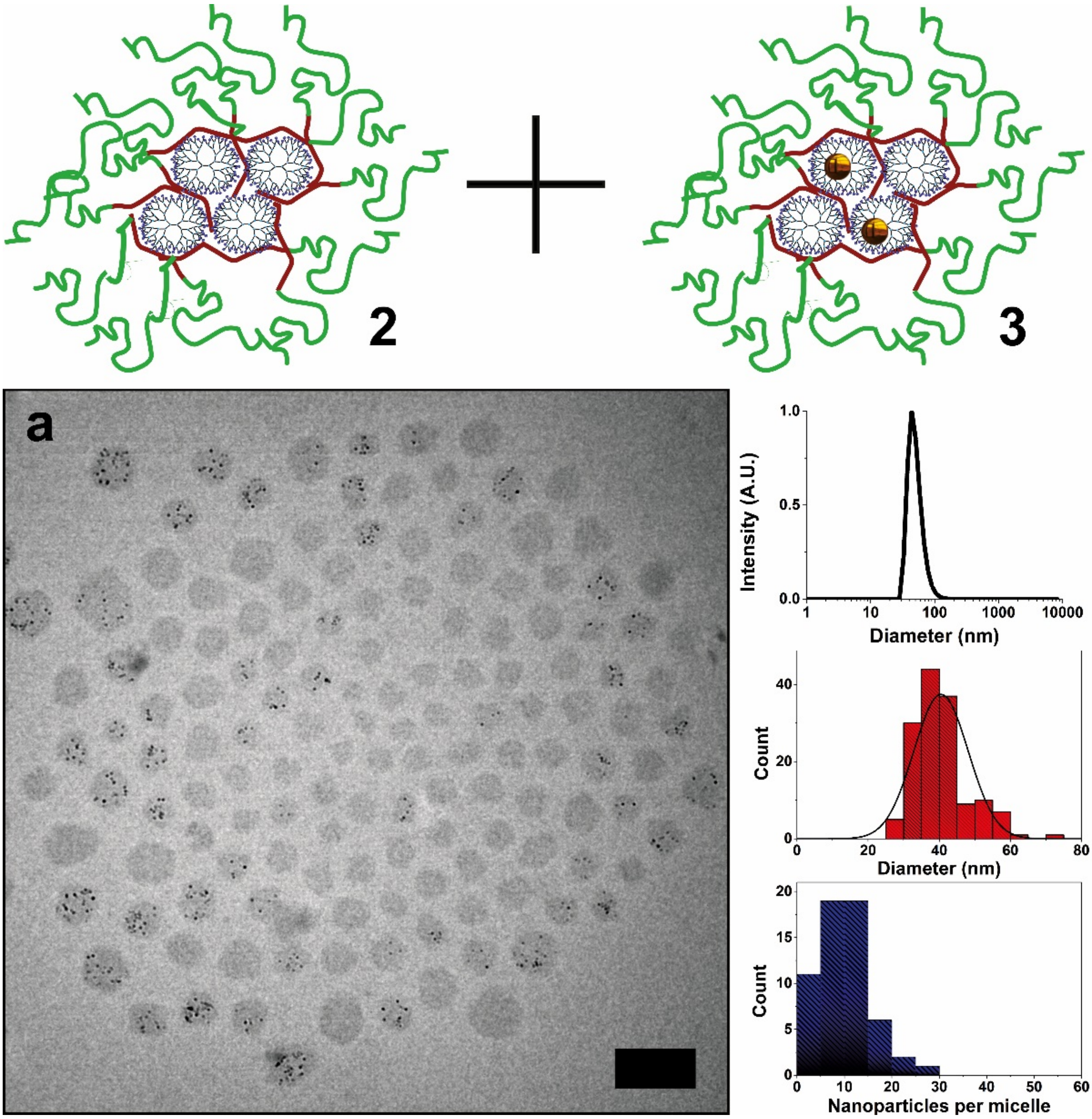

*Figure **6-1** **a**: Schematic overview of the mixed dendrimicelles: ‘empty’ (**I**) and ‘half-full’ (**II**) dendrimicelles. **b**: CryoTEM micrograph of a dendrimicelle superstructure containing ‘empty’ and ‘half-full’ dendrimicelles made from sixth-generation PAMAM dendrimers and dendrimer-encapsulated nanoparticles. Analysis of this superstructure shows that 40% of the dendrimicelles contain nanoparticles, and 60% contain no nanoparticles at all. DLS indicates that the hydrodynamic diameter is 51 nm (**c**), cryoTEM shows that the average core diameter is 40 ± 8 nm (**d**) and that the average number of nanoparticle per dendrimer is 10 ± 5 (**e**), slightly lower than the expected number for ‘half-full’ sixth generation-based dendrimicelles.*

Size-sorting as separation tool

Analysis of the cryoTEM micrographs of dendrimicelle superstructures in Chapter 5 pointed to the co-formation of vesicles among the dendrimicelles when using off-stoichiometric ratios of block copolymer to PAMAM generation five dendrimers. Under the influence of the biconcave thin film template, both populations size-sorted inside the formed superstructure. As the dendrimicelles were significantly smaller than the vesicles, the center of the superstructure contained only dendrimicelles, and the vesicles were located toward the edges of the superstructure. Separating these large aggregates from the well-defined dendrimicelles would be required to study both types of particles in more detail. Potentially, the size-sorting induced by biconcave thin films could be developed as a separation technique to separate the bilayer vesicles from the dendrimicelles, or even to decrease the polydispersity of a dendrimicelle sample. As the size of the formed superstructures is ~1 μm, this might be a challenging path to pursue. The well-defined and regularly-spaced QUANTIFOIL grids that were mostly used throughout this thesis can be obtained in a range of hole sizes. Using cryoTEM grids with larger grid holes, and higher dendrimicelle concentrations could help here.

6.4 Studying Thin Film and Superstructure Dynamics at the Nanoscale

In chapter 4, the processes leading to the rupture of dendrimicelle superstructures, exposed to prolonged electron beam irradiation, are investigated. Sustained exposure results in controlled thinning of the biconcave thin film, and a shrinkage of the dendrimicelle core —as indicated by the embedded gold nanoparticles— is observed. Upon further irradiation, a sudden rupture of the superstructure takes place, similar to the rupture of a soap bubble. The thin films formed during cryoTEM sample preparation are similar to soap bubbles in thickness, which ranges between a few nanometers and a few hundred nanometers.[12] The analogy between a soap bubble and the thin films extends further: Like soap films, thin films prepared with cryoTEM often have surfactants at their interfaces, too, and can therefore be considered flat soap films.[13,14] For soap bubbles, the mechanism of rupture has been attributed to first a thinning of the film through capillary interactions, followed by a stochastically-determined rupture of the bubble.[15] Thin films prepared during cryoTEM are also subjected to thinning by capillary draining, however, rapid freezing of the sample by immersion in liquid ethane 'captures' the film before it ruptures. Consequently, the formed films vary in thickness, depending on the local conditions on the sample grid during sample preparation.

To study the electron beam-induced thin film rupture in detail, checking and controlling the quality of the thin film is important. The thickness of the thin film can be estimated from an image intensity profile plot over the cryoTEM grid hole. In the absence of dendrimicelles, the water film is biconcave-shaped and the intensity/thickness profile over the film resembles a parabola, as shown in Figure **1-5**. The presence of a 'monolayer-' dendrimicelle superstructure results in a flattening of the intensity profile in the area where the dendrimicelles are located, as shown in Figures **4-2a** and **4-S6**. The image intensity profiles over the cryoTEM grid holes therefore give a good impression of the thickness and quality of the thin water film. Interestingly, these observations also point to a reciprocal interaction between the dendrimicelles and the biconcave thin film: The biconcave film induces the size-sorting of the dendrimicelles, but at the same time, the dendrimicelles also reshape the (local) shape of the biconcave film.

During the prolonged electron beam irradiation, both a global migration of the dendrimicelles proceeding outward, as well as a local migration of the nanoparticles inside the dendrimicelle was observed. The migration of dendrimicelles embedded in a water film at ~100 K is rather unexpected, and suggests that the thin film formed are likely not a solid, but rather highly viscous and liquid-like. Recording the rupture with a higher time-domain resolution, for example, using an electron microscope with a direct electron detector, would allow investigation of the processes that take place before and during rupture in even more detail. The effect of the superstructure composition and thickness would be interesting to study as superstructures that were embedded in a thick vitreous ice layer, for example, were observed to ‘tear’, rather than ‘rupture’. In addition, the influence of nanoparticle density in the dendrimicelles, and the density of the nanoparticle-loaded dendrimicelles on the superstructure rupture propagation would be particularly interesting to investigate. Compared to the organic dendrimicelle core and corona, the gold nanoparticles have a significantly higher density, resulting in the absorption and scattering of more electrons. As such, the micelle-embedded nanoparticles might not only serve as ‘tracer’, but also have an active role in the induction of the superstructure rupture. The nanoparticles could, for example, affect the local temperature inside the superstructure. Lastly, studying the effect of electron beam irradiation flux, and the effect of the average electron flux per unit time, on the thin film rupture could provide information on whether the rupture is induced pure by evaporation of water, stressing the sample, or that a local increase in temperature plays a role as well.

6.5 Subcomponent Analysis from the Nano- to the Mesoscale using CryoTEM

Dendrimicelle modularity

The dendrimicelle strategy used in this thesis is highly modular. Not only the dendrimer generation used for dendrimicelle formation can be changed, also the nanoparticle-loading per dendrimicelle can be controlled, by simply mixing ‘nanoparticle-loaded’ dendrimers with ‘empty’ dendrimers (Chapter 2). Similarly, the type of dendrimer-encapsulated nanoparticle can be changed from a gold- to a palladium nanoparticle. Figure **6-2** below shows cryoTEM micrographs obtained from dendrimicelles made from Pd_{256}DENs (left), dendrimicelles made from a 1:1 mix of Pd_{256}DENs and Au_{256}DENs (middle) and dendrimicelles made from only Au_{256}DENs (right). The Pd-only sample contained ~15 nanoparticle per dendrimicelle whereas the Au-only sample contained ~23 nanoparticles per dendrimicelle. The Pd-Au sample contained ~18 nanoparticles per dendrimicelle, agreeing well with the values found for Pd- and the Au-dendrimicelles. The slightly lower observed number of nanoparticles inside dendrimicelles made from PdDENs as opposed to those made from AuDENs can be explained by the instability of Pd-DENs (oxidation), and by the lower contrast of Pd versus Au hindering nanoparticle counting. To confirm that the micelles as show in the center do contain a mix of Pd- and Au-DENs, techniques such as Augier spectroscopy, or Energy-Dispersive X-ray spectroscopy should be used. These techniques should show the (co-)localization of the respective metal(s) inside the dendrimicelles, and hence confirm the micelle loading. These examples indicate that the dendrimer content (*e.g.* the type of nanoparticle) does not affect the dendrimicelles substantially, highlighting the modularity of this dendrimicelle approach.

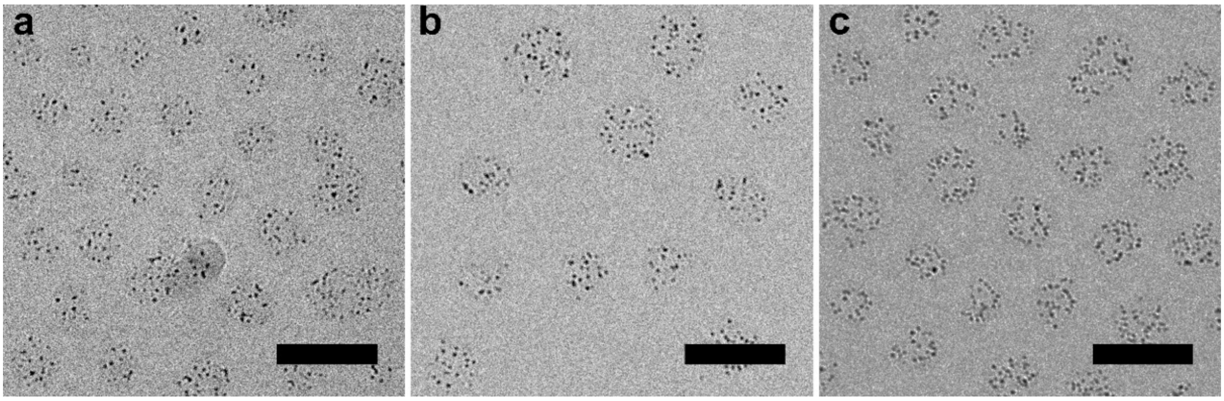

*Figure **6-2** CryoTEM micrographs of seventh generation-based dendrimicelles. The dendrimicelles contain: G7-Pd_{256} DENs (**a**); G7-Pd_{256} and G7-Au_{256} DENs in a 1:1 mix (**b**), and G7-Au_{256} DENs (**c**). Analysis of the cryoTEM micrographs showed that the Pd-only dendrimicelles contain 15 ± 9 nanoparticles per dendrimicelle (69 micelles analyzed), the Pd/Au mixed dendrimicelles contain 18 ± 6 nanoparticles (65 micelles analyzed), and the Au-only dendrimicelles contain 23 ± 7 nanoparticles (128 micelles analyzed). The scale bars are 50 nm.*

Besides mixing nanoparticle-loaded dendrimers with empty dendrimers, or mixing dendrimers with different types of metal nanoparticles embedded, different dendrimer generations can also be mixed and co-assembled into dendrimicelles. Mixing dendrimer generations in a single dendrimicelle could, for example, be used to tune the stability of the obtained dendrimicelles. Throughout this thesis, the obtained results point to a decrease in dendrimicelle stability with a decrease in dendrimer generation used for dendrimicelle formation. Additionally, by using nanoparticles with a significantly different size, it should be possible to study the distribution of different generations dendrimers inside a single dendrimicelle can be studied. The above discussed examples show that cryo-transmission electron microscopy is a powerful technique that not only allows to determine dendrimicelle (core) size, shape, and polydispersity, but also to investigate the micelle subcomponent compositions, and fluctuations thereof, using the micelle-embedded nanoparticles.

Co-assembly of dendrimer–encapsulated and –stabilized nanoparticles

In Chapter 5, size analysis of the micelle-embedded nanoparticles showed that not only dendrimer-encapsulated nanoparticles, but also the dendrimer-stabilized nanoparticles co-assembled into the dendrimicelles. The catalytic activity of nanoparticles is known to be size-dependent,[16,17] and for the PAMAM dendrimers used in this thesis, the maximum dendrimer-encapsulated nanoparticle that can be synthesized inside a single dendrimer is ~4 nm for a generation 9 dendrimer. Moreover, the large number of surface groups in higher-generation dendrimers is known to restrict molecules from entering the dendrimer, affecting the catalytic activity of the encapsulated nanoparticle. This 'nanofilter' property might be enhanced for dendrimer-encapsulated nanoparticles embedded inside a dendrimicelle. Chapter 2, for example, showed already that the dendrimicelles slowed down the degradation of the embedded gold nanoparticle. For catalytic applications, the co-assembly of dendrimer-stabilized nanoparticles is therefore of interest. Not only can dendrimer-stabilized nanoparticles be obtained with larger sizes than achievable with dendrimer-encapsulated nanoparticles —those observed in Chapter 5 were already ~6 nm—, they are also often formed using lower-generation dendrimers. This could potentially circumvent or reduce the 'nanofilter' effect that higher-generation dendrimers exhibit. Lastly, the previous work of Wang *et al.* indicated that PAMAM generations 0 and 1 did not form well-defined dendrimicelles. Dendrimer-stabilized nanoparticles made using these generations might still assemble into well-defined dendrimicelles, as the many individual dendrimers on a single nanoparticle could provide sufficient charged groups or charge density to allow for self-assembly into dendrimicelles.

6.6 Outlook

Improving or adapting the dendrimicelle stability

The dendrimicelles reported in this thesis are interesting for studying the self-assembly behavior of complex coacervates into hierarchically built-up and well-defined micelles. Throughout this thesis, a $pMAA_{64}pEO_{885}$ block copolymer was used for dendrimicelle formation. Other, similarly-sized block copolymers were tested as well. Interestingly, using $pAA_{50}pEO_{250}$ resulted in well-defined ~50 nm-sized micelles, indicating that changing from a methacrylic acid block to an acrylic acid block hardly affects the formed micelles. Using a $pAA_{100}pEO_{500}$ block copolymer, however, did not result in the formation of well-defined dendrimicelles. This highlights that the formation of well-defined complex coacervate core micelles depends on a complex interplay between many interaction parameters. Not only the ratio between the charged and neutral blocks of the block copolymer, but also on total charge and block length.[18,19] Both the block copolymer, and the dendrimer terminal amines allow for bio-conjugation, which could be of interest for applications, from synthesizing novel fluorescent nanoparticles, to generating artificial cascade enzymes, and potentially even for responsive nanocarriers. Expanding the modular dendrimicelle toolbox by including fluorescent dendrimers and block copolymers should open up a plethora of options for further investigation, and warrants further study.

The dendrimicelles presented in this thesis are highly stable against ionic strength, and dilution, but their pH stability is limited by the pKa of both the block copolymer (~6) as well as the dendrimer terminal amine (~9).[4,5] Effectively, the dendrimicelles are stable at pH ~7 ± 1, (Figure **2-S10**). This limited pH stability window could have an effect on catalytic applications of the dendrimicelles. For example, the catalytic conversion of nitrophenol to nitroaniline requires addition of sodium borohydride, a strong base that could lead to the dissociation of the dendrimicelles. To extend the pH stability of the formed dendrimicelles, one of the approaches could be to pursue crosslinking of the dendrimicelle core, for example, by introducing polymerizable groups on the dendrimers. Alternatively, covalently linking the dendrimer-amines to the block copolymer acid groups by, for example, using protein coupling chemistry could be pursued. Additionally, using building blocks with a pH-independent charge should increase the pH stability of the dendrimicelles. Block copolymers employing a poly(styrene sulfonate) block as charged block should render the dendrimicelles stable at low pH. Quaternizing the dendrimer terminal amines results in a pH-independent charge, which should increase dendrimicelle stability at high pH.[20]

Dendrimicelles for Catalysis

Over the past two decades, the catalytic activity of dendrimer-encapsulated nanoparticles has been extensively studied by, among others, Crooks and collaborators.[20-23] Examples of the catalytic reactions that be done with dendrimer-encapsulated nanoparticles include the catalysis of resazurin to resorufin as catalyzed by AuNPs, and the catalysis of nitrophenol to nitroaniline by Pd or AuNPs.[16,23] As shown in Chapter **2** and Section **6.5**, the dendrimicelle strategy allows not only for tuning the number of nanoparticles per dendrimicelle, but also for the co-assembly of different metal nanoparticles, and even for the co-assembly of dendrimer-encapsulated and -stabilized nanoparticles inside a single dendrimicelle. Reactivity in a confined space is of interest for many different research fields, from (multistep) catalysis to the development of artificial enzymes.[24-26] The results obtained in Chapter **2** indicated that the dendrimicelles themselves act as barrier, as they delayed the thiol-induced etching of gold nanoparticles. Therefore, future research should assess to what extent dendrimer-encapsulated nanoparticles, embedded inside dendrimicelles, are still available to participate in catalytic reactions.

Using fluorescent building blocks to form dendrimicelles.

The use of the dendrimicelles as stable fluorescent nanoparticles could include covalently attaching fluorescent molecules to the dendrimer periphery, and subsequent assembly into dendrimicelles would be interesting to pursue. The covalently attaching a few, low molecular weight, fluorescent dyes to the dendrimer is not expected to affect the formed dendrimicelles. The functionalization of dendrimers could be employed to investigate the stability of dendrimicelles against *inter*-micelle exchange, to study the phase-transition of dendrimicelles into other complex coacervate nanoaggregates, or to create micelles with a color-tunable emission. Förster resonance energy transfer (FRET) or fluorescence quenching by nanoparticles could be used to study dendrimer exchange in between dendrimicelles. With FRET, *inter*-dendrimicelle exchange of dendrimers should change the donor and acceptor dye emission. Similarly, fluorescence quenching associated with gold nanoparticles could be employed in order to study *inter*-micelle exchange of dendrimers as well. Likewise, the exchange of block copolymers in between dendrimicelles could be studied by using fluorescently labelled block copolymers and dendrimers. Fluorescent PAMAM dendrimers have been used as pH sensors to investigate the intracellular pH of cells.[27] Dendrimicelles could here, for example, serve to investigate and follow the dissociation behavior of dendrimicelles in *in vitro* and *in vivo* studies.

Using dendrimicelles in nanomedine and as nanocarriers

Further down the line, other applications for the dendrimicelles could include the use in nanomedicine or as nanocarriers for drugs. Dendrimers are known to interact with and encapsulate anti-tumor medication or gene vectors.[28-31] A wide variety of cell-targeting moieties is known, and could potentially be added to the block copolymer to make it responsive. The introduction of specific targeting moieties at the block copolymer poly(ethylene oxide) end group, or on the dendrimer terminal amines could result in selective interactions of the dendrimicelle, respectively the dendrimer, with, for example, cell receptor overexpressing tumor cells. Here, the limited pH stability of the dendrimicelles could be an asset as upon endocytosis in a cell, the pH is significantly lowered,[32] resulting in the disassembly of the dendrimicelle and a release of the embedded cargo. In this case, the dendrimicelle would act as a nanocarrier, and facilitate the targeting of the cell of interest. Furthermore, the complexation of radio nucleotides inside (fluorescent) PAMAM dendrimers and subsequent self-assembly into dendrimicelles using a (targeting) block copolymer could result in novel and stable multimodal targeting and imaging agents for use in nanomedicine.

6.7 Summarizing Main Concluding Remarks

This thesis shows a unique strategy to determine dendrimicelle aggregation numbers, by simply counting the number of nanoparticles per dendrimicelle. This allows for directly looking into the complex coacervate core of the micelle, and for studying the composition thereof. It also allowed us to study the effect of dendrimer generation on the aggregation number of the formed dendrimicelles, and raise some questions on the aggregation numbers as determined from light scattering. Additionally, by carefully examining the cryoTEM micrographs, well-defined dendrimicelles could be discerned from other nanoaggregates. The bulk characterization of nanostructures is often done with scattering techniques such as dynamic and static light scattering, small-angle X-ray scattering (SAXS) these techniques provide a statistical average size of the sample. Microscopy is often used to study the ‘local’ characteristics and fluctuations in a sample, and is less suitable for determining the average size of a sample, as it requires the collection of many images to calculate the statistical average size of a sample.

The biconcave thin film templated self-organization of dendrimicelles —as shown in this thesis— yields dendrimicelle superstructures that contain hundreds of micelles each, yet still provide information with unprecedented detail on the local fluctuations (*e.g.,* of micelle size and aggregation numbers) inside the dendrimicelle sample. The induced self-organization reduces the number of images that should be acquired in order to obtain relevant bulk characteristics of a micelle sample. Moreover, induced self-organization of dendrimicelles could be a valuable tool to obtain mesoscopic structures from nanometer-sized building blocks. Chapter 4 already shows how these superstructures can be used to study the electron beam-induced rupture. The size-sorting effect observed has the potential to generate non-periodic structures that could be used for novel metamaterials. The micelles obtained from dendrimer building blocks allow for many variations, to study both fundamental topics like self-assembly, but likely also for applications, such as catalysis.

To conclude: First, the dendrimicelle strategy, as reported in this thesis, provides highly modular dendrimicelles that allow for an elegant and thorough investigation of the self-assembly of complex coacervate core micelles. Moreover, the high stability and adjustability of the dendrimicelles renders them of interest for a plethora of applications in a range of research fields. Second, thin water film templates proved to be a highly useful and novel tool for creating self-assembled mesoscale materials. Thin film templating and the resulting size-sorting, have potential for generating new, a-periodic, metamaterials. Finally, this thesis shows that cryoTEM is a powerful analysis tool in nanotechnology; expanding its use in nanotechnology should lead to many more exciting discoveries.

6.8 References

1. Wang, J.; Voets, I. K.; Fokkink, R.; van der Gucht, J.; Velders, A. H. Controlling the Number of Dendrimers in Dendrimicelle Nanoconjugates from 1 to More Than 100. *Soft Matter* **2014**, 10, 7337-7345.
2. Gröhn, F.; Bauer, B. J.; Akpalu, Y. A.; Jackson, C. L.; Amis, E. J. Dendrimer Templates for the Formation of Gold Nanoclusters. *Macromolecules* **2000**, 33, 6042-6050.
3. Wen, S.; Yin, X.; Stevenson, W. T. K. Preparation and Characterization of Polyelectrolyte Copolymers Containing Methyl Methacrylate and 2-Hydroxyethyl Methacrylate. I. Polymers Based on Methacrylic Acid. *Journal of Applied Polymer Science* **1991**, 42, 1399-1406.
4. Ruiz-Pérez, L.; Pryke, A.; Sommer, M.; Battaglia, G.; Soutar, I.; Swanson, L.; Geoghegan, M. Conformation of Poly(Methacrylic Acid) Chains in Dilute Aqueous Solution. *Macromolecules* **2008**, 41, 2203-2211.
5. Pande, S.; Crooks, R. M. Analysis of Poly(Amidoamine) Dendrimer Structure by Uv–Vis Spectroscopy. *Langmuir* **2011**, 27, 9609-9613.
6. van Dongen, M. A.; Desai, A.; Orr, B. G.; Baker, J. R.; Banaszak Holl, M. M. Quantitative Analysis of Generation and Branch Defects in G5 Poly(Amidoamine) Dendrimer. *Polymer* **2013**, 54, 4126-4133.
7. Mullen, D. G.; Desai, A.; van Dongen, M. A.; Barash, M.; Baker, J. R.; Banaszak Holl, M. M. Best Practices for Purification and Characterization of Pamam Dendrimer. *Macromolecules* **2012**, 45, 5316-5320.
8. Wei, S.; Wang, J.; Venhuizen, S.; Skouta, R.; Breslow, R. Dendrimers in Solution Can Have Their Remote Catalytic Groups Folded Back into the Core: Enantioselective Transaminations by Dendritic Enzyme Mimics-Ii. *Bioorganic & Medicinal Chemistry Letters* **2009**, 19, 5543-5546.
9. Bosman, A. W.; Janssen, H. M.; Meijer, E. W. About Dendrimers: Structure, Physical Properties, and Applications. *Chemical Reviews* **1999**, 99, 1665-1688.
10. Maiti, P. K.; Çağın, T.; Lin, S.-T.; Goddard, W. A. Effect of Solvent and Ph on the Structure of Pamam Dendrimers. *Macromolecules* **2005**, 38, 979-991.
11. Feja, B.; Aebi, U. Determination of the Inelastic Mean Free Path of Electrons in Vitrified Ice Layers for on-Line Thickness Measurements by Zero-Loss Imaging. *Journal of Microscopy* **1999**, 193, 15-19.
12. Gurkov, T. D.; Angarska, J. K.; Tachev, K. D.; Gaschler, W. Statistics of Rupture in Relation to the Stability of Thin Liquid Films with Different Size. *Colloids and Surfaces A: Physicochemical and Engineering Aspects* **2011**, 382, 174-180.
13. Frederik, P. M.; Hubert, D. H. W. Cryoelectron Microscopy of Liposomes. In *Methods in Enzymology*; Academic Press: 2005; pp 431-448.
14. Glaeser, R. M.; Han, B. G.; Csencsits, R.; Killilea, A.; Pulk, A.; Cate, J. H. D. Factors That Influence the Formation and Stability of Thin, Cryo-Em Specimens. *Biophysical Journal* **2016**, 110, 749-755.
15. Saulnier, L.; Champougny, L.; Bastien, G.; Restagno, F.; Langevin, D.; Rio, E. A Study of Generation and Rupture of Soap Films. *Soft Matter* **2014**, 10, 2899-2906.
16. Johnson, J. A.; Makis, J. J.; Marvin, K. A.; Rodenbusch, S. E.; Stevenson, K. J. Size-Dependent Hydrogenation of P-Nitrophenol with Pd Nanoparticles Synthesized with Poly(Amido)Amine Dendrimer Templates. *The Journal of Physical Chemistry C* **2013**, 117, 22644-22651.

17. Zhou, X.; Xu, W.; Liu, G.; Panda, D.; Chen, P. Size-Dependent Catalytic Activity and Dynamics of Gold Nanoparticles at the Single-Molecule Level. *Journal of the American Chemical Society* **2010**, 132, 138-146.

18. van der Burgh, S.; de Keizer, A.; Cohen Stuart, M. A. Complex Coacervation Core Micelles. Colloidal Stability and Aggregation Mechanism. *Langmuir* **2004**, 20, 1073-1084.

19. van der Kooij, H. M.; Spruijt, E.; Voets, I. K.; Fokkink, R.; Cohen Stuart, M. A.; van der Gucht, J. On the Stability and Morphology of Complex Coacervate Core Micelles: From Spherical to Wormlike Micelles. *Langmuir* **2012**, 28, 14180-14191.

20. Kim, Y.-G.; Oh, S.-K.; Crooks, R. M. Preparation and Characterization of 1−2 Nm Dendrimer-Encapsulated Gold Nanoparticles Having Very Narrow Size Distributions. *Chemistry of Materials* **2004**, 16, 167-172.

21. Crooks, R. M.; Zhao, M. Q.; Sun, L.; Chechik, V.; Yeung, L. K. Dendrimer-Encapsulated Metal Nanoparticles: Synthesis, Characterization, and Applications to Catalysis. *Accounts of Chemical Research* **2001**, 34, 181-190.

22. Scott, R. W. J.; Wilson, O. M.; Crooks, R. M. Synthesis, Characterization, and Applications of Dendrimer-Encapsulated Nanoparticles. *The Journal of Physical Chemistry B* **2005**, 109, 692-704.

23. Weir, M. G.; Knecht, M. R.; Frenkel, A. I.; Crooks, R. M. Structural Analysis of Pdau Dendrimer-Encapsulated Bimetallic Nanoparticles. *Langmuir* **2010**, 26, 1137-1146.

24. Guy, L.; Dutasta, J.-P.; Martinez, A. Endohedral Functionalization of Molecular Cavities for Catalysis in Confined Spaces. In *Effects of Nanoconfinement on Catalysis*; Poli, R., Ed.; Springer International Publishing: Cham, 2017; pp 1-15.

25. Chen, P.-C.; Liu, G.; Zhou, Y.; Brown, K. A.; Chernyak, N.; Hedrick, J. L.; He, S.; Xie, Z.; Lin, Q.-Y.; Dravid, V. P.*; et al.* Tip-Directed Synthesis of Multimetallic Nanoparticles. *J. Am. Chem. Soc.* **2015**, 137, 9167-9173.

26. Koblenz, T. S.; Wassenaar, J.; Reek, J. N. H. Reactivity within a Confined Self-Assembled Nanospace. *Chemical Society Reviews* **2008**.

27. Albertazzi, L.; Storti, B.; Marchetti, L.; Beltram, F. Delivery and Subcellular Targeting of Dendrimer-Based Fluorescent Ph Sensors in Living Cells. *Journal of the American Chemical Society* **2010**, 132, 18158-18167.

28. Haensler, J.; Szoka, F. C. Polyamidoamine Cascade Polymers Mediate Efficient Transfection of Cells in Culture. *Bioconjugate Chemistry* **1993**, 4, 372-379.

29. Kesharwani, P.; Banerjee, S.; Gupta, U.; Mohd Amin, M. C. I.; Padhye, S.; Sarkar, F. H.; Iyer, A. K. Pamam Dendrimers as Promising Nanocarriers for Rnai Therapeutics. *Materials Today* **2015**, 18, 565-572.

30. Li, Y.; He, H.; Lu, W.; Jia, X. A Poly(Amidoamine) Dendrimer-Based Drug Carrier for Delivering Dox to Gliomas Cells. *RSC Advances* **2017**, 7, 15475-15481.

31. Zhu, S.; Qian, L.; Hong, M.; Zhang, L.; Pei, Y.; Jiang, Y. Rgd-Modified Peg-Pamam-Dox Conjugate: In Vitro and in Vivo Targeting to Both Tumor Neovascular Endothelial Cells and Tumor Cells. *Adv. Mater.* **2011**, 23, H84-H89.

32. Cain, C. C.; Sipe, D. M.; Murphy, R. F. Regulation of Endocytic Ph by the Na+,K+-Atpase in Living Cells. *Proceedings of the National Academy of Sciences of the United States of America* **1989**, 86, 544-8.

Chapter 7

Summary

This chapter summarizes the main findings and outcomes of this thesis.

Chapter 1 of this thesis provides an introduction to the field of self-assembled nanomaterials and the analysis thereof. For this thesis, the goal was to investigate:

1) the self-assembly of amine-terminated dendrimers into well-defined dendrimicelles
2) the use of the micelle embedded nanoparticles as 'spy' particles
3) the effect of a templating matrix on the self-organization of these dendrimicelles into mesoscale superstructures.

Throughout the thesis, it is shown that well-defined, 50 nm-sized dendrimicelles can be obtained from PAMAM dendrimer generations five through nine. By combining cryoTEM and light scattering experiments, the self-assembly behavior of the dendrimicelles is studied in unique detail. The dendrimicelle-embedded nanoparticles serve a dualistic purpose; not only do they provide additional contrast in the cryoTEM micrographs, they also allow for the direct determination of the micelle aggregation numbers by simply counting the number of nanoparticles.

In **Chapter 2**, a highly flexible, modular, and robust strategy is shown as a way to obtain well-defined complex coacervate core dendrimicelles by combining positively-charged PAMAM dendrimers with an oppositely-charged block copolymer. The presence of a single metal nanoparticle per dendrimer allowed for a novel strategy to determine micelle aggregation numbers. The dendrimer-encapsulated nanoparticles act as a 'spy' particle, and reveal the dendrimicelle aggregation numbers: Counting the number of nanoparticles per dendrimicelle in cryoTEM micrographs yields the average dendrimicelle aggregation number. The number of nanoparticles per dendrimicelle can be controlled by simply mixing 'nanoparticle-filled' with 'empty' dendrimers. Addition of block copolymer results in the formation of 'half-full' dendrimicelles. The dendrimicelles formed in this chapter are highly stable in time, tolerate ionic strengths up to at least 0.5 M NaCl, and have CMCs of ~mg.L^{-1} based on total polymer amount present. CryoTEM showed that *inter*-dendrimicelle exchange of dendrimers did not proceed for PAMAM generation seven-based dendrimicelles, not even at extended timescales: Three months after mixing 'empty' and 'nanoparticle-loaded' dendrimicelles, only 'empty' and 'nanoparticle-loaded' dendrimicelles were observed, and no 'half-full' dendrimicelles were observed. This strongly suggests that the complex coacervate core of dendrimicelles formed from PAMAM generation seven-based dendrimers is kinetically trapped, explaining the high stability of the formed dendrimicelles.

The dendrimicelles also appeared to act as barrier, slowing down the thiol-induced degradation of the micelle-embedded gold nanoparticles. In conclusion, the dendrimicelle system shown in this chapter is highly modular and allows for many variations to obtain dendrimicelles. First, the number of nanoparticles per dendrimicelle can be controlled by mixing ‘nanoparticle-filled’ with ‘empty’ dendrimers. Second, the nanoparticle type embedded inside the dendrimicelle can be changed by using different dendrimer-encapsulated nanoparticles. Moreover, dendrimicelles containing mixed-metal nanoparticles can be obtained as well, as has been later shown in Chapter 6, for example. Third, the size of the dendrimer-encapsulated nanoparticle can be tuned by adjusting the metal ion:dendrimer ratio during the synthesis of the dendrimer-encapsulated nanoparticles. Fourth, the synthesis of well-defined dendrimicelles is not limited to generation seven-based PAMAM dendrimers, as shown in chapters 3-5.

Chapter 3 shows that besides PAMAM generation seven, described in chapter 2, also generation eight and nine self-assemble into stable and well-defined dendrimicelles under charge-stoichiometric mixing conditions. These dendrimicelles self-organize into micrometer-sized pseudo-2D superstructures, in which a pronounced size-sorting of dendrimicelles is observed. The dendrimicelle size follows the thickness of the biconcave thin film, with the bigger dendrimicelles residing toward the edge, and the smaller dendrimicelles residing more toward the center of the superstructure. This size-sorting is attributed to the reciprocal interactions between the PEG coronas of the dendrimicelles with the biconcave thin film that forms in between a thin air-water-air interface. Excess block copolymer to dendrimer is shown to increase the polydispersity of the formed dendrimicelles. This increase in polydispersity was more pronounced for generation seven-based dendrimicelles than for generation eight- or generation nine-based dendrimicelles, indicating a slightly lower stability of the first. More importantly, the increased polydispersity at off-stoichiometric mixing conditions was visually amplified inside the formed dendrimicelle superstructures, that showed a more pronounced size-sorting over the superstructure. Inside the superstructure, the dendrimicelles did not appear to organize into periodic structures; the size-gradient over the superstructure likely played a role in this. Instead, the dendrimicelles appear to form spiral domains, and some of the observed superstructures appear to contain double spiral domains, resembling those found in nature in, for example, sunflowers and pineapples.

In conclusion, the self-organization and size-sorting induced by the biconcave thin film template is a novel self-assembly technique for the construction of pseudo-2D monolayer superstructures that potentially could be used for the generation of novel, non-periodic metamaterials. Additionally, the templated organization of dendrimicelles results in a closely-packed dendrimicelle superstructure containing many dendrimicelles. The dendrimicelle core size is indicated by the dendrimer-encapsulated nanoparticles, and the total dendrimicelle size (core + corona) can be obtained by measuring the dendrimicelle core-core distances in the cryoTEM micrographs.

Generation six-based dendrimers are used in **Chapter 4** to form well-defined dendrimicelles. These dendrimicelles are subsequently self-assembled into superstructures, templated by a biconcave-shaped thin film. The dendrimicelle-embedded gold nanoparticles are then used to study local and global processes that take place before and during electron beam-induced rupture of vitrified thin films. Exposure of the superstructures to an electron beam first results in local radiation damage of the dendrimicelles, appearing in the form of (hydrogen) gas bubbles. Next, continued exposure results in a thinning of the thin film containing the dendrimicelle superstructure, as shown by image analysis of cryoTEM micrographs. The thin film is slowly ‘etched away’, with a rate on the order ~nanometers per second. Upon further exposure, the dendrimicelle cores, as indicated by the encapsulated gold nanoparticles, appear to shrink, suggesting the loss of water from the dendrimers. Shortly after, the complete superstructure ruptures quickly, leaving a hole in the thin film behind. The processes that take place before rupture are investigated and likely include first a gradual evaporation of water from the biconcave thin film. Next, the apparent shrinkage of the dendrimicelle core is likely due to the evaporation of water from the dendrimer interiors, finally leaving a freely suspended thin polymer film in between the vitreous ice film. Upon continued exposure of the dendrimicelle film, the dendrimicelle suddenly and explosively ruptured, leaving a hole in the thin water film behind. The rupture appears to start from the thinnest section of the superstructure, and moves radially outward with speeds on the order of 10^1-10^2 nm.s^{-1}. In conclusion, the rupture of thin films is induced by the controlled irradiation of dendrimicelle superstructures. The micelle-embedded gold nanoparticles function as tracer particle, visualizing the processes taking place before and during superstructure rupture.

Chapter 5 shows that generation five-based dendrimers result in the formation of both dendrimer-encapsulated as well as dendrimer-stabilized gold nanoparticles. Interestingly, these nanoparticles co-assemble into well-defined dendrimicelles upon charge stoichiometric combination with an oppositely-charged block copolymer. Using off-stoichiometric mixing ratios of block copolymer to dendrimer is shown to yield either ill-defined nanostructures (when using excess dendrimer to block copolymer) or nanostructures with a large polydispersity (when using excess block copolymer to dendrimer). The templated self-organization induced by a biconcave thin film results in a visually-amplified size-sorting of these dendrimicelles. CryoTEM proved to be a powerful tool to investigate and analyze the nanoparticle-loaded structures in great detail. The cryoTEM micrographs showed that, besides well-defined dendrimicelles, additional nanoaggregates with a ‘core’ size of 50-100 nm are present. Not only are these too large to be dendrimicelles, they also contain fewer nanoparticles than expected for dendrimicelles of similar size. This strongly suggested that these structures are not dendrimicelles, but rather another type of complex coacervate structure, likely bilayer vesicles. These results are in agreement with results reported in literature, that showed that dendrimicelles made from carboxylic acid-terminated dendrimers only formed stable dendrimicelles at off-stoichiometric mixing conditions for dendrimer generations six and higher.

Chapter 6 discusses the most important outcomes and implications of the four experimental chapters, and provides some additional observations to extend to discussion. An outlook and suggestions for further research lines are provided, ending with a general conclusion.

Samenvatting

Hoofdstuk 1 van deze thesis introduceert het gebied van de zelf-geassembleerde nanomaterialen en de analyse daarvan. Het doel van deze thesis was het onderzoeken van:

1) de zelf-assemblage van dendrimeren, goed gedefinieerde vertakte polymeren met een amine als eindgroep, in clusters genaamd dendrimicellen.

2) het bestuderen van het gebruik van nanodeeltjes ingekapseld in dendrimeren waardoor zij als ‘spion’ fungeren, om daarmee te onderzoeken hoeveel dendrimeren zich in een dendrimicel bevinden.

3) het bestuderen van het effect van een biconcave mal op de ordening van deze dendrimicellen in superstructuren.

In deze thesis laten we zien dat we goed gedefinieerde dendrimicellen van 50 nanometer groot kunnen maken met PAMAM-dendrimeren van generatie vijf tot en met negen. Met het gebruik van cryo-transmissie elektronenmicroscopie en lichtverstrooiingstechnieken bestuderen we het zelforganisatie gedrag van de dendrimicellen in hoog detail. De nanodeeltjes die zich in de dendrimeren bevinden, hebben een duale functie: enerzijds zorgen ze voor contrast in de elektronenmicroscopie plaatjes, anderzijds zorgen ze ervoor dat het aantal dendrimeren in een dendrimicel bepaald kan worden door simpelweg het aantal deeltjes te tellen.

In **Hoofdstuk 2** laten we een flexibele, modulaire, en robuuste strategie zien voor het verkrijgen van goed gedefinieerde en stabiele complex coacervaat-kern micellen. Deze micellen worden gemaakt door een positief geladen PAMAM-dendrimeer te combineren met een negatief geladen blok-copolymeer. De aanwezigheid van één metaal nanodeeltje per dendrimeer is een nieuwe manier voor het bepalen van de componenten van de gevormde micel. De ingekapselde metaaldeeltjes functioneren als een ‘spion’ en geven het aantal dendrimeren per micel:

door het tellen van het aantal nanodeeltjes weten we hoeveel dendrimeren er in een micel zitten. We laten ook zien dat het aantal nanodeeltjes per micel gevariëerd kan worden door dendrimeren met en dendrimeren zonder nanodeeltjes te mengen en hiervan vervolgens één micel te maken door het blok copolymer toe te voegen. De micellen zoals wij ze vormen zijn stabiel voor lange tijd en kunnen ionische sterktes tot ten minste 0.5 M NaCl doorstaan. De micellen hebben een kritische micel concentratie, de concentratie waarbij ze uit elkaar vallen, van ongeveer één miligram per liter, gebaseerd op de totale polymeer massa. Ook laten we zien dat er geen uitwisseling plaatsvindt van de kernen van micellen die op de PAMAM generatie 7 zijn gebaseerd, zelfs niet in de loop van enkele maanden: drie maanden na het mengen van micellen <u>met</u> nanodeeltjes in de kern, met micellen <u>zonder</u> nanodeeltjes in de kern, worden alleen de afzonderlijke varianten en geen gemengde of micellen met slechts een aantal deeltjes erin gezien. Deze waarneming wijst erop dat de kern van deze micellen ‘kinetisch vast’ is, wat daarmee ook de stabiliteit van deze micellen verklaard. De micellen lijken tevens een barrièrefunctie te hebben, aangezien ze de snelheid van het etsen van de gouddeeltjes door thiolen lijken te vertragen. Concluderend zijn de micellen zoals beschreven in dit hoofdstuk uiterst modulair.

Als gevolg daarvan kan er met veel parameters gevariëerd worden. Ten eerste kunnen we het aantal nanodeeltjes per micel variëren door dendrimeren <u>met</u> en dendrimeren <u>zonder</u> nanodeeltjes te mengen. Ten tweede kunnen we met het soort nanodeeltje dat zich in de micellen bevindt variëren door een ander soort metaaldeeltje in de dendrimeer te plaatsen. Hierop voortbordurend kunnen we ook micellen maken met verschillende soorten nanodeeltjes erin. Ten derde kunnen we ook de grootte van het nanodeeltje veranderen door de ratio van de metaalprecursor en de dendrimeer te veranderen bij de synthese van nanodeeltjes. Als laatste is de synthese van micellen niet beperkt tot dendrimeer generatie 7, zoals we ook laten zien in hoofdstuk 3 tot en met 5.

Hoofdstuk 3 beschrijft dat stabiele en goed-gedefinieerde micellen naast dendrimeer generatie 7 ook gemaakt kunnen worden van generaties 8 en 9. We laten zien dat de gevormde micellen zich ordenen in pseudo 2D superstructuren van een micrometer groot. In deze superstructuren volgt de grootte van de micellen de dikte van de biconcave dunne waterfilm waar zij zich in bevinden. De grotere micellen zitten meer aan de randen van de superstructuur, terwijl de kleinere micellen zich meer in het midden van de superstructuur bevinden. Deze groottesortering schrijven wij toe aan de reciproke interacties tussen de poly(ethylene oxide) schil van de micel met de biconcave dunne water film die zich vormt tussen een lucht-water-lucht grensvlak. We laten zien dat het gebruik van een exces aan blok-copolymeer ervoor zorgt dat de polydispersiteit van de micellen groter wordt. Deze toename in polydispersiteit is groter voor de op generatie 7 gebaseerde micellen dan voor de op generatie 8 of 9 gebaseerde micellen, wat een iets lagere stabiliteit van micellen van de lagere generatie dendrimeren indiceert.

Nog belangrijker is dat de toename in polydispersiteit resulteerde in een duidelijkere groottesortering van de micellen in de superstructuur. In deze superstructuren lijken de micellen zich niet in een periodieke structuur te oriënteren, wat waarschijnlijk toe te wijzen is aan de groottegradiënt die aanwezig is in de superstructuur. In plaats van periodieke structuren lijken de micellen zich te organiseren in dubbele-spiraal structuren zoals die in de natuur voorkomen in bijvoorbeeld zonnebloemen en dennenappels. Concluderend is de organisatie en de sortering zoals die geïnduceerd wordt door de biconcave water film-mal een nieuwe methode voor het vormen van pseudo-2D superstructuren, met mogelijke toepassingen in de synthese van a-periodieke metamaterialen. Ook zorgt deze methode voor een superstructuur waarin de micellen zich dicht bij elkaar bevinden. Hierdoor kunnen we de grootte van de micelkern en de totale micelgrootte bepalen door het meten van de kerngrootte en de afstand tussen individuele micel kernen in de cryoTEM plaatjes.

In **Hoofdstuk 4** gebruiken we zesde generatie dendrimeren voor het vormen van goed gedefinieerde micellen. Na het vormen van de micellen gebruiken we de biconcave-mal methode voor het vormen van micel superstructuren. We gebruiken de ingekapselde nanodeeltjes daarna voor het bestuderen van de lokale en globale processen die plaatsvinden tijdens het barsten van de dunne films ten gevolge van belichting door een elektronenbundel. De blootstelling van de superstructuren aan deze elektronenbundel resulteert eerst in lokale stralingsschade van de micellen in de vorm van het ontstaan van waterstofgasbellen. Beeldanalyse laat vervolgens zien dat de film waarin de superstructuur zich bevindt, dunner wordt. De snelheid waarmee deze laag dunner wordt, is ongeveer één nanometer per seconde.

Als we vervolgens nog langer op deze dunne laag schijnen, lijkt aan de gouddeeltjes te zien dat de micelkernen krimpen, hetgeen suggereert dat er ook water uit de dendrimeren verdampt. Kort erna zien we dat de superstructuur barst waarna zich een gat in de dunne laag bevindt ter grootte van de superstructuur die daarin aanwezig was. De processen die hierin een rol spelen zijn waarschijnlijk de geleidelijke verdamping van de dunne waterlaag waarin de micel superstructuur zich bevindt, gevolgd door het krimpen van de micelkern wanneer daar ook water uit verdampt. Dit zorgt ervoor dat de superstructuur veranderd naar een vrijstaande dunne polymeer film. Wanneer we daarna de film nog langer belichten, explodeert deze en blijft er een gat ter grootte van de originele superstructuur over. Deze ‘nano-explosie’ begint vanuit het dunste gedeelte van de superstructuur en lijkt zich dan radiaal naar buiten te bewegen met een snelheid van ~10-100 nanometer per seconde. Concluderend kunnen we zeggen dat we het barsten van micel superstructuren kunnen bewerkstelligen door gecontroleerde belichting met een elektronenbundel. De gouddeeltjes in de micellen hebben de rol van een tracer en helpen om het barsten van de film te visualiseren.

In **Hoofdstuk 5** laten we zien dat in vijfde generatie dendrimeren zowel dendrimeer-gestabiliseerde als dendrimeer-ingekapselde nanodeeltjes vormen. Beide soorten deeltjes worden ingekapseld in een micel na toevoeging van een negatief geladen blok copolymeer. Als we een exces van dendrimeer tot blok copolymeer gebruiken zien we alleen slecht gedefinieerde aggregaten. Als we een exces van blok-copolymeer tot dendrimeer gebruiken, zien we dat er nanostructuren met grote polydispersiteit worden gevormd.

Het gebruik van de biconcave dunne film-mal zorgt ervoor dat deze polydispersiteit visueel versterkt wordt door de geïnduceerde groottesortering van de micellen. CryoTEM blijkt een krachtige techniek te zijn voor het bestuderen en analyseren van de nanodeeltjes-bevattende micellen. De cryoTEM foto’s laten zien dat niet alleen micellen, maar ook andere nanostructuren zich vormen. Deze structuren hebben een kern van 50-100 nanometer en zijn te groot om dendrimicellen te zijn. Ook bevatten ze minder nanodeeltjes dan we zouden verwachten voor micellen van deze grootte. Dit suggereert dat deze gevormde structuren waarschijnlijk geen dendrimicellen zijn, maar een ander soort complex coacervaat structuur zoals een vesikel. Onze resultaten zijn in overeenstemming met eerder onderzoek naar dendrimeren met een carboxyl-zuur eindgroep, waarin men liet zien dat het gebruik van een exces van blok copolymeer tot dendrimeer alleen resulteerde in micellen voor dendrimeer generaties groter dan generatie 5.

In **Hoofdstuk 6** bediscussiëren we als laatste de belangrijkste resultaten van de vier experimentele hoofdstukken en de implicaties daarvan. Ook laten we een aantal voorbeelden zien ter discussie. We geven een vooruitblik voor de toekomst en suggesties voor vervolgonderzoek om te eindigen met een algemene conclusie.

Acknowledgements

So, this is it, the acknowledgements section. Four years of research yielded this thesis, which, of course, could not have been done without the help of many people, some of whom I'd like to acknowledge specifically. I would have liked to include everyone who ever helped me, but many of you know that my memory is similar to that of a goldfish. Therefore, I tried to include and address the people who helped me most — directly or indirectly — in this section, but bear with me if I forgot a name.

First of all, I am grateful to my promotor and co-promotor for guiding me through the process of doing a PhD. Aldrik, your passion for research and art (and especially the combination of both) is inspiring! It helped me to stay motivated throughout the past four years, while finishing up my experiments, and while writing my thesis. I appreciated your feedback, our scientific discussions and your standards with respect to scientific publications, which improved the quality of our work tremendously. I valued the amount of freedom that you gave me, and appreciated you having faith in me that switching topics halfway would still yield a thesis that was finished in time and contained a significant scientific contribution. Fijs, I am thankful for your advice and feedback on the projects that I worked on. I valued your direct way of giving feedback and your suggestions toward my thesis. Although not much of my work done in Leiden is included in this thesis, I was grateful for the opportunity to collaborate with you, that I learned flow cytometry, and that gained more experience with confocal microscopy.

Regarding BioNT, I would like to start with thanking some of the ‘Office 1044’ crew. The number of inside jokes that originated in 1044 was special, and those contributing will always be remembered. Vittorio, you’ve been my office mate for most of my PhD, and I appreciate your input on my thesis, our scientific — and the less scientific — discussions, and your broad interests that range from assembling 3D printers, to our ant colony and the diverse selection of music that we listened to in the office. Laura, you’ve been part of 1044 as well, and you liked it, rright? Especially the moments when I tried to explain a (mushroom) joke, you did not seem to get that I was a fun guy… Anyway, sometime soon you will miss my *morel* support. When thanking office 1044, I should also extend my gratitude to the neighboring offices, which probably wished the walls were better sound-proofed, and non-magnetic.

Starting with the BioNT-ABC: Anton, thank you for everything that you have done, for the scientific discussions and for helping out whenever necessary! Banu, thank you for your help with the logistical part of my PhD, with booking conferences, and with printing and sending out the draft of my thesis when I was in Florida. Camilla, your Italian enthusiasm and your sense of humor are much appreciated.

Julia, I really loved our (societal and scientific) discussions, and admired your preparation and planning skills, both at work as well as during our climbing trips. Stan, your humor and your brewing (and driving) skills were very much appreciated! Gerben, your view on both life and doing a PhD are encouraging, and your musical talent seemed to progress over time! ;) Koen, now that I finished my PhD, the honorable title of “quantum dot bakker” is yours, enjoy!

Pieter (*met baard*), your NMR knowledge has been a great help during my PhD, both on the technical side, with getting experiments to run, as well as with explaining to me how NMR works! Your alternative facts and ideas on many different topics were food for thought! Maria, thanks for introducing- and showing me how to DOSY spectroscopy! Rosa, even though you did most of your PhD in Spain, it was great having you around in the lab for a couple months! Suzanne, you are a wonderful person to work, discuss science, and drink a beer with. Stay awesome! ☺

I should not forget to thank all of the BioNT students; it was fun having you guys around in the lab! I valued the discussions and interactions that we had, both scientifically as well as during Friday afternoon drinks.

I would like to thank my co-authors as well, as your contributions have been important for finishing this work. Specifically, Junyou, thank you for working with me on the dendrimicelle project; I really value the work that we did together, the efficiency with which we collected a large amount of data in just a couple of weeks, and the discussions we had! In the end, our collaboration led to two published papers so far, and hopefully to more in the future! Matthias, thank you for working with me on the data analysis of the cryoTEM images, and for the useful discussions we had on how to represent the data! Of the IMI-lab in Leiden: Silvia, Mark and Tessa, I'd like to thank you for help with the confocal microscopy and the flow cytometry experiments that I did in Leiden. Mick, besides your scientific contributions, I greatly appreciated your sense of humor and your jokes! Danny, it was always great talking to you, especially those moments in the lab, with your music on the background!

I would also like to thank the Physical Chemistry and Soft Matter group for their help and support, especially during the first years of my PhD. In particular, many thanks to the three queens of PCC: Mara, Anita and Josie. Thank you for your support, your help and the conversations that we had! Anita, I really appreciated you helping me out with getting some documents signed! Josie, I appreciated you showing interest in everyone's (PhD) life, and for always being positive! Mara, you are a special person, and you know it. Thanks for everything that you have done, from ordering chemicals, *etc.*, to the good conversations that we had. Pieter (*zonder baard*), I appreciate going to the gym with you; your constant motivational support (*i.e.*, in the form of references to South Park) was delightful, and I appreciate the shenanigans that we've been up to! At some point I might finally figure out what exercise trains what muscle. ;)

I would also like to thank Marcel Giesbers and Jan van Lent for their help with the (cryo-) Transmission Electron Microscopy. Jan, thank you for all your help troubleshooting the cryoTEM sample preparation issues, for providing suggestions and for helping me with the various issues that encountered during cryoTEM.

I would also like to thank my friends, Alex, Eduard, Martin and Jan for their support and for always being there. Maybe it wasn't so bad that I was busy finishing my PhD, I think our average bowling score increased…

Although BioNT was like a family to me, I should also acknowledge my actual family: Pa en Ma, zonder jullie support zou deze thesis waarschijnlijk niet mogelijk geweest zijn. Ik ben jullie ontzettend dankbaar voor alles wat jullie voor mij gedaan hebben, en nog steeds doen. Ik kan geen betere manier vinden om jullie te bedanken, dan door deze thesis aan jullie op te dragen. Rianne, binnenkort zijn wij allebei ‘dokter’, maar gelukkig wel een verschillend soort dokter. Ik wil je bij deze bedanken voor je hulp en support tijdens mijn promotietraject.

Kelsey, I think I should finish with thanking you. You have been a constant supporter throughout my thesis, and I am really grateful for that. Your support, tips, patience, and motivation made writing my thesis way easier! I am very grateful for you reading through my papers and drafts, and for spotting the spelling and grammar mistakes, even though the content was a mystery to you. ;)

About the Author

Jan Bart ten Hove was born on August 3rd 1990 in Ede, The Netherlands. He obtained his bachelor's degree in Molecular Life Sciences from Wageningen University in 2011, for which he completed a thesis in the Organic Chemistry Group, working on surface-initiated polymerization of polystyrene brushes. He then obtained his master's degree in Molecular Life Sciences from Wageningen University, with a specialization in Physical Chemistry. He completed his master's thesis in the Sprakel Lab, where, under the supervision of Dr. Appel and Dr. Sprakel, he worked on the synthesis of polyfluorene shells on colloidal templates. During his master's internship he worked in the Solid Mechanics, Design and Manufacturing group of Dr. Angelini at the University of Florida, where he studied the effect of symmetry and geometry on the collective migration of cells on a lattice. In 2013 he joined the Laboratory of BioNanoTechnology, Wageningen University, and the Interventional Molecular Imaging laboratory, department of Radiology, Leiden University and Medical Center, where he started his PhD work under the supervision of Prof. Dr. A.H. Velders and Dr. F.W.B. van Leeuwen. The result of his PhD thesis is this thesis.

List of Publications

“Size-sorting and pattern formation of nanoparticle-loaded micellar superstructures in biconcave thin films” **Jan Bart ten Hove**, Junyou Wang, Matthias N. van Oosterom, Fijs W.B. van Leeuwen, Aldrik H.Velders, *ACS Nano*, **2017**, 11, 11225-11231

“Dendrimer-encapsulated nanoparticle-core micelles as modular strategy for particle-in-a-box-in-a-box nanostructures” **Jan Bart ten Hove**, Junyou Wang, Fijs W.B. van Leeuwen and Aldrik H. Velders. *Nanoscale*, **2017**, 9, 18619-18632

“All-Aqueous Synthesis of Silica-Encapsulated Quantum Dots with Functional Shells” Huanhuan Feng, **Jan Bart ten Hove**, Tingting Zheng, Aldrik H. Velders, Joris Sprakel, *European Journal of Inorganic Chemistry,* **2017**, 5152-5157

“Obtaining control of cell surface functionalizations via Pre-targeting and Supramolecular host guest interactions” Marcus. T M Rood, Silvia Spa, Mick M Welling, **Jan Bart ten Hove**, Danny Michel Van Willigen, Tessa Buckle, Aldrik H. Velders, Fijs W.B. van Leeuwen. *Scientific Reports*, **2017**, 7:39908

“Assembling quantum dots via critical Casimir forces” Emanuele Marino, Thomas E Kodger, **Jan Bart ten Hove**, Aldrik H. Velders and Peter Schall, *Solar Energy Materials and Solar Cells*, **2016**, 158, 154-159

“Mechanical properties derived from phase separation in co-polymer hydrogels” Ryan Michael Nixon, **Jan Bart ten Hove**, Adrian Orozco, Zechariah Jenkins, P.C. Baenen, Marina Wiatt, J. Zuluaga, Gregory W. Sawyer, Thomas Ettore Angelini, *Journal of the Mechanical Behavior of Biomedical Materials*, **2015**, 55, 286-294

“MMP-2/9-Specific Activatable Lifetime Imaging Agent”, Marcus T M Rood, Marcel Raspe, **Jan Bart ten Hove**, Kees Jalink, Aldrik H. Velders, Fijs W.B. van Leeuwen, *Sensors*, **2015**, 15, 11076-11091

“Temperature Controlled Sequential Gelation in Composite Microgel Suspensions”, Jeroen Appel, Niek de Lange, Hanne van der Kooij, Ties van der Laar, **Jan Bart ten Hove**, Thomas E Kodger, Joris Sprakel, *Particle and Particle systems Characterization*, **2015**, 32(7)

“Conjugated Polymer Shells on Colloidal Templates by Seeded Suzuki–Miyaura Dispersion Polymerization”, **Jan Bart ten Hove**, Jeroen Appel, Johanna M. van der Broek, Alexander Kuehne, Joris Sprakel, *Small*, **2014**, 10(5)

“Nanoparticles Reveal Extreme Size-Sorting and Phase-Transition of Dendrimicelles in Biconcave Thin Films” **Jan Bart ten Hove**, Matthias N. van Oosterom, Fijs W.B. van Leeuwen, Aldrik Velders, *Manuscript submitted*

“Synthesis and characterization of size-controlled, water-soluble gold nanoparticles using UV-induced phase transfer” **Jan Bart ten Hove**, Laura Schijven, Junyou Wang, Aldrik H. Velders, *Manuscript in preparation*

“Monitoring Global and Local Motion in Biconcave Thin Films with Gold Nanoparticle Containing Superstructures” **Jan Bart ten Hove**, Fijs W.B. van Leeuwen and Aldrik Velders, *Manuscript submitted*

Overview of completed training activities (VLAG)

Discipline specific:

CHAINS-2014	NWO	2014
CHAINS-2015	NWO	2015
Microscopy and Spectroscopy in Food and Plant sciences	EPS	2014
Advanced Chemistry Course 2014-2015	VLAG	2014-2015
Interventional Molecular Imaging Symposium	LUMC	2015
Basic and Cryo Electron Microscopy	WEMC	2014-2016
Lunch Lecture Electron Microscopy Oral Presentation	WEMC	2016
NMR-DG	WUR	2016
CHAINS-2016	NWO	2016
CHAINS-2016 Oral Presentation		2016
ACS Meeting April 2017	ACS	2017
CHAINS-2017	NWO	2017
CHAINS-2017 Poster Presentation	NWO	2017

General Courses:

VLAG PhD week	VLAG	Oct 2014
Scientific writing	WGS	June 2016
Techniques for writing and presenting a scientific paper	WGS	Sept 2016
Career Orientation	WGS	Oct 2017

Optional:

Preparation of research proposal	BNT	2014
PhD study tour to UK	PCC / BNT	May 2015
Weekly group meetings	BNT	2014-2017
LUMC project discussion meetings	BNT	2014-2017

The research described in this thesis was financially supported by the Netherlands Organisation for Scientific Research (NWO), under the MONALISA project with project number 717.013.006.

Cover designed by the author

Printed & Lay Out by Proefschriftmaken.nl | | Digiforce Vianen

Propositions

1. Modular strategies are crucial for the systematic investigation of self-assembled nanostructures. (this thesis)
2. Charge-stoichiometry should not be assumed when adding equal amounts of positive and negative charge. (this thesis)
3. Progress in science is hindered by the limited opening hours of university buildings. (*Personality and Individual Differences*, Volume 47, Issue 7, **2009**, 685-690)
4. The increased use of social media decreases the social skills of people. (*Cyberpsychology, Behavior, and Social Networking*, Volume 14, Issue 4, **2011**, 253-258)
5. Passion for research should be the main motivation for doing a PhD. (Litalien, D.; Guay, F. *Contemporary Educational Psychology* **2015**, 41, 218-231)
6. Net neutrality should be a fundamental right.
7. The equality of votes in a democracy compromises its functioning.

Propositions belonging to the thesis, entitled:

“Mesoscale Organization of Nanoparticle Assemblies: Looking Into Superstructures and Aggregates”

Jan Bart ten Hove

Wageningen, April 20, 2018